Computational Investigations of Atmospheric Pressure Discharges

A thesis for the degree of

PHILOSOPHIAE DOCTOR

Presented to

DUBLIN CITY UNIVERSITY

By

Muhammad Munawar Iqbal
School of Physical Sciences
Dublin City University

Research Supervisor:
Prof. M. M. Turner

External Examiner: Prof. M. G. Kong
Internal Examiner: Dr. Paul Swift

July 2009

Declaration

I hereby certify that this material, which I now submit for assessment on the programme of study leading to the award of Philosophiae Doctor is entirely my own work, that I have exercised reasonable care to ensure that the work is original, and does not to the best of my knowledge breach any law of copyright, and has not been taken from the work of others save and to the extent that such work has been cited and acknowledged within the text of this work.

Signed.....

Muhammad Munawar Iqbal
ID No. 55130810
Date. 6 July, 2009

Abstract

This research work presents the numerical simulations of multispecies multi-dimensional fluid model of atmospheric pressure discharge. The semi-implicit sequential iterative scheme is used to solve the coupled system of plasma fluid model equations with a proper set of boundary conditions. A one-dimensional self consistent drift-diffusion fluid model is developed to investigate the characteristics of atmospheric pressure discharge in pure helium and He-N_2 gases. The uniform atmospheric pressure glow and Townsend discharge modes are examined under different operating conditions. The intricate dynamic patterns are evolved with the temporal evolution of discharge current densities at lower frequencies ($\lesssim$7 kHz), which represent the discharge plasma operation between atypical lower and higher ionization modes in several consecutive cycles. To deduce different aspects of internal distributions of atmospheric pressure discharge, a two-dimensional fluid model is advanced with symmetric boundary conditions in the parallel plate reactor geometry. The filamentary and uniform behavior of discharge is emerged by the presence and removal of specific imposed conditions in APD. The periodic stationary pattern of various discharge parameters are exhibited at different times during the prebreakdown, breakdown, formation of cathode fall layer and decay phases. The Penning ionization process performs an outstanding role during the different phases of a complete cycle, which is explored with the temporal evolution of averaged chemical reaction rates. The analysis of spatio-temporal species distribution demonstrates that they are distinguished with their distinctive properties in various regimes of APD.

In the presence of bulk gas flow, the two-dimensional symmetric uniform distributions of discharge species are transformed into non-symmetric form. The transport effects of heavy species, such as He^+, He_2^+, N_2^+, He^* and He_2^* are considered for the numerical solution of gas temperature equation and the numerical magnitude of gas temperature in the glow mode decreases with the increase of imposed bulk gas flow speed. The temporal profiles of discharge current density provide an insight in different bulk gas flow regimes, which are elucidated with the spatial structures of discharge species densities in the uniform, filamentary and constricted filamentary modes of APD. Finally, the three-dimensional fluid model is developed and employed to describe the space and time variations of discharge variables in the uniform and filamentary discharges. The homogeneous uniform slice distributions of electrons density are compared at different frequencies, which show the trapping of electrons in the positive column at higher frequencies. The non-uniform distribution of axial electric field illustrates that the field strength is higher in the constricted part than the smooth part of the dielectric barrier surface. The shape and configuration of filaments exhibit that they are directed from the anode towards the cathode barrier in the filamentary APD. The noticeable structures of filaments are prominently observed from 5 to 20 kHz than higher frequencies because of the coalescence of filaments at higher frequencies, leading to the formation of uniform APD. The temporal evolution of discharge current density exhibits that it represents the composite behavior in different driving frequency regimes from 20 to 100 kHz. The numerical simulation study reveals that it is useful to deliver a satisfactory information for the uniform and filamentary atmospheric pressure discharges, and describes the origin of non-uniformities.

Acknowledgements

First of all, I would like to express profound gratitude to my supervisor, Prof. Miles Turner, for his invaluable support, encouragement, supervision and stimulating suggestions throughout the postgraduate research work. His moral support and continuous guidance enabled me to complete my postgraduate thesis successfully.

During my stay in NCPST, I have benefited from many people, either directly or indirectly. I wish to acknowledge NCPST members Dr. Derek Monahan, Dr. Chanel Hayden, Dr. Shane Linnane and Dr. Vic Law as well as my fellow research student Huw Leggate.

I am also thankful to all administrative staff members, Sarah Hayes and Sheila Boughton for their help and support regarding different departmental matters. I am also thankful to project manager, Samantha Fahy for the guidance and moral support whenever I needed. Special thanks to Ray Murphy for his assistance dealing with the network problems and software installations.

I am grateful to Prof. Bill Graham for hosting my research visits in the Queen's University Belfast. During that time, I had the chance to learn the operation of large experimental chamber for the atmospheric pressure dielectric barrier discharges. I did number of discussions with different plasma physics experts to discuss several aspects of atmospheric pressure discharge during the conference sessions.

I would like to acknowledge and appreciate my wife Farah for her dedication, support, love and all the joyfulness she provides in my life. I want to thank my mother and father for all the betterment they brought and are still bringing in my life. I am thankful to my brother, Mubasher Iqbal for his encouragement during postgraduate studies. I am also grateful to my sister, Mehvish Iqbal (Late) for true moral support during her life.

List of Presentations and Papers

- Characteristics of atmospheric pressure discharge using a two-dimensional fluid model, Contributed paper in XXIX ICPIG, Cancun, Mexico, 12 - 17 July, 2009.
- Numerical simulations of atmospheric pressure discharge using a three-dimensional fluid model, Contributed paper in XXIX ICPIG, Cancun, Mexico, 12 - 17 July, 2009.
- Poster presentation, 62nd Annual Gaseous Electronics Conference, Saratoga Springs, NY, USA, October 20 - 23, 2009.
- Poster presentation, 19th IPBPG Annual Conference, 28 - 29 May, 2009, QUB, Belfast, U.K.
- Poster presentation, 61st Annual Gaseous Electronics Conference, Dallas, Texas, U.S.A, October 14 - 17, 2008.
- Poster presentation, 19th European Conference on the Atomic and Molecular Physics of Ionized Gases, Granada, Spain, July 15 - 19, 2008.
- Oral presentation, 18th IPBPG Annual Conference, 8 - 9 May, 2008, NCPST, DCU, Ireland.
- Oral presentation, 2nd NCPST Research Postgraduate Seminar, 25th April, 2008, NCPST, DCU, Ireland.
- Oral presentation, Atmospheric Pressure Discharge Plasma Meeting, 5th February, 2008, UCD, Dublin, Ireland.
- Poster presentation, 5th Technological Plasma Workshop, Queen's University, 18 - 19 December, 2007 (TPW07), Belfast, U.K.
- Poster presentation, Plasma Processes for Biomedical Applications, 24th May, 2007, Plasma Physics, NCPST, DCU, Dublin, Ireland.
- Oral presentation, 34th IoP Annual Conference on Plasma Physics, 2 - 5 April, 2007, NCPST, DCU, Dublin, Ireland.
- Poster presentation, 4th Technological Plasma Workshop, 14 - 15 December, 2006 (TPW06), School of Chemistry, University of Manchester, Manchester, U.K.
- Oral presentation, First Postgraduate Seminar Series, 22 September, 2006, NCPST, Dublin City University, Dublin, Ireland.
- Oral presentation, Atmospheric Pressure Discharge Plasma Workshop, 15 June, 2006, NCPST, DCU, Dublin, Ireland.
- Oral presentation, Atmospheric Pressure Discharge Plasma Meeting, 4th April, 2006, Queen's University, Belfast, U.K.

Contents

[1] APGD: Atmospheric pressure glow discharge
[2] APTD: Atmospheric pressure Townsend discharge

[3] **APD: Atmospheric pressure discharge**

List of Figures

[4]

[4]Some figures in this thesis are in multiple colours and can view only in electronic version.

List of Tables

List of Symbols

APD	Atmospheric pressure discharge
APG	Atmospheric pressure glow
APT	Atmospheric pressure Townsend
APGD	Atmospheric pressure glow discharge
APTD	Atmospheric pressure Townsend discharge
SEEC	Secondary electrons emission coefficient
BOLSIG+	Boltzmann solver
EME	Electron mean energy
BL	Barrier length
BW	Barrier width
GW	Gap width
SG	Scharfetter-Gummel
SOR	Successive over relaxation
MSI	Modified strongly implicit
ADI	Alternating direction implicit
kHz	Kilo Hertz
ppm	Parts per million
Re	Reynold number
M	Mach number
d1×d2	Area of cross section of parallel plate reactor
CF	Cathode fall
NG	Negative glow
FDS	Faraday's dark space
PC	Positive column
kV	Kilo volt
mA	milli ampere
RC	Recombination coefficient
FDM	Finite difference method
CFL	Courant-Friedrichs-Lewy
CGS	Centimetre-gram-second system

[5]

[5] CGS: Centimetre-gram-second system of units is used throughout this thesis for the representation of units of various physical quantities

Chapter 1

Atmospheric Pressure Discharges

1.1 Introduction

The plasma discharge is an immediate and transient electric current that travels between two bodies of opposite potential created by any source. The nomenclature "plasma discharge" is linked with the configuration of capacitor that comprises of two electrodes, which are separated by a partially ionized gas. The properties of a discharge plasma, such as color, intensity, efficiency and applicability are dependent on the operating gas, which exists between the electrodes. During the discharge progress, the breakdown of gases occurs in the open reactor when the large potential difference is applied between the objects. As a result, the electrons and ions start moving towards their respective anode and cathode electrodes. The ionization, excitation and other chemical processes are progressed at enormous rate and ultimately form a discharge plasma. Due to the emission of lights of different colors, the discharge illuminates in the gap and the cathode electrode looks like burning. Generally, the typical features of discharge plasma critically depend on the frequency or modulation of current. The gas discharge plasma can exist in different mediums when there is a constant supply of electrical energy from the external power source. The stationary-state of discharge plasma is developed when the ionization rate exceeds the recombination rate in the gas, which can be used effectively for the discharge plasma applications in different branches of science. The recombination events are formed with the collisions of gas atoms and molecules, which associate with the gas pressure during the discharge operation.

In this chapter, section 1.2 discusses different types of the electrical discharges in gases. Section 1.3 explains the important collision interactions in the atmospheric pressure discharges. Section 1.4 describes the drift and diffusion of charged particles. Section 1.5 provides an insight in the breakdown mechanism and criterion for breakdown using Paschen's law. Section 1.6 expresses the operation of electrical model

of dielectric barrier discharge. Section 1.7 enhances the concept of computational modelling of discharge plasma. Finally, in section 1.8, we define the scope of the research work presented in this thesis and give an outlook over the following chapters.

1.2 Electrical discharges in gases

An electrical discharge is the transit of electrical current through a material which normally acts as an insulator. To understand this process, a simple experiment is performed with two linked wires. The wires are separated by a small distance and clip each to one terminal of a battery. There is no flow of current between the wires because the air acts as an insulator. If the applied voltage of battery is increased to few hundred volts for very small gap, i.e., few cm, the sparks will travel between them. This exhibits that the breakdown of air has occurred and transformed into the conductive medium. The air is a mixture of nitrogen, oxygen and other gases, in which the electrons are bound to the atomic nuclei. During the breakdown process, some of the negatively charged electrons are ejected from their parent atoms and molecules, and leaving them with a positive charge particles. The negatively and positively charged particles are then free to move separately under the influence of the applied voltage, moreover the movement of charged particles establishes an electrical current. The collection of ions and electrons is known as a plasma discharge, and one of its more important properties is that a plasma can conduct electrical current [1].

The complex gas discharge plasma is categorized into number of disciplines that depend on the pressure, gas and electrode configurations. The novel field of discharge plasma is employed with the passage of electric current in any conductive gaseous medium by implying any external power source. The present thesis work deals with the atmospheric pressure discharges under specific imposed conditions. So, the major branches of atmospheric pressure discharge are divided into the following categories

- Corona discharges
- Arc discharges
- Atmospheric pressure glow and Townsend discharges

The corona is defined as a discharge, occurring when a highly inhomogeneous electric field is imposed. Typically, there is a very high electric field adjacent to a sharp electrode, and a net production of new electron-ion pairs occur in this vicinity. The corona discharge has a very low current, and very high voltage [2]. The arc discharge is an electrical breakdown of a gas which produces an ongoing plasma discharge, resulting from a current that is flowing through normally nonconductive media, such as air.

The phenomenon was first described by Vasily V. Petrov, a Russian scientist who discovered it in 1802 [3]. The various shapes of electric arc are observable properties of nonlinear patterns of current and electric field. The arc occurs in the gas-filled space between two conductive electrodes and it results in a very high temperature, which is capable of melting or vaporizing most of the materials. An electric arc is a continuous discharge, while a similar electric spark discharge is momentary. The electric arc may occur either in direct current circuits or in alternating current circuits. The electric arc has distinct structure in which the current density is quite high, and the voltage drop within the arc is small; at the cathode, the current density may be as high as one million amps per square centimeter [5].

The last type of discharge plasma captured a great attention since its discovery. The stable, large volume and highly non-equilibrium characteristics of dielectric barrier discharge are evolved and sustained under suitable conditions at atmospheric pressure. It is highly usable and attractive for the number of industrial applications, such as sterilization of biological samples [6], deposition of thin films [7], surface modification and etching [8], aerospace and aerodynamics applications [9, 10], pollution control [11], ozone generation [12, 13] and plasma display panels [14] prevail at various pressures, which can be used without any restrictions of low-pressure discharge plasma. The gas discharge plasmas are diagnosed and employed for different purposes to understand the basic physical insight and to apply as a tool in the application industry, such as in the lighting industry as well as in electrically excited gas lasers. The new applications in gas insulation, in high-power electrical switching, and in materials reclamation and processing are continuously modified with a consistent effort to better comprehend all aspects of the gas discharges.

In order to investigate and improve the properties of atmospheric pressure discharge, it is essential to identify and explore the fundamental characteristics and perception of discharge plasma applications. The computational modeling tool is very attractive and result-oriented in the field of discharge plasma physics to describe the nature and internal dynamics of different physical phenomenon. This research work provides an analysis of discharge modelling in different regimes and applies with the help of fluid modelling technique for the attributes of the atmospheric pressure discharges.

1.2.1 Domains of atmospheric pressure discharge

The atmospheric pressure discharges are classified into three major domains, i.e., partial discharges, lasers and cold plasma processing [15]. The partial discharge and laser branches are not the topic of interest in this research thesis but the major emphasis is on the non-thermal plasma discharges. There are some important and interesting properties of non-thermal discharge plasma, which produce under variable conditions of atmospheric pressure discharge. The electrons have very smaller temperature of few electron volts, gas at room temperature and lower frequency regime [16]. The attractive and

useful type of discharges are the uniform atmospheric pressure discharges. It further divides into two modes, such as glow and Townsend modes. The glow and Townsend discharges are two different kinds of uniform discharge plasma, containing a variety of plasma species, i.e., electrons, ions, atoms, excited and molecular species. The plasma species can in principle collide with each other, which give rise to a large number of plasma interactions. As the glow and Townsend discharges are employed for the analytical purpose, they mostly consider different gases as a discharge operating gas. However, the modeling work in this thesis is concentrated in pure helium gas and in the presence of small amount of nitrogen impurities. The major and important chemical processes, occurring in a helium glow and Townsend discharge will be described here. In addition to the most important collision processes in the bulk plasma, an overview will be given of the different collisional processes, developing at the walls of the glow and Townsend discharge chamber.

1.3 Collision interaction of discharge species

As the weakly ionized plasma is composed of large number of species, these species can move in random directions and collide with each other. The number of plasma processes are tremendous and probably not all processes are known in the literature. It is therefore not feasible to give a systematic and comprehensive overview of all the possible chemical reaction processes. We will explain the most important and relevant processes for the uniform and filamentary discharges, i.e., elastic and inelastic collision processes. All other categories of electron collision processes are inelastic and the major inelastic collision processes are of different types, such as excitation and different types of ionization, deexcitaion and recombination. The discharge plasma species, such as electrons, single positive atomic and molecular ions play an important role for the description of atmospheric pressure discharges and the physical explanation of these processes are discussed in number of text books [17, 18] for different gases. The collision processes involving multiple charged particles and molecules will be considered in this analysis.

1.3.1 Elastic collisions

Elastic collisions conserve kinetic energy and momentum during the interaction of any type of particles, i.e., charged and neutral particles. The internal energy of collision species is not changed but only readjust and exchange the kinetic energy of particles. This redistribution is considerable for the species with comparable masses but it is negligible for the particles with very different masses. An elastic collision is represented symbolically as

$$B + e^- \longrightarrow B + e^-$$

where B shows the neutral gas atom and e^- is the electron in the above chemical reaction.

1.3.2 Ionization and excitation

The electron impact ionization and excitation are the most important and dominant processes in the atmospheric pressure discharges. They are represented respectively by the following equations as

$$\begin{aligned} B + e^- &\longrightarrow B^+ + e^- + e^- \\ B + e^- &\longrightarrow B^* + e^- \end{aligned}$$

In different gases, the ionization of atoms and molecules by an electron impact is the source of production of charge carriers in the bulk of gas discharge. The rate of ionization is defined as

$$\left(\frac{dn_e}{dt}\right)_i = \nu_i n_e = k_i n_g n_e \tag{1.1}$$

where ν_i is the ionization frequency, n_g is neutral gas species density, k_i is called as the rate constant, which represents the number of ionization events performed by an electron per second. The ionization process is essential for the self-sustaining of discharge because it is a source of creation of electrons, which ultimately leads to the electron multiplication. When an electron collides with the neutral atom B, it may eject the electron from the atom and ultimately, the atom becomes positively charged ion. For helium, 19.8 and 20.6 eV are the excitation potentials for the singlet and triplet states of metastables. The minimum electron energy required for the first ionization potential is 24.58 eV, whereas the second process can already occur at electron energies above 4.0 eV. Although, the first process is much more important in atmospheric pressure discharge due to the much higher density of helium ground state atoms as compared to the density of helium metastable atoms [4, 18].

The mechanism of electron impact excitation is the same as for the ionization but less energy is transferred to the atom, so that no electron can be ejected, it can only jump to a higher energy level within the atom. The total cross section of electron impact excitation as a function of the electron energy shows the same behavior as for the case of electron impact ionization.

1.3.3 Stepwise ionization

$$B^* + B^* \longrightarrow B^+ + B + e^-$$

When two helium metastable atoms collide with each other, they have together sufficient energy (2 times 19.80 eV) to knock off one electron and to bring about the ionization of one of the atoms. The process is very useful and changes the behavior of atmospheric pressure discharge.

1.3.4 Penning ionization

The Penning ionization process is the most prominent and effective in a mixture of gases. For example, when a metastable atom or excimer collides with a neutral nitrogen molecule (N_2), the neutral molecule can become ionized if its ionization energy is less than the excitation energy of the excited atom [19]. Assume the nitrogen is used as an impurity in the inert gases with the consideration of above condition, the reaction can be written as

$$\begin{aligned} B^* + N_2 &\longrightarrow B + N_2^+ + e^- \\ B_2^* + N_2 &\longrightarrow 2B + N_2^+ + e^- \end{aligned}$$

1.3.5 Associative ionization

This process is discovered by Hornbeck and Molnar in 1951 [20]. It is important in the inert gases and the symbolic representation is

$$B + B^* \longrightarrow B_2^+ + e^-$$

The electrons are free to move with the release of small binding energy of ~ 1 eV in association with an ion and an atom into a molecular ion.

1.3.6 Ion conversion

$$B^+ + B + B \longrightarrow B_2^+ + B$$

When the positive ions collide with the neutral gas atoms, the gas atoms are converted into molecular gas ions as well as neutral gas atoms [21].

1.3.7 Deexcitation

$$B^* + e^- \longrightarrow B + e^-$$

The excited states of gas atoms return to their ground state with the release of large amount of energy. As the recombination is the inverse of ionization, similarly deexcitation is the inverse of excitation. Although, except from the metastable levels, the excited levels of the atoms have short life time, and the electrons return to the ground state in one or several transitions. The photons are emitted during the transitions of electrons from different energy levels. Our eyes can possibly detect the photons, which have energy in between 1.7 and 3.0 eV. Hence, the deexcitation processes produce a glow and, therefore they are responsible for the characteristic name of the atmospheric pressure glow discharge [21].

1.3.8 Dissociative recombination

The dissociative recombination occurs as a very fast process in the weakly ionized plasma and can be written as

$$B^+ + e^- + e^- \longrightarrow B + e^-$$

The electron-ion recombination is the reverse process of ionization, i.e., an electron combines with a positive ion to form a neutral atom. From the conservation laws of momentum and energy, it follows that a simple two-body coalescence is not allowed. However, some alternative recombination processes can also occur during the coalescence. There are different types of channels in the atmospheric pressure discharges for the dissociative recombination.

$$B_2^+ + e^- \longrightarrow B^* + B$$

When the helium ion is molecular, a two-body recombination process is possible because the collision product can dissociate and the recombination energy is converted into kinetic and potential energy of the dissociation products [22].

1.3.9 Processes occurring at the walls

When the gas particles strike with the walls of dielectric barrier, different types of phenomena may occur, depending on the type of particle. An electron may be reflected, absorbed or cause the emission of secondary electrons. The ions or neutrals may be reflected, implanted, cause secondary electrons emission or knock out one of the wall atoms. The latter two processes are of special importance for the glow discharge, and will therefore be discussed in more detail. However, the secondary electrons emission can possible only from the surface of dielectric barriers, whereas sputtering is more or less concerned with the material of cathode barrier because the high energy particles are essential for this process. As the electrodes are covered with the dielectric barriers of variable permittivity for different case studies, different materials have variable secondary electron emission coefficients.

1.3.10 Secondary electrons emission

When a particle strikes with the barrier surface, an electron can be emitted. Therefore, it is defined as the ratio of the number of secondary electrons emitted from the dielectric barrier surface to the incident primary particles. This process is especially important to maintain the glow discharge, i.e., new electrons can be supplied to compensate for the electron losses at the walls. Secondary electrons emission may be caused by the bombardment of electrons, ions, neutrals and photons under different conditions of

discharge plasma. The number of electrons emitted per incident particle is called as the secondary electron emission coefficient. It depends on the kind of bombarding of particles and their energy, and on the type of wall material. Normally, the secondary electron emission coefficient for helium and molecular nitrogen ions is considered in the present research work, i.e., 0.01 for pure helium and He-N_2 gas mixture [23], instead of some special cases. The effect of secondary electron emission coefficient can be analyzed by the evolution of different discharge parameters.

1.4 Drift and diffusion of charged particles

1.4.1 Drift of charged particles

A weakly ionized gas consists of charged and neutral particles, which can randomly move in various directions of gas chamber. When an electron collides with a neutral atom, it may produce the electrons and positive ions, which accelerate along the direction of electric field. The collisions perform an important role to change the directions of colliding particles in the ionized gas. The collisions between the charged particles are distinctive in the above mentioned plasma, moreover the neutrals and electrons sharply collide and enhance the ionization and excitation processes in the gas. The motion of charged particles along the direction of external imposed electric field is called a drift. Due to drift, the average drift velocity of charged particles is given by

$$\mathbf{v}_d = -\frac{e\mathbf{E}}{m\nu_c} \tag{1.2}$$

where $\mathbf{E}$ is the electric field in the discharge plasma, m is the mass of the particle, e is the charge on the particle, ν_c is the collision frequency of momentum transfer.

1.4.2 Mobility of charged particles

The random or thermal motion of charged particles has remarkable influence in the gas when the electric field is absent. However, in the plasma discharges, the electric field is present which transfers energy to the charged particles from the external applied source. Therefore, the random motion of charged particles is followed by the effect of electric field strength. In different types of discharges, the mobility of charged particles is defined as the proportionality coefficient between the drift velocity of a charged particle and the electric field. For example, the mobility of electrons is defined as

$$\mu_e = \frac{e}{m_e\nu_c} \qquad \text{and} \qquad \mathbf{v}_d = \mu_e\mathbf{E} \tag{1.3}$$

The electron mean energy is linked with the electric field of ionized discharge plasma, whereas the mobility is dependent on the electric field. The reasonable effective values of mobility (μ_e) are considered for the numerical simulation models.

1.4.3 Diffusion

Diffusion is considered as the transport of particles from higher density to lower density gradient in the plasma gas. In a similar way, the two separate gases are mixed with each other after a specific interval of time. For example, a gas contains n number of particles, moving in a specific direction, i.e., along x-axis. The concentration gradient is proportional to the total number of particles passing through the unit area of plane per second. The diffusion constant of proportionality is defined as

$$D = \frac{v^2}{3\nu_c} \tag{1.4}$$

1.5 Breakdown process in a gas

The atmosphere contains a small number of electrons and ions. At ground level, 10 - 100 positive and negative ions per cm^{-3} are present in non-electronegative gases due to the cosmic radiations in the atmosphere. The magnitude of ionization rate falls in the range of $\sim 1.0 \times 10$ cm^{-3} s^{-1} for the mentioned number density. In air, the charged particles are immediately attached with oxygen and their density increase to $\sim 10^3$ cm^{-3}. The same number of electrons and ions are available due to these sources when an electrical setup is developed for the experimental purpose at atmospheric pressure.

In equilibrium situations, the rate of creation of charged particles is approximately balanced by the rate of recombination in the absence of electric field. Assume a small voltage is imposed on the electrodes, which produces the electric field and develops a current due to the already existing electrons and ions in the chamber. The small current cannot disturb the equilibrium situation and the mobilities of particles are nearly constant under these conditions. Hence, the current density j, is proportional to E. The gas behaves like a conductor and its conductivity depends upon the rate of ion and electron production, recombination and mobility coefficient.

As the current density and electric field increase, the equilibrium is disturbed by the formation of ions and electrons. The major deficiency is observed near the electrodes, where they annihilate and increase the loss rate in the gas. So, the current decreases with the increase in voltage in these circumstances. In specific situations, the destruction of total number of charged particles near the electrode is equal to

the production. Thus, the following relation is employed for the evaluation of current density j as

$$j = de\frac{dn}{dt} \tag{1.5}$$

where d is the distance between the electrodes, e is the charge of gas particles and n is density of the charged particles per unit volume. When the saturation stage is reached, the current density possesses a very small value under these conditions. The discharge appears in quite dark form because the emission is very weak due to the lower rate of ionization. This kind of discharge is not self-sustaining because of dependence on the external source of radiation. As the voltage is further increased after saturation, the current starts increasing again after some time. The nature of this increase of current depends on the gas pressure. The current continuously increases with the rise in voltage until a breakdown voltage is reached. The value of breakdown voltage depends on the gas conditions, electrode gap, dielectric material and secondary electron emission coefficient. The characteristics between the saturation and breakdown voltage fall in the Townsend discharge regime [4].

1.5.1 Paschen's law

Paschen's discovered the relationship among the breakdown voltage, gas pressure and gap distance between the parallel plates in 1889 [1]. In his work, it is proved that the breakdown voltage of parallel plates reactor is a function of pressure and gap distance. This can be written in the mathematical form as

$$V_t = f(pd) \tag{1.6}$$

for a uniform electric field.

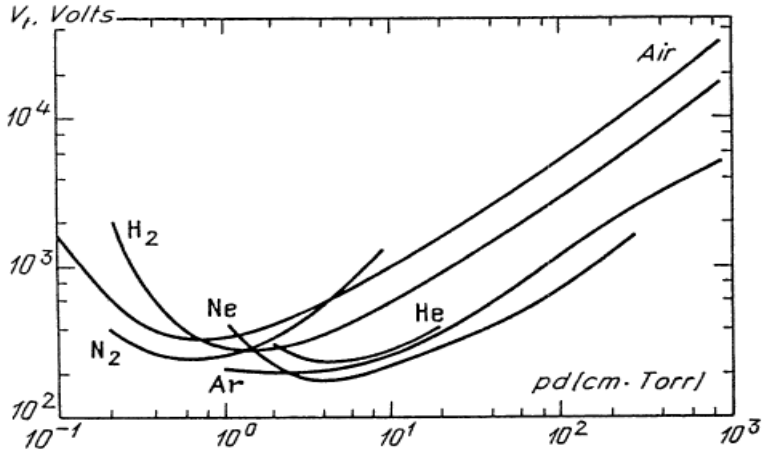

Figure 1.1. Breakdown potentials in different gases over a wide range of pd values [24, 25].

This represents the experimental relationship known as Paschen's law. The graphical curves of breakdown voltage V_t versus pd for different gases and electrode material has a unique minimum value. The smallest value of breakdown is called as the minimum sparking or breakdown potential. It has a value of several hundred volts. The graph shows some experimental curves of breakdown voltage V_t versus pd. There is huge impact on the breakdown voltage in the case of mixture of two different gases. For example, a small impurity of argon in neon atoms enhancing the ionization due to Penning effect. This kind of gas mixture is usually called as Penning mixture. The curves in figure 1.1 display the change in breakdown voltage for the specific gases. In the range of large pd on the right hand branch of the Paschen's curve, the threshold value of V_t reduces slowly as pd increases. The breakdown voltage is consistently increased with pd (slightly slower). This type of behavior emerges because in case of large gaps and elevated pressures, the electrons can produce the numerous ionizing collisions even at very reduced electric field. On the contrary, the occurrence of collisions is very small on the left-hand branch at lower pd. The ionization is possible in case of strong electric field to achieve the required amplification. The breakdown rises rapidly as pd falls. It means that the sufficient ionization is not present at very smaller pd, regardless of the electric field strength. The left-hand and right-hand branches enhance the understanding of breakdown voltage with the pd [4].

1.5.2 Time of breakdown

The breakdown of a gas acts as a final constraint of stationary-state for the Townsend criterion and Paschen's law, which maintains the condition of self-sustaining. Let us calculate the time taken by the gas for the achievement of breakdown. To understand about the individual processes, when a single electron is created from any source, it is accelerated by the electric field and produces further electrons in the gap. This process develops an electron avalanche in the reactor gap. It is termed as the transient process because the electrons production from different sources are mixed with each other. The breakdown condition means that the individual electron creates a secondary electron, which develops an avalanche without any restriction on the applied voltage.

Generally, the breakdown process is divided into two parts. First, the time used for the creation of primary and secondary electrons, which forms a weak avalanche or starts the breakdown. This is termed as the statistical time lag. Secondly, the time spent for the complete development of breakdown called as the formative time lag. The statistical time lag is defined in terms of the primary electrons produced per second from the cathode or in the gap. The source of radiation for the production of primary electrons and gap size also effect on the statistical time lag. The formative time lag is also defined as the passage of time elapsed by the positive ions from the anode towards the cathode.

The primary electrons and corresponding avalanche march fastly towards the anode because of high

electron mobility. The secondary electrons are emitted from the cathode when the positive ions strike with the cathode electrode. The time taken by the positive ions is greater than the electrons. Suppose the ions transit time is t_i. However, the number of avalanches are occurred before the current reaches to the breakdown value. The rise in current is measured in terms of t_i.

1.5.3 Breakdown at high pressure

At very high (pd), the increase in breakdown voltage (V_t) falls. Paschen's law is not very suitable for the high pressure plasma discharges. The formative time lag should be smaller or approximately equal to the ions transit time t_i. It is observed that the total time lag for breakdown at high pressure is much smaller than t_i. This supports that the breakdown not only depends on the positive ions bombardment on the cathode but the Townsend theory also plays an important role. Although, there is no evidence available for the secondary electrons emission before the breakdown. It has been noticed that the electrons originate from the cathode and move towards the anode, whereas the high luminous and concentrated streamers travel from the anode and vice versa. These types of result contradict to the Townsend criterion for high pressure breakdown.

In theory, the space charge is created by an electron avalanche. The electrons are moved abruptly and reached near the anode, whereas the ions remain at their original location, develop a concentrated positive space charge layer near the anode and crawl towards the cathode. This process may be very fast and the rapid movement of the positive space charge towards the cathode forms a streamer. The streamer reaches the cathode and produces a huge number of secondary electrons. The streamers can also start from any remote place in the gap.

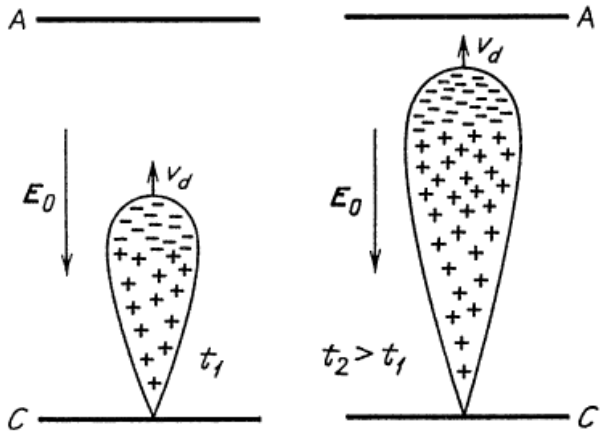

Figure 1.2. Formation of streamers at two variable instants of time [4].

Meek has discussed that the breakdown can be possible under the specific conditions, i.e., if the electric field due to the space charges is equivalent to the imposed voltage at some particular instant of time

during the discharge progression. When the space charge field, size and ions concentration of an avalanche and of the first ionization coefficient (α), comparing it to the imposed electric field, then the Meek's criterion is obtained. This provides a reasonable agreement with the experiment.

Townsend theory still provides a sufficient explanation for the breakdown. It is observed that the Townsend process may occur under specific conditions but is absorbed in the streamer process at high pressure. Townsend mechanism is possible when the applied voltage is equal to the breakdown voltage (V_t) or just exceeds (V_t) [17, 24].

1.6 Electrical model of dielectric barrier discharge

Let us consider a plane discharge gap of sufficiently large length L between the solid flat surfaces. Suppose the electrodes are insulated from the plasma by the dielectric plates, with dielectric constant ε and thickness l. For simplicity, assume $\varepsilon = 1$ in the formulation of equations. The continuity equation for the space charge density ρ, the equation of electrostatics, and Ohm's law for the conduction current in the plasma is given by,

$$\frac{\partial \rho}{\partial t} + \frac{\partial j_1}{\partial x} = 0, \qquad \frac{\partial E}{\partial x} = 4\pi\rho, \qquad j_1 = \sigma E \tag{1.7}$$

where j_1 is the conduction current density at variable distance x and E is the electric field in the gap. The total current is the sum of conduction and displacement currents and can be expressed as

$$j(t) = j_1 + j_{dis} = j_1 + \frac{1}{4\pi}\frac{\partial E}{\partial t} \tag{1.8}$$

which is free of coordinate x at each moment of time. Suppose an electrically neutral plasma is present in the gap except near the boundaries of the dielectric barriers, where the changes due to polarization are concentrated. The charges are called as surface charges. This is equivalent to assuming the homogeneity of plasma in space. For example, if $\rho = 0$, then E, j_1 and σ are independent of x. On the contrary, consider a homogeneity in the gap and the plasma is electrically neutral. The surface charge density in the plasma and electrodes are represented by q_1 and q respectively. The dielectric layers do not allow them to pass through into the plasma. The direction and sign are assigned to the charges and electric field at a certain time.

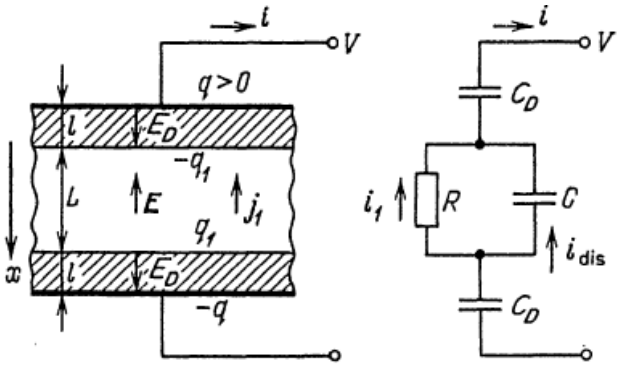

Figure 1.3. Section of discharge chamber and electrical circuit of the discharge device.

By using the general electrostatic equations, the electrode-insulator and insulator-plasma interfaces are taking into account that the field in the metal is negligible owing to its very high conductivity. It is found from the figure 1.3 that the surface charge density in the plasma and at the electrodes can be written as

$$\varepsilon E_D = 4\pi q, \qquad E - \varepsilon E_D = -4\pi q_1 \tag{1.9}$$

where E_D is the electric field in the dielecric barrier and use the continuity equation for the same boundaries, then

$$j_1 = \frac{dq_1}{dt}, \qquad \dot{q} = \frac{i}{S} \tag{1.10}$$

where i is the current in the external circuit and S is the area of the electrodes. A combination of equation (1.9) and (1.10) implies that the current *i(t)* in the external circuit coincides with the total current in each dielectric and in the gap. This exhibits the law of conservation of the total current due to conduction and displacement along the entire electric circuit.

Potential drops across the layers do not exist within the framework of the assumption of the surface nature of charges at the plasma boundaries, that is, of zero thickness of these space-charge layers. The voltage drop across the upper and lower dielectric barriers and the plasma can expressed in the mathematical form as

$$V = 2E_D l + EL \tag{1.11}$$

Equation (1.10) can be written as

$$V = \frac{8\pi l}{\varepsilon} q + \frac{j_1 L}{\sigma}, \qquad j_1 = 4\pi\sigma(q - q_1), \qquad \dot{q} = j_1, \qquad \dot{q} = j \tag{1.12}$$

which determine the current and the parameter σ is called as conductivity. The conduction current travels through the active impedance and the displacement current passes through the plasma capacitance, with $i_1 + i_{dis} = i$ [4].

1.7 Computational modelling of discharge plasma

A computational model is a mathematical model that requires extensive computational resources to study the behavior of a complex system by computer simulations. The system under study is often a complex nonlinear system for which simple, intuitive analytical solutions are not readily available. Rather than driving a mathematical analytical solution to the problem, experimentation with the model is done by changing the parameters of the system in the computer, and study the differences in the outcome of the experiments. The different types of theories of operation for the simulation model can be deduced from these computational experiments but this field is emerging with various kinds of new applications. The discharge plasma modelling is also a branch of computational modelling under idealized conditions. It is possible to explore the discharge characteristics by applying this approach. The goal of discharge modelling is to develop an understanding of the physical features and aspects of discharge plasma, such as electrical characteristics and utilization of applied power, and may be even a set of "Scaling rules" that exhibit the modification of discharge species parameters as a function of process input quantities [25, 26].

A computational model is used to represent the system of differential equations, data, and assumptions, which correspond to the original physical phenomena under specific constraints. Although, the simulation results are obtained from the numerical solution of system of differential equations under different constraints of boundary conditions. Now a days, the computational models are considered to make a bridge between the experimental and theoretical branches of physics. For example, the gas discharges can provide a useful solution with the help of computational modelling. The computer machines are excellent tools in modern industry to solve the large system of partial differential equations for various assignments. The numerical models can be used for the implementation of real time problems, like flight simulator, computational fluid dynamics simulations of flowing air, water and other fluids, etc. In the past few decades, the number of numerical models have been developed, which can be used for different research purposes successfully.

In the fluid approach, the moment equations are derived from the Boltzmann equation to describe the macroscopic quantities, such as species density, momentum and electron mean energy [27, 28, 29]. The space and time variations of these quantities provide the structure of macroscopic quantities. The implementation of secondary electron emission coefficient is considered as the boundary condition in the fluid model. To understand the influence of space charge, Poisson's equation is coupled with the moments of the Boltzmann's equation. Consequently, the discharge plasma is described by the help of above mentioned system of equations. There are some assumptions, which make the implementation of fluid models quite difficult. The system of fluid model equations depends on the input data, which is evaluated from the solution of Boltzmann equation in the uniform electric field. With the consideration

of all assumptions, the fluid theory can only be applied over a limited range of discharge conditions. However, in the case of atmospheric pressure discharge, the fluid models have proved to be very useful in helping to understand the basic discharge properties and in predicting trends [9, 11, 12, 15]. The fluid model simulations are computationally efficient and can simulate the time evolution of a discharge in multi-spatial dimensions within a manageable period of computation time.

Kinetic models describe the distribution function of particle velocity at each point in the discharge plasma and they are generally more computationally difficult and intensive than the fluid models. Particle modelling is useful method to extract kinetic information, such as distribution function, reaction rates, etc., self-consistently and to study the transport of particles across the discharge volume simultaneously. In Particle-in-cell simulation technique, the superparticles represent the position and momenta of charged particles instead of real particles and the equation of motion for superparticles is solved along with the Poisson's equation. However, the collisional effects are included by using the Monte Carlo treatment. As there are no assumptions for the Particle in cell simulations, they can be applied over a wide range of discharge conditions. The particle models require large computational effort for the numerical simulations, so they are not suitable for the complex geometries and chemistries. They are more often used to validate the fluid models for different scientific problems [26].

Another approach is now considered and applied in different scientific disciplines, usually called as hybrid models [29, 30]. In hybrid models, one part of the particles is described by the fluid model equations, and the other part is treated with a Monte Carlo simulation model. The fluid model equations satisfy the atmospheric pressure discharge conditions for their physical description. The discharge conditions of microdischarges are on the edge of what can be reliably simulated with a fluid model. However, the simulation of the rather complex operation of these discharges absolutely demands the computational efficiency of the fluid approach.

1.8 The scope of this thesis

The main objective of the research work presented in this thesis is to obtain a multi-dimensional drift-diffusion self-consistent fluid model, which is suitable for the numerical simulations of the atmospheric pressure dielectric barrier discharges, which helps to understand the uniform and filamentary behavior of discharge plasma, and which can be used as a tool for the understanding of dielectric barrier discharge operating conditions and gas composition.

Chapter 2 provides the details of the two-dimensional mathematical formulation of fluid model in the stagnant and flowing helium gas in the presence of nitrogen impurities. The boundary conditions are discussed and described for the parallel plate reactor geometry. The gas temperature equation is

also solved numerically by the effect of heavy particle species. Chapter 3 illustrates the finite difference formulation of three-dimensional fluid model and the numerical algorithm for the solution of partial differential equations in three-dimensional space. Chapter 4 examines the one-dimensional fluid model results and the spatio-temporal characteristics are explored for different sets of input parameters. Chapter 5 enhances the understanding of properties in the uniform and filamentary atmospheric pressure discharges with two-dimensional fluid model in the stagnant bulk gas. The space and time variations of discharge parameters are investigated and discussed the behavior of discharge plasma under different conditions. Chapter 6 analyzes the overall effect of bulk gas flow and the behavior of discharge plasma is explained by the influence of bulk gas flow. Chapter 7 elaborates the characteristics of real time three-dimensional fluid model simulations of atmospheric pressure glow and filamentary discharge. The origin of non-uniformities is inquired by using three-dimensional fluid model. Chapter 8 summarizes the brief conclusions of present research work.

Chapter 2

Formulation of system of fluid model equations

2.1 Introduction

This chapter gives a brief review of the multi-dimensional self-consistent fluid models in the presence of pure helium and He-N_2 gases at atmospheric pressure. The discharge properties, such as transport of particles, transport of momentum, transport of energy, plasma chemistry, space and surface charge density, and electric field are described to explore the detailed insight of the atmospheric pressure discharges. The geometry and configuration of discharge plasma reactor play an important role to inquire the characteristics of atmospheric pressure discharge under different conditions. The mathematical formulation of system of fluid model equations is investigated with a proper set of boundary conditions for the simulation domain. The relationship among different physical quantities in the bulk gas is established with the fluid model equations. The surface processes of dielectric barriers are incorporated as the boundary conditions for the basic fluid model equations by using variable secondary electron emission coefficient for different cases. The input data for the fluid model simulations is presented by displaying physical quantities graphically with the literature source references. The multi-dimensional fluid model for the atmospheric pressure discharges provides many additional features as compared to the previously described fluid models.

In this chapter, Section 2.2 displays the parallel plate dielectric barrier discharge geometry with precise description. Section 2.3 outlines the system of equations for the fluid model in the stagnant bulk gas. Section 2.4 explains the fluid model in the presence of bulk gas flow and concentrates on the gas temperature equation. Section 2.5 solves the Poisson's equation for the profile of electric field strength.

Sections 2.6 and 2.7 focus to enhance the understanding of the Scharfetter-Gummel exponential scheme and the boundary conditions of coupled system of fluid equations. The additional features of present fluid model are discussed in section 2.8. In section 2.9, the input data is described for the fluid model in case of pure helium and He-N_2 gases.

2.2 Parallel plate dielectric barrier configuration

Let us consider a parallel flat plate electrodes discharge geometry and the dielectric barriers are attached with the electrodes as shown in figure 2.1.

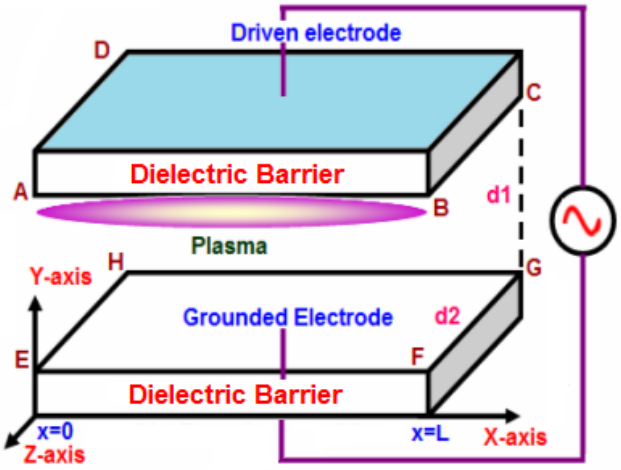

Figure 2.1. Parallel plate dielectric barrier reactor with driven and grounded electrodes in the presence applied sinusoidal voltage.

A sinusoidal voltage is imposed on the driven electrode and the other electrode is grounded. The front dielectric barrier surfaces, i.e., ABCD and EFGH are directly linked with the discharge plasma in the positive and negative half cycles of sinusoidal input voltage. The dielectric barriers have smaller widths as compared to the gap width. The combination of d1 and d2 represents the area of cross section (d1×d2) for the incoming gas, while the coordinates x, y and z represent the three-dimensional geometrical arrangement. The objective of this chapter is to formulate a mathematical fluid model in such a way that the parallel plate dielectric barrier discharge configuration is employed in the two dimensional cartesian form. The electrodes are covered by the dielectric barriers of variable width and a gap width (d1) between them for different case studies in this thesis work. The discharge is ignited in the open rectangular area near the dielectric barriers alternatively and the vertical discharge symmetry is assumed in the (x-y) cartesian coordinates as shown in figure 2.1. The different types of impurities always exist at atmospheric pressure and the influence of nitrogen impurities is considered in the simulation model because the ionization potential of nitrogen is smaller than the excitation of helium atoms. The

number of studies discussed the effects of the variable amount of nitrogen impurities present in the helium discharge [31, 32, 33]. The drift-diffusion flux approximation is used for the continuity equations and electron energy density equation. However, the semi-implicit sequential iterative scheme is used to solve all the plasma fluid model equations.

2.3 Description of fluid model equations

The Boltzmann equation is considered to provide the distribution function of discharge plasma species, which depends on the space, time and velocity. The Boltzmann equation in three-dimensional form can be written as

$$\frac{\partial f_{sp}(x,y,z,t)}{\partial t} + \mathbf{v}.\boldsymbol{\nabla} f_{sp}(x,y,z,t) + \mathbf{a}_{sp}.\boldsymbol{\nabla}_v f_{sp}(x,y,z,t) = \left(\frac{\partial f_{sp}(x,y,z,t)}{\partial t}\right)_c \tag{2.1}$$

where *sp* corresponds to the different discharge species, $\boldsymbol{\nabla}_v$ stands for the gradient in velocity space, $\boldsymbol{\nabla}$ represents the gradient in the (*x, y, z*) space. The variable $\mathbf{a}_{sp}$ is the acceleration of discharge species and can be mathematically expressed as $\mathbf{a}_{sp} = \frac{\mathbf{F}}{m_{sp}}$, m_{sp} is the mass of different discharge species. The R.H.S of equation (2.1) describes the elastic and inelastic collision processes that result in the redistribution of species (*sp*) in velocity space as well as the creation and destruction of discharge plasma species. It is very difficult to solve the Boltzmann equation for the number of discharge problems due to the strict restrictions. The distribution function contains a large amount of information and generally, the complete information is not necessary for all physical problems. Thus, an adequate approach is used to describe the information of macroscopic properties of discharge plasma based on the moments of Boltzmann equation. The Boltzmann equation can provide the infinite number of moments but a finite set of moments is considered in the present simulation model to examine the atmospheric pressure discharge behavior. The first three moments of Boltzmann equation, which provide the equation of mass, momentum and energy balance for each species. The derived macroscopic quantities of hydrodynamic fluid model are present in the distribution function of the Boltzmann equation (2.1). The fluid approach, in which the behavior of the charged particles in a weakly ionized gas is described by the particle density, momentum, and energy density balances obtained from the moments of Boltzmann equation, is well known [34, 35]. The mathematical procedure for the derivation of moment equations is not covered here and the details can be found in the number of elementary books [26, 36]. The weakly ionized discharge plasma exists at atmospheric pressure in the present simulation model, whereas the electrons and ions behave in a non-equilibrium fashion. For simplicity, the ions and neutral particles are assumed to be in equilibrium with the gas temperature and obey the equation of state. The above mentioned moments of Boltzmann equation are also coupled with the Poisson's equation for the electric field. Given the

lower ionization degree, the density and temperature of the gas particles are assumed to be constant and unaffected by the discharge. The first moment of Boltzmann equation, usually called as the particle balance equation can be written in the x-y plane as

$$\frac{\partial n_{sp}(x,y,t)}{\partial t} + \frac{\partial \mathbf{\Phi}_{sp_x}(x,y,t)}{\partial x} + \frac{\partial \mathbf{\Phi}_{sp_y}(x,y,t)}{\partial y} = G_{sp} - L_{sp} \tag{2.2}$$

where t stands for the time; $n_{sp}(x,y,t)$ represents the particle species density, $\mathbf{\Phi}_{sp_x}(x,y,t)$ and $\mathbf{\Phi}_{sp_y}(x,y,t)$ correspond to the flux calculated by the drift and diffusion parts in the x and y directions, G_{sp} and L_{sp} denote the generation and loss of each type of charged particles in the gas by different collision processes, which are calculated from the reaction rates of the chemical reactions. The discharge species flux is calculated by the drift-diffusion approximation of the momentum balance equation as

$$\mathbf{\Phi}_{sp_x}(x,y,t) = \mathrm{sgn}(q_{sp})\mu_{sp}E_x n_{sp}(x,y,t) - D_{sp}\left(\frac{\partial n_{sp}(x,y,t)}{\partial x}\right) \tag{2.3}$$

and similarly, the expression for $\mathbf{\Phi}_{sp_y}$. Here E_x and E_y are the electric field strengths in the x and y directions, q is the particle charge, μ_{sp} is the mobility and D_{sp} is the diffusion coefficient. The first term represents the drift of the particles due to the electric field strength and the second term defines the diffusion of the particles due to the concentration gradients. The Einstein relation is valid for the transport of charged particles and the mathematical form is given by

$$\frac{D}{\mu} = \frac{k_B T}{q} \tag{2.4}$$

where k_B is the Boltzmann constant and T is the particle species temperature, corresponding to the energy of the random particle motion. The local field approximation is not useful for the electrons but can provide satisfactory results for the ionic species in the specific pressure ranges. This approximation develops a direct relationship between the particle energy distribution and the electric field. The transport and rate coefficients are regarded as a function of the electric field. These relations can be found in the literature as a result of experiments and classical theories [37]. In particular, the ion diffusion coefficients are found from the mobilities by the Einstein relation (2.4), in which the ion temperature is related to the electric field by [38, 39]

$$k_B T = k_B T_g + \frac{m + m_g}{5m + 3m_g} m_g (\mu E)^2 \tag{2.5}$$

where T_g is the gas temperature, m and m_g are the ion and gas particle mass respectively. When the accelerated charged particles gain energy through the electric field, the energy is balanced by the local

collisional losses and this approximation is called local field approximation. The local field approximation is not suitable for the treatment of electrons due to the less effective energy transfer between electron and neutral collisions. In this research work, the electron transport coefficients and rate coefficients of electron impact chemical reactions are supposed to be a function of electron mean energy. Therefore, the transport coefficients of gas can be written as a function of electron mean energy [40, 41] with the following relations:

$$\mu_e = \mu_e(\overline{\varepsilon}), \quad D_e = D_e(\overline{\varepsilon}), \quad k = k(\overline{\varepsilon}) \tag{2.6}$$

where the subscript e refers to the electrons and the electron mean energy $\overline{\varepsilon}$ is evaluated from an electron energy balance equation. Here k is the rate coefficient for the different collisional processes. For simplicity, we consider room temperature (300 K) as the gas temperature for the ionic species in the stagnant bulk gas of atmospheric pressure discharge. To find the electron temperature in the gas, the electron mean energy is calculated by using the electron energy density balance equation as

$$\frac{\partial n_\varepsilon(x,y,t)}{\partial t} + \frac{\partial \mathbf{\Phi}_{\varepsilon_x}(x,y,t)}{\partial x} + \frac{\partial \mathbf{\Phi}_{\varepsilon_y}(x,y,t)}{\partial y} = S_\varepsilon \tag{2.7}$$

In this equation, n_ε is the electron energy density and written as a product of

$$n_\varepsilon(x,y,t) = n_e(x,y,t)\overline{\varepsilon}(x,y,t) \tag{2.8}$$

where $\overline{\varepsilon}$ is the electron mean energy and n_e is the electron density. The electron energy density flux in the drift-diffusion form can be expressed as

$$\mathbf{\Phi}_{\varepsilon_x}(x,y,t) = -\frac{5}{3}\mu_e E_x n_\varepsilon(x,y,t) - \frac{5}{3} D_e \left(\frac{\partial n_\varepsilon(x,y,t)}{\partial x}\right) \tag{2.9}$$

and the similar expression of $\mathbf{\Phi}_{\varepsilon_y}$ in the y - direction. The source term for the electron energy density is composed of the following terms as

$$S_\varepsilon = -e\mathbf{\Phi}_e.\mathbf{E} - n_e \sum_r \overline{\varepsilon}_r k_r n_r \tag{2.10}$$

where $-e\mathbf{\Phi}_e.\mathbf{E}$ shows the joule heating, which is developed by the electric field and $n_e(x,y,t)\sum_r \overline{\varepsilon}_r k_r n_r(x,y,t)$ expresses the electron energy losses due to the elastic and inelastic collisions, respectively. The summation in the last term is only over the electron impact reactions, with n_r the density of the target particles and ε_r is the threshold energy for the particular process.

2.4 Fluid model in the presence bulk gas flow

The fluid model equations of discharge species are modified with gas flow and their description provide the better understanding of the effects of bulk gas flow. We now proceed to formulate a multispecies multitemperature two-dimensional fluid model in such a way that the parallel plate dielectric barrier discharge configuration is employed in the presence of He-N_2 bulk gas flow under specific boundary conditions. The fluid model equations are changed in the presence of bulk gas flow and modify their mathematical representation. Thus, the continuity equation for the discharge plasma species in the presence of bulk gas flow can be written as

$$\frac{\partial n_{sp}(x,y,t)}{\partial t} + \frac{\partial(\mathbf{\Phi}_{sp_x} + n_{sp}V_x)}{\partial x} + \frac{\partial(\mathbf{\Phi}_{sp_y} + n_{sp}V_y)}{\partial y} = G_{sp} - L_{sp} \tag{2.11}$$

Here, the variables in equation (2.11) are defined in the previous section except $\mathbf{V} = V_x\mathbf{i} + V_y\mathbf{j}$, here $\mathbf{V}$ is the imposed bulk flow velocity, V_x and V_y are the components along the x and y directions. The parabolic profile of bulk flow velocity is calculated by the following expression $V_x = \frac{V_0}{4}\left(\frac{y}{\delta}\right)^2 \mathbf{i}$ for $y \leq \delta$ from the lower and upper parallel plate and $V_x = V_0\mathbf{i}$ for $y > \delta$ corresponding to a turbulent boundary layer profile [42, 43]. The variable δ is the turbulent boundary layer thickness that is supposed to be 0.1 cm on both sides of barriers inside the reactor because of smaller gap width, i.e., 0.5 cm. The state of gas is determined by its pressure, volume, and temperature according to the ideal gas equation. Suppose an ideal gas contains N number of gas particles per unit volume, which exert a pressure P on its surrounding. The standard symbolic form of ideal gas equation can be composed of the following terms as

$$P = nk_BT_g + n_ek_BT_e + \sum_p n_pk_BT_g \tag{2.12}$$

where n is the background species density, T_g and T_e are the gas and electron temperatures, here p represents the discharge species instead of electrons, such as He^+, He_2^+, N_2^+, He^* and He_2^* in He-N_2 gas. The gas temperature equation is calculated by using the following relation [44] as

$$\frac{\partial n_g(x,y,t)}{\partial t} + \frac{\partial(\mathbf{\Phi}_{g_x} + \frac{5}{3}n_gV_x)}{\partial x} + \frac{\partial(\mathbf{\Phi}_{g_y} + \frac{5}{3}n_gV_y)}{\partial y} = S_g \tag{2.13}$$

where the subscript g corresponds to the gas temperature. In this equation, n_g is the gas temperature density and written as a product of

$$n_g = \sum_{p=1}^{P_g} n_ph_{p,sens} \quad \text{and} \quad h_{p,sens} = C_{pk}T_g \text{ is the sensible enthalpy} \tag{2.14}$$

where P_g covers the heavy gas species (He^+, He_2^+, N_2^+, He^* and He_2^*) and C_{pk} corresponds to the specific heat at constant pressure, here $C_{pk} = \frac{5}{2}k_B$ for the monatomic species, i.e., carry energy due to translational motion and $C_{pk} = \frac{7}{2}k_B$ for diatomic species, i.e., carry energy with the translational and rotational motion because of the quantization of vibrational and to a smaller extent, rotational states. The flux of bulk gas energy density in the drift-diffusion form can be expressed as

$$\mathbf{\Phi}_{g_x}(x,y,t) = -\frac{5}{3}\mu_p E_{p,x}^{eff} n_g(x,y,t) - \frac{5}{3}D_p\left(\frac{\partial n_g(x,y,t)}{\partial x}\right) \tag{2.15}$$

and the similar expression for $\mathbf{\Phi}_{g_y}$ in the y direction. The source terms for the gas temperature equation is comprised of the following parts as

$$S_g = \mathrm{JH}_{\text{Eff electric field}} + \mathrm{ET}_{\text{Thermal Conduction}} + \mathrm{EL}_{\text{Elastic}} + \mathrm{EL}_{\text{Inelastic}} \tag{2.16}$$

where $\mathrm{JH}_{\text{ Eff electric field}} = e\sum_p Z_p(\mathbf{\Phi}_p + n_p\mathbf{V}).\mathbf{E}_{eff}$ shows the joule heating of ionic species, $\mathrm{ET}_{\text{Thermal Conduction}} = \boldsymbol{\nabla}.(\eta_k \boldsymbol{\nabla} T_k)$ corresponds to the energy transport due to thermal conduction, $\mathrm{EL}_{\text{Elastic}} = \frac{3}{2}k_B n_e \frac{2m_e}{m_{p_b}}(T_e - T_g)\overline{\nu}_{e,p_b}$ illustrates the energy loss due to the elastic collisions with the background gas atoms and molecules, and $\mathrm{EL}_{\text{Inelastic}} = e\sum_{i=1}^{I_g}\Delta E_i^e R_i$ represents the loss of energy due to electron-impact inelastic collisions, respectively. The thermal conductivity η_k of the gas species is defined as $\eta_k = \frac{5}{2}n_k k_B D_k$, where the collision frequency between any species k and the background species k_b is calculated as $\overline{\nu}_{k,\,k_b} = n_{k_b}\overline{\sigma}_{k,\,k_b}\overline{g}_k$. Here, the term $\overline{\sigma}_{k,\,k_b}$ represents the hard-sphere momentum transfer cross section for the collision and $\overline{g}_k$ is the average molecular speed of species k; where the term is given by $g_k = \left(\frac{8k_B T_k}{\pi m_{k,\,k_b}}\right)^{\frac{1}{2}}$ and $m_{k,\,k_b} = \frac{m_k m_{k_b}}{m_k + m_{k_b}}$ is the reduced mass of species k with k_b [45].

2.5 Formulation of Poisson's equation

The Poisson's equation for the electric field is expressed in the two dimensional form as

$$\frac{\partial(\varepsilon E_x)}{\partial x} + \frac{\partial(\varepsilon E_y)}{\partial y} = -\sum_p q_p n_p \tag{2.17}$$

where ε is the relative permittivity of the dielectric barrier material, E_x and E_y are the electric field strengths in x and y directions that depend on the space charge density ($q_p n_p$). This can also be written in the two-dimensional electric potential formulation as

$$\frac{\partial^2(\varepsilon\phi_a)}{\partial x^2} + \frac{\partial^2(\varepsilon\phi_a)}{\partial y^2} = -\sum_p q_p n_p \tag{2.18}$$

where ϕ_a is the electric potential in the rectangular gap. The electric field strengths in both directions are calculated from the change in the electric potential along x and y axes as

$$E_x = -\frac{\partial \phi_a(x,y,t)}{\partial x},\ E_y = -\frac{\partial \phi_a(x,y,t)}{\partial y} \tag{2.19}$$

The effective electric field is calculated for the ions transport equations and the procedure is described as

$$\frac{\partial E_p^{eff}}{\partial t} = \nu_{eff}(E - E_p^{eff}) \tag{2.20}$$

where $\nu_{eff} = \frac{q_i}{\mu_i m_i}$, q_i is the charge on the ionic species, μ_i is the mobility of ions and m_i is the corresponding mass of ionic particles, E_p^{eff} is the effective electric field for the ionic species of discharge plasma and E is the resultant electric field in the discharge plasma. Therefore, the effective electric field E_p^{eff} is used for the evaluation of ionic particle balance equation in the discharge fluid model and described in [26].

2.6 Scharfetter-Gummel exponential scheme

This scheme is employed for the discretization of transport terms in the fluid model equations. The SG[1] scheme is a special finite difference method and different types of interpretations are available depending on the applications [46]. The term $\mathbf{Z}_{i+\frac{1}{2},j}$ is used to calculate exponential functions in the discretized fluid model equations and can be expressed according to the following technique as

$$\mathbf{Z}_{i+\frac{1}{2},j} = -\frac{sgn(q)\mu_{i+\frac{1}{2},j}}{D_{i+\frac{1}{2},j}}\left((\phi_a)_{i+1,j} - (\phi_a)_{i,j}\right)\mathbf{a} = \frac{sgn(q)\mu_{i+\frac{1}{2},j}}{D_{i+\frac{1}{2},j}}\mathbf{E}_{i+\frac{1}{2},j}\Delta x, \tag{2.21}$$

Here, $\mathbf{a}$ is a unit vector and the particle flux can be written by the substitution of $\mathbf{E}_{i+\frac{1}{2},j} = -\left(\frac{(\phi_a)_{i+1,j}-(\phi_a)_{i,j}}{\Delta x}\right)\mathbf{a}$ as

$$\mathbf{\Phi}_{i+\frac{1}{2},j} = \frac{\mathbf{Z}_{i+\frac{1}{2},j}}{\Delta x}\frac{n_{i,j}D_{i,j}e^{Z_{i+\frac{1}{2},j}} - n_{i+1,j}D_{i+1,j}}{e^{Z_{i+\frac{1}{2},j}} - 1} = \boldsymbol{\alpha 1}_{i,j}n_{i,j} - \boldsymbol{\beta 1}_{i,j}n_{i+1,j} \tag{2.22}$$

where

$$\boldsymbol{\alpha 1}_{i,j} = \frac{\mathbf{Z}_{i+\frac{1}{2},j}}{\Delta x}\frac{D_{i,j}e^{Z_{i+\frac{1}{2},j}}}{e^{Z_{i+\frac{1}{2},j}} - 1}, \qquad \boldsymbol{\beta 1}_{i,j} = \frac{\mathbf{Z}_{i+\frac{1}{2},j}}{\Delta x}\frac{D_{i+1},j}{e^{Z_{i+\frac{1}{2},j}} - 1} \tag{2.23}$$

The main advantage of Scharfetter-Gummel exponential scheme is to provide numerically stable estimate of the particle flux under different conditions. We consider the variable cases with $|\mathbf{Z}_{i+\frac{1}{2},j}| >> 1$ and $|\mathbf{Z}_{i+\frac{1}{2},j}| << 1$ because these approximations provide the drift and diffusion parts of flux. It has been

[1] SG: Scharfetter-Gummel

observed that the solution of partial differential equations are stable by using the SG scheme. The influence of these conditions discussed in [47] for the particle flux of discharge plasma. Hence, the particle flux can be written as

$$\begin{aligned}\mathbf{\Phi}_{i+\frac{1}{2},j} &= \frac{n_{i,j}e^{Z_{i+\frac{1}{2},j}} - n_{i+1,j}}{e^{Z_{i+\frac{1}{2},j}} - 1}\mu_{i+\frac{1}{2},j}\mathbf{E}_{i+\frac{1}{2},j} \\ \mathbf{\Phi}_{i+\frac{1}{2},j} &= \frac{n_{i,j}e^{k} - n_{i+1,j}}{e^{k} - 1}\mu_{i+\frac{1}{2},j}\mathbf{E}_{i+\frac{1}{2},j} \end{aligned} \tag{2.24}$$

where $k = \mathbf{Z}_{i+\frac{1}{2},j}$. When $|\mathbf{Z}_{i+\frac{1}{2},j}| >> 1$

$$\mathbf{\Phi}_{i+\frac{1}{2},j} = \lim_{k\to+\infty}\frac{n_{i,j} - n_{i+1,j}e^{-k}}{1 - e^{-k}}\mu_{i+\frac{1}{2},j}\mathbf{E}_{i+\frac{1}{2},j} = n_{i,j}\mu_{i+\frac{1}{2},j}\mathbf{E}_{i+\frac{1}{2},j} \tag{2.25}$$

$$\mathbf{\Phi}_{i+\frac{1}{2},j} = \lim_{k\to-\infty}\frac{n_{i,j}e^{k} - n_{i+1,j}}{e^{k} - 1}\mu_{i+\frac{1}{2},j}\mathbf{E}_{i+\frac{1}{2},j} = n_{i+1,j}\mu_{i+\frac{1}{2},j}\mathbf{E}_{i+\frac{1}{2},j} \tag{2.26}$$

The above equations (2.25 and 2.26) show the drift flux of particle species in the discharge plasma.

When $|\mathbf{Z}_{i+\frac{1}{2},j}| << 1$

$$\begin{aligned}\mathbf{\Phi}_{i+\frac{1}{2},j} &= \lim_{k\to0}\frac{n_{i,j}e^{k} - n_{i+1,j}}{e^{k} - 1}\mu_{i+\frac{1}{2},j}\mathbf{E}_{i+\frac{1}{2},j} = \lim_{k\to0}\frac{n_{i,j}e^{k} - n_{i+1,j}}{e^{k} - 1}k\frac{D_{i+\frac{1}{2},j}}{\Delta x} \\ &= \frac{D_{i+\frac{1}{2},j}}{\Delta x}\lim_{k\to0}\frac{\frac{d}{dk}\left\{k\left[n_{i,j}e^{k} - n_{i+1,j}\right]\right\}}{\frac{d}{dk}\left[e^{k} - 1\right]} \\ &= \frac{D_{i+\frac{1}{2},j}}{\Delta x}\lim_{k\to0}\frac{n_{i,j}(1+k)e^{k} - n_{i+1,j}}{e^{k}} \\ &= D_{i+\frac{1}{2},j}\frac{n_{i+1,j} - n_{i,j}}{\Delta x}\end{aligned} \tag{2.27}$$

This equation (2.27) corresponds to the diffusion part of particle flux and these estimates are derived by applying the approximate conditions to the particle flux of discharge species along x - direction. Similarly, the term $(\mathbf{Z}_{i,j})$ is approximated for other directions of discharge geometry.

2.7 Boundary conditions for the fluid equations

The exact description of physical phenomenon is not possible without proper implementation of boundary conditions. In regard to the atmospheric pressure discharges, the meaningful boundary conditions are applied for the fluid model equations on the rectangular simulation domain as shown in the figure 2.2.

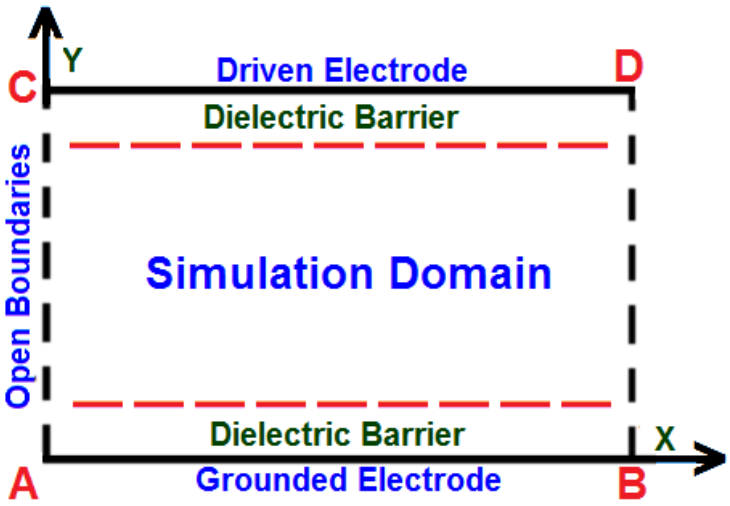

Figure 2.2. Rectangular simulation domain with its boundaries.

The two types of boundary conditions are assumed in the present simulation domain. One deals with the solid dielectric barriers and other with open boundaries. A set of Von Neumann symmetry boundary conditions are imposed on the virtual boundaries designated by AC and BD, whereas the Dirichlet boundary conditions are considered for AB and CD solid electrodes. Therefore, a zero abscissa derivative is supposed for the discharge species density, electron energy density, gas energy density and electrical potential at $x = 0$ and $x = L$ (Barrier Length), which can be written in the mathematical form as

$$\frac{\partial n_p(x,y,t)}{\partial x} = 0, \qquad (p = e, i, n, g \text{ and } \varepsilon) \tag{2.28}$$

$$\frac{\partial \phi_a(x,y,t)}{\partial x} = 0 \tag{2.29}$$

where e, i, n, g and ε correspond to the electrons, ions, neutrals, gas energy density and electron energy density. As the Dirichlet boundary conditions are applied on the physical solid boundaries [37, 48, 49], Therefore, the flux of the heavy particle species, electrons, electron energy density and neutrals at the solid dielectric boundaries are expressed as

$$\mathbf{\Phi}_p.\mathbf{n} = (\mathbf{2}\beta - 1)\mathrm{sgn}(q_p)\mu_p \mathbf{E}_p^{eff}.\mathbf{n} n_p(x,y,t) + \frac{1}{2} v_{th,p} n_p(x,y,t) \tag{2.30}$$

$$\mathbf{\Phi}_e.\mathbf{n} = -(\mathbf{2}\beta - 1)\mu_e \mathbf{E}.\mathbf{n} n_e(x,y,t) + \frac{1}{2} v_{th,e} n_e(x,y,t) - 2(1-\beta)\sum_p \gamma_p \mathbf{\Phi}_p.\mathbf{n} \tag{2.31}$$

$$\mathbf{\Phi}_\varepsilon.\mathbf{n} = -(\mathbf{2}\beta - 1)\frac{5}{3}\mu_e \mathbf{E}.\mathbf{n} n_\varepsilon(x,y,t) + \frac{2}{3} v_{th,e} n_\varepsilon(x,y,t) \tag{2.32}$$

$$\mathbf{\Phi}_n.\mathbf{n} = \frac{1}{2} v_{th,n} n_n(x,y,t) \tag{2.33}$$

where $\mathbf{n}$ is the normal vector pointing towards the dielectric barriers; Here $\mathbf{E}_p^{eff}$ is the effective electric field for the particular ionic species and the $v_{th,p}$ is the thermal velocity of discharge species and can be written as

$$v_{th,p} = \sqrt{\frac{8k_B T_p}{\pi m_p}}$$

here k_B is the Boltzmann constant, T_p is the gas species temperature and m_p is the particle species mass. The $v_{th,p}$ represents the thermal velocity of discharge species at the gas temperature (300 K). The integer number β is set to one if the drift velocity is directed towards the dielectric barriers and to zero otherwise

$$\beta = \left\{ \begin{array}{ll} 1 & \mathrm{sgn}(q)\mu\mathbf{E}.\mathbf{n} > \mathbf{0} \\ 0 & \mathrm{sgn}(q)\mu\mathbf{E}.\mathbf{n} \leqslant \mathbf{0} \end{array} \right\}$$

where γ_p exhibits the secondary electron emission coefficient for the ionic species and is defined as the average number of the electrons emitted per incident ion. The secondary electron emission coefficient for He^+, He_2^+ and N_2^+ ions is considered as 0.01 in the present simulation model.

Suppose a sinusoidal voltage is applied on the large flat plate electrodes, which provides the electric potential along the electrode surface and satisfies the Dirichlet boundary conditions as

$$\phi_a = \left\{ \begin{array}{ll} \phi_0 \sin(2\pi f t) & \text{at driven electrode} \\ 0 & \text{at grounded electrode} \end{array} \right\} \tag{2.34}$$

where ϕ_0 is the amplitude of the applied voltage on the driven electrode, f is the driving frequency for the simulation domain and t is the time elapsed for the discharge progress. The list of the chemical reactions between the active discharge species are described in the tables 2.1 and 2.2 with their reaction rates and source references. The charges are accumulated on the dielectric barrier surfaces during the operation of atmospheric pressure discharge and the surface charge density σ_s is taken into account by using Gauss's law [37], which can be calculated by the equation:

$$\sigma_s(x, y, t) = \varepsilon_0 \varepsilon_r \mathbf{E}_{\text{dielectric}}.\mathbf{n} - \varepsilon_0 \mathbf{E}_{\text{plasma}}.\mathbf{n} \tag{2.35}$$

where $\mathbf{E}_{\text{dielectric}}$ and $\mathbf{E}_{\text{plasma}}$ are the electric fields at the dielectric surface and outside the dielectric barrier material respectively. The discharge current density j is calculated by using Sato's equation [50] in one-dimensional formulation with time-dependent applied voltage as

$$j = \frac{e}{d} \int_0^d (\Phi_i - \Phi_e) dx + J_D \tag{2.36}$$

where the first term is composed of fluxes (Φ_i and Φ_e) of charged particles on the surface of dielectric barriers and second term (J_D) represents the displacement current, i.e., $J_D = \varepsilon_0 \frac{\partial V_a}{\partial t}$, here V_a is the amplitude of applied voltage and ε_0 is the permittivity of free space.

2.8 Major features of fluid model

1. The electron temperature is calculated from the solution of electron energy density equation rather than implying so called the local field approximation.

2. The chemistry set is composed of all major processes, such as ionization, excitation, stepwise ionization, charge transfer, Penning ionization and dissociative recombination through multiple channels in pure helium as well as in He-N_2 mixture.

3. An effective electric field is employed for the numerical solution of ionic particle balance equations. The equation for the evaluation of effective electric field has been explained in section 2.5.

4. The constant bulk gas flow velocity is introduced in the reactor chamber along the horizontal direction by using the parabolic profile.

5. The gas temperature equation is solved due to the effects of heavy particle species (He^+, He_2^+, N_2^+, He^* and He_2^*) in the stagnant and flowing atmospheric pressure discharges.

2.9 Input data for the simulations of atmospheric pressure discharge

The two dimensional simulation model is composed of the following species, such as electrons, atomic and molecular ions (He^+ and He_2^+), helium metastables and excimers (He^* and He_2^*) and molecular nitrogen ions (N_2^+). The helium excited states (2^3S and 2^1S) are grouped into single form He^* and $He_2(a^3\sum_u^+)$ is represented as He_2^*. The model is based on the continuity equations for the plasma particle species, electron energy equation, gas temperature equation, and Poisson's equation for the electric field. The list of chemical reactions between the active discharge species are described in the tables 2.1 and 2.2 with their standard symbolic form, reaction rates and source references. The table 2.1 represents the chemical reactions in pure helium gas, whereas the table 2.2 corresponds to the additional reactions for the nitrogen impurities.

Table 2.1: List of chemical reactions with reaction rates in pure helium gas

No	Symbolic Form	Reaction Rate	Source
R1	$He + e^- \longrightarrow He^+ + 2e^-$	Boltzmann Solver (BOLSIG+)	[51]
R2	$He + e^- \longrightarrow He^* + e^-$	Boltzmann Solver (BOLSIG+)	[51]
R3	$He^+ + 2He \longrightarrow He_2^+ + He$	1.5×10^{-31} cm^6 s^{-1}	[55]
R4	$He^* + He^* \longrightarrow He^+ + He + e^-$	2.9×10^{-9} cm^3 s^{-1}	[56]
R5	$He^* + He^* \longrightarrow He_2^+ + e^-$	2.0×10^{-9} cm^3 s^{-1}	[59]
R6	$He^* + e^- \longrightarrow He + e^-$	2.9×10^{-9} cm^3 s^{-1}	[56]
R7	$He^+ + e^- + e^- \longrightarrow He + e^-$	7.1×10^{-20} cm^6 s^{-1}	[57]
R8	$He^+ + He + e^- \longrightarrow He + He^*$	1.0×10^{-27} cm^6 s^{-1}	[55]
R9	$He_2^+ + e^- \longrightarrow He^* + He$	5.3×10^{-7} $T_e^{-0.5}$ cm^3 s^{-1}	[58]
R10	$He_2^+ + He + e^- \longrightarrow 3He$	2.0×10^{-27} cm^6 s^{-1}	[55]
R11	$He^* + 2He \longrightarrow He_2^* + He$	1.3×10^{-33} cm^6 s^{-1}	[37]
R12	$He_2^* + He_2^* \longrightarrow He_2^+ + 2He + e^-$	1.5×10^{-9} cm^3 s^{-1}	[55]
R13	$He^* + He_2^* \longrightarrow He^+ + 2He + e^-$	2.5×10^{-9} cm^3 s^{-1}	[55]
R14	$He^* + He_2^* \longrightarrow He_2^+ + He + e^-$	2.5×10^{-9} cm^3 s^{-1}	[55]

As the nitrogen impurities are introduced in pure helium gas, then the helium gas atoms interact with the nitrogen molecules and the major chemical reaction scheme is represented in the following table as

Table 2.2: List of chemical reactions with reaction rates in He-N_2 gas

No	Symbolic Form	Reaction Rate	Source
R1	$N_2 + e^- \longrightarrow N_2^+ + 2e^-$	4.5×10^{-7} $T_e^{-0.3} e^{\frac{-1.85\times10^5}{T_e}}$ cm^3 s^{-1}	[53]
R2	$N_2^+ + e^- + e^- \longrightarrow N_2 + e^-$	5.6×10^{-27} $T_e^{-0.8}$ cm^6 s^{-1}	[53]
R3	$N_2^+ + e^- \longrightarrow N + N$	2.0×10^{-7} cm^3 s^{-1}	[59]
R4	$He^* + N_2 \longrightarrow He + N_2^+ + e^-$	5.0×10^{-11} cm^3 s^{-1}	[60]
R5	$He^* + N_2 + He \longrightarrow 2He + N_2^+ + e^-$	3.3×10^{-30} cm^6 s^{-1}	[59]
R6	$He_2^+ + N_2 \longrightarrow 2He + N_2^+$	1.1×10^{-9} cm^3 s^{-1}	[59]
R7	$He_2^+ + N_2 + He \longrightarrow 3He + N_2^+$	1.3×10^{-29} cm^6 s^{-1}	[59]
R8	$He_2^* + N_2 \longrightarrow 2He + N_2^+ + e^-$	3.0×10^{-11} cm^3 s^{-1}	[60]

Some reactions in the above tables are a function of the electron temperature T_e, as shown in the tables 2.1 and 2.2. The electron temperature T_e is calculated from the solution of the electron energy density equation that consider all the elastic and inelastic energy losses due to the electron impact reactions. The electron mobility and the reaction rate coefficients of the electron impact reactions are

evaluated with the freeware Boltzmann solver BOLSIG+[2] [51], which consider the electron energy distribution function in uniform electric field with a set of cross sections. The reduced diffusion coefficients and mobilities of ionic species (He^+, He_2^+ and N_2^+) in pure helium and He-N_2 gases are calculated from the data available in [30, 52]. The diffusion coefficients of the neutral species, $D_{He^*} = 4.116$ cm^2 s^{-1}, $D_{He_2^*} = 2.029$cm^2 s^{-1} [53], are used in the present simulation model. The Scharfetter-Gummel exponential scheme is employed for the discretization of transport terms in the continuity equations of discharge species and electron energy density equation as described in section 2.6.

The reactions taken into account in the fluid model simulations of the atmospheric pressure discharges are listed above in the tables 2.1 and 2.2. The reaction scheme described in the tables 2.1 and 2.2 is composed of all major chemical processes, which analyses the behavior of atmospheric pressure discharge in pure helium and He-N_2 gas. We consider a two-dimensional uniform grid of size 34×34 cells, which fulfils the criteria for the reliable simulation results according to [10, 54]. The cartesian grid consists of straight lines along the horizontal and vertical axis with equally spaced intervals $\Delta x = \frac{\mathrm{BL}}{(\mathrm{cells})_x}$, $\Delta y = \frac{\mathrm{GW}}{(\mathrm{cells})_y}$, where BL[3] and GW[4] correspond to the barrier length and gap width along the x and y directions. The plasma fluid model equations are solved on the entire grid, except inside the electrode areas.

We use constant secondary electron emission coefficients for different mixtures of the atmospheric pressure discharges. The dependence of SEEC[5] on the reduced electric field is ignored because the data contains few contradictions in this area [61]. However, the dependence of electric field is prominently associated with the backscattering of emitted electrons as discussed in the literature. As follows from our discussion in Section 2.3, the exact understanding is not enhanced when such field-dependent secondary emission coefficients are coupled with the fluid model boundary conditions of electron transport. The secondary electron emission coefficient is not so effective due to the metastables and excimers, so the SEEC[5] is ignored for the neutral discharge species [37].

The metastable-metastable ionization processes (R4 and R5 of table 2.1) produce electrons at 15 - 19 eV of energy, which is not enough to excite or ionize helium atoms but at the same time too much to be efficiently lost in elastic collisions. In pure helium, the metastable-metastable ionization performs a substantial role for the description of atmospheric pressure discharge.

[2] BOLSIG+: Boltzmann's Solver
[3] BL: Barrier length
[4] GW: Gap Width
[5] SEEC: Secondary electron emission coefficient

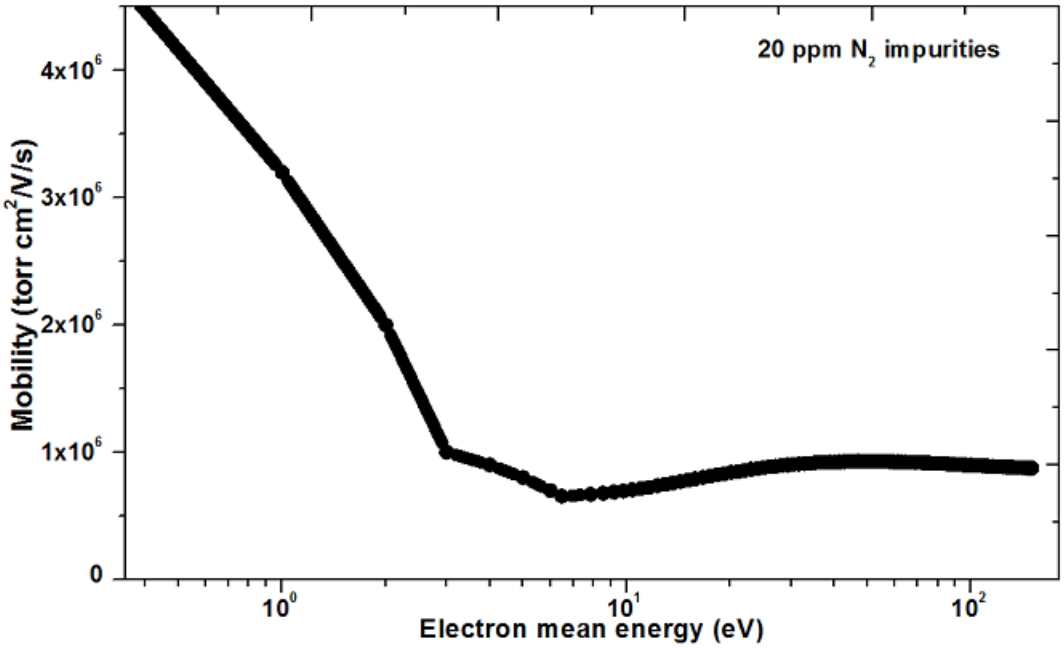

Figure 2.3. Electron mobility versus electron mean energy with 20 ppm N_2 impurities in He-N_2 gas [51].

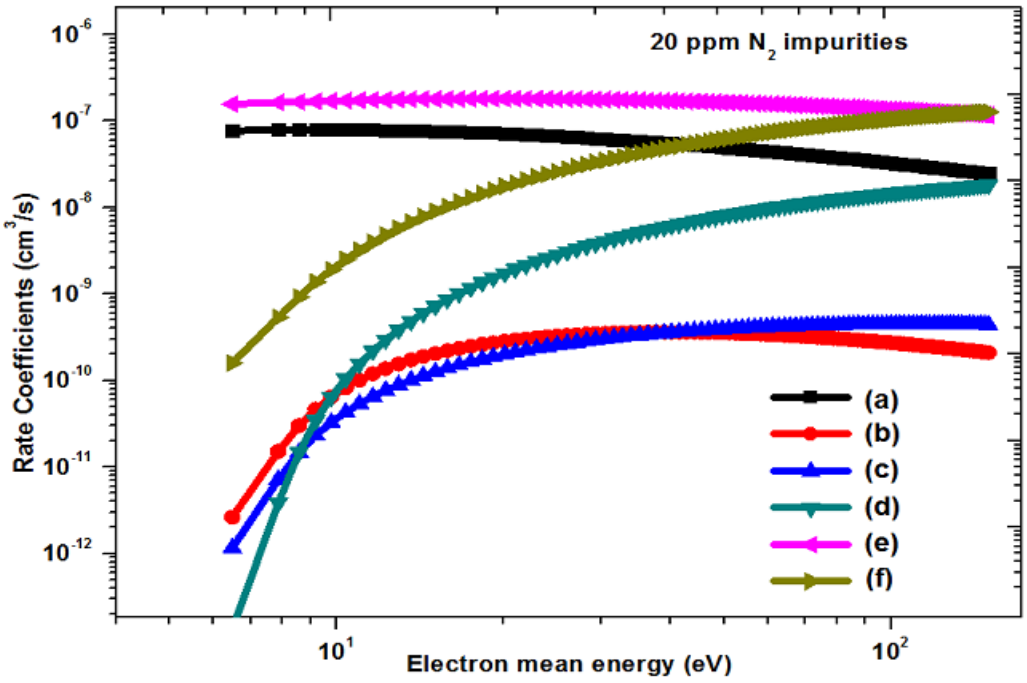

Figure 2.4: Rate Coefficients of electron impact reactions with 20 ppm nitrogen impurity, (a) He elastic (b) He (2 ^{3}S) excitation, (c) He (2 ^{1}S) excitation, (d) He direct ionization, (e) N_2 elastic and (f) N_2 direct ionization [51].

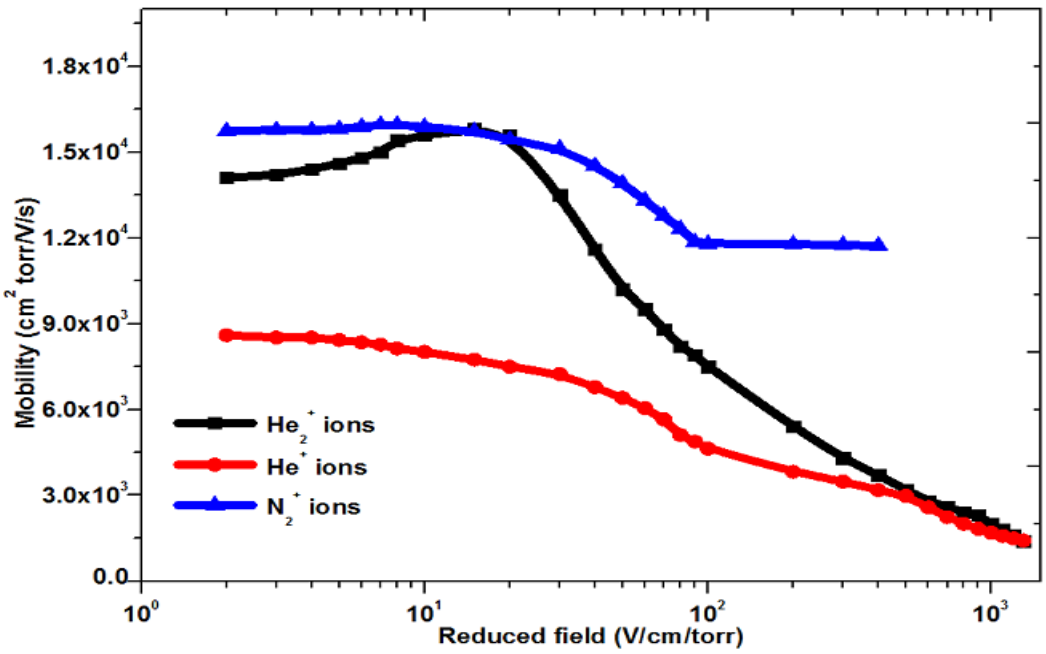

Figure 2.5. Ion mobilities of He^+ and He_2^+ ions in Pure helium gas [38, 62].

The spatial variations of electronic and ionic mobilities in pure helium and He-N_2 gases provide the insight and intuition of their evolution with the reduced electric field for these particular cases as shown in figure 2.3, 2.4 and 2.5. In He-N_2 mixture, the values of mobilities and diffusion coefficients are modified according to trace amount of molecular nitrogen impurities, i.e., 5, 10, 20, 50 and 100 ppm N_2.

Chapter 3

Numerical solution of fluid equations in three-dimensional form

3.1 Introduction

In this chapter, the computational techniques are discussed and applied to the system of fluid model equations for the atmospheric pressure discharges. The solution of a coupled system of fluid model equations correspond to the original description of the discharge phenomenon. The system of fluid model equations are discretized in cartesian space and time by using the finite difference scheme [63]. A semi-implicit sequential algorithm is advanced in time to find the stable solution of system of fluid model equations. The stationary-state achievement is mandatory to justify the fluid model results because the non-stationary state shows the unstable and nonphysical results. We describe in detail the discretization procedure for the partial differential equations of plasma fluid model and the algorithms for their solution in different sections of this chapter.

In this chapter, Section 3.2 describes the representation of cartesian grid in finite difference form. Section 3.3 explains the fluid model equations with electron energy equation in the implicit form. Section 3.4 exhibits the three-dimensional grid with nodes and half nodes. Sections 3.5 and 3.6 solve the discretized form of transport and Poisson's equations. Finally, the solution of seven-point equations are performed by using different numerical techniques in section 3.7.

3.2 Representation of cartesian grid

The discretization is the process by which a closed-form mathematical expression, such as a function or a differential or integral equation involving functions, all of which are viewed as having an infinite continuum of values throughout some domain, is approximated by analogous expressions which prescribe values at only a finite number of discrete points in the domain. The analytical solutions of partial differential equations involve closed-form expressions which give the variation of dependent variables continuously throughout the domain. On the contrary, the numerical solutions can provide answers only at discrete points in the domain, called as the grid points. The different discretization methods, such as finite difference method, finite element method and finite volume method are used for the solution of partial differential equations. These numerical methods are considered in different scientific disciplines for the number of industrial applications. As the discharge area is rectangular between the flat parallel plates, the finite difference method will provide stable and physical numerical simulation results [64].

3.2.1 Finite difference method

To understand the physical description of the fluid model, the partial differential equations of the fluid model are discretized by using the finite difference method. The partial derivatives are replaced with the suitable algebraic difference quotients. The most common finite-difference representation of derivatives is based on the Taylor's series expansion. For example,

$$u_{i+1,j,k} = u_{i,j,k} + \left(\frac{\partial u}{\partial x}\right)_{i,j,k} \Delta x + \left(\frac{\partial^2 u}{\partial x^2}\right)_{i,j,k} \frac{(\Delta x)^2}{2} + \left(\frac{\partial^3 u}{\partial x^3}\right)_{i,j,k} \frac{(\Delta x)^3}{6} + ... \tag{3.1}$$

The equation (3.1) is mathematically an exact expression for $u_{i+1,j,k}$, if the number of terms are infinite and the series converges for $\Delta x \to 0$. The simplified form of equation (3.1) can be written as

$$\left(\frac{\partial u}{\partial x}\right)_{i,j,k} = \frac{u_{i+1,j,k} - u_{i,j,k}}{\Delta x} + \mathrm{O}((\Delta x)^2) \tag{3.2}$$

where $\mathrm{O}(\Delta x)$ is the formal mathematical notation which shows "terms of order Δx". The equation (3.2) is called as the forward difference method (FDM), whereas the backward and central difference methods can be expressed as

$$\left(\frac{\partial u}{\partial x}\right)_{i,j,k} = \frac{u_{i,j,k} - u_{i-1,j,k}}{\Delta x} + \mathrm{O}((\Delta x)^2) \quad \text{and} \quad \left(\frac{\partial u}{\partial x}\right)_{i,j,k} = \frac{u_{i+1,j,k} - u_{i-1,j,k}}{2\Delta x} + \mathrm{O}((\Delta x)^2)$$

There are number of advantages of finite difference method (FDM) and some of them are described as under

- The values of boundary variables are directly used in the Dirichlet boundary conditions.
- The gradient of variables are easily evaluated in the Von Neumann symmetry boundary conditions.

3.3 System of fluid model equations

The discretized system of fluid model equations are evaluated by using different numerical schemes, such as explicit, implicit and semi-implicit. To understand the role of these numerical schemes and their effect on the solution of fluid model equations. The continuity equation for the discharge species is analyzed under different constraints and can be written as

$$\frac{\partial n_{sp}}{\partial t} - \boldsymbol{\nabla}.\boldsymbol{\Phi}_{sp} = S_{sp} \tag{3.3}$$

where sp corresponds to the different discharge species. The forward finite difference scheme is used to discretize the continuity equation as

$$n_{sp}^{k_t+1} - n_{sp}^{k_t} = \zeta(t^{k_t}, n_{sp}^{k_t})\Delta t \tag{3.4}$$

When the species flux and source terms in the function (ζ) are available from the previous time step (k_t), equation (3.4) provides the explicit solution of discharge species equation. The implicit solution of species density equation can be formulated as

$$n_{sp}^{k_t+1} - n_{sp}^{k_t} = \zeta(t^{k_t+1}, n_{sp}^{k_t+1})\Delta t \tag{3.5}$$

Here, the flux and source terms of (ζ) are evaluated at the current time step $(k_t + 1)$, the semi-implicit form of discharge species equation can be written as

$$n_{sp}^{k_t+1} - n_{sp}^{k_t} = \frac{1}{2}\left[\zeta(t^{k_t}, n_{sp}^{k_t}) + \zeta(t^{k_t+1}, n_{sp}^{k_t+1})\right]\Delta t \tag{3.6}$$

where the function (ζ) is divided into previous and current time steps, and take the average of them. This scheme is better than the explicit method and also provides the relaxation for some time step restrictions. The density in the transport term is always calculated implicitly $(k_t + 1)$ because the explicit treatment would lead to the strict time step constraints due to the Courant-Friedrichs-Lewy (CFL) condition as discussed in [65, 66]. The continuity equation for the particle species in the discretized form can be expressed as

$$\frac{n_{sp}^{k_t+1} - n_{sp}^{k_t}}{\Delta t} + \boldsymbol{\nabla}.\boldsymbol{\Phi}_{sp}(n_{sp}^{k_t+1}, \mathbf{E}^{k_t}, \mu_{sp}^{k_t}, D_{sp}^{k_t}) = S_{sp}^{k_t} \tag{3.7}$$

If the electric field is calculated explicitly, then the following time step restriction must be considered and applied to the fluid model [67], $\Delta t = \frac{\varepsilon_0}{\sum_{sp} |q_{sp}| \mu_{sp} n_{sp}}$ in order to avoid the numerical instabilities. Therefore, the electric field is calculated at (t^{k_t+1}) after the calculation of species density. Equation (3.7) is independent of time step restrictions and the electric field is calculated by the substitution of discharge species density as

$$\boldsymbol{\nabla}.(\varepsilon \mathbf{E}^{k_t+1}) = \sum_{sp} q_{sp} n_{sp}^{k_t+1} \tag{3.8}$$

The CFL time step constraint may be prohibitive for high plasma densities ($> 10^9$ cm^{-3}) as described in [68]. However, we can skip from the strict time step restrictions by using a semi-implicit approach. The semi-implicit approach is attractive for the discharge plasma at high pressure, whereas the Poisson's equation solves before the continuity equations in this approach. Since the space charge density at time t^{k_t+1} is not known yet, an approximate initial estimated numerical value can be considered for the solution of Poisson's equation as

$$\boldsymbol{\nabla}.(\epsilon \mathbf{E}^{k_t+1}) = \sum_{sp} q_{sp} \widetilde{n}_{sp}^{k_t+1} \tag{3.9}$$

where $\widetilde{n}_{sp}^{k_t+1}$ is an approximate estimate for $n_{sp}^{k_t+1}$, arising from the continuity equation (3.3). The calculated electric field is used at the current time step (k_t+1) and the discharge species density is given by

$$\widetilde{n}_{sp}^{k_t+1} = n_{sp}^{k_t} + \Delta t \ \boldsymbol{\nabla}.\boldsymbol{\Phi}_{sp}(n_{sp}^{k_t}, \mathbf{E}^{k_t+1}, \mu_{sp}^{k_t}, D_{sp}^{k_t}) \tag{3.10}$$

The source term S_{sp} is ignored in this case because no space charge is formed after the substitution in equation (3.7), all source terms would cancel each other. By using the above mentioned semi-implicit procedure, the larger time step can be used for the numerical solution of fluid model equations, which makes the calculation fast.

3.3.1 Implicit treatment of the electron energy source term

The electron energy density equation is solved additionally to verify the profile of electron temperature in the atmospheric pressure discharges. The source term of electron energy equation is composed of the following parts and can be written in the simplified form as

$$S_\varepsilon = -e\mathbf{E}.\boldsymbol{\Phi}_e - n_e \sum_r \overline{\varepsilon}_r k_r n_r \tag{3.11}$$

After linearization and substitution of number of expressions, the above source term can be written in complex form as

$$S_{\varepsilon_c} = -e\mathbf{E}^{k_t}.\mathbf{\Phi}_e^{k_t} - n_e^{k_t}\sum_r \varepsilon_r k_r^{k_t} n_r^{k_t} - \left[\begin{array}{c} \frac{e}{n_e^k}\mathbf{E}^{k_t}.\left(\frac{\partial \mathbf{\Phi}_e}{\partial \mu_e}\right)^{k_t}\left(\frac{\partial \mu_e}{\partial \overline{\varepsilon}}\right)^{k_t} + \frac{e}{n_e^k}\mathbf{E}^{k_t}.\left(\frac{\partial \mathbf{\Phi}_e}{\partial D_e}\right)^{k_t}\left(\frac{\partial D_e}{\partial \overline{\varepsilon}}\right)^{k_t} \\ +\sum_r \overline{\varepsilon}_r\left(\frac{\partial k_r}{\partial \overline{\varepsilon}}\right)^{k_t} n_r^{k_t} \end{array}\right]\left(n_\varepsilon^{k_t+1} - n_e^{k_t+1}\overline{\varepsilon}^{k_t}\right) \tag{3.12}$$

The last term on the R.H.S of equation (3.12) represents the correction of the energy source term for the variations in the electron mean energy, which stops oscillations for the solution of energy equation [37]. As the transport coefficients are the smooth functions of electron mean energy equation, the continuity equation of electrons must be solved before solving the electron mean energy equation. Therefore, the value of $n_e^{k_t+1}$ is available before the solution [69]. The semi-implicit technique is coupled with this implicit method and finally developed the consecutive steps.

The Poisson's equation for the calculation of electric field $\mathbf{E}^{k_t+1}$ can be written as

$$\boldsymbol{\nabla}.\left(\varepsilon\mathbf{E}^{k_t+1}\right) = \sum_{sp} q_{sp}\left(n_{sp}^{k_t} + \Delta t\boldsymbol{\nabla}.\mathbf{\Phi}_{sp}\left(n_{sp}^{k_t+1}, \mathbf{E}^{k_t+1}, \mu_{sp}^{k_t}, D_{sp}^{k_t}\right)\right) \tag{3.13}$$

Then for every species sp, the density $n_{sp}^{k_t+1}$ is evaluated from the equation as

$$\frac{n_{sp}^{k_t+1} - n_{sp}^{k_t}}{\Delta t} - \boldsymbol{\nabla}.\mathbf{\Phi}_{sp}\left(n_{sp}^{k_t+1}, \mathbf{E}^{k_t+1}, \mu_{sp}^{k_t}, D_{sp}^{k_t}\right) = S_{sp}^{k_t} \tag{3.14}$$

Thus the solution of electron energy density equation is evaluated after the solution of electron density equation as

$$\frac{n_\varepsilon^{k_t+1} - n_\varepsilon^{k_t}}{\Delta t} - \boldsymbol{\nabla}.\mathbf{\Phi}_\varepsilon\left(n_\varepsilon^{k_t+1}, \mathbf{E}^{k_t+1}, \mu_e^{k_t}, D_e^{k_t}\right) = S_\varepsilon^{k_t} - \left[\begin{array}{c} \frac{e}{n_e}\mathbf{E}.\left(\frac{\partial \mathbf{\Phi}_e}{\partial \mu_e}\frac{\partial \mu_e}{\partial \overline{\varepsilon}} + \frac{\partial \mathbf{\Phi}_e}{\partial D_e}\frac{\partial D_e}{\partial \overline{\varepsilon}}\right) \\ +\sum_r \overline{\varepsilon}_r\left(\frac{\partial k_r}{\partial \overline{\varepsilon}}\right) n_r \end{array}\right]^{k_t}\left(n_\varepsilon^{k_t+1} - n_e^{k_t+1}\overline{\varepsilon}^{k_t}\right) \tag{3.15}$$

where the time step Δt is calculated by trail and error for the achievement of steady-state in the atmospheric pressure discharge simulations.

3.4 Finite difference form of spatial grid

Let us consider a cartesian equally spaced spatial grid in three x, y and z directions and a finite difference technique is used to divide the physical spatial domain into a set of discrete points between the flat plate dielectric barriers. There are n_x, m_y and p_z number of grid points in the x, y and z directions. So the

smallest possible element along x, y and z direction is given by

$$\Delta x = \frac{\mathrm{L}_x}{\mathrm{n}_x}, \qquad \Delta y = \frac{\mathrm{L}_y}{\mathrm{m}_y}, \qquad \Delta z = \frac{\mathrm{L}_z}{\mathrm{p}_z} \tag{3.16}$$

where L_x, L_y, and L_z are the lengths of the simulation domain along x, y and z - axis. The minimum number of grid points are considered as $\mathrm{n}_x \times \mathrm{m}_y \times \mathrm{p}_z$ to verify the characteristics of atmospheric pressure discharge and $\mathrm{n}_x = \mathrm{m}_y = \mathrm{p}_z = 34$ for different cases in the present simulation modelling. This is in accordance with the criteria for the numerical simulations [10], which describes the minimum number of grid points for the physically reliable numerical solution. The grid points in figure 3.1 are designated by an index i which moves in the x direction, an index j which travels in the y direction and an index z which steps in the z direction. So, if (i, j, k) is the index at the central point O, then the point next to the positive x-axis (east) of O is labeled as (i + 1, j, k), the point immediately to the negative x-axis (west) is (i - 1, j, k), the point towards positive y-axis (north) is (i, j + 1, k), the point below (south) is (i, j - 1, k), the point towards positive z-axis (front) is (i, j, k + 1), and the point back (back) is (i, j, k - 1). The set of partial differential equations in finite difference form is evaluated at each discrete point of the spatial domain for every time step interval. The large number of algebraic equations are formed by applying the finite difference discretization scheme. These equations provide the reflection of the original phenomenon of atmospheric pressure discharge plasma. The small difference between the nearest grid points in x, y and z directions are calculated by the following parametric equations as

$$\Delta x = x_{i+1,j,k} - x_{i,j,k}, \quad \Delta y = y_{i,j+1,k} - y_{i,j,k}, \quad \Delta z = z_{i,j,k+1} - z_{i,j,k} \tag{3.17}$$

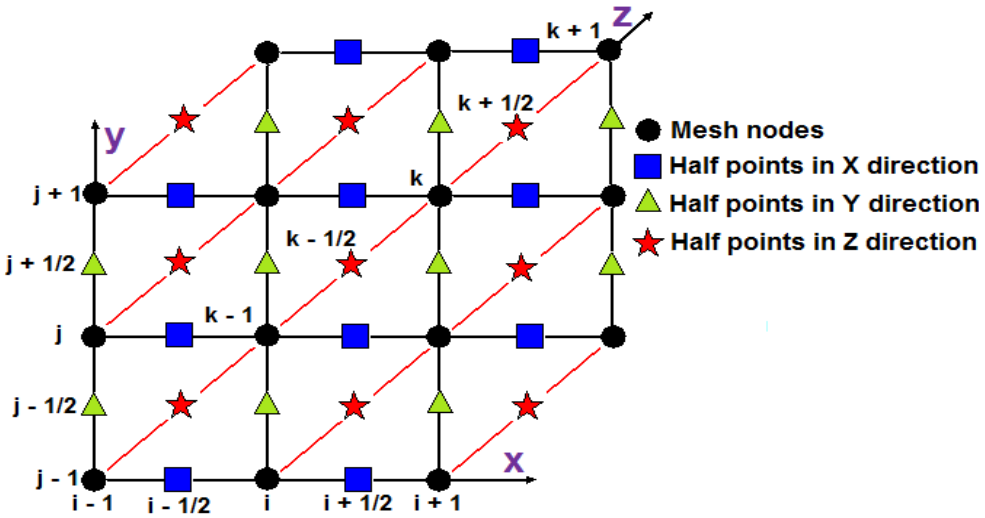

Figure 3.1 Computational mesh in three-dimensional xyz plane.

From the figure 3.1, it is clear that the symbols, such as circle, square, triangle and star are assigned at different locations of the cartesian three-dimensional grid. These symbols represent the scalar and vector quantities in the fluid model at specific grid points of rectangular geometry in three-dimensions. The scalar parameters in the fluid model, such as charged particle densities ($n_{sp_{i,j,k}}$), electron energy density ($n_{\varepsilon_{i,j,k}}$) and the electric potential $(\phi_a)_{i,j,k}$ are evaluated at the node locations, designated by the circles. The electric field ($\mathbf{E}$) and particle species fluxes ($\mathbf{\Phi}$) are the vector quantities and represented by the squares in between the nodes along x-axis. The continuity equation for the discharge species can be written in the xyz - plane based on the mentioned discretization scheme as

$$\frac{\partial n_{sp}(x,y,z,t)}{\partial t} + \boldsymbol{\nabla}.\mathbf{\Phi}_{sp}(x,y,z,t) = G_{sp} - L_{sp} \tag{3.18}$$

where G_{sp} corresponds to the generation and L_{sp} represents the loss of discharge species due to the chemical reactions of the atmospheric pressure discharges.

3.5 Spatial discretization of the transport equations

The transport part of particle balance equation has an immense influence and discretized according to the following procedure as

$$(\boldsymbol{\nabla}.\mathbf{\Phi})_{i,j,k} = \frac{\mathbf{\Phi}_{x,i+\frac{1}{2},j,k} - \mathbf{\Phi}_{x,i-\frac{1}{2},j,k}}{\Delta x} + \frac{\mathbf{\Phi}_{y,i,j+\frac{1}{2},k} - \mathbf{\Phi}_{y,i,j-\frac{1}{2},j,k}}{\Delta y} + \frac{\mathbf{\Phi}_{z,i,j,k+\frac{1}{2}} - \mathbf{\Phi}_{z,i,j,k-\frac{1}{2}}}{\Delta z} \tag{3.19}$$

The drift-diffusion approximation is used for the evaluation of particle flux of different species. As the species density fluctuations are present in the particle flux term, the Scharfetter and Gummel exponential technique is suitable in this case and provides the stable solution under different conditions. The particle flux in the y - direction can be written as,

$$\mathbf{\Phi}_{y,i,j+\frac{1}{2},k} = -\frac{1}{\Delta y} D_{i,j+\frac{1}{2},k} \left(f_1(\mathbf{Z}_{y,i,j+\frac{1}{2},k}) n_{i,j+1,k} - f_2(\mathbf{Z}_{y,i,j+\frac{1}{2},k}) n_{i,j,k} \right) \tag{3.20}$$

$$\text{with} \qquad \mathbf{Z}_{y,i,j+\frac{1}{2},k} = \frac{\mathrm{sgn}(q)\mu_{i,j+\frac{1}{2},k}\mathbf{E}_{y,i,j+\frac{1}{2},k}\Delta y}{D_{i,j+\frac{1}{2},k}} \tag{3.21}$$

and the functions $f_1(Z)$ and $f_2(Z)$ are composed of the following terms as

$$f_1(Z) = \frac{Z}{e^Z - 1} \tag{3.22}$$

$$f_2(Z) = \frac{Ze^Z}{e^Z - 1} = f_1(Z) + Z \tag{3.23}$$

When $Z \neq 0$, then the functions are calculated as, $f_1(0) = f_2(0) = 1$. The particle flux ($\mathbf{\Phi}_x$ and $\mathbf{\Phi}_z$) in x and z directions are calculated similarly. The particle continuity equation is transformed into seven-point linear equation by the substitution of above expressions. The mathematical form of seven-point linear equation can be expressed as

$$A^E_{i,j,k} n^{k_t+1}_{i+1,j,k} + A^W_{i,j,k} n^{k_t+1}_{i-1,j,k} + A^N_{i,j,k} n^{k_t+1}_{i,j+1,k} + A^S_{i,j,k} n^{k_t+1}_{i,j-1,k} + A^F_{i,j,k} n^{k_t+1}_{i,j,k+1} + A^B_{i,j,k} n^{k_t+1}_{i,j,k-1} + A^C_{i,j,k} n^{k_t+1}_{i,j,k} = A_{i,j,k} \tag{3.24}$$

Here, the subscripts (i, j, k) represent the x, y and z axis and the superscripts of A, such as E, W, N, S, F, B and C show the east, west, north, south, front, back and central. The above equation (3.24) is able to make a relationship of particle species density at every grid point with six neighboring grid points in three spatial directions. The east, west, north, south, front, back, central and the source coefficients of above equation can be expressed as

$$A^E_{i,j,k} = -\frac{\Delta t}{\Delta x^2} D_{i+\frac{1}{2},j,k} f_1(Z_{x,i+\frac{1}{2},j,k}), \tag{3.25}$$

$$A^W_{i,j,k} = -\frac{\Delta t}{\Delta x^2} D_{i-\frac{1}{2},j,k} f_2(Z_{x,i-\frac{1}{2},j,k}), \tag{3.26}$$

$$A^N_{i,j,k} = -\frac{\Delta t}{\Delta y^2} D_{i,j+\frac{1}{2},k} f_1(Z_{y,i,j+\frac{1}{2},k}), \tag{3.27}$$

$$A^S_{i,j,k} = -\frac{\Delta t}{\Delta y^2} D_{i,j-\frac{1}{2},k} f_2(Z_{y,i,j-\frac{1}{2},k}), \tag{3.28}$$

$$A^F_{i,j,k} = -\frac{\Delta t}{\Delta z^2} D_{i,j,k+\frac{1}{2}} f_1(Z_{z,i,j,k+\frac{1}{2}}), \tag{3.29}$$

$$A^B_{i,j,k} = -\frac{\Delta t}{\Delta z^2} D_{i,j,k-\frac{1}{2}} f_2(Z_{z,i,j,k-\frac{1}{2}}), \tag{3.30}$$

$$A^C_{i,j,k} = 1 - A^E_{i-1,j,k} - A^W_{i+1,j,k} - A^N_{i,j-1,k} - A^S_{i,j+1,k} - A^F_{i,j,k-1} - A^B_{i,j,k+1} \tag{3.31}$$

$$A_{i,j,k} = n^{k_t}_{i,j,k} + \Delta t S_{i,j,k}, \tag{3.32}$$

respectively. The seven-point formulation is developed for the grid points between the parallel plate dielectric barriers and a proper set of boundary conditions is considered for the geometric configuration. The boundary conditions for the electron flux in cartesian discretization form can be written as

$$(\mathbf{\Phi}.\mathbf{n})_{i,j,k} = (2\beta - 1)\mathrm{sqn}(q)\mu_{i,j,k} n_{i,j,k} \mathbf{E}_{y,i,j+\frac{1}{2},k} + \frac{1}{2} v_{th,i,j,k} n_{i,j,k} - 2(1-\beta) \sum_p \gamma_p \mathbf{\Phi}_p.\mathbf{n} \tag{3.33}$$

on a south dielectric barrier boundary. Here, the index p in the third term of above equation (3.33) corresponds to the ionic species, which are responsible for the production of secondary electrons emission from the surface of dielectric barriers. So, the seven-point coefficients for the south boundary layer after

substitution of above equation is given by

$$A^N_{i,j,k} = -\frac{\Delta t}{\Delta y^2} D_{i,j+\frac{1}{2},k} f_1(Z_{y,i,j+\frac{1}{2},k}), \tag{3.34}$$

$$A^S_{i,j,k} = A^E_{i,j,k} = A^W_{i,j,k} = A^F_{i,j,k} = A^B_{i,j,k} = 0, \tag{3.35}$$

$$A^C_{i,j,k} = \frac{1}{2} - A^S_{i,j+1,k} + \frac{\Delta t}{\Delta y}(2\beta - 1)\mathrm{sqn}(q)\mu_{i,j,k} E_{y,i,j+\frac{1}{2},k} + \frac{\Delta t}{2\Delta y} v_{th,i,j,k} \tag{3.36}$$

$$A_{i,j,k} = \frac{1}{2} n^{k_t}_{i,j,k} + \frac{\Delta t}{2} S_{i,j,k}, \tag{3.37}$$

where

$$\begin{aligned} \beta &= 1 \qquad \mathrm{sgn}(q)\mu \mathbf{E}.\mathbf{n} > \mathbf{0} \\ &= 0 \qquad \mathrm{sgn}(q)\mu \mathbf{E}.\mathbf{n} \leq \mathbf{0} \end{aligned} \tag{3.38}$$

In equation (3.37), the factor $\frac{1}{2}$ in both terms corresponds to the interval $(\frac{\Delta y}{2})$ rather than Δy. The numerical expressions for the north, east, west, front and back boundaries, and for other particle species, are similar. However, the secondary electron emission coefficient γ_p is used for electron flux term instead of heavy and neutral species as in equation (3.20). The γ_p is dominant for heavy species because they can easily knock out the electrons from the dielectric barrier material.

The source term of electron energy equation plays a significant role and the inner product in the y direction is defined as,

$$\begin{aligned} \left[\left(\frac{\partial \Phi_e}{\partial \mu_e}\right)\left(\frac{\partial \mu_e}{\partial \overline{\varepsilon}}\right) + \left(\frac{\partial \Phi_e}{\partial D_e}\right)\left(\frac{\partial D_e}{\partial \overline{\varepsilon}}\right)\right]_{y,i,j+\frac{1}{2},k} &= \frac{-2}{3e\Delta y}\mu_{e,i,j+\frac{1}{2},k} h(Z_{y,i,j+\frac{1}{2},k})(n_{e,i,j+1,k} - n_{e,i,j,k}) \\ &\quad + \frac{1}{\mu_{e,i,j+\frac{1}{2},k}}\left(\frac{\partial \mu_e}{\partial \overline{\varepsilon}}\right)_{i,j+\frac{1}{2},k} \Phi_{e,i,j+\frac{1}{2},k}, \end{aligned} \tag{3.39}$$

where the function $h(Z)$ is defined as

$$h(Z) = f_1(Z) - \frac{\partial f_1(Z)}{\partial z} Z = f_2(Z) - \frac{\partial f_2(Z)}{\partial Z} Z = \frac{Z^2 e^Z}{(e^Z - 1)^2} \tag{3.40}$$

The above equation (3.39) is derived by using the Einstein relation and defined in chapter 2. The energy source term is not appeared in the optimal discretized form of equation (3.24). It is divided into two parts, one absorbs in A and other in A^C. The electron energy equation can be written in the presence of implicit correction part as

$$\frac{n^{k_t+1}_{\varepsilon}(x,y,z,t) - n^{k_t}_{\varepsilon}(x,y,z,t)}{\Delta t} - \boldsymbol{\nabla}.\boldsymbol{\Phi}_{\varepsilon}(n^{k_t+1}_{\varepsilon}, \mathbf{E}^{k_t+1}, \mu^{k_t}_e, D^{k_t}_e) = S^{k_t}_{\varepsilon} + \nu^{k_t}(n^{k_t+1}_{\varepsilon} - n^{k_t+1}_e \overline{\varepsilon}) \tag{3.41}$$

The L.H.S of equation (3.41) is comprised of time variations of electron energy density and spatial change in drift-diffusion flux, whereas the R.H.S corresponds to the energy source term and implicit correction part. The central and source coefficients are written in the discretized format as

$$A^C_{i,j,k} = 1 - A^E_{i-1,j,k} - A^W_{i+1,j,k} - A^N_{i,j-1,k} - A^S_{i,j+1,k} - A^F_{i,j,k-1} - A^B_{i,j,k+1} - \Delta t \nu^{k_t}_{i,j,k} \tag{3.42}$$

and

$$A_{i,j,k} = n^{k_t}_{i,j,k} + \Delta t S_{\varepsilon,i,j,k} - \Delta t \nu_{i,j,k} n^{k_t+1}_{e,i,j,k} \bar{\varepsilon}^{k_t}_{i,j,k} \tag{3.43}$$

3.6 Spatial discretization of Poisson's equation

The Poisson's equation in the simplified form is exhibited by equation (3.8). It can be written in the finite difference form as

$$\begin{aligned}(\boldsymbol{\nabla}.(\epsilon \mathbf{E}))_{i,j,k} = \frac{\epsilon_{i+\frac{1}{2},j,k} E_{x,i+\frac{1}{2},j,k} - \epsilon_{i-\frac{1}{2},j,k} E_{x,i-\frac{1}{2},j,k}}{\Delta x} \quad + \\ \frac{\epsilon_{i,j+\frac{1}{2},k} E_{y,i,j+\frac{1}{2},k} - \epsilon_{i,j-\frac{1}{2},k} E_{y,i,j-\frac{1}{2},k}}{\Delta y} \quad + \frac{\epsilon_{i,j,k+\frac{1}{2}} E_{z,i,j,k+\frac{1}{2}} - \epsilon_{i,j,k-\frac{1}{2}} E_{z,i,j,k-\frac{1}{2}}}{\Delta z}\end{aligned} \tag{3.44}$$

The transport terms are present in the R.H.S of the above equation (3.44) and the discretization should be in accordance with the transport terms of the continuity equation of discharge plasma species. It is difficult to perform implicit discretization because of the presence of electric field in the exponential part. Thus, the central difference scheme is considered and applied to calculate the flux of transport terms in the Poisson's equation as

$$\begin{aligned}\boldsymbol{\Phi}_{y,i,j+\frac{1}{2},k} &= \boldsymbol{\Phi}^{k_t}_{y,i,j+\frac{1}{2},k} + \left(\frac{\partial \boldsymbol{\Phi}}{\partial E}\right)^{k_t}_{y,i,j+\frac{1}{2},k} \left(E^{k_t+1}_{y,i,j+\frac{1}{2},k} - E^{k_t}_{y,i,j+\frac{1}{2},k}\right) \\ &= \left[\mathrm{sqn}(q)\mu_{i,j+\frac{1}{2},k}\left(g_1(\mathbf{Z}_{y,i,j+\frac{1}{2},k}) n_{i,j+1,k} - g_2(\mathbf{Z}_{y,i,j+\frac{1}{2},k}) n_{i,j,k}\right)\right]^{k_t} E^{k_t+1}_{y,i,j+\frac{1}{2},k} \\ &\quad - \left[D_{i,j+\frac{1}{2},k} h(\mathbf{Z}_{y,i,j+\frac{1}{2},k}) \frac{n_{i,j+1,k} - n_{i,j,k}}{\Delta y}\right]^{k_t},\end{aligned} \tag{3.45}$$

where the functions $g_1(Z)$, and $g_2(Z)$ are defined as

$$g_1(Z) = \frac{\partial f_1(Z)}{\partial Z} = \frac{(1-Z)e^Z - 1}{(e^Z - 1)^2}, \tag{3.46}$$

$$g_2(Z) = \frac{\partial f_2(Z)}{\partial Z} = e^Z \frac{e^Z - (1+Z)}{(e^Z - 1)^2}, \tag{3.47}$$

for $Z \neq 0$, and $g_1(0) = -\frac{1}{2}$ and $g_2(0) = \frac{1}{2}$; $h(Z)$ is evaluated by using an equation (3.40). The equation (3.20) is more useful and provides the flux for the transport terms of Poisson's equation even at higher time steps for the numerical simulations. The electric field in the y direction between two grid points is calculated by the gradient of the electric potential as

$$E_{y,i,j+\frac{1}{2},k} = -\frac{(\phi_a)_{i,j+1,k} - (\phi_a)_{i,j,k}}{\Delta y} \tag{3.48}$$

and the similar expressions for $E_{x,i+\frac{1}{2},j,k}$ and $E_{z,i,j,k+\frac{1}{2}}$. The formulation of Poisson's equation in seven-point form can be written by the substitution of $U = \phi_a$ as

$$A^E_{i,j,k}U_{i+1,j,k}+A^W_{i,j,k}U_{i-1,j,k}+A^N_{i,j,k}U_{i,j+1,k}+A^S_{i,j,k}U_{i,j-1,k}+A^F_{i,j,k}U_{i,j,k+1}+A^B_{i,j,k}U_{i,j,k-1}+A^C_{i,j,k}U_{i,j,k} = A_{i,j,k}, \tag{3.49}$$

where

$$A^E_{i,j,k} = \frac{1}{\Delta x^2}\varepsilon_{i+\frac{1}{2},j,k} - \frac{\Delta t}{\Delta x^2}\sum_p \left[|q|\mu_{i+\frac{1}{2},j,k}(n_{i+1,j,k}g_1(Z_{x,i+\frac{1}{2},j,k}) - n_{i,j,k}g_2(Z_{x,i+\frac{1}{2},j,k}))\right]_p, \tag{3.50}$$

$$A^W_{i,j,k} = \frac{1}{\Delta x^2}\varepsilon_{i-\frac{1}{2},j,k} - \frac{\Delta t}{\Delta x^2}\sum_p \left[|q|\mu_{i-\frac{1}{2},j,k}(n_{i,j,k}g_1(Z_{x,i-\frac{1}{2},j,k}) - n_{i-1,j,k}g_2(Z_{x,i-\frac{1}{2},j,k}))\right]_p, \tag{3.51}$$

$$A^N_{i,j,k} = \frac{1}{\Delta y^2}\varepsilon_{i,j+\frac{1}{2},k} - \frac{\Delta t}{\Delta y^2}\sum_p \left[|q|\mu_{i,j+\frac{1}{2},k}(n_{i,j+1,k}g_1(Z_{y,i,j+\frac{1}{2},k}) - n_{i,j,k}g_2(Z_{y,i,j+\frac{1}{2},k}))\right]_p, \tag{3.52}$$

$$A^S_{i,j,k} = \frac{1}{\Delta y^2}\varepsilon_{i,j-\frac{1}{2},k} - \frac{\Delta t}{\Delta y^2}\sum_p \left[|q|\mu_{i,j-\frac{1}{2},k}(n_{i,j,k}g_1(Z_{y,i,j-\frac{1}{2},k}) - n_{i,j-1,k}g_2(Z_{y,i,j-\frac{1}{2},k}))\right]_p, \tag{3.53}$$

$$A^F_{i,j,k} = \frac{1}{\Delta z^2}\varepsilon_{i,j,k+\frac{1}{2}} - \frac{\Delta t}{\Delta z^2}\sum_p \left[|q|\mu_{i,j,k+\frac{1}{2}}(n_{i,j,k+1}g_1(Z_{z,i,j,k+\frac{1}{2}}) - n_{i,j,k}g_2(Z_{z,i,j,k+\frac{1}{2}}))\right]_p, \tag{3.54}$$

$$A^B_{i,j,k} = \frac{1}{\Delta z^2}\varepsilon_{i,j,k-\frac{1}{2}} - \frac{\Delta t}{\Delta z^2}\sum_p \left[|q|\mu_{i,j,k-\frac{1}{2}}(n_{i,j,k}g_1(Z_{z,i,j,k-\frac{1}{2}}) - n_{i,j,k-1}g_2(Z_{z,i,j,k-\frac{1}{2}}))\right]_p, \tag{3.55}$$

$$A^C_{i,j,k} = -A^E_{i,j,k} - A^W_{i,j,k} - A^N_{i,j,k} - A^S_{i,j,k} - A^F_{i,j,k} - A^B_{i,j,k} \tag{3.56}$$

and

$$\begin{aligned} A_{i,j,k} = & -\sum_p [qn_{i,j,k} + \frac{\Delta t}{\Delta x^2}qD_{i+\frac{1}{2},j,k}h(Z_{x,i+\frac{1}{2},j,k})(n_{i+1,j,k} - n_{i,j,k}) \\ & -\frac{\Delta t}{\Delta x^2}qD_{i-\frac{1}{2},j,k}h(Z_{x,i-\frac{1}{2},j,k})(n_{i,j,k} - n_{i-1,j,k}) + \frac{\Delta t}{\Delta y^2}qD_{i,j+\frac{1}{2},k}h(Z_{y,i,j+\frac{1}{2},k})(n_{i,j+1,k} - n_{i,j,k}) \\ & -\frac{\Delta t}{\Delta y^2}qD_{i,j-\frac{1}{2},k}h(Z_{y,i,j-\frac{1}{2},k})(n_{i,j,k} - n_{i,j-1,k}) + \frac{\Delta t}{\Delta z^2}qD_{i,j,k+\frac{1}{2}}h(Z_{z,i,j,k+\frac{1}{2}})(n_{i,j,k+1} - n_{i,j,k}) \\ & -\frac{\Delta t}{\Delta z^2}qD_{i,j,k-\frac{1}{2}}h(Z_{z,i,j,k-\frac{1}{2}})(n_{i,j,k} - n_{i,j,k-1})]_p \end{aligned} \tag{3.57}$$

The Poisson's equation is solved inside the reactor gap, whereas the Dirichlet boundary conditions apply on the solid plate electrodes. During the discharge progress, the charge is deposited on the dielectric barriers and the expression for the surface charge density can be written as

$$\varepsilon_{i,j+\frac{1}{2},k} E_{y,i,j+\frac{1}{2},k} - \varepsilon_{i,j-\frac{1}{2},k} E_{y,i,j-\frac{1}{2},k} = \sigma_{s,i,j,k}, \tag{3.58}$$

for the south dielectric barrier. Although, the exact convergent solution of physical problem is not possible without proper implementation of boundary conditions. Now the boundary conditions of Poisson's equation are described by the following expressions for open east, west, front and bottom surfaces. For the westward and eastward rectangular surfaces, the coefficients for the boundary points of the surface can be written as $A^{W}_{0,j,k} = 0$ and $A^{E}_{0,j,k} \neq 0$ for the westward and similarly for other open boundaries. As the electric potential is applied on the north and south surfaces, therefore the north and south coefficients are treated by a using different method. The coefficient matrix $(A_{i,j,k})$ is modified due to the effect of south and north coefficients on the solid dielectric barriers. Thus, it can be expressed as

$$A_{i,j,k} - = A^{S,N}_{i,j,k} U_{i,j,k} \text{ for } j = 0, \text{ (cells)}_{y} \tag{3.59}$$

for the solid dielectric barriers.

3.7 The solution of seven-point equations

The finite difference scheme is used to simplify the complex equations. The general simplified linear seven-point equation is described by the following representation as

$$A^{E}_{i,j,k} X_{i+1,j,k} + A^{W}_{i,j,k} X_{i-1,j,k} + A^{N}_{i,j,k} X_{i,j+1,k} + A^{S}_{i,j,k} X_{i,j-1,k} + A^{F}_{i,j,k} X_{i,j,k+1} + A^{B}_{i,j,k} X_{i,j,k-1} + A^{C}_{i,j,k} X_{i,j,k} = A_{i,j,k}, \tag{3.60}$$

The above equation (3.60) is solved to calculate the variables of bulk gas at every time step. The number of numerical techniques are available to solve the set of seven-point linear equation. However, the iterative scheme is most commonly used and considered to evaluate the accurate solution of linear system of equations. In this method, the iterative procedure improves an initial estimated input until the convergence criteria is satisfied. There are different numerical algorithmic schemes available in the literature [70, 71] for the numerical solution of linear seven-point equation. The famous iterative techniques, such as Alternating direction implicit [72, 73], Successive over relaxation [74] and Modified strongly implicit [71, 75], are applied to solve the linear system of seven-point equations. The MSI[1]

[1] MSI: Modified strongly implicit

iterative method is used to find the solution of transport equations, whereas the SOR[2] is applied for the Poisson's equation. The alternating direction implicit solver is considered and employed to find the solution of electron energy density equation. The combination of these three methods provide the solution of linear system of partial differential equations of fluid model in three-dimensional form.

3.7.1 Modified implicit solver for transport equations

As the expressions are large and intricate in the coefficients of Modified strongly implicit solver, the different expressions of coefficients are divided into small parts by assigning the arbitrary variables. The C_1, C_2 and C_3 variables are used to calculate the coefficients of $a_{i,j,k}$ as

$$\begin{aligned} C_1 &= h_{i,j,k}(h_{i+1,j,k-1} + r_{i+1,j,k-1}), \qquad C_2 = r_{i,j,k-1} - p_{i+1,j,k-1}h_{i,j,k-1}, \\ \text{and } C_3 &= h_{i,j+1,k-1} + p_{i,j+1,k-1} + r_{i,j+1,k-1}, \end{aligned} \tag{3.61}$$

if $(1 + \alpha(p_{i,j,k-1} - C_1 - C_2C_3) < 0.5)$

$$a_{i,j,k} = 2A^B_{i,j,k}, \tag{3.62}$$

else

$$a_{i,j,k} = \frac{A^B_{i,j,k}}{1 + \alpha(p_{i,j,k-1} - C_1 - C_2C_3)},$$

$$b_{i,j,k} = -a_{i,j,k}h_{i,j,k-1}, \tag{3.63}$$

$$c_{i,j,k} = -a_{i,j,k}r_{i,j,k-1} - b_{i,j,k}p_{i+1,j,k-1}, \tag{3.64}$$

The C_4 to C_7 variables are employed to evaluate the coefficients of $d_{i,j,k}$ as

$$\begin{aligned} C_4 &= (h_{i+1,j-1,k} + 2s_{i+1,j-1,k} + v_{i+1,j-1,k})b_{i,j,k}s_{i+1,j,k-1},\ C_5 = s_{i-1,j,k}(A^W_{i,j,k} - a_{i,j,k}u_{i,j,k-1}), \\ C_6 &= 2s_{i,j-1,k} + u_{i,j-1,k} - s_{i-1,j,k}p_{i,j-1,k},\ C_7 = h_{i,j-1,k}(h_{i+1,j-1,k} + 2s_{i+1,j-1,k} + v_{i+1,j-1,k}), \end{aligned} \tag{3.65}$$

if $(1 + \alpha(C_6 - C_7) < 0.5)$

$$d_{i,j,k} = 2(A^S_{i,j,k} - a_{i,j,k}s_{i,j,k-1} + \alpha(C_4 - C_5)), \tag{3.66}$$

[2]SOR: Successive over relaxation

else

$$d_{i,j,k} = \frac{2(A^S_{i,j,k} - a_{i,j,k}s_{i,j,k-1} + \alpha(C_4 - C_5))}{1 + \alpha(C_6 - C_7)},$$

$$e_{i,j,k} = -b_{i,j,k}s_{i+1,j,k-1} - d_{i,j,k}h_{i,j-1,k} \tag{3.67}$$

The C_8 to C_{10} variables are contributed to evaluate the coefficients of $f_{i,j,k}$ as

$$\begin{aligned} C_8 &= A^W_{i,j,k} - a_{i,j,k}u_{i,j,k-1} - d_{i,j,k}p_{i,j-1,k},\ C_9 = \alpha(a_{i,j,k}p_{i,j,k-1} + c_{i,j,k}p_{i,j+1,k-1} + d_{i,j,k}u_{i,j-1,k}) \\ C_{10} &= 1 + \alpha(2p_{i-1,j,k} + s_{i-1,j,k} + 2u_{i-1,j,k}) \end{aligned} \tag{3.68}$$

if $(1 + \alpha(2p_{i-1,j,k} + s_{i-1,j,k} + 2u_{i-1,j,k}) < 0.5)$

$$f_{i,j,k} = 2(C_8 - C_9), \tag{3.69}$$

else

$$f_{i,j,k} = 2\frac{C_8 - C_9}{C_{10}}, \tag{3.70}$$

The coefficients of matrix product are defined by the following variables from $\phi^1_{i,j,k}$ to $\phi^{12}_{i,j,k}$ as

$$\begin{aligned} \phi^1_{i,j,k} &= b_{i,j,k}h_{i+1,j,k-1},\ \phi^2_{i,j,k} = a_{i,j,k}p_{i,j,k-1},\ \phi^3_{i,j,k} = b_{i,j,k}r_{i+1,j,k-1} + c_{i,j,k}h_{i,j+1,k-1}, \\ \phi^4_{i,j,k} &= c_{i,j,k}p_{i,j,k-1},\ \phi^5_{i,j,k} = c_{i,j,k}r_{i,j+1,k-1},\ \phi^6_{i,j,k} = e_{i,j,k}h_{i+1,j-1,k}, \\ \phi^7_{i,j,k} &= f_{i,j,k}p_{i-1,j,k},\ \phi^8_{i,j,k} = d_{i,j,k}s_{i,j-1,k},\ \phi^9_{i,j,k} = e_{i,j,k}s_{i+1,j-1,k}, \\ \phi^{10}_{i,j,k} &= d_{i,j,k}u_{i,j-1,k} + f_{i,j,k}s_{i-1,j,k},\ \phi^{11}_{i,j,k} = e_{i,j,k}v_{i+1,j-1,k},\ \phi^{12}_{i,j,k} = f_{i,j,k}u_{i-1,j,k}, \end{aligned} \tag{3.71}$$

So, the arbitrary variables can be calculated by the following equations:

$$\begin{aligned} C_{11} &= A^C_{i,j,k} - a_{i,j,k}v_{i,j,k-1} - b_{i,j,k}u_{i+1,j,k-1} - c_{i,j,k}s_{i,j+1,k-1} \\ &\quad -d_{i,j,k}r_{i,j-1,k} - e_{i,j,k}p_{i+1,j-1,k} - f_{i,j,k}h_{i-1,j,k}, \end{aligned} \tag{3.72}$$

$$C_{12} = 2(\phi^1_{i,j,k} + \phi^2_{i,j,k} + \phi^3_{i,j,k}) + 3\phi^4_{i,j,k},\ C_{13} = 2(\phi^5_{i,j,k} + \phi^6_{i,j,k} + \phi^7_{i,j,k} + \phi^8_{i,j,k}), \tag{3.73}$$

$$C_{14} = 2(\phi^{10}_{i,j,k} + \phi^{11}_{i,j,k} + \phi^{12}_{i,j,k}), \tag{3.74}$$

Thus the coefficients $g_{i,j,k}$, $h_{i,j,k}$, $p_{i,j,k}$, $r_{i,j,k}$, $s_{i,j,k}$ and $v_{i,j,k}$ are described as

$$g_{i,j,k} = C_{11} + \alpha(C_{12} + C_{13} + C_{14}), \tag{3.75}$$

where the variables C_{11} to C_{14} are substituted from the equation (3.72) to equation (3.74) in equation (3.75),

$$h_{i,j,k} = \frac{A^E_{i,j,k} - b_{i,j,k}v_{i+1,j,k-1} - e_{i,j,k}r_{i+1,j-1,k} - \alpha(2\phi^1_{i,j,k} + \phi^3_{i,j,k} + \phi^9_{i,j,k} + \phi^{11}_{i,j,k})}{g_{i,j,k}}, \quad (3.76)$$

$$p_{i,j,k} = \frac{(-c_{i,j,k}u_{i,j+1,k} - f_{i,j,k}r_{i-1,j,k})}{g_{i,j,k}}, \quad (3.77)$$

$$r_{i,j,k} = \frac{A^N_{i,j,k} - c_{i,j,k}v_{i,j+1,k} - \alpha(\phi^2_{i,j,k} + \phi^3_{i,j,k} + 2\phi^4_{i,j,k} + 2\phi^5_{i,j,k} + \phi^7_{i,j,k})}{g_{i,j,k}}, \quad (3.78)$$

$$s_{i,j,k} = \frac{(-d_{i,j,k}v_{i,j-1,k} - e_{i,j,k}u_{i+1,j-1,k})}{g_{i,j,k}}, \quad u_{i,j,k} = \frac{-f_{i,j,k}v_{i-1,j,k}}{g_{i,,j,k}}, \quad (3.79)$$

and

$$v_{i,j,k} = \frac{A^F_{i,j,k} - \alpha(\phi^8_{i,j,k} + \phi^9_{i,j,k} + \phi^{10}_{i,j,k} + \phi^{11}_{i,j,k} + \phi^{12}_{i,j,k})}{g_{i,j,k}},$$

where α is a constant variable and its range cover the numerical values from 0 to 1. Consequently, the iterative procedure for the solution of system of fluid equations in the three-dimensional form can be expressed by the following steps. The above coefficients a through v remain the same for one complete iteration process. The residual vector (R) is evaluated by the formula as

$$R_{i,j,k} = A^C_{i,j,k} - A^E_{i,j,k}X_{i+1,j,k} - A^W_{i,j,k}X_{i-1,j,k} - A^N_{i,j,k}X_{i,j+1,k} - A^S_{i,j,k}X_{i,j-1,k} - A^F_{i,j,k}X_{i,j,k+1} - A^B_{i,j,k}X_{i,j,k-1}, \quad (3.80)$$

The intermediate vectors are calculated according to the backward and forward substitutions as

$$V_{i,j,k} = \frac{R_{i,j,k} - f_{i,j,k}V_{i-1,j,k} - d_{i,j,k}V_{i,j-1,k} - a_{i,j,k}V_{i,j,k-1}}{g_{i,j,k}}, \quad (3.81)$$

$$\delta_{i,j,k} = V_{i,j,k} - h_{i,j,k}\delta_{i+1,j,k} - r_{i,j,k}\delta_{i,j+1,k} - v_{i,j,k}\delta_{i,j,k+1}, \quad (3.82)$$

where $\delta_{i,j,k}$ is the change over an iteration. The final iterative solution is appeared in the following form as

$$X^*_{i,j,k} = X_{i,j,k} + \delta_{i,j,k} \quad (3.83)$$

The combination of previous four steps of iterative procedure from equation (3.80) to (3.83) is continued until the magnitude of the residual vector $||R||$ is smaller than the convergence criterion $||R|| < 10^{-4}\left(||A|| + ||A^C|| \times ||X||\right)$. The rate of convergence depends on the choice of α. The fastest convergence is achieved for the species continuity equations at $\alpha = 0.6$ in the atmospheric pressure discharge. However, the following assumptions also avoid the divergence of numerical solution during the evaluation

of the continuity equation of fluid model as,

$$a_{i,j,k} = \left\{ \begin{array}{ll} 2A^B_{i,j,k}, & 1+\alpha(p_{i,j,k-1}-C_1-C_2C_3) < \frac{1}{2} \\ \frac{A^B_{i,j,k}}{1+\alpha(p_{i,j,k-1}-C_1-(C_2C_3))}, & 1+\alpha(p_{i,j,k-1}-C_1-C_2C_3) \geq \frac{1}{2} \end{array} \right\}, \tag{3.84}$$

$$d_{i,j,k} = \left\{ \begin{array}{ll} 2(A^S_{i,j,k} - a_{i,j,k}s_{i,j,k-1} + \alpha(C_4-C_5)), & 1+\alpha(C_6-C_7) < \frac{1}{2} \\ \frac{2(A^S_{i,j,k}-a_{i,j,k}s_{i,j,k-1}+\alpha(C_4-C_5))}{1+\alpha(C_6-C_7)}, & 1+\alpha(C_6-C_7) \geq \frac{1}{2} \end{array} \right\}, \tag{3.85}$$

and

$$f_{i,j,k} = \left\{ \begin{array}{ll} 2(C_8-C_9), & 1+\alpha(2p_{i-1,j,k}+s_{i-1,j,k}+2u_{i-1,j,k}) < \frac{1}{2} \\ \frac{C_8-C_9}{C_{10}}, & 1+\alpha(2p_{i-1,j,k}+s_{i-1,j,k}+2u_{i-1,j,k}) \geq \frac{1}{2} \end{array} \right\} \tag{3.86}$$

The solution becomes divergent if the denominators of coefficient a, d and f are zero. Therefore, the coefficients a through v along with the above mentioned imposed conditions are used to find the solution of transport equations.

3.7.2 Successive over relaxation method for Poisson's equation

The successive over relaxation (SOR) numerical method is implemented to evaluate the solution of Poisson's equation in the discretized three-dimensional cartesian grid. However, the coefficients $A^E_{i,j,k}$, $A^W_{i,j,k}$, $A^N_{i,j,k}$, $A^S_{i,j,k}$, $A^F_{i,j,k}$, $A^B_{i,j,k}$, $A^C_{i,j,k}$ and $A_{i,j,k}$ are directly used to find the residual vector (R). The following iterative steps are followed to calculate the required solution. Hence, the residual vector (R) during the calculation at any stage is given by the following relation:

$$R_{i,j,k} = A^E_{i,j,k}X_{i+1,j,k}+A^W_{i,j,k}X_{i-1,j,k}+A^N_{i,j,k}X_{i,j+1,k}+A^S_{i,j,k}X_{i,j-1,k}+A^F_{i,j,k}X_{i,j,k+1}+A^B_{i,j,k}X_{i,j,k-1}-A_{i,j,k}, \tag{3.87}$$

Then the SOR algorithm can be written as

$$X^{\text{new}}_{i,j,k} = X^{\text{old}}_{i,j,k} - \delta_{i,j,k} \tag{3.88}$$

where

$$\delta_{i,j,k} = \frac{\omega R_{i,j,k}}{A^C_{i,j,k}} \tag{3.89}$$

Here ω is called the overrelaxation parameter, and the method is called as successive overrelaxation (SOR). The method SOR is convergent for the numerical simulations only if $0 < \omega < 2$. The overrelaxation range ($0 < \omega < 2$) can provide the faster convergence than other iterative techniques. This formulation is very easy to program and the norm of the residual vector $||R||$ may be considered as a criterion for terminating the iteration. The previous three iterative steps from equation (3.87) to equa-

tion (3.89) are continued until the magnitude of the residual vector $||R||$ is smaller than the convergence criterion $||R|| < 10^{-4}||A||$. The convergence is achieved fastly by the careful selection of accelerator factor ω. We use $\omega = 1.9$ for the fastest possible convergence of solution of Poisson's equation in two and three-dimensional fluid model algorithms.

3.7.3 Alternating direction implicit method for electron energy density equation

Consider an implicit solution of electron energy density equation using an Alternating direction implicit solver. As long as we are dealing with the linear system of equations, the implicit solutions are directly obtained from the application of Thomas' algorithm. This is possible in the situation when the finite difference scheme gives the equation in tridiagonal form. The standard tridiagonal form is solved by the use of Thomas' algorithm. The three time steps are used in three-dimensional case to update the quantities between t and $t + \Delta t$. During first $t_1 = t + \frac{\Delta t}{3}$, the integration steps are marched along the x - direction, the finite difference equations are solved along the y - direction in $t_2 = t + \frac{2\Delta t}{3}$ with updated quantities of previous step and finally the integration solution is evaluated in the z - direction during $t_3 = t + \Delta t$.

$$\frac{n_{i,j,k}^{k_t+\frac{\Delta t}{3}} - n_{i,j,k}^{k_t}}{\left(\frac{\Delta t}{3}\right)} + \frac{\mathbf{\Phi}_{x,i+\frac{1}{2},j,k}^{k_t+\frac{\Delta t}{3}} - \mathbf{\Phi}_{x,i-\frac{1}{2},j,k}^{k_t+\frac{\Delta t}{3}}}{\Delta x} = S_{i,j,k}^{k_t} - \frac{\mathbf{\Phi}_{y,i,j+\frac{1}{2},k}^{k_t} - \mathbf{\Phi}_{y,i,j-\frac{1}{2},k}^{k_t}}{\Delta y} - \frac{\mathbf{\Phi}_{z,i,j,k+\frac{1}{2}}^{k_t} - \mathbf{\Phi}_{z,i,j,k-\frac{1}{2}}^{k_t}}{\Delta z}, \tag{3.90}$$

$$\frac{n_{i,j,k}^{k_t+\frac{2\Delta t}{3}} - n_{i,j,k}^{k_t+\frac{\Delta t}{3}}}{\left(\frac{\Delta t}{3}\right)} + \frac{\mathbf{\Phi}_{y,i,j+\frac{1}{2},k}^{k_t+\frac{2\Delta t}{3}} - \mathbf{\Phi}_{y,i,j-\frac{1}{2},k}^{k_t+\frac{2\Delta t}{3}}}{\Delta y} = S_{i,j,k}^{k_t+\frac{2\Delta t}{3}} - \frac{\mathbf{\Phi}_{x,i+\frac{1}{2},j,k}^{k_t+\frac{\Delta t}{3}} - \mathbf{\Phi}_{x,i-\frac{1}{2},j,k}^{k_t+\frac{\Delta t}{3}}}{\Delta x} - \frac{\mathbf{\Phi}_{z,i,j,k+\frac{1}{2}}^{k_t+\frac{\Delta t}{3}} - \mathbf{\Phi}_{z,i,j,k-\frac{1}{2}}^{k_t+\frac{\Delta t}{3}}}{\Delta z}, \tag{3.91}$$

$$\frac{n_{i,j,k}^{k_t+\Delta t} - n_{i,j,k}^{k_t+\frac{2\Delta t}{3}}}{\left(\frac{\Delta t}{3}\right)} + \frac{\mathbf{\Phi}_{z,i,j,k+\frac{1}{2}}^{k_t+\Delta t} - \mathbf{\Phi}_{z,i,j,k-\frac{1}{2}}^{k_t+\Delta t}}{\Delta z} = S_{i,j,k}^{k_t+\frac{2\Delta t}{3}} - \frac{\mathbf{\Phi}_{x,i+\frac{1}{2},j,k}^{k_t+\frac{2\Delta t}{3}} - \mathbf{\Phi}_{x,i-\frac{1}{2},j,k}^{k_t+\frac{2\Delta t}{3}}}{\Delta x} - \frac{\mathbf{\Phi}_{y,i,j+\frac{1}{2},k}^{k_t+\frac{2\Delta t}{3}} - \mathbf{\Phi}_{y,i,j-\frac{1}{2},k}^{k_t+\frac{2\Delta t}{3}}}{\Delta y}, \tag{3.92}$$

The ADI[3] method is stable and provides the convergent solution for different types of complex problems. The above set of electron energy density equations are transformed into tridiagonal standard form and their representations along x, y and z directions are discussed in the following equations, In the x

[3] ADI: Alternating direction implicit

direction, Suppose

$$A^x_{i,j,k} = A^{k_t}_{i,j,k} - A^N_{i,j,k}X^{k_t}_{i,j+1,k} - A^S_{i,j,k}X^{k_t}_{i,j-1,k} - A^F_{i,j,k}X^{k_t}_{i,j,k+1} - A^B_{i,j,k}X^{k_t}_{i,j,k-1}, \tag{3.93}$$

then the tridiagonal representation can be expressed by the substitution of $A^x_{i,j,k}$ as

$$\begin{aligned} A^E_{i,j,k}X^{k_t+\frac{\Delta t}{3}}_{i+1,j,k} + A^C_{i,j,k}X^{k_t+\frac{\Delta t}{3}}_{i,j,k} + A^W_{i,j,k}X^{k_t+\frac{\Delta t}{3}}_{i-1,j,k} &= A^x_{i,j,k} & (3.94)\\ A^E_{i,j,k}X^{k_t+\frac{\Delta t}{3}}_{i+1,j,k} + A^C_{i,j,k}X^{k_t+\frac{\Delta t}{3}}_{i,j,k} + A^W_{i,j,k}X^{k_t+\frac{\Delta t}{3}}_{i-1,j,k} &= B_{i,j,k}, & (3.95)\end{aligned}$$

where $B_{i,j,k} = A^x_{i,j,k}$, Similarly the tridiagonal forms are formulated by the substitution of similar type of expressions in the y and z directions. In the y direction,

$$A^y_{i,j,k} = A^{k_t+\frac{\Delta t}{3}}_{i,j,k} - A^E_{i,j,k}X^{k_t+\frac{\Delta t}{3}}_{i+1,j,k} - A^W_{i,j,k}X^{k_t+\frac{\Delta t}{3}}_{i-1,j,k} - A^F_{i,j,k}X^{k_t+\frac{\Delta t}{3}}_{i,j,k+1} - A^B_{i,j,k}X^{k_t+\frac{\Delta t}{3}}_{i,j,k-1},$$

$$\begin{aligned} A^N_{i,j,k}X^{k_t+\frac{2\Delta t}{3}}_{i,j+1,k} + A^C_{i,j,k}X^{k_t+\frac{2\Delta t}{3}}_{i,j,k} + A^S_{i,j,k}X^{k_t+\frac{2\Delta t}{3}}_{i,j-1,k} &= A^y_{i,j,k}, & (3.96)\\ A^N_{i,j,k}X^{k_t+\frac{2\Delta t}{3}}_{i,j+1,k} + A^C_{i,j,k}X^{k_t+\frac{2\Delta t}{3}}_{i,j,k} + A^S_{i,j,k}X^{k_t+\frac{2\Delta t}{3}}_{i,j-1,k} &= C_{i,j,k}, & (3.97)\end{aligned}$$

where $C_{i,j,k} = A^y_{i,j,k}$ and similarly, in the z direction,

$$A^z_{i,j,k} = A^{k_t+\frac{2\Delta t}{3}}_{i,j,k} - A^E_{i,j,k}X^{k_t+\frac{2\Delta t}{3}}_{i+1,j,k} - A^W_{i,j,k}X^{k_t+\frac{2\Delta t}{3}}_{i-1,j,k} - A^N_{i,j,k}X^{k_t+\frac{2\Delta t}{3}}_{i,j+1,k} - A^S_{i,j,k}X^{k_t+\frac{2\Delta t}{3}}_{i,j-1,k},$$

$$\begin{aligned} A^F_{i,j,k}X^{k_t+\Delta t}_{i,j,k+1} + A^C_{i,j,k}X^{k_t+\Delta t}_{i,j,k} + A^B_{i,j,k}X^{k_t+\Delta t}_{i,j,k-1} &= A^z_{i,j,k} & (3.98)\\ A^F_{i,j,k}X^{k_t+\Delta t}_{i,j,k+1} + A^C_{i,j,k}X^{k_t+\Delta t}_{i,j,k} + A^B_{i,j,k}X^{k_t+\Delta t}_{i,j,k-1} &= E_{i,j,k}, & (3.99)\end{aligned}$$

where $E_{i,j,k} = A^z_{i,j,k}$. The Alternating direction implicit solver provides the stable and convergent solution for the electron energy density equation in three spatial directions. The effect of boundary conditions are spread over the complete volume by implementing the ADI[4] solver. It is comparatively slow as compared to the MSI solver for the calculation of system of seven-point equations.

Chapter 4

Numerical simulations using one-dimensional fluid model

4.1 Introduction

In this chapter, the numerical simulation results are described by using one-dimensional fluid model of atmospheric pressure discharge. As the number of scientists already performed research work in this field, a short and necessary outline is described of their recent work. The experimental and numerical investigations are explored for the atmospheric pressure discharges, whereas the glow and Townsend discharge modes elaborate the brief perception of uniform dielectric barrier discharge in [15, 76]. Plasma diagnostics and numerical modelling tools are considered to discuss the effects of impurities for the uniform and filamentary atmospheric pressure discharge modes in [77]. The one-dimensional fluid model is used to examine the influence of interaction between the charged particles and dielectric surface over a homogeneous barrier discharge in nitrogen at atmospheric pressure in [78]. The clear and precise understanding of uniform atmospheric pressure glow discharge is the major objective for high pressure discharge applications and the cathode fall region plays a significant role for the description of discharge plasma characteristics in this regard. The comparative experimental study is performed to understand the features of diffuse barrier discharges in different gases by electrical measurements and by spatially and temporally resolved optical emission spectroscopy in [79]. The stability of atmospheric pressure dielectric barrier discharge is explicated with the help of positive and negative differential conductivity, whereas the period multiplication and chaotic behavior provide the precise understanding of discharge plasma in pure helium gas [80]. The experimental observations and findings are characterized in an open reactor with flowing helium gas in the presence of impurities and the comparison of current limitation

effects through the dielectric in atmospheric pressure glow discharge also enhances an insight in the high pressure discharge regimes [33, 81].

We discuss the spatio-temporal characteristics of atmospheric pressure discharge in the presence of discharge species, such as He^+, He_2^+, N_2^+, He^* and especially the excimers He_2 ($a^3\sum_u^+$). The space and time variations of electric field and electron density are investigated at 20 kHz, which enhance the understanding of the evolution of atmospheric pressure glow discharge. The analysis of atmospheric pressure discharge is performed at different quenching frequencies, which shows the transition from the glow to Townsend discharge mode. The temporal profile of metastables and excimers show that they are dominant species with higher density in the uniform glow and Townsend discharge modes. As the nitrogen impurities have substantial impact on the helium discharge, so their implications are explored for the atmospheric pressure glow and Townsend discharge modes. The spatial structures of ionization rate and electron mean energy are shown that link the higher and lower rates to APG[1] and APT[2] discharges. The spatio-temporal evolution of discharge species is manifested by the influence of external operating parameters. The examination of lower ($\lesssim$ 7 kHz) and higher frequencies ($>$ 7 kHz) exhibit that the intricate and uniform discharge structures are described in pure helium gas. The lower and higher ionization modes of atmospheric pressure discharge are randomly appeared in the discharge current pulses of several cycles, which provide the evidence of chaotic behavior in the lower frequency regime. The presence and absence of stepwise ionization processes of metastables and excimers develop the non-uniform and uniform discharge plasma, which are illustrated with the temporal evolution of discharge current density. The sufficient amount of nitrogen impurities is considered for the uniform discharge plasma because the higher amount of impurities causes the possibility of formation of filamentary atmospheric pressure discharge due to atypical destruction of metastables. The chaotic and bifurcation processes are identified in the lower frequency regime ($\lesssim$ 7 kHz) and develop the further perception of the dielectric barrier discharges at high pressure. The reliability of numerical simulations are provided by comparing the modelling and experimental results.

In this chapter, Section 4.2 describes the characteristics of atmospheric pressure discharges under variable conditions. Section 4.3 explores the spatial structures of discharge species parameters. Section 4.4 illustrates the effect of impurities and secondary electron emission coefficient. Section 4.5 provides the chaotic behavior and bifurcation processes of the atmospheric pressure discharges. Section 4.6 compares the experimental and one-dimensional fluid model results. Finally, the last section discusses the conclusions of one-dimensional fluid model simulations.

[1] APG: Atmospheric pressure glow
[2] APT: Atmospheric pressure Townsend

4.2 Characteristics of atmospheric pressure discharge

We consider an AC sinusoidal voltage for the parallel plate dielectric barrier discharge configuration at reference constant gas pressure 760 torr. The density of neutral helium gas is calculated by the equation of state, $p = nkT$, whereas the gas temperature is considered at room temperature (300 K) for the numerical simulations. Initially, a quasi-neutral plasma with equal electrons and ions of $\sim 10^8$ cm^{-3} is assumed in pure helium and He-N_2 gases. The numerical simulations of dielectric barrier discharge are discussed at variable driving frequencies and amplitudes of the applied voltage. It is discussed and described in [55, 82] that the lifetime of excimers ($a^3 \sum_u^+$) is uncertain and its collisional lifetime may reach tens of millisecond at below 100 torr. The quenching of excimers into ground state is also small because of high energy interval. If the lifetime of excimer molecules exceed the 10^{-5} s, the ionization processes interacting with this molecule may influence on the total ionization rate. However, the destruction frequency of excimers He_2^* is used as 1.0×10^6 s^{-1} for the numerical simulations of atmospheric pressure discharge. The quantitative influence of nitrogen impurities is varied with their concentration in pure helium and use 10, 20, 50 and 100 ppm molecular nitrogen impurities in this chapter under different external input conditions. In the parallel plate dielectric barrier discharge arrangement, the dielectrics perform an important role and the charge is deposited on the dielectric barrier surface. Due to charge deposition, the voltage is dropped across the dielectric barriers and consequently, the gap voltage becomes smaller than the external applied voltage. The applied voltage is calculated by using the formula, $V_a = V_g + V_d$, whereas V_a is applied voltage, V_g is gap voltage and V_d is the voltage trap across the barriers. The voltage trap is developed due to the charge accumulation on the dielectric barrier surface and assumed the charge accumulation of previous cycle before starting the numerical simulations [83]. Although, an analytic model is proposed of a dielectric barrier discharge in the Townsend ionization mode, which describes the complete discharge operation in two parts, such as the active and passive phases. The conduction current is sharply changed in the active phase due to the higher electric field as compared to the passive phase, whereas the activities of breakdown occur in the active phase along with the variation of surface charge density [84]. The discharge plasma is called as self-sustaining, when each primary electron creates a secondary electron and this process becomes continuous. A stage is reached after sometime, when the production of electrons becomes independent of the applied voltage. This condition is usually called as self-sustaining of discharge. The spatio-temporal characteristics are explored in the atmospheric pressure glow and Townsend discharges, which provide the justification about the exchange of discharge modes. The chaotic and bifurcation processes are demonstrated in pure helium gas, whereas the stationary state achievement requires for the physical understanding of the atmospheric pressure discharge and it takes normally five to six cycles.

4.3 Spatial distribution of discharge species parameters

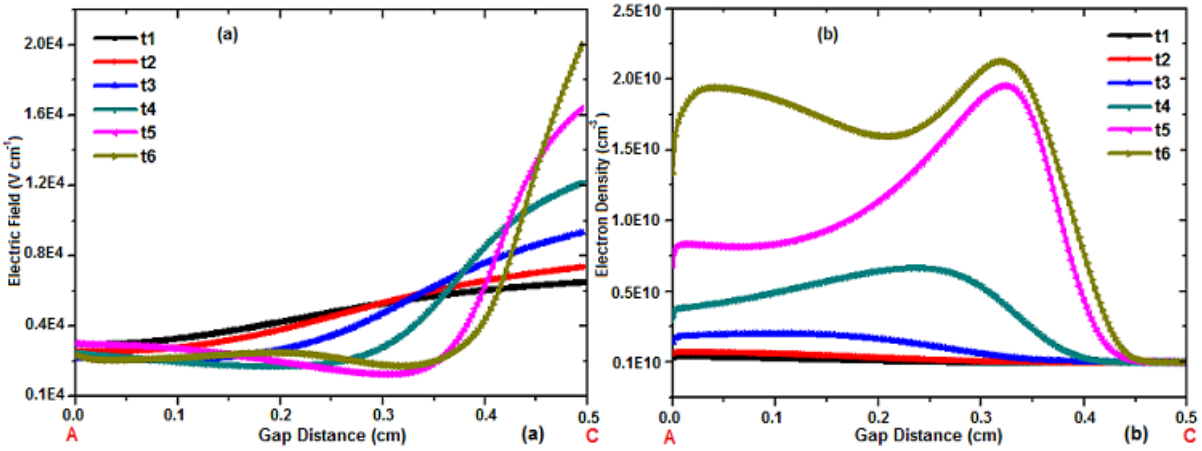

Figure 4.1. Spatial distribution of (a) electric field and (b) electron density for $f = 20$ kHz, $\varepsilon_r = 7.5$, Barrier width = 0.1 cm, $V_{appl} = 2.4$ kV in pure helium gas, t1 - t3 = 2 μs and t4 - t6 = 1 μs.

When a discharge breakdown initiates in the parallel plate reactor, a strong avalanche is formed in which the electrons, ions, metastables and excimers are produced and interacted with each other for the development of weakly ionized discharge plasma. The temporary cathode and anode barriers are represented by the symbols C and A, which change their polarities according to the external applied voltage. The space and time variations of the electric field and electron density are displayed in figure 4.1 (a, b). The time elapsed for the electric field and electron density distributions are approximately (< 3 μs) after initialization of the breakdown of gas. The interval between these time instants is not exactly same and the first three time instants (t1 - t3) take approximately 2 μs, whereas the last three events develop at very rapid rate and use less than 1 μs approximately. Initially, the profile of electric field exhibits the gradual change for the first three time events and then a sudden rise appears during the evolution of atmospheric pressure glow discharge. The strong electric field is observed near the cathode barrier (C), which falls from the higher value 2.0×10^4 V cm^{-1} to very smaller values in the reactor gap as shown in the figure 4.1 (a). The magnitude of electron density also follows the similar trend during the evolution at these time instants. The electron density increases gradually from t1 to t3 in the gap and then an abrupt change is observed in the last three steps. The electron density has a peak away from the cathode barrier and reduces to smaller values in the gap as shown in the figure 4.1 (b). The presence of electrons in the gap as well as a little away from the cathode barrier are due to the large mobility of electrons as compared to the ionic and neutral species, which confine in the narrow space near the cathode barrier. The spatial and temporal evolution of electric field and electron density manifest that their numerical magnitudes are increased during the rise of discharge current pulse from t1 to t6.

4.3.1 Effect of excimer destruction frequencies

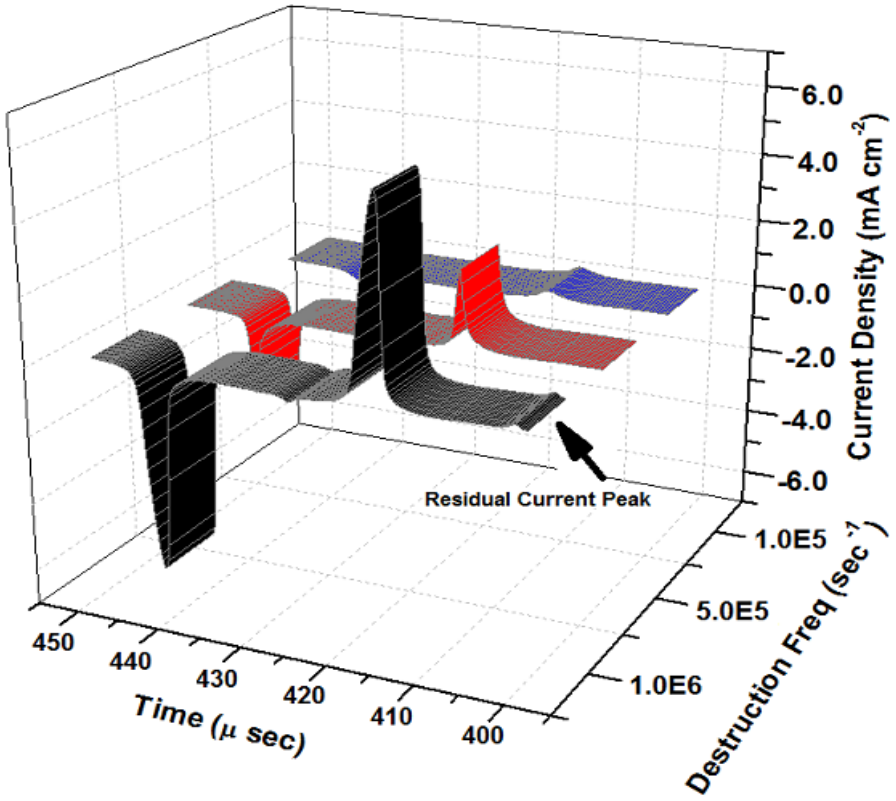

Figure 4.2. Distribution of discharge current density at variable destruction frequencies for $f = 20$ kHz, $\varepsilon_r = 7.5$, Barrier width = 0.1 cm and $V_{appl} = 2.4$ kV in pure helium gas.

As the metastables and excimers play crucial role in the atmospheric pressure discharges, the excitation rate of metastables is dominant during the whole cycle and they are destroyed through deexcitation, stepwise ionization and three-body chemical reaction processes. The major source of production of excimers is the three body chemical reaction R11 of table 2.1 and annihilates through the stepwise ionization process of metastables and excimers in pure helium gas. The figure 4.2 illustrates the temporal evolution of discharge current density at different destruction frequencies under the same conditions of input parameters. The discharge current density possesses its maximum value when the destruction frequency of excimers is 1.0×10^6 s^{-1} as shown in figure 4.2. However, the physical understanding can be explained by the help of chemical reaction analysis. When the destruction frequency of excimers increases, the production of large number of electrons and helium ions become greater and results a higher discharge current density. The residual current density is observed in the atmospheric pressure glow discharge mode, which disappears at lower destruction frequencies, such as 5.0×10^5 s^{-1} and 1.0×10^5 s^{-1} because of weak discharge plasma. The presence and absence of residual current density peak in the higher and lower destruction frequency cases exhibit that the discharge plasma is operated

in the glow and Townsend discharge modes. The profiles of breakdown voltage are formed by the effect of variable destruction frequencies, which enhance the development of Townsend discharge mode from the glow discharge mode. Correspondingly, the stationary-state results of current density is displayed in figure 4.2 for different quenching frequencies. The discharge current density at different destruction frequencies follow the similar trend as described in [82]. Now, the analysis of spatial distribution of discharge species parameters are essential to identify the uniform glow and Townsend discharge modes at variable destruction frequencies.

4.3.2 Spatial evolution of APGD[3] and APTD[4]

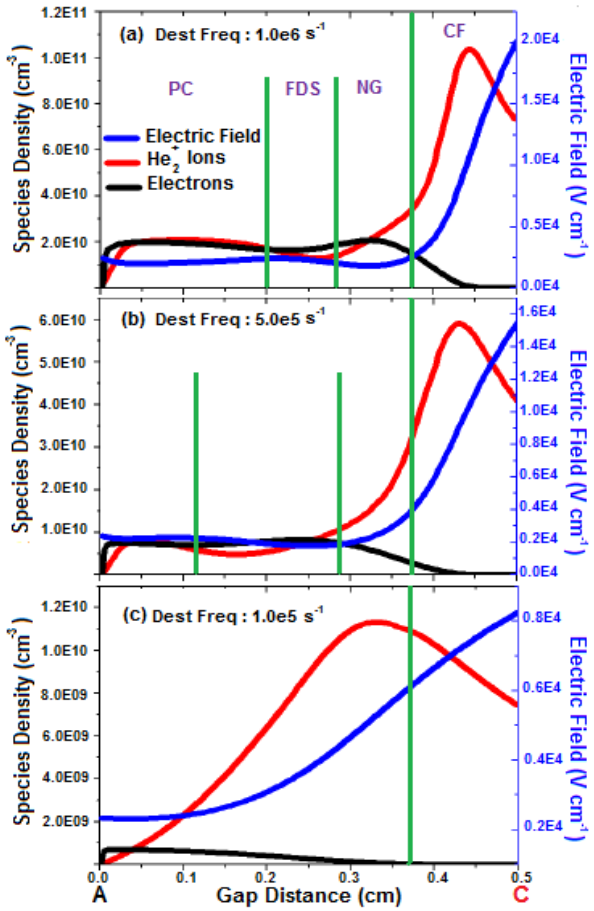

Figure 4.3. Spatial distribution of electrons, He_2^+ ions and electric field in the (a) APGD (b) Partial glow discharge and (c) APTD modes for $f = 20$ kHz, $\varepsilon_r = 7.5$, Barrier width = 0.1 cm and $V_{appl} = 2.4$ kV in pure helium gas.

[3] **APGD: Atmospheric pressure glow discharge**
[4] **APTD: Atmospheric pressure Townsend discharge**

The homogeneous uniform atmospheric pressure glow discharge is obtained when the excimers destruction frequency rises to 1.0×10^6 s^{-1}. The spatial structures of electrons, He_2^+ ions and electric field are exhibited in figure 4.3 (a, b, c) at various destruction frequencies in pure helium gas. The four distinct regions are developed in the atmospheric pressure glow discharge mode, such as cathode fall region, negative glow, Faraday's dark space and positive column at 20 kHz frequency and 2.4 kV external applied voltage. The cathode fall (CF) is defined as the region where the electric field falls from higher value $\sim 2.0 \times 10^4$ V cm^{-1} to very small value $\sim 1.0 \times 10^3$ V cm^{-1}. The negative glow (NG) region is expressed in the gap space, whereas the electron density possesses its maximum value $\sim 2.0 \times 10^{10}$ cm^{-3}. The lowest values of electrons and He_2^+ ions density are present in the Faraday's dark space (FDS) $\sim 0.8 \times 10^{10}$ cm^{-3}, whereas a quasi-neutral plasma form is developed in the fourth section of gap, called as positive column (PC). The role of positive column is very important because it traps the electrons, which use in the next breakdown pulse. The four prominent regions are remarkably observed in figure 4.3 (a), which can consider as a criteria for the homogeneous uniform atmospheric pressure glow discharge [81, 85]. It is evident from the figure 4.3 (b, c) that these regions are effected due to variation of destruction frequencies. As the destruction frequency of excimers decreases, the cathode fall region is extended but the negative glow and Faradays's dark space regions are coupled together and become indistinguishable. This represents the process of mode transformation from the glow to Townsend discharge plasma. We can say that this mixed mode behaves as a partial uniform glow discharge mode as shown in figure 4.3 (b). The complete transformation is enhanced in figure 4.3 (c), which displays the emergence of uniform Townsend mode and the discharge activity builds up near the anode as clearly illustrated in figure 4.3 (c) for 1.0×10^5 s^{-1} quenching frequency. In this case, the electron density increases towards the anode from $\sim 1.0 \times 10^8$ cm^{-3} to $\sim 1.1 \times 10^9$ cm^{-3}, whereas the cathode fall region expands in the gap, which absorbs other regions of the atmospheric pressure glow discharge especially the positive column. The uniform atmospheric pressure Townsend discharge mode corresponds to the lower ionization mode as compared to the higher ionization mode, like atmospheric pressure glow and non-uniform discharge modes. In Townsend discharge mode, the electron density is maximum near the anode barrier and the maximum density of ions exists a little away from the cathode barrier. The distortion in the electric field is reduced and varies slowly. Sometimes, the Townsend discharge is usually called as dark glow discharge at atmospheric pressure because of lower ionization rate in this mode. The secondary electrons from the cathode barrier play a substantial role for the next breakdown pulse and the secondary electron emission coefficient of numerical value, 0.01 is considered in this research work for the numerical simulations. The electrons are not trapped in the Townsend mode due to the absence of positive column. Thus the discharge is sustained by the secondary electrons emission from the dielectric barrier and effective role performed by the metastables. The above discussion indicates that the excimers are destroyed at variable

destruction frequencies in the atmospheric pressure discharges and produce different types of discharge characteristics in pure helium gas. Therefore, the reduction of destruction frequency of excimers causes the shift of APGD into APTD because of smaller ionization growth during the discharge progression.

4.3.3 Temporal profile of metastables and excimers

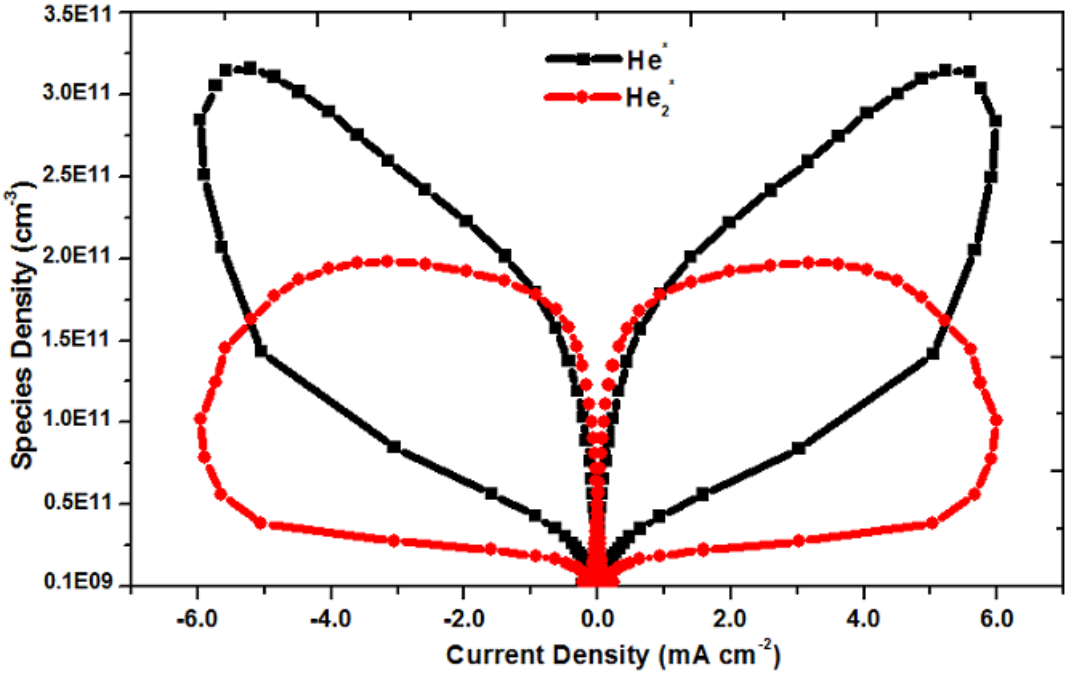

Figure 4.4. Temporal profile of metastables (He^*) and excimers (He_2^*) density for $f = 20$ kHz, $\varepsilon_r = 7.5$, Barrier width = 0.1 cm and $V_{appl} = 2.4$ kV in pure helium gas.

The temporal profile of metastables (He^*) and excimers (He_2^*) are displayed for a complete cycle as shown in figure 4.4 for quenching frequency 1.0×10^6 s^{-1}. The role of metastables and excimers is entirely different as compared to the electronic and ionic species. The metastables provide a rich source of ionization through stepwise ionization of metastables and excimers in pure helium gas. The figure 4.4 provides the average magnitude of the metastables and excimers at different times along with the discharge current density during the different phases of evolution of atmospheric pressure glow discharge. The density of metastables and excimers increases continuously after the discharge current density peak, which are shown by two different closed loops. The density of excimers is always smaller than metastables throughout the whole cycle except in the last phase of decay of half cycle. The density of metastables increases gradually during the rise of discharge current pulse, whereas the density of excimers increases slowly at first and then swiftly after breakdown during the glow discharge activity. The density of excimers is suddenly increased at higher values of discharge current density and becomes

maximum during the fall of discharge current pulse. The behavior of metastables and excimers are approximately similar at very small values of current density as shown in figure 4.4. The excimers have sharp behavior during the rise of current pulse and before the polarity reversal of electric field. The large density of metastables is converted into excimers by using three body reaction (R11 in table 2.1), which exhibits in figure 4.4. The metastables are actively interacted with other discharge species and have a higher average density in the atmospheric pressure glow discharge mode. The higher slope $\left(y = \frac{\Delta n_{He^*,He_2^*}}{\Delta j} = \frac{\text{Difference between neutral species densities}}{\text{Difference between current densities}}\right)$ of metastables also verifies this argument that they have higher densities in the growing phase of atmospheric pressure glow discharge than excimers.

4.3.4 Spatial distribution of electron mean energy and ionization rate

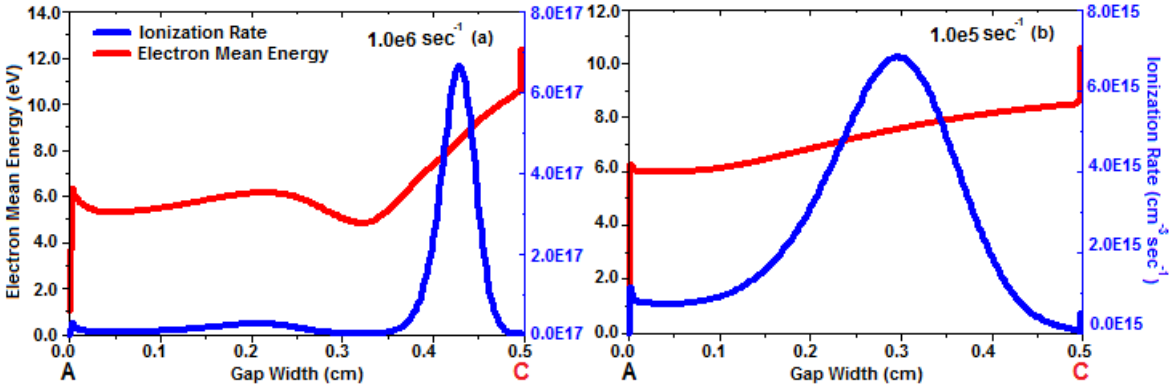

Figure 4.5. Spatial structures of electron mean energy and ionization rate in (a) APGD and (b) APTD for $f = 20$ kHz, $\varepsilon_r = 7.5$, Barrier width = 0.1 cm and $V_{appl} = 2.4$ kV in pure helium gas.

The electron energy density equation is solved with the addition of a set of particle balance equations and Poisson's equation. The structures of ionization rate and electron mean energy are illustrated in the atmospheric pressure glow and Townsend discharge modes, which correspond to the highest and lowest destruction frequencies. The electron mean energy in figure 4.5 (a) indicates the sharp falling trend in the cathode fall region and varies smoothly in the gap. The electron mean energy becomes smaller and flat when the destruction frequency is decreased to 1.0×10^5 s^{-1} as shown in figure 4.5 (b). The sharp and small change in electron mean energy are observed in the atmospheric pressure glow and Townsend discharge modes as shown in figure 4.5 (a, b). The electron mean energy varies from 12.0 to 5.0 eV near the cathode barrier and $\sim$ 6.0 eV in the remaining part of gap at 1.0×10^6 s^{-1}. The ionization rate provides the production of electrons and ions from the helium gas atoms, which develops the discharge plasma in the glow and Townsend discharge modes due to different destruction frequencies. The ionization rate is maximum near the cathode barrier and possesses very small values in the gap. On the contrary, the ionization rate is extended in the remaining part of gap and reduces from

$\sim 7.0\times10^{17}$ cm^{-3}s^{-1} to 7.0×10^{15} cm^{-3}s^{-1}, when the excimers quenching frequency decreases from 1.0×10^{6} to 1.0×10^{5} s^{-1}. The distribution of ionization rate and electron mean energy accentuate the electron related activities near the cathode barrier, which further enhance the perception of atmospheric pressure glow and Townsend discharge modes under different quenching frequencies. The above discussion shows that the activities of electrons near the cathode barrier play an extensive role in the glow discharge mode as compared to the Townsend discharge mode at atmospheric pressure.

4.3.5 Electrical characteristics of atmospheric pressure glow discharge

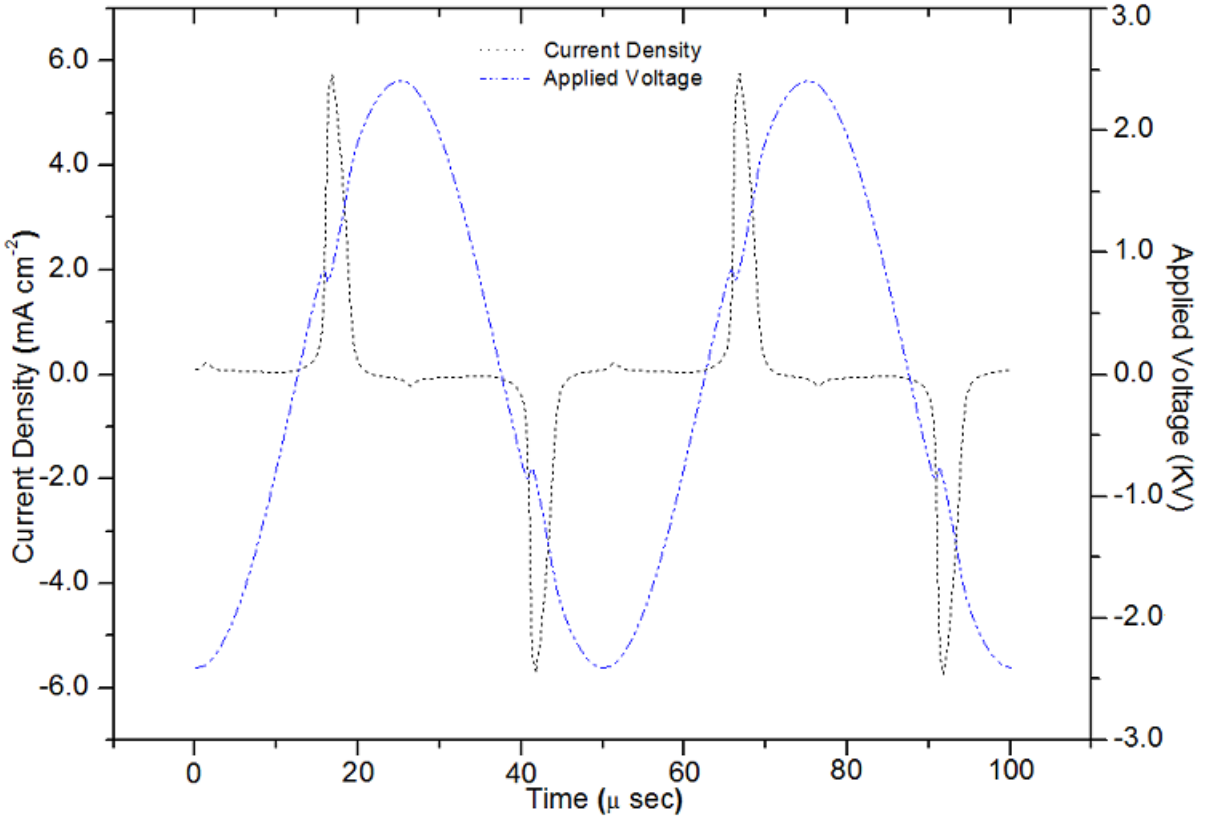

Figure 4.6. Current voltage characteristics for $f = 20$ kHz, $\varepsilon_r = 7.5$, Barrier width = 0.1 cm and $V_{appl} = 2.4$ kV in pure helium gas.

The temporal evolution of discharge current density and applied voltage are described which illustrate the steady-state situation of atmospheric pressure glow discharge as shown in figure 4.6. The amplitude of applied sinusoidal voltage to the parallel plate driven electrode is 2.4 kV and the driving frequency is 20 kHz. The profile of applied voltage is evaluated by using the relation, which described in section 4.2. The discharge current density is calculated from the equation (2.36) that forms with the combination of conduction and displacement currents. The rising time of discharge current density is very small as

compared to the fall time, which corresponds to the similarity of atmospheric pressure glow discharge and follows the similar trend of current-voltage characteristics [15]. The sharp and large current density peak represents the glow discharge mode and the further details of the temporal profile are explored by analyzing the spatial distribution of discharge species parameters, such as electric field, species density, ionization rate and electron mean energy. A small current density peak is also observed in figure 4.6, which represents the residual current peak. The residual current is produced when the trapped electrons in the positive column begin to move quickly during the polarity reversal of electric field.

4.4 Influence of nitrogen impurities

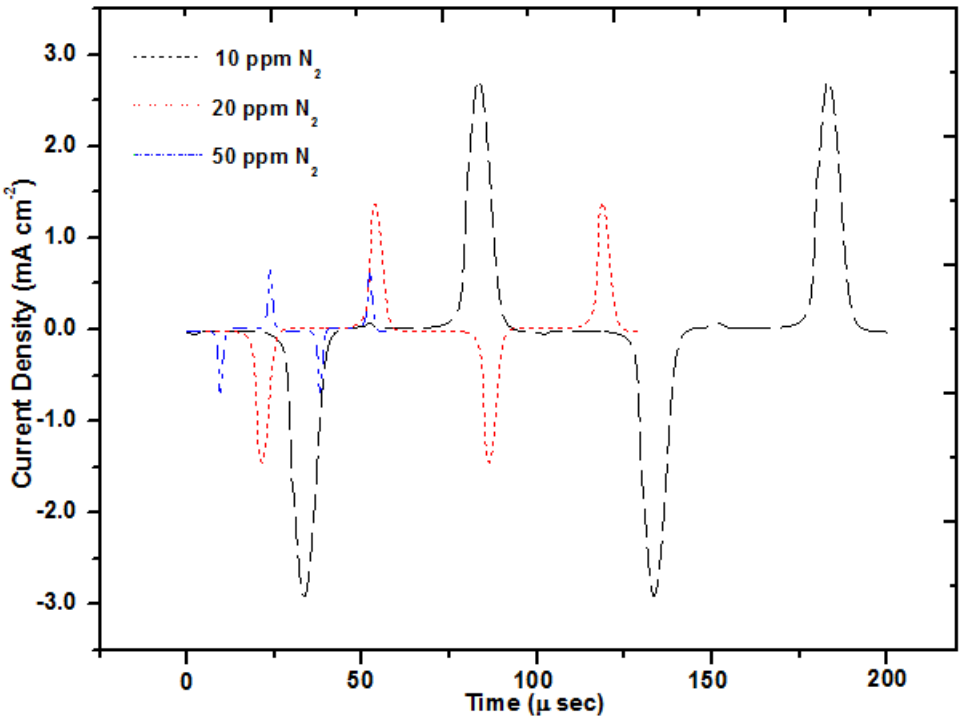

Figure 4.7. Temporal profile of discharge current density for $f = 10$ kHz, $\varepsilon_r = 7.5$, Barrier width = 0.1 cm and $V_{appl} = 1.7$ kV in the presence of 10, 20 and 50 ppm N_2.

To understand the influence of nitrogen impurities, a temporal profile of discharge current density is considered at 10 kHz with 10, 20 and 50 ppm nitrogen impurities. The remarkable influence of nitrogen impurities provides the strong ionization due to small ionization potential of nitrogen in He-N_2 gas and the Penning ionization of metastables (He^*) and excimers (He_2^*) play a dramatic role to change the characteristics of atmospheric pressure discharge. It has been observed that the breakdown voltage of helium gas is decreased with small amount of nitrogen impurities [86] and the Penning ionization process becomes dominant, which destroys the metastables through this process. As the breakdown

voltage falls in the presence of nitrogen impurities, the amplitude of applied sinusoidal voltage in this case is used as 1.7 kV for the numerical investigations. The ionization process becomes faster in the presence of nitrogen impurities, such as 10, 20 and 50 ppm in pure helium gas. The large amount of nitrogen impurities transforms the atmospheric pressure glow discharge into filamentary discharge because the metastables are annihilated through Penning ionization process. The smaller amount of nitrogen impurities is acceptable in certain situations, when the overvoltage possesses a smaller difference between the applied and breakdown voltage. Therefore, the discharge current density is reduced from $\sim$ 4.0 to 0.6 mA cm^{-2}, when the nitrogen impurities vary from 10 to 50 ppm in He-N_2 gas as shown in figure 4.7. This evidence explores the effect of nitrogen impurities in different quantities, which convert the atmospheric pressure glow discharge mode into Townsend mode. The higher amount of nitrogen impurities ($\gtrsim$ 500 ppm) changes the internal structure of atmospheric pressure discharge and the discharge is operated in the filamentary discharge mode. The present research thesis deals with the variable amount of nitrogen impurities especially from 10 to 100 ppm. The discharge is in homogeneous uniform Townsend mode, although the metastables and excimers destroy through Penning ionization process. The Penning ionization process works fastly as compared to the stepwise ionization process in pure helium gas and the destruction of metastables and excimers due to stepwise ionization are not effected strongly in He-N_2 than pure helium gas.

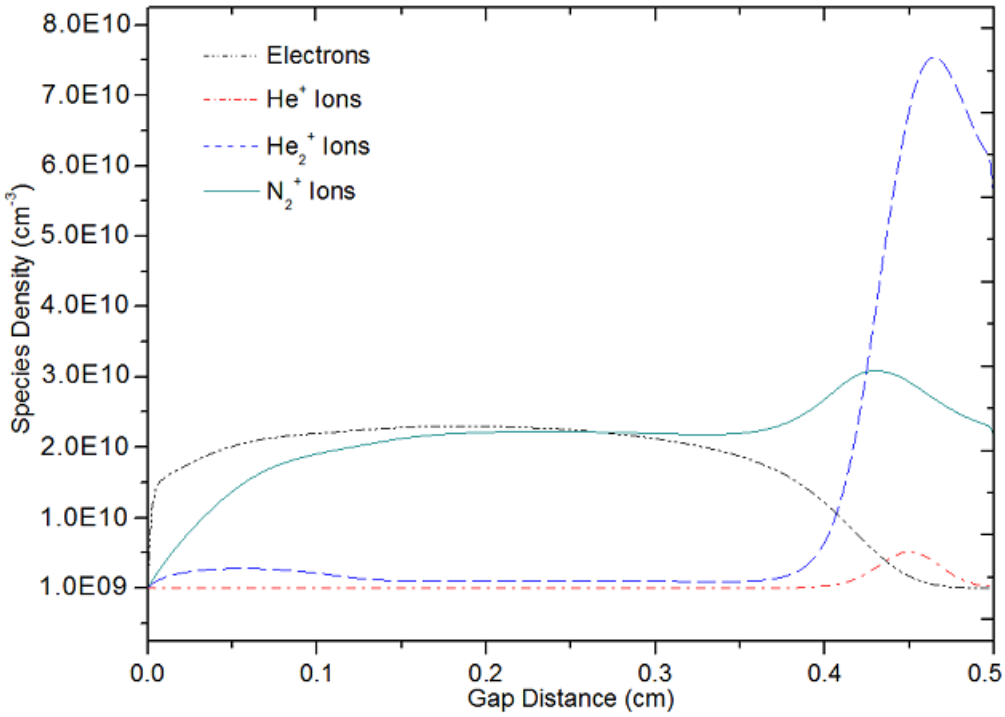

Figure. 4.8. Spatial evolution of species density for $f = 10$ kHz, $\varepsilon_r = 7.5$, Barrier width = 0.1 cm and $V_{appl} = 1.7$ kV in the presence of 10 ppm N_2.

To perceive the internal spatial distribution of electrons and ionic species (He^+, He_2^+ and N_2^+) in the He-N_2 discharge plasma, the spatial distributions of electrons and ionic species are analyzed in He-N_2 gas with 10 ppm nitrogen impurities. The homogeneous uniform structure of discharge species shows that the molecular helium ions are dominated near the cathode barrier (C) and has a higher numerical value of $\sim 8.0 \times 10^{10}$ cm^{-3} as compared to other ionic species. The density of molecular nitrogen ions are higher throughout the gap as compared to the He^+ and He_2^+ ions density. The He^+ ions density is smaller than other ionic species because the three-body chemical reaction (R3 in table 2.1) converts a major portion of He^+ into He_2^+ ions density during the discharge progression. The electronic and ionic structures of discharge species are extracted at the maximum discharge current density during the half cycle as shown in figure 4.8. The positive column exhibits that a quasi-neutral region is developed in the larger portion of the gap due to the electrons and N_2^+ ions. The overall species structure verifies that the discharge plasma is carried out in the homogeneous uniform glow discharge mode. It is evident that the nitrogen impurities actively perform a significant role in He-N_2 discharge plasma in the presence of even 10 ppm nitrogen impurities.

4.4.1 Effect of secondary electron emission coefficient

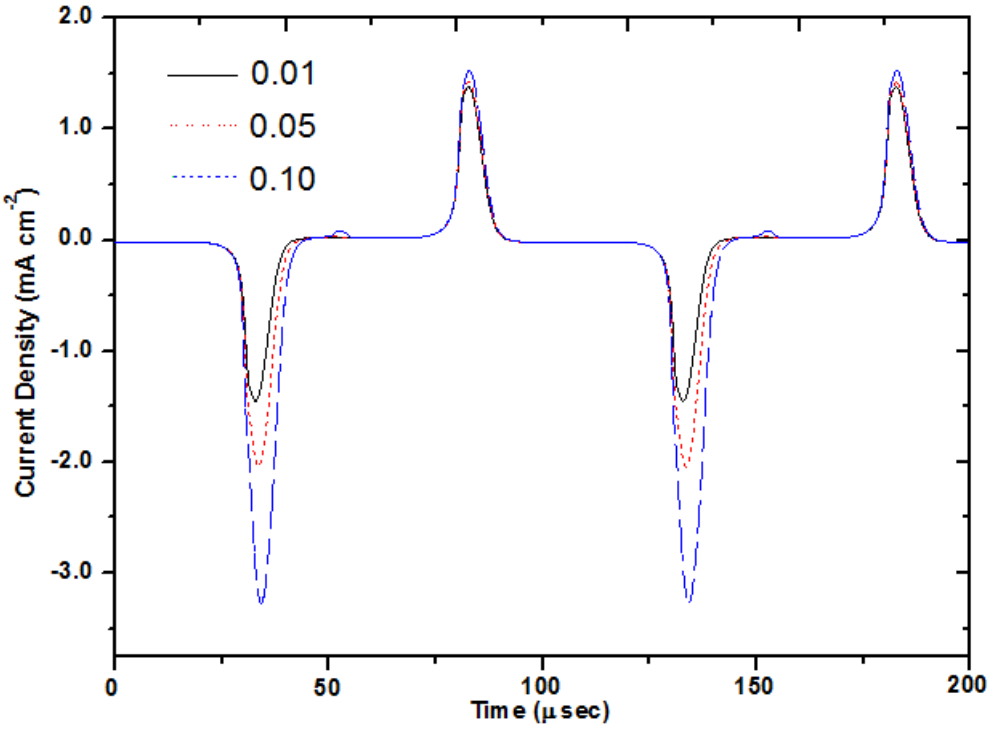

Figure 4.9. Temporal evolution of discharge current density with variable SEEC for $f = 10$ kHz, $\varepsilon_r = 7.5$, Barrier width = 0.1 cm and $V_{appl} = 1.7$ kV in the presence of 10 ppm N_2.

The surface characteristics of dielectric barriers are implied by considering the effect of SEEC[5] due to ionic species bombardment in the atmospheric pressure discharge. When the gas breakdown occurs, the electrons and ions are rapidly moved towards the anode and cathode dielectric barriers by the influence of strong electric field. The heavier ionic species strike the cathode barrier energetically and knock out the secondary electrons from the dielectric barrier surface. The emission of secondary electrons from the dielectric barrier surface due to the metastables and excimers are negligibly small and can be neglected in high pressure discharges [87]. To understand the discharge characteristics due to the effect of SEEC, the temporal progression of discharge current density is elaborated at different values of SEEC under similar input conditions during the complete cycle. The figure 4.9 exhibits that the discharge current density is increased by the increment of SEEC. As the value of SEEC varies from 0.01 to 0.1, the symmetric current density structure is modified into asymmetric form due to the strong secondary electrons emission from the cathode barrier. The asymmetric atmospheric pressure discharge is remarkable in case of 0.1 SEEC. This shows that the strong breakdown is occurred with higher SEEC and the discharge plasma cannot decay during the remaining part of half cycle. Therefore, the weaker breakdown is the most probable in the next half cycle. The fundamental understanding of SEEC is developed for the dielectric barrier surface when the atmospheric pressure glow and Townsend discharge modes are formulated in weakly ionized He-N_2 gas.

4.5 Emergence of chaotic behavior

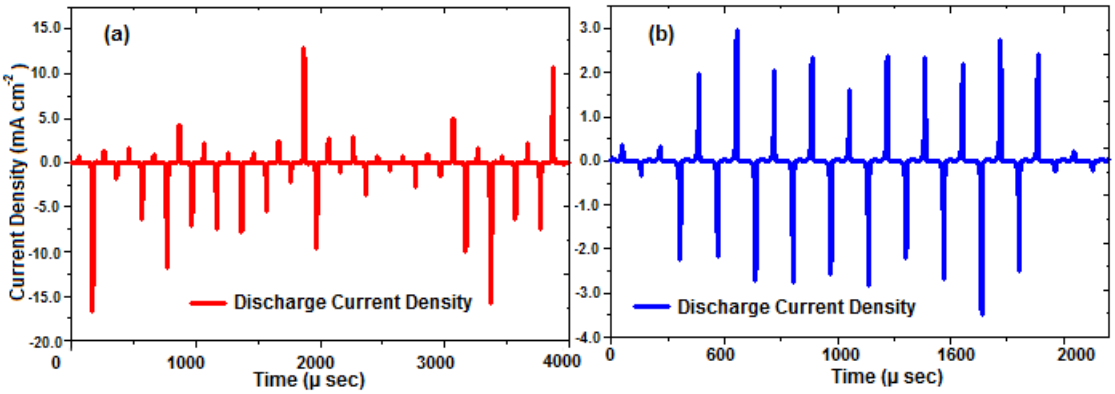

Figure 4.10. Chaotic behavior of discharge current density for (a) 5 kHz and (b) 6 kHz, $\varepsilon_r = 7.5$, GW=0.5 cm and $V_{appl} = 2.4$ kV in pure helium gas.

In order to understand the chaotic behavior of atmospheric pressure discharge, the temporal evolution of discharge current density is examined at the driving frequencies of $f = 5.0$ and 6.0 kHz as shown in figure

[5]SEEC: Secondary electron emission coefficient

4.10 (a, b). The strong instabilities are prominently present in the lower frequency regime ($1.0 \lesssim f \lesssim 7.0$ kHz) as compared to higher frequencies, which has been discussed in [4, 15, 88]. These instabilities appear in the mentioned frequency range and then they are suppressed under different operating circumstances. We discuss the chaotic behavior of the atmospheric pressure discharges in this section and the procedures are explored for the removal of instabilities in the non-uniform discharges. The discharge is randomly operated in the higher and lower ionization modes for the positive and negative half cycles, which exhibits the chaotic behavior of atmospheric pressure discharge at 5.0 and 6.0 kHz in pure helium gas. The figure 4.10 shows the chaotic behavior of discharge current density for the number of consecutive cycles. The physical understanding of strongly asymmetric discharge current pulses can be explained by providing the details of discharge breakdown mechanism. When a strong gas breakdown is occurring during the half cycle, the discharge operates in the uniform homogeneous glow mode. Consequently, the discharge cannot decay completely and the weaker breakdown is formed for the next discharge. The atypical breakdown process is observed frequently at lower frequencies in this range and this argument is supported with the temporal profile of atmospheric pressure discharge current density. This means that the development due to the chemical processes are carried on strongly in a random fashion, which enhances the chaotic behavior of discharge current density as shown in figure 4.10 (a, b). The development of inhomogeneous modes at lower frequencies are the major cause of instabilities in the atmospheric pressure discharges. These instabilities illustrate the ionization oscillations, which are occurred due to the various reasons. As the metastables have higher density as compared to the other species in the atmospheric pressure discharges, so they prominently influence the discharge characteristics in the lower frequency regime. The major and important target is to identify the source of instabilities with the numerical modelling and produces the recipes for the removal of instabilities.

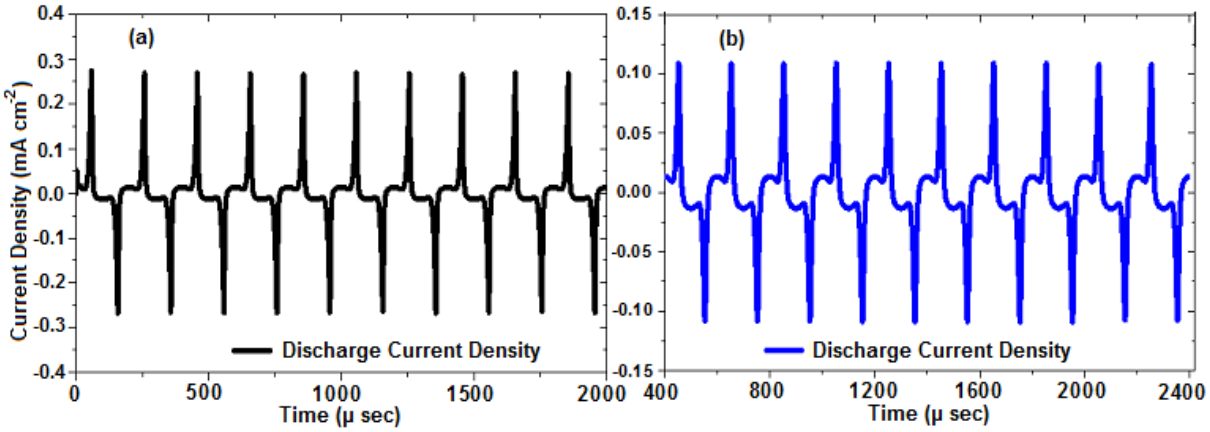

Figure 4.11. Temporal profiles of current density for $f = 5.0$ kHz, $\varepsilon_r = 7.5$, GW=0.5 cm and $V_{appl} = 2.4$ kV due to (a) absence of stepwise ionization (b) presence of impurities in pure helium gas.

The logical understanding of instabilities can be explained by the effect of different chemical reactions, such as the stepwise ionization of metastables and excimers in pure helium gas. When the stepwise ionization processes of metastables and excimers are switched off in the fluid modelling exercise under similar input conditions at 5 kHz, the source of ionization stops due to the metastables and excimers stepwise ionization. The chaotic behavior of discharge is abolished and emerges in the atmospheric pressure Townsend discharge mode as shown in figure 4.11 (a). This establishes a valid argument that the metastables are very important in the atmospheric pressure discharges and effect the discharge characteristics resolutely. The instabilities are normally appeared in the lower frequency regime because the discharge species interactions have more time to interact and produce the resultant in the form of strong and weak discharge breakdown during the half cycle. However, the instabilities are suppressed in the higher frequency regime ($\gtrsim$ 7.0 kHz) because the discharge species interacts optimally during the small time period and generates discharge plasma quickly in both positive and negative half cycles. The authors [15, 89] discussed the possibility of non-uniform discharge in different frequency regimes and especially in the lower frequency range ($<$ 10 kHz) and the uniform discharge structure is prominently observed at higher frequencies. The nitrogen impurity is also used as an efficient quencher for the metastables and excimers. Therefore, the Penning ionization process destroys the metastables as well as excimers and the discharge plasma is enhanced in the homogeneous uniform glow and Townsend discharge modes based on the amount of nitrogen impurities as shown in figure 4.11 (b). The figure 4.11 (a, b) provides the uniform structures of the atmospheric pressure discharges under the above mentioned imposed conditions.

4.6 Chaotic and bifurcation behavior at lower frequencies

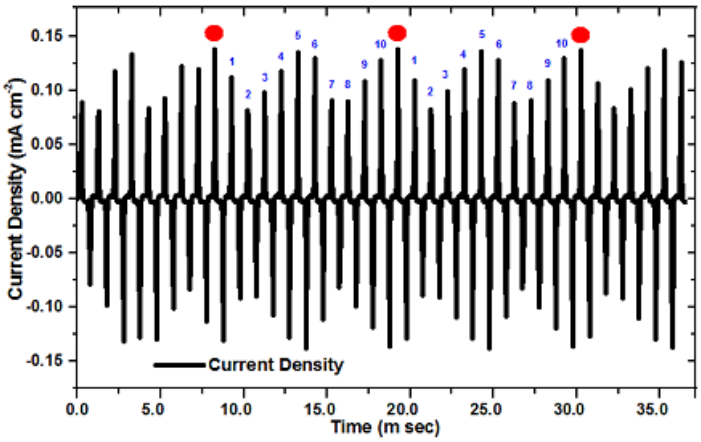

Figure 4.12. Chaotic and bifurcation behavior of current density for $f = 1$ kHz, $\varepsilon_r = 7.5$, GW=0.5 cm and $V_{appl} = 2.4$ kV in pure helium gas.

The different types of chemical processes are involved for the production of atmospheric pressure glow and Townsend discharges. The excitation and ionization processes perform a governing role as compared to the other chemical processes because they have large production rates than others. We provide the discharge current density structure at 1 kHz in pure helium and the magnitude of current density falls in the Townsend regime. The chaotic and bifurcation processes are clearly observed as shown in figure 4.12, which verify the experimental predictions in the lower driving frequency regime [15]. The bifurcation process means the repetition of event after a certain time interval and the pattern of current pulses follows a similar trend at 1 kHz. It is observed from the figure 4.12 that the pattern from 1 to 10 between small solid balls is repeated, whereas the magnitude of current pulses in the pattern are not exactly similar. Thus, the chaotic behavior is identified in this pattern because the magnitude of current pulses in the consecutive patterns are not matched perfectly. The combination of both behaviors provide the filamentary discharge at 1 kHz. This simulation result strongly supports the experimental observations in the lower frequency regime. The above distribution in figure 4.12 exhibits that the chaotic behavior is dominant at lower frequencies, while the discharge plasma operates in the lower ionization mode, usually called as Townsend discharge mode.

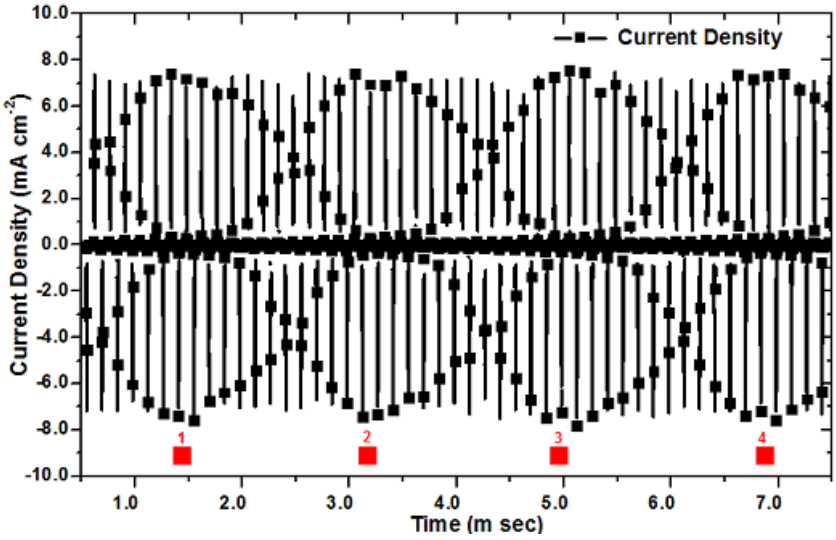

Figure 4.13. Chaotic and bifurcation behavior of current density for $f = 7.0$ kHz, $\varepsilon_r = 7.5$, GW=0.5 cm, $V_{appl} = 2.4$ kV in pure helium gas.

It is believed that the chaotic and bifurcation processes are dominant in the lower frequency regime especially from 1 to 7 kHz approximately. The mixed type of pattern are exhibited in the figures 4.12 and 4.13 at 1 and 7 kHz to explore these phenomena in the atmospheric pressure discharges. The pattern of discharge current density shows that the discharge plasma is operated in the glow mode with higher magnitudes of current density. Therefore, it is evident from the figures 4.12 and 4.13 that the chaotic and

bifurcation processes are prominently existed in the lower frequency regime, which has no association with the mode of discharge plasma at atmospheric pressure. The filamentary discharge is also observed at 7 kHz driving frequency and the magnitude of current density falls in the atmospheric pressure glow discharge mode, whereas it appears in the Townsend discharge mode at 1 kHz. The third and fourth pattern in figure 4.13 shows that the number of rising pulses are same and repeated but their magnitudes are not exactly similar. The above structures exhibit that the chaotic behavior and bifurcation processes are central in the lower frequency regime. From the above analysis in the lower frequency regime, it is clear that the filamentary behavior is dominant in pure helium gas, which can be suppressed with the described mechanisms in section 4.5. The range of different operating conditions are considered to explore the characteristics of atmospheric pressure discharge.

4.7 Comparison of one-dimensional fluid model and experimental results

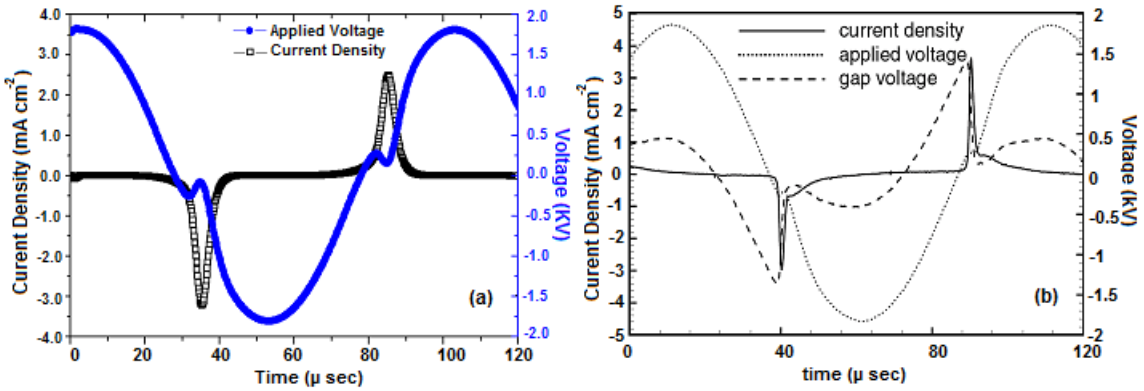

Figure 4.14. Distribution of current-voltage characteristics for $f = 10$ kHz, $\varepsilon_r = 9.0$, BL=0.1 cm, GW=0.5 cm and $V_{appl} = 1.85$ kV in 100 ppm N_2 impurities.

The reliability of fluid model results can be provided with number of methods, such as comparison with experimental work, analysis of physical phenomenon under different conditions and spatio-temporal profiles. Here, the temporal evolution of applied voltage and discharge current density are explored in the presence of 100 ppm nitrogen impurities and compared with the experimental work published in [81]. The similar amplitude of applied voltage 1.85 kV, driving frequency 10 kHz, gap width 0.5 cm, barrier width 0.1 cm and dielectric barrier permittivity as 9.0 are considered in one-dimensional fluid model to evaluate the current-voltage characteristics. The fluid model simulation results are compared with the experimental work as shown in figure 4.14 (a, b). The figure 4.14 (a, b) exhibits that the fluid model results are approximately matched with the experimental results.

4.8 Conclusions and summary

In this chapter, a one-dimensional fluid model is developed to understand the basic physical insight of atmospheric pressure discharge. The simulation results are obtained by the variation of external input discharge parameters, such as applied voltage, driving frequency, SEEC and trace amount of nitrogen impurities. We explore the role of important metastables in the atmospheric pressure glow and Townsend discharge modes, which enhance their behavior in the growth and decay phases. The influence of destruction frequencies is analyzed in the glow and Townsend discharge modes, which provides the importance of excimers in the atmospheric pressure discharges. The four distinct regions, such as cathode fall, negative glow, Faraday's dark space and positive column are discussed in the homogeneous uniform atmospheric pressure glow discharges, which can be used and considered as a criterion for the uniform atmospheric pressure glow discharges. These prominent regions are disappeared at lower destruction frequency of excimers and in the presence of excess amount of nitrogen impurities because the atmospheric pressure discharge operates and persists in the Townsend discharge mode. The influence of nitrogen impurities exhibit that they play an important and glaring role in He-N_2 discharge plasma. The spatial profile of ionization rate and electron mean energy are displayed, which provide the evolvement of electrons near the cathode barrier in the atmospheric pressure glow and Townsend discharges. The chaotic behavior is discerned in the lower frequency regime usually ($1.0 \lesssim f \lesssim 7.0$ kHz), which shows the particular details at 5.0 and 6.0 kHz for the number of cycles. The chaotic behavior is suppressed in the absence of stepwise ionization and the presence of nitrogen impurities in pure helium gas. Finally, the one-dimensional fluid model simulations and experimental results are compared with a specific set of parameters, which display the authenticity and reliability of fluid model results.

Chapter 5

Evolution of two-dimensional uniform and filamentary APD[1]

5.1 Introduction

In this chapter, we apply a two-dimensional fluid model to explore the behavior of atmospheric pressure discharge in the parallel plate reactor geometry. In industry, it has been demonstrated that the discharge plasma can be successfully used as an excellent tool for different industrial applications [90, 91, 92]. However, the mechanisms and conditions for the evolution of different phases of the atmospheric pressure discharge demand a more comprehensive knowledge. The evolution of non-uniformities entails a special attention during the transition of different discharge modes. In this specific area, the significant development has been performed in the technology modelling, simulation modelling of the atmospheric pressure discharges and the immense recent progress of different applications during the last decade [4, 12, 93, 94]. The ultimate solution is the bridge between the experiment and numerical simulations to understand and describe the transverse characteristics of the uniform and non-uniform discharges at atmospheric pressure. Initially, the two-dimensional fluid modelling of the dielectric barrier discharge in air and nitrogen has been investigated the four marked phases, a Townsend phase, an ionization wave, a cathode layer formation, and a decay phase. The streamer dynamics of the space-charge dominated plasma simulations are considered in the nitrogen plasma and the ionization growth exhibits itself constriction of the discharge [95, 96, 97]. So, the complete description of discharge plasma can be provided in detail by the help of two-dimensional modelling in different gas mixtures under different conditions.

[1] **APD: Atmospheric pressure discharge**

In order to enhance our intuition for the numerical simulations of the atmospheric pressure discharges, it becomes necessary to model the spatio-temporal evolution of the external discharge parameters under variable conditions. We have developed a two-dimensional self-consistent homogeneous fluid model to describe the spatio-temporal characteristics of the atmospheric pressure discharge in pure helium and He-N_2 gases. This chapter provides the basic concepts of dielectric barrier discharge in three different phases. The different phases are elaborated to provide the brief insight of atmospheric pressure discharge.

In the first phase, the uniform glow discharge structure is discussed in pure helium gas, which illustrates the four distinct regimes of atmospheric pressure discharge and describes the effective role of chemical processes. In the second phase, the profile of constricted filamentary glow discharge is explored by the help of streamer breakdown mechanism and the decay phase demonstrates the evolution of filamentary discharge clearly. The transition between the uniform and non-uniform discharge modes are investigated with and without combined imposed conditions in the dielectric barrier discharges. In the third phase, the electrical characterization and spatial distribution of uniform atmospheric pressure discharges are elaborated. The uniform discharge modes can be expressed by an adjustment of barrier thickness, which develops the atmospheric pressure glow and Townsend discharge modes. The temporal evolution of the discharge species density exhibits that the metastables and excimers are actively interacted with other discharge species because they have a dominant concentration during the complete cycle. The influence of nitrogen impurities, Penning ionization of metastables, relative permittivity of the dielectric barriers and variable frequencies are analyzed with the spatio-temporal distribution of the atmospheric pressure discharges. It is noted that the major difference between the electrons and He_2^+ ions density is greater in pure helium as compared to the He-N_2 discharge because of the absence of Penning ionization of nitrogen impurities. This confirms that the nitrogen impurities have a large influence and decrease the difference between the electrons and He_2^+ ions density with the help of Penning ionization process. Overall, this chapter is useful to deliver satisfactory information for the uniform and non-uniform atmospheric pressure discharges, and describes the origin of non-uniformities.

In this chapter, Section 5.2 describes the distribution of discharge species and chemical reaction analysis in pure helium gas. Section 5.3 explores the filamentary discharge behavior in He-N_2 discharge plasma. Section 5.4 analyzes the electrical and spatial properties of uniform atmospheric pressure discharge modes. Section 5.5 investigates the space and time variations of electron density and surface charge density in the uniform atmospheric pressure discharge. Section 5.6 describes the temporal variations of discharge parameters. Sections 5.7 and 5.8 inquire about the relative permittivity of dielectric barrier and variable driving frequencies of atmospheric pressure discharge. Section 5.9 examines the summary and conclusions of two-dimensional fluid model in stagnant bulk gas.

Let us consider a sinusoidal AC voltage for the parallel plate dielectric barrier discharge geometry at

constant pressure 760 torr. The numerical simulations are discussed in pure helium and He-N_2 gases, whereas the nitrogen impurities are changed from 20 to 100 ppm. Initially, a quasi-neutral plasma is assumed in the gap with equal electrons and ions density of $\sim 10^8$ cm^{-3}. We discuss the spatial and temporal evolution of the atmospheric pressure discharge in the lower frequency range from 20 to 50 kHz and the variable amplitude of the applied voltages are considered to understand the influence of external discharge parameters. The special features and aspects are examined for the atmospheric pressure glow discharge with fixed gap width and barrier length, and the stationary state achievement requires few number of cycles after the first breakdown.

5.2 Spatial distribution of discharge species and electric field

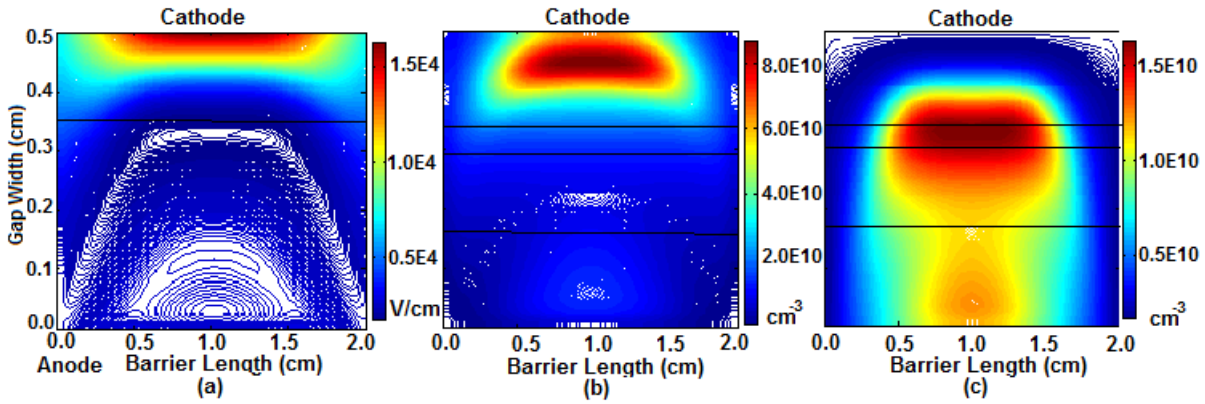

Figure 5.1. (a) Electric field E_y in axial direction, (b) He_2^+ ions and (c) electrons density distribution for f = 20 kHz, $\varepsilon_r = 7.5$, $\gamma_p = 0.1$ and $V_{appl} = 2.1$ kV in pure helium gas.

We consider the periodic stationary-state of atmospheric pressure discharge with 20 kHz driving frequency and 2.1 kV amplitude of applied voltage in pure helium gas. As the sinusoidal voltage increases gradually, the electrons acquire enough energy to excite and ionize the helium gas atoms and molecules, i.e., He^*, He^+ and He_2^+. The next stage is the breakdown of gas, which occurs only when the applied voltage V_{appl} is greater than the breakdown voltage V_b. The breakdown voltage depends on the following factors, such as gap distance between the barriers, operating gas and pressure of a reactor and varies for gas mixtures. When the breakdown electric field strength is occurred in the reactor, the dielectric barriers behave like conducting materials and offer a very small resistance. The ionization rate is enhanced to higher values and a discharge is established in the gap. The dielectrics accumulate the charges on their surfaces and the charge accumulation depends on the voltage drop across the dielectric barriers. Correspondingly, the spatial structure of electrons, He_2^+ ions and electric field explicate the four distinct regions of atmospheric pressure glow discharge as mentioned in chapter 4. In the cathode fall

region, the electric field distribution shows the drastic fall from 1.0×10^4 V cm^{-1} to nearly zero because a large positive space charge layer is formed due to He^+ and He_2^+ ions as shown in figure 5.1 (a). The He_2^+ ions have a maximum density of $\sim 8.0 \times 10^{10}$ cm^{-3} near the cathode barrier surface and becomes small on the cathode peripheral edges as shown in figure 5.1 (b). The electrons are accelerated to high energies in this region and develop a strong ionization and avalanche in the negative glow region. The maximum electrons density is of $\sim 1.5 \times 10^{10}$ cm^{-3} and satisfies the criteria for the quasineutrality. The evolution of Faraday's dark space exhibits that the density of He_2^+ ions is greater than electrons and the smallest values are obtained in this particular discharge region. Lastly, the electrons are trapped in the positive column due to the interaction with the He_2^+ ions and exist approximately in equal density values in the positive column. The preionization level of electrons is achieved by the presence of electrons in the positive column before the next breakdown pulse. The electrons response in the positive column is not very sharp during the sudden rise of electric field and ionic species density during the glow discharge evolution. However, the discharge properties in this section are explored in pure helium gas without excimer species. The above contour structures in figure 5.1 provide a concise picture of the uniform atmospheric pressure glow discharge at the peak of maximum discharge current density, which are similar to the traditional DC glow discharge at low pressure [4].

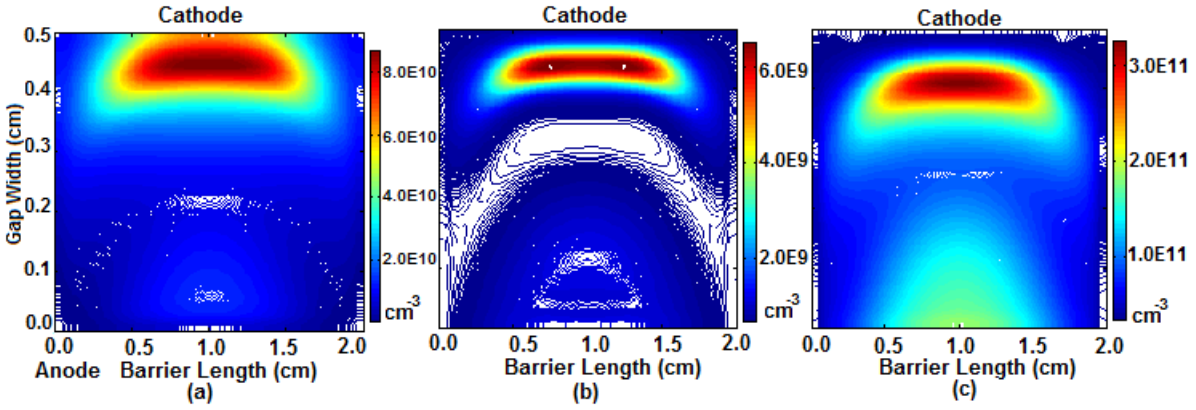

Figure 5.2. (a) He_2^+, (b) He^+ and (c) He^* species density for $f = 20$ kHz, $\varepsilon_r = 7.5$, $\gamma_p = 0.1$ and $V_{appl} = 2.1$ kV in pure helium gas.

In the atmospheric pressure glow discharges, the metastables are created by the excitation of helium atoms from the ground state due to the less ionization potential (He (^{1}S) and He (^{3}S) for 19.8 and 20.6 eV) respectively and perform an important role for the production of ions (R2, R4 and R5 in table 2.1). The three-step conversion process explores the formation of He_2^+ ions from the metastables (He^*) by considering the related chemical reactions. The spatial profile of metastables and helium ions (He^+ and He_2^+) show that the maximum values of density are present near the cathode barrier as shown in figure 5.2 (a, b, c). The metastable species form a remarkable twin peak distribution as compared to the other

discharge species as exhibited in figure 5.2 (c). The large and small peaks are created simultaneously and their density magnitudes vary from the higher 3.0×10^{11} cm^{-3} to lower values 1.5×10^{11} cm^{-3}. The lower density peak of metastables near the anode barrier provides the seed electrons for next discharge pulse, whereas the higher density peak near the cathode barrier supplies the He^+ ions for the maintenance of the atmospheric pressure glow discharge consecutively. The small peak exhibits that the metastables are not vanished completely in the previous discharge pulse due to their long life time and the low loss rate. They also supply electrons in the positive column when the electric field has the lowest values during the discharge progress. The above discussion indicates the distinct behavior of metastables as compared to other discharge species in the glow discharge formation. The twin peak structure of metastables is similar to the previous one-dimensional fluid modelling results as discussed in [99]. The He^+ ions are created by the chemical reactions, such as the direct ionization of helium gas atoms and stepwise ionization of metastables, and fastly transformed into He_2^+ ions using the main channel of three body reaction (R3 of table 2.1). Therefore, the density of He^+ ions is very small as compared to He_2^+ ions as displayed in figure 5.2 (b). The density of He_2^+ ions distribution show that they are spread and strongly attached with the surface of cathode barrier than He^+ ions and metastables (He^*) respectively as shown in figure 5.2 (a). The distance between the peak of maximum species density and cathode surface increases from He_2^+ ions to He^* (left to right) in figure 5.2 (a, b, c), which provides their peak spatial occurrence in the atmospheric pressure glow discharge. The distribution of metastables (He^*) in figure 5.2 (c) illustrates that the secondary electron emission coefficient is not very effective because they have maximum spatial density a little away from the cathode barrier. The above discussion in pure helium gas provides an insight for the uniform atmospheric pressure glow discharge and the effect of major chemical processes for the production of active discharge species in pure helium gas.

5.3 Filamentary structure of an APD

The filamentary discharge is defined as an aggregate of thin conducting plasma channels developing chaotically between the dielectric barriers. The real atmospheric pressure discharge always possesses small amounts of different gas impurities and they have a substantial impact in pure helium gas. The nitrogen impurities are considered in the present modelling study and the gas breakdown voltage is decreased due to the effect of nitrogen impurity. The nitrogen is recognized as a very effective quencher for the helium metastables and excimers because the ionization potential of nitrogen is smaller than the metastables and this helps in Penning ionization process for the production of the electrons. It is supposed that the nitrogen impurities are very small and the electron distribution function is not influenced with the trace amount of nitrogen impurities in He-N_2 gas. We now analyze the spatio-

temporal profiles and current-voltage characteristics of the filamentary and uniform atmospheric pressure discharges under different conditions. The filamentary discharge is achieved by the help of imposed conditions, such as overvoltage effect and increased recombination of molecular nitrogen ions and the mechanism of discharge creation is explained in this section.

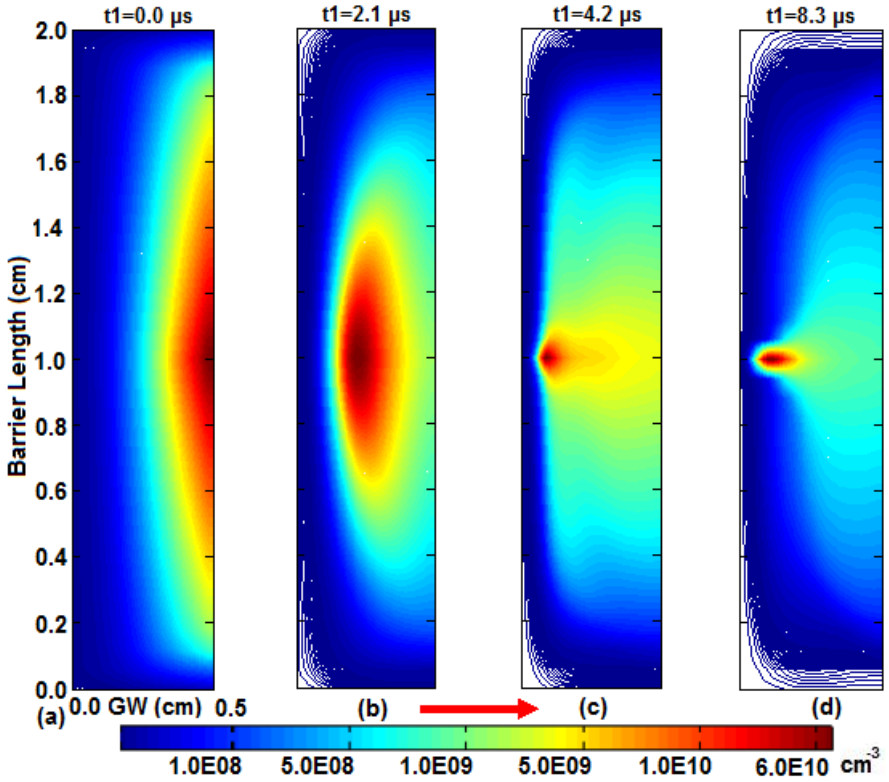

Figure 5.3. Phases of electron density evolution for $f = 20$ kHz, $\varepsilon_r = 9.0$, RC $= 5.0 \times 10^{-6}$ cm^3 s^{-1} and $V_{appl} = 1.7$ kV with 50 ppm N_2 impurities.

The space and time variations of electron density are illustrated in figure 5.3 (a - d) during the evolution of different steps of filamentary discharge, which describe the prebreakdown, breakdown and filamentary discharge formation and start of decay phases. The powered cathode and anode dielectric barriers are not shown in the diagram and their polarities link with the external applied voltage. The discharge parameters continuously update during the complete cycle, whereas the major and quick distortion is seen during the breakdown pulse as compared to the evolution of different phases in the filamentary discharge plasma. Initially, a quasi-neutral plasma is considered in the gap and the initial avalanche develops from the assumed seed electrons and ions present in the gap. It is described in the experimental work [101, 102] that the breakdown initiates at the same position of the former cathode fall and in the middle of the gap. The direct excitation, ionization and Penning ionization processes are the leading and governing processes in He-N_2 gas during the evolution of breakdown. The time duration (t1 - t4) represents that

the evolution of filamentary discharge covers the four distinct phases with a gap of approximately 3 μs. The figure 5.3 (a) corresponds to the prebreakdown phase and the magnitude of electron density is $\sim 0.7 \times 10^9$ cm^{-3} in this case. As the gas breakdown starts, the ionization processes are lead off at an enormous rate and create a remarkable change in the avalanche structure as shown in figure 5.3 (b), whereas the magnitude of electron density in this case is $\sim 1.0 \times 10^{10}$ cm^{-3}. The distorted cathode fall region evolves when the discharge current density is maximum and the distribution of electron density is shown in figure 5.3 (c) with the numerical magnitude of $\sim 5.0 \times 10^{10}$ cm^{-3}. The electron density further increases after the maximum discharge current density until the end of current pulse. The figure 5.3 (d) provides the electron density when the distorted cathode fall region start smashing and the magnitude is $\sim 6.0 \times 10^{10}$ cm^{-3}. This phase is termed as the start of decay in the filamentary discharge. The distinct phases of the filamentary atmospheric pressure discharge are obtained due to the overvoltage effect at 20 kHz driving frequency. It is clear from the figure 5.3 (a - d) that the density of the electrons is varied in different phases of atmospheric pressure discharge. A streamer is formed of an avalanche if the electric field of its space charge reaches a value of the order of the external field. This avalanche creates enough ions to localize the electric field. The structure of filaments in figure 5.3 (c, d) is created due to the streamer ionization mechanism because the electric field is higher at the streamer head than the filamentary discharge in the reactor gap. The figure 5.3 (c) exhibits that there is a strong interaction between the electron impact processes at the streamer head near the cathode barrier as compared to the whole reactor gap. The higher electric field is developed due to the accumulation of positive ions in the distorted cathode fall region near the cathodic dielectric barrier. Consequently, the noticeable steps of electron density distribution in figure 5.3 (a - d) constitute the pre-breakdown, breakdown, filamentary structure in constricted form and start of decay in the filamentary atmospheric pressure dielectric barrier discharges.

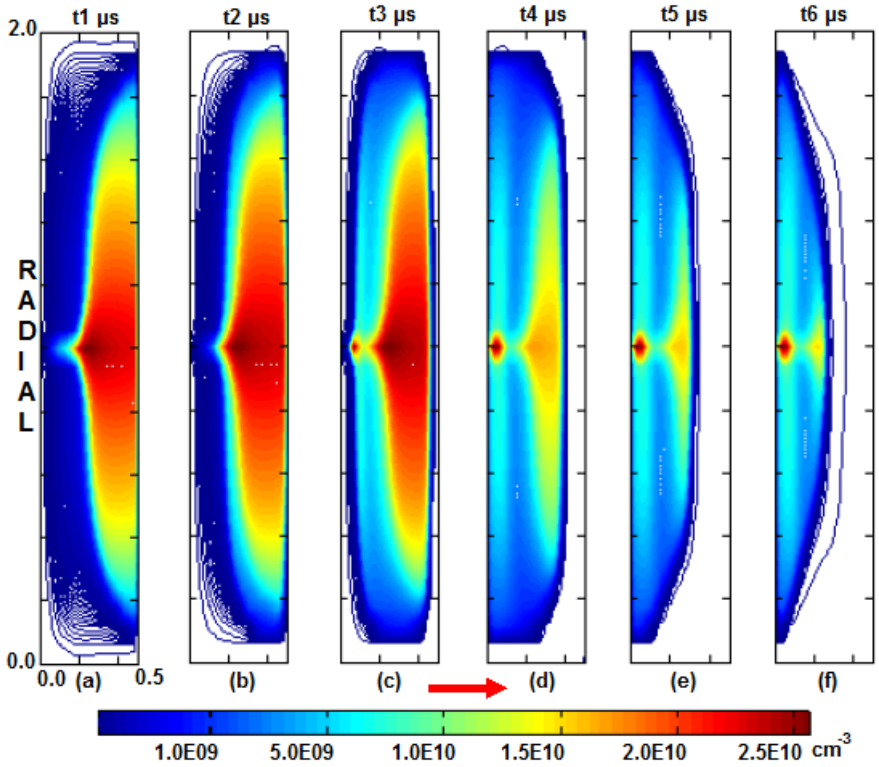

Figure 5.4. Profiles of electron density in the afterglow phase for $f = 20$ kHz, $\varepsilon_r = 9.0$, RC $= 5.0 \times 10^{-6}$ cm^3 s^{-1} and $V_{appl} = 1.7$ kV with 50 ppm N_2 impurities.

To understand the non-uniform discharge behavior with combined imposed conditions, such as the overvoltage and increased recombination coefficient of N_2^+ ions, the analysis of the filamentary discharge is also performed in the afterglow phase from t1 to t6 μs in order to understand the effect of increased recombination coefficient of molecular nitrogen ions. As the recombination reaction processes (R7 - R10 in table 2.1, R1 - R3 in table 2.2) play a significant role in the afterglow phase as compared to the other reactions, so the higher recombination rate destroys the electrons before the next breakdown. Therefore, a non-uniform distribution of electron density develops in the gap and the evolution of electron density is shown at different time instants with an approximately equal time interval of 1.25 μs as shown in figure 5.4 (a - f). The electron density is decreased to the smaller values $\sim 1.0 \times 10^9$ cm^{-3} in the filamentary discharge because the filaments create due to Townsend ionization mechanism in the afterglow phase. The origin of non-uniformities is described by the streamer and Townsend ionization mechanisms, which enhance the processes of constricted glow discharge formation and afterglow filamentary form as shown in the figures 5.3 (b, c) and 5.4 (c - e). In the decay phase, the constricted filamentary structure of electrons density is divided into two layers, which show the strong and weak formation of filaments on both sides of electron density structure due to the existence of variable density gradient as shown in

figure 5.4 (d - f). The authors [100, 101] discussed the source of filamentation in the discharge plasma with two-dimensional fluid model, which has been produced under different imposed conditions than discussed in this section. The stages of electron density structure build up the better perception for the formation of non-uniform discharge distribution in the afterglow phase as displayed in figure 5.4 (a - f).

5.3.1 Absence of imposed conditions

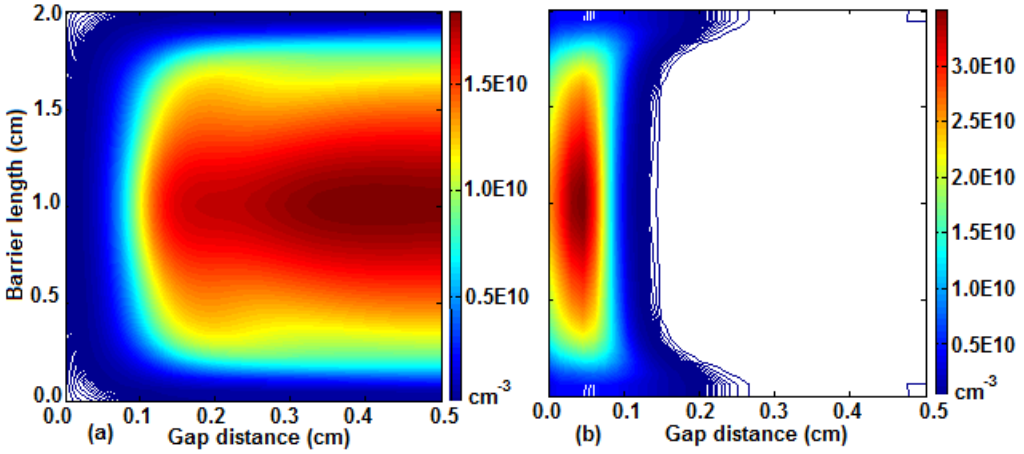

Figure 5.5. Uniform structure of (a) electrons and (b) He_2^+ ions density for $f = 20$ kHz, $\varepsilon_r = 9.0$, RC $= 2.0 \times 10^{-7}$ cm^3 s^{-1} and $V_{appl} = 1.5$ kV with 50 ppm N_2 impurities.

The uniform structure of discharge species is recovered without the combined imposed conditions, such as overvoltage and increased recombination coefficient as shown in figure 5.5 (a, b). The previously discussed four distinct regions are identified precisely as shown in figure 5.5 (a, b), which provide a sufficient indication for the uniform distribution of atmospheric pressure glow discharge. The uniform distribution of electrons and He_2^+ ions density manifest the source of non-uniformities under variable conditions in helium gas with 50 ppm nitrogen impurities. When the applied voltage is slightly greater than the breakdown voltage, the probability of Townsend ionization mechanism becomes greater as compared to the streamer breakdown of the dielectric barrier discharges at atmospheric pressure. Therefore, the uniform glow discharge is possible only under normal conditions, such as trace amount of nitrogen impurities, small positive difference between the applied and breakdown voltages and standard recombination coefficient of ionic species. The large positive difference between the applied and breakdown voltage causes the filamentation in the atmospheric pressure discharge and the above results support these arguments. The species distribution of uniform and non-uniform discharges represent the stationary-state of discharge, which can be verified with the temporal evolution of current-voltage characteristics.

5.4 Characteristics of uniform APD

5.4.1 Electrical characterization of the APGD

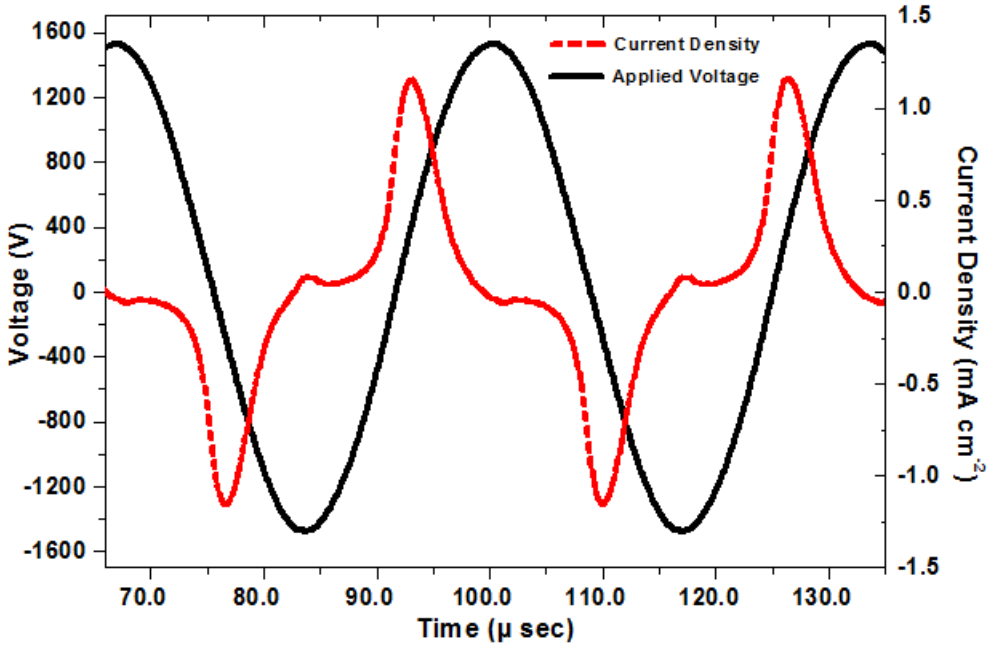

Figure 5.6. V - i characteristics for the periodic stationary-state of APGD for $f = 30$ kHz, $\varepsilon_r = 7.5$, Barrier width = 0.1 cm and $V_{appl} = 1.5$ kV with 20 ppm N_2 impurities.

The V - i electrical characterization profile is demonstrated with the temporal evolution of the voltage-current parameters and the voltage boundary conditions [15, 104] are used in the present two-dimensional fluid model for the dielectric barrier discharge. The pattern in figure 5.6 shows that the higher and lower current density peaks are noticed per half cycle and the remaining discharge properties are identical from one cycle to another. The stationary asymmetric structure can be dominant for the large current densities but the magnitude of positive and negative discharge current density pulses are equivalent. The stationary-state means the equal generation of electrons and ions pair in a number of consecutive cycles. The electric field accelerates the charged particles which absorb the energy from the field. Therefore, the electrons absorb sufficient energy to ionize the gas particles in the breakdown pulse and release the energy in the decay phase, and this process becomes continuous in steady-state. Although, the large current density peak corresponds to the uniform homogeneous glow discharge and its rise time is small as compared to the fall time as shown in figure 5.6. The origin of the small current density peak or residual current density peak differs from the large current density peak because it is created due to the trapped electrons in the positive column during the glow discharge. The residual current is induced when these trapped electrons swiftly move during the polarity reversal of the electric field. The above

voltage-current characteristics structure is similar to the structure observed in [100, 101].

5.4.2 Difference between Glow and Townsend discharges

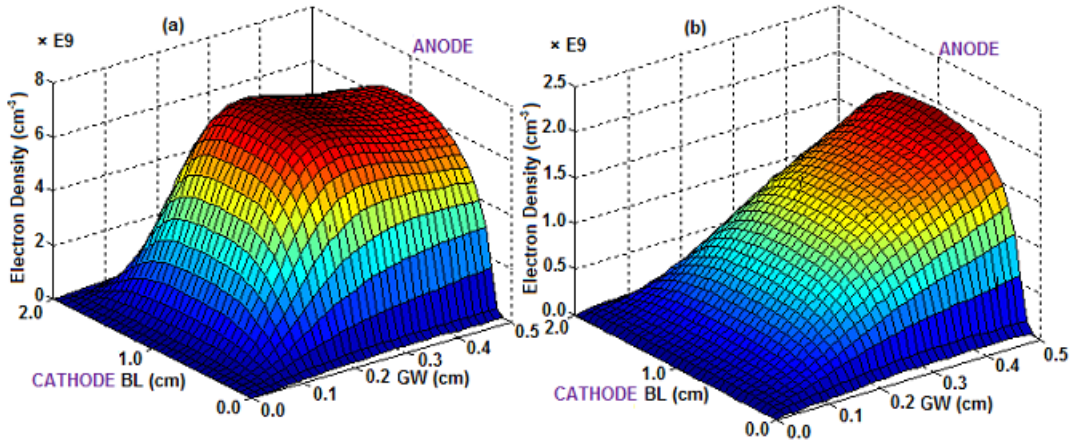

Figure 5.7. Electron density in the (a) glow and (b) Townsend modes for $f = 30$ kHz, $\varepsilon_r = 7.5$, Barrier width = 0.1 and 0.3 cm, $V_{appl} = 1.5$ kV with 20 ppm N_2 impurities.

The major and important species in the atmospheric pressure discharges are the electrons, which represent the state of discharge during the progress. We consider the mesh distribution of electrons, which are illustrated with the atmospheric pressure glow and Townsend discharge modes. These structures are developed by the effect of dielectric barrier thickness and the discharge characteristics manifest in two distinct uniform discharge modes. The glow discharge mode shows the maximum electron density near the cathode fall region and the Townsend mode displays near the anode barrier respectively as shown in figure 5.7 (a, b). The electric field is strongly distorted due to presence of space charge in case of glow discharge mode as compared to the Townsend discharge mode. However, the intense and weak uniform discharge plasma are developed in the glow and Townsend discharge modes in He-N_2 gas. The atmospheric pressure glow discharge is obtained with an axial gap width of 0.5 cm and the dielectric barrier thickness of 0.1 cm and the corresponding maximum electron density is $\sim 7.3 \times 10^9$ cm^{-3}. The Townsend discharge mode is accomplished by increasing the barrier thickness to 0.3 cm and the positive column disappears in this case. This indicates that the atmospheric pressure glow discharge is shifted into Townsend mode because of the large voltage drop across the gap and higher impedance of dielectric barrier due to the higher thickness. The result is confirmed with the electron density mesh structure as shown in figure 5.7 (b), which describes the maximum electron density $\sim 2.0 \times 10^9$ cm^{-3} near the anode and minimum $\sim 1.0 \times 10^8$ cm^{-3} near the cathode. The figure 5.7 (a, b) shows that the location of discharge activities are changed in the uniform glow and Townsend discharge modes. The above mentioned difference between atmospheric glow and Townsend discharge modes can be verified with the

previous modelling results [99, 101].

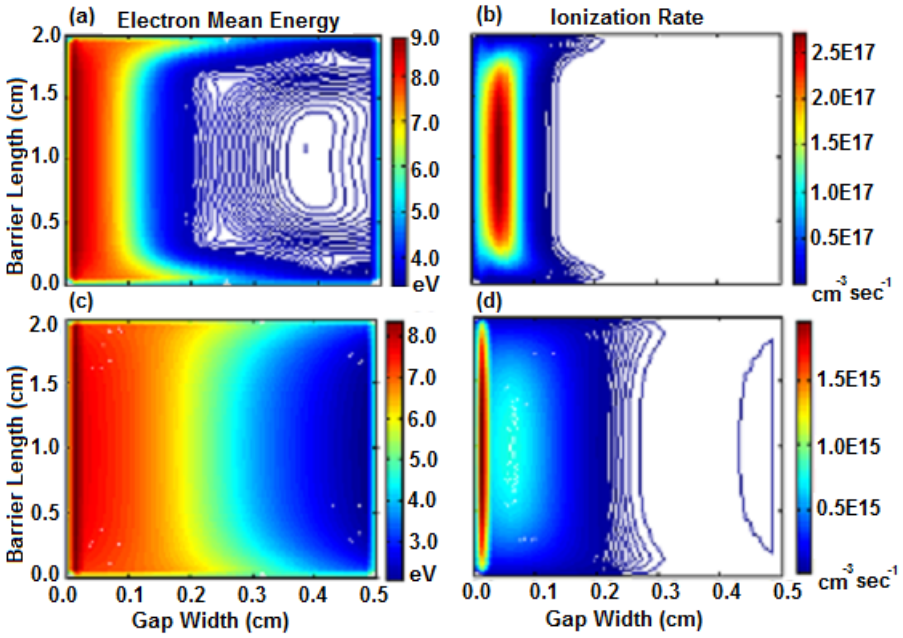

Figure 5.8. Electron mean energy (a, c) and ionization rate (b, d) for $f = 30$ kHz, $\varepsilon_r = 7.5$, Barrier width = 0.1 and 0.3 cm, $V_{appl} = 1.5$ kV with 20 ppm N_2 impurities.

As the number of the atmospheric pressure discharge studies [52, 100] assumed a local field approximation and the simulation model in this study solves an electron energy density equation using the drift-diffusion approximation in addition to the plasma fluid model equations. The figure 5.8 (a - d) exhibits the spatial discharge structures of the electron mean energy and ionization rate for the APGD and APTD respectively. The structures of electron mean energy show that the electron energy is maximum and suddenly falls from 9.0 to 3.0 eV near the cathode in case of APGD, whereas the inclined slope of the electron mean energy structure is noted and varies smoothly from 8.0 to 3.0 eV in APTD as shown in figure 5.8 (a, c). The ionization rate is maximum near the cathode in the glow mode and immediately drops from the numerical value $\sim 1.0\times10^{17}$ $cm^{-3}s^{-1}$ to $\sim 1.0\times10^{15}$ $cm^{-3}s^{-1}$ in case of Townsend discharge mode as exhibited in figure 5.8 (b, d). The ionization rate in figure 5.8 (b) displays that the volume concentration is strongly dense and uniform in the central part as compared to the peripheral edges of the barriers in APGD. The one-dimensional structure of the electron mean energy calculated from the hybrid model at the current density peak is matched with the above electron mean energy distribution [29]. The simulation results of two-dimensional fluid model are consistent with the one-dimensional fluid model results, which provide the reliability of analysis of atmospheric pressure discharge.

5.5 Evolution of electrons density in uniform APD

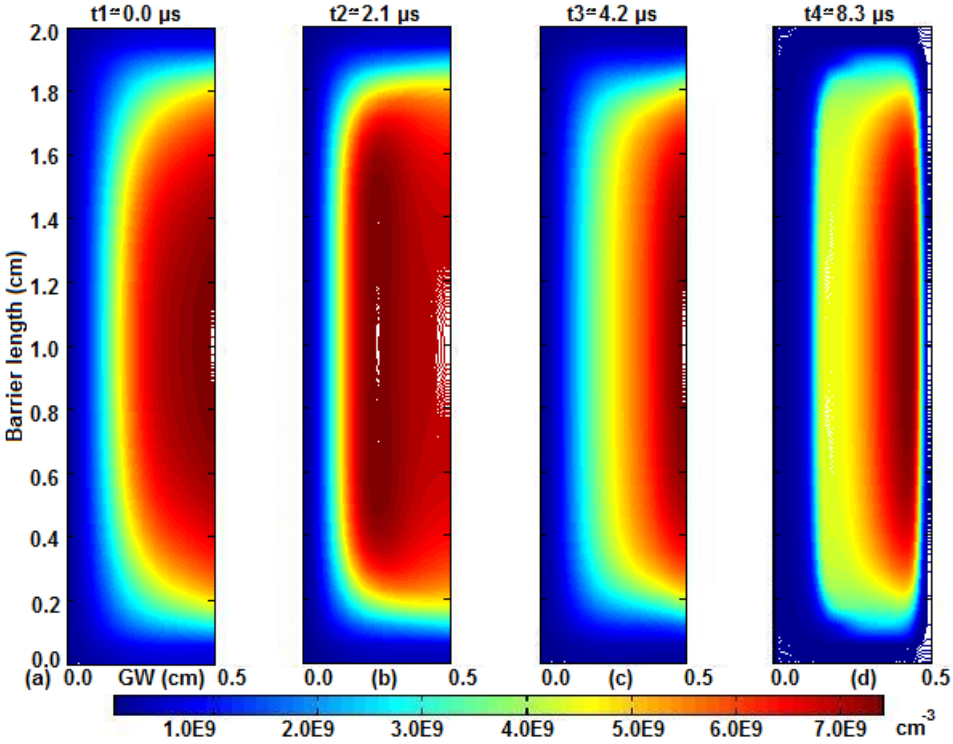

Figure 5.9. Phases of electron density evolution for $f = 30$ kHz, $\varepsilon_r = 7.5$, Barrier width = 0.1 cm and $V_{appl} = 1.5$ kV with 20 ppm N_2 impurities.

To understand the features of uniform atmospheric pressure discharge during its progression, the distributions of electron density are explored at different time instants from (t1 - t4) as shown in the figure 5.9 (a - d). The time duration covers approximately quarter of a cycle from 0 to 8.3 μs. The structure of electrons density is shown in figure 5.9 (a) at time t1 $\cong$ 0, which represents the state of electrons just before the breakdown with a numerical magnitude of $\sim 3.5 \times 10^9$ cm^{-3}. The electrons do not occupy the whole space in the reactor gap as clearly shown in the figure 5.9 (a). As the breakdown completely occurs at t2 $\cong$ 2 μs approximately, the electron density is forced to extend radially outward due to the influence of the radial electric field. Although the diffusion of the electrons is supported by the radial field along with the axial progress of the avalanche in the direction of axial electric field. The source of electrons and ions near the cathode barrier is the direct ionization of helium atoms and Penning ionization process for the maintenance of uniform atmospheric pressure glow discharge. The uniform cathode fall region evolves with four distinct parts due to the fast movement of charge particles in the gap, which discussed in section 5.2 in detail. The magnitude of higher current density is acquired during the fast progression of discharge plasma towards the cathode barrier and enhances a strong displacement current

at the position of the cathode. In this case, the discharge current density reaches to the higher values and the structure of electron density is exhibited in figure 5.9 (b). The electron density increases after the maximum discharge current density because the ionization processes continuously produce the electrons in the presence of impurities during this phase. The electron density increment process halts at the position of new cathode fall layer in the gap near the end of current pulse. The figure 5.9 (c) represents the electron density distribution in the decay of discharge current density at t3 $\cong$ 4 μs. During the discharge progress, the creation and destruction of discharge species persist along with the electron energy losses. The electron energy losses play a meaningful role because they are composed of the joule heating, elastic and inelastic electron impact collision processes. These energy losses are not exactly balanced by the ionization processes but act to reduce the production of electrons. The atmospheric pressure glow discharge is stable in the presence of energy losses and avoids to move in the filamentary form. Finally, the electron density approaches to its maximum value at the position of new cathode fall layer of next breakdown pulse after t4 $\cong$ 8.3 μs approximately. This indicates that the significant contribution of electrons is emerged during the evolution of breakdown phase and the discharge characteristics provide a better perception of the evolution of uniform atmospheric pressure discharge phases. The figure 5.9 (a - d) displays the course of consecutive events betided in the atmospheric pressure uniform discharge, whereas the magnitude of the electron density increases in the mentioned phases. The spatial structures of electron density are synchronized with the temporal evolution of discharge current density pulse as shown in figure 5.6.

5.5.1 Spatio-temporal evolution of surface charge density

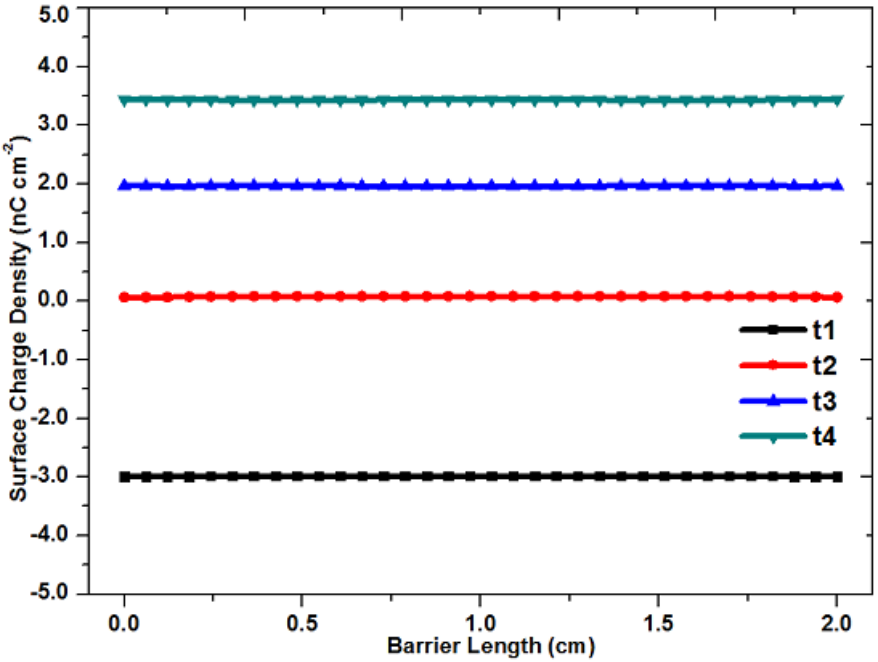

Figure 5.10. Spatio-temporal evolution of surface charge density for $f = 30$ kH, $\varepsilon_r = 7.5$, Barrier width $= 0.1$ cm and $V_{appl} = 1.5$ kV with 20 ppm N_2 impurities.

As the surface charge density is calculated by using the Gauss's law, which described in chapter 2 by the equation (2.35). The figure 5.10 exhibits the distribution of surface charge density on the powered dielectric barriers as well as with the spatial evolution of electrons density in the reactor gap at the same time instants (t1 - t4) of figure 5.9 (a - d). The temporary cathode and anode dielectric barriers change their polarities with the external applied voltage. Just before the breakdown, the dielectric barrier is negatively charged, which mention the memory effect of the last breakdown at t1. With the effect of large number of positive ions on the surface of cathodic barrier, the resultant surface charge density becomes positive, which has a peak value at the end of current pulse. The electric field in the cathode fall region decreases due to the accumulation of positive charges on the dielectric barrier. The charge particles in the reactor gap are destroyed through different chemical processes, such as dissociative recombination of different ionic species. However, the recombination process performs a significant role in the positive column of the discharge in the decay phase. Therefore, the cathode fall region smashes in the afterglow phase due to the effect of above mentioned processes and these results are agreed with the previous modelling results in [100].

5.6 Temporal evolution of discharge species variables

5.6.1 Temporal profiles of averaged species density

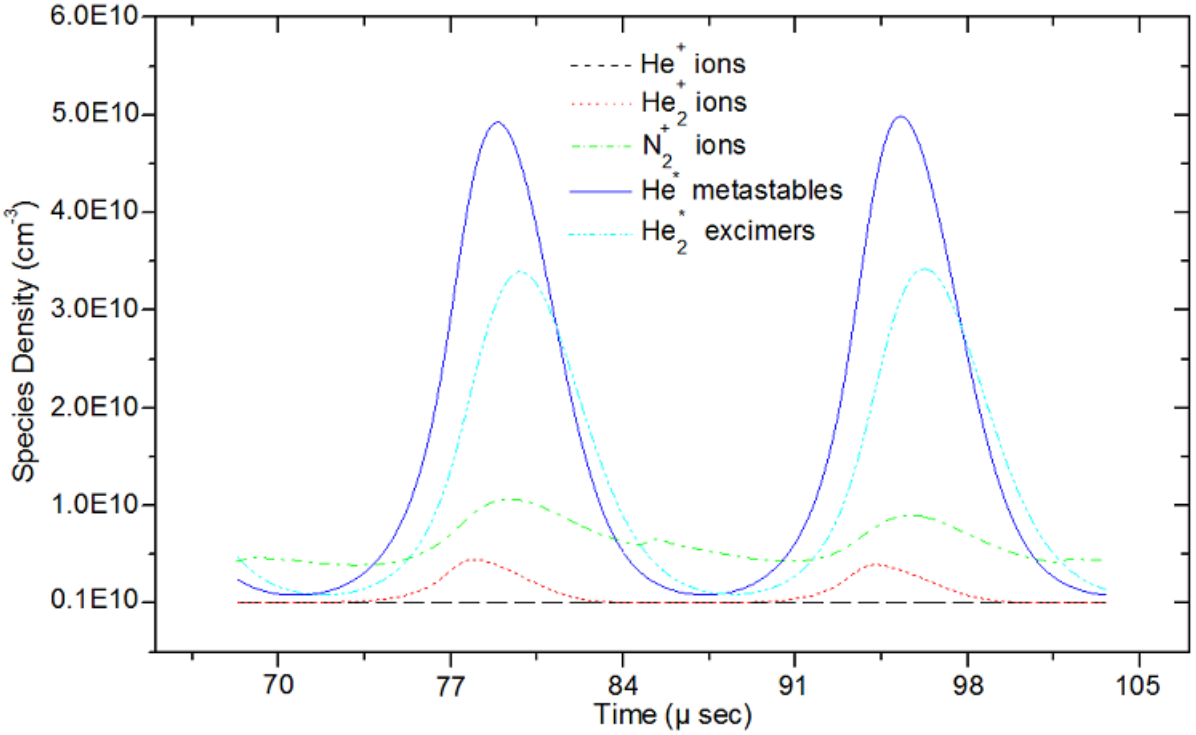

Figure 5.11. Temporal profiles of averaged species density for $f = 30$ kHz, $\varepsilon_r = 7.5$, Barrier width = 0.1 cm and $V_{appl} = 1.5$ kV with 20 ppm N_2 impurities.

The overall behavior of atmospheric pressure discharge can be expressed by the temporal evolution of average species density for a complete cycle as illustrated in figure 5.11. The metastables (He^*) perform the governing role during the APGD and have a maximum density after the ionic species density in the presence of 20 ppm nitrogen impurities. The chemical reaction R11 in table 2.1 shows that the metastables are converted into excimers through a three body collision process and this strongly explicates the average profile of excimers during the temporal evolution. The metastables and excimers interact with the nitrogen molecules through the Penning ionization process (R4, R5 and R8 in table 2.2) and produce the N_2^+ ions. The temporal distribution of molecular nitrogen ions shows that the average density of N_2^+ ions is greater than He^+ and He_2^+ ions, whereas they have different behavior in the afterglow phase as shown in figure 5.11. Therefore, the average density of N_2^+ ions is greater than other ionic species in the APGD, which expresses the importance of nitrogen impurities. Lastly, the volume concentration of vast majority of He^+ ions are converted into the He_2^+ ions using the three body reaction (R3 in table 2.1) [97] and emerge as the lowest density of species in the glow discharge. The

temporal evolution of averaged discharge species density illustrates the distinct role of different species in the atmospheric pressure glow discharge.

5.6.2 Temporal distribution of production rates

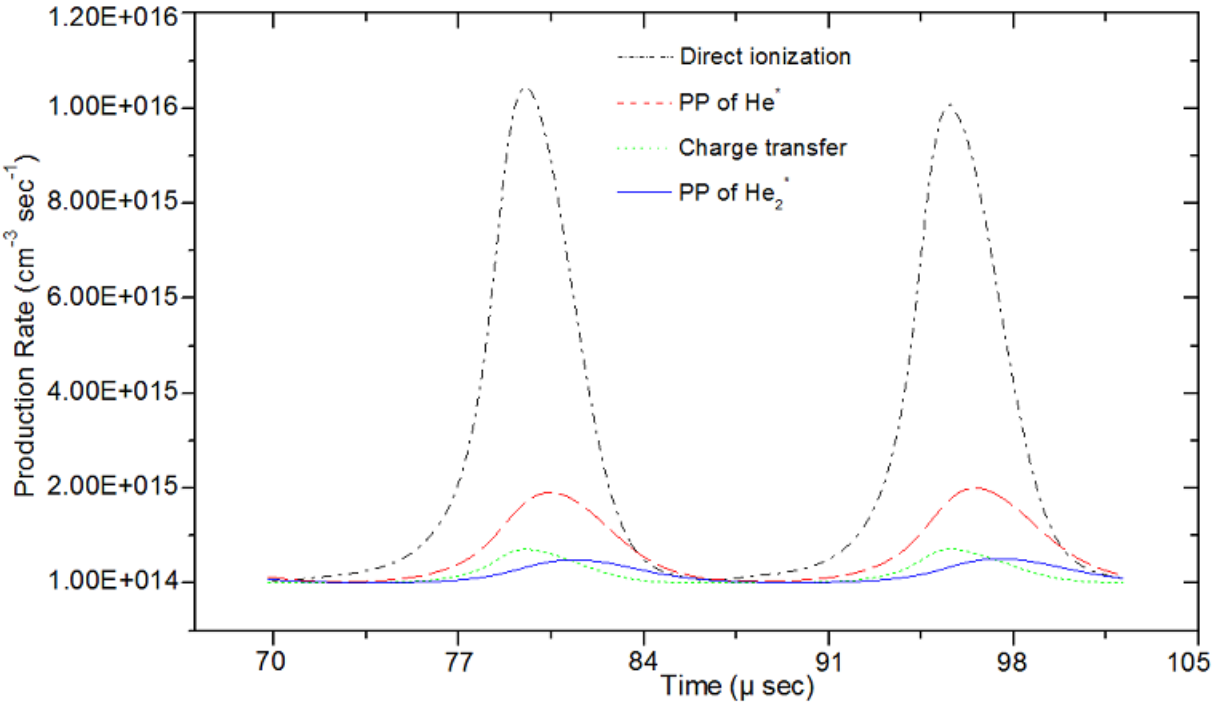

Figure 5.12. Production rates of major chemical processes for $f = 30$ kHz, $\varepsilon_r = 7.5$, Barrier width = 0.1 cm and $V_{appl} = 1.5$ kV with 20 ppm N_2 impurities.

As we consider only 20 ppm nitrogen impurities in helium gas for the evolution of uniform atmospheric pressure discharge but the substantial influence of N_2^+ ions over the other density of ionic species is analyzed by the production rates of main plasma processes. The temporal evolution of the ionization rates of different species exhibit that the direct ionization of helium atoms is the dominant as compared to the other ionization processes as shown in the figure 5.12. Secondly, the Penning ionization process of metastables is greater than the charge transfer between He_2^+ and N_2^+ ions and Penning ionization of excimers. The direct ionization of nitrogen, the step-wise ionization of helium metastables and excimers, and other production rates are smaller as compared to the displayed production rates and not shown here due to the smaller influence. The delay in the peak of Penning ionization as compared to the direct ionization of helium helps us to understand that the N_2^+ ions continuously produce long after the glow discharge due to their long lifetime of metastables and excimers. The density of N_2^+ ions has a strong influence on the discharge characteristics because they perform an outstanding role in the decay

phase and effectively influence on the characteristics of discharge plasma. The direct ionization process is linked with the electric field strength and it is maximum when the electric field has large values. This provides the precise role of different production processes during the progression of a complete cycle.

5.6.3 Dissociative recombination of ionic species

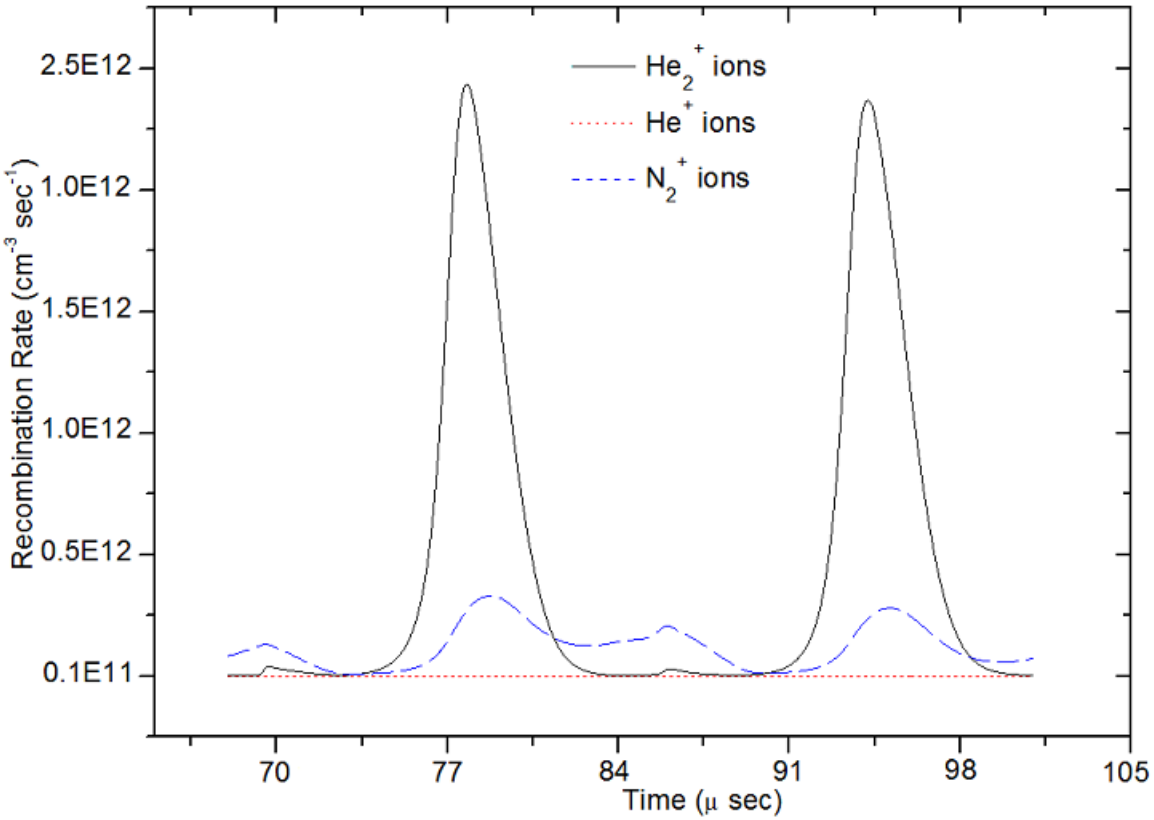

Figure 5.13. Recombination rates of ionic species for $f = 30$ kHz, $\varepsilon_r = 7.5$, Barrier width = 0.1 cm and $V_{appl} = 1.5$ kV with 20 ppm N_2 impurities.

The ionic species are created by the number of sources during the progression of atmospheric pressure discharge, which were discussed by the temporal evolution of mean production rates. The dissociative recombination rates of ionic species reactions are exhibited in figure 5.13 for a complete cycle. It is observed that the temporal evolution of averaged recombination rates is partially similar except for the molecular nitrogen ions. As we have discussed the strange behavior of filamentary discharge in the decay phase, which were emerged due to the higher recombination coefficient of molecular nitrogen ions. The behavior of dissociative recombination rate of molecular nitrogen ions is completely different than other ionic discharge species in the decay phase, which clearly displays by an arrow in figure 5.13. However, the behavior of molecular nitrogen ions is modified by the influence of variable amount of nitrogen

impurities. This evidence supports the effective role of molecular nitrogen ions in the decay phase when they are considered for use as an impurity in helium gas.

5.6.4 Influence of Penning ionization

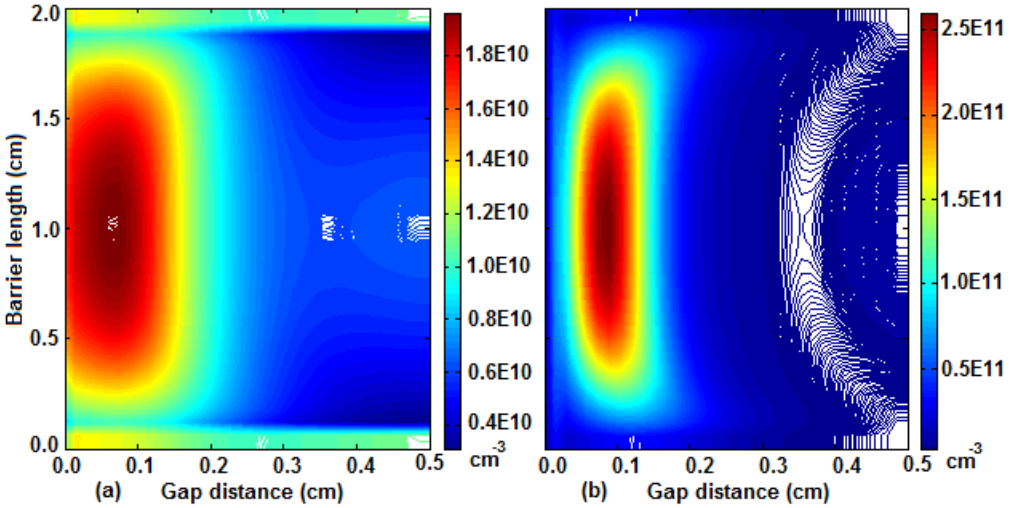

Figure 5.14. Spatial distribution of N_2^+ ions and He^* metastables density for $f = 30$ kHz, $\varepsilon_r = 7.5$, Barrier width = 0.1 cm and $V_{appl} = 1.5$ kV with 20 ppm N_2 impurities.

The spatial evolution of N_2^+ ions and metastables (He^*) density are shown in the figure 5.14 (a, b), when the discharge current density possesses its maximum value. The distribution of N_2^+ ions and metastables (He^*) are uniform in the gap and they have maximum concentration near the cathode barrier. The figure 5.14 (a) shows that there are small density gradients of N_2^+ ions on both sides of the cathode periphery as compared to the metastables. This can be examined by the help of the production rates of N_2^+ ions as defined in table 2.2. The Penning ionization is the strongest source of N_2^+ ions as compared to the direct ionization of N_2 and charge transfer between He_2^+ and N_2^+ ions. However, the reason for the density gradient near the edges can be explained with the properties of weakly ionized plasma. As the molecular nitrogen ions are heavier than other discharge species of atmospheric pressure discharge, the collisions are remarkable in weakly ionized plasma at high pressure. When the ionic species and electrons travel to their respective cathode and anode barriers, the lighter particles are rushed quickly and heavier particles crawled gradually. If this process continue for some time, then the heavier species also slide towards the edges as well as to the cathode barrier due to the effect of different collisional interactions. They form a thick layer of molecular nitrogen ions on the cathodic barrier as compared to the thin layer of molecular helium ions and their density magnitude is higher in the reactor gap than the molecular helium ions. As the metastables density is very small near the peripheral edges of the cathodic barrier as shown in figure 5.14 (b), so the Penning ionization is negligible near the edges. The charge transfer and

direct ionization of nitrogen molecules continuously produce molecular nitrogen ions with the smaller production rates at the cathodic barrier edges, which supplies a smaller quantity of molecular nitrogen ions at the peripheral edges. This develops a small change in the density of molecular nitrogen ions at the peripheral edges and the effect is varied with the amount of nitrogen impurities. This analysis shows that the small amount, i.e., 50 ppm nitrogen impurities has a remarkable effect on the characteristics of discharge plasma. The analysis shows that the small amount (20 ppm) has a remarkable effect on the discharge characteristics in He-N_2 discharge plasma. It is also noticed that the twin peak structure of metastables in pure helium as shown in figure 5.2 (c) is not matched with metastables in He-N_2 gas as shown in figure 5.14 (b). The small peak of metastables in He-N_2 gas is extinguished due to the effect of Penning ionization and the metastables don't trap in the positive column. This enhances the role of Penning ionization in He-N_2 gas for the atmospheric pressure discharges.

5.6.5 Effect of dielectric barrier length (diameter)

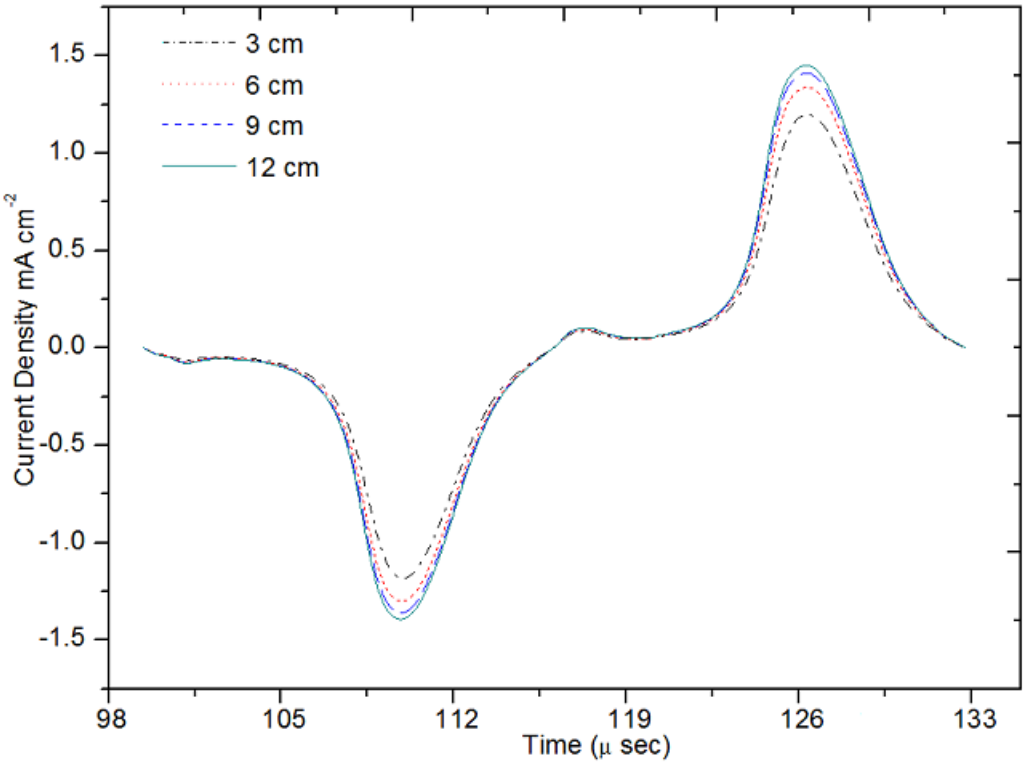

Figure 5.15. Discharge current density for $f = 30$ kHz, $\varepsilon_r = 7.5$, BL=3, 6, 9 and 12 cm, Barrier width = 0.1 cm and $V_{appl} = 1.5$ kV with 20 ppm N_2 impurities.

As the voltage drop across the dielectric barrier depends on the barrier width and the discharge characteristics are modified substantially with the change in the barrier width as discussed in case of atmospheric

pressure glow and Townsend discharge modes in section 5.4. The temporal evolution of the periodic steady-state of the discharge current density is displayed in figure 5.15, which shows a small increase in the current density with the increase in barrier length. This assumption is ignored in one-dimensional fluid model case but their role can be analyzed by the help of two-dimensional fluid model. The discharge current density is evaluated for different barrier lengths under similar input conditions. It is evident from figure 5.15 that the current density increases slightly when the barrier length is increased from 3 to 12 cm. This indicates that the uniformity and structural properties are the same at variable barrier radii without changing other discharge parameters. Hence, the fluid model can be applied for different types of geometric dimensions of parallel plate reactor.

5.7 Effect of relative permittivity of dielectric barrier

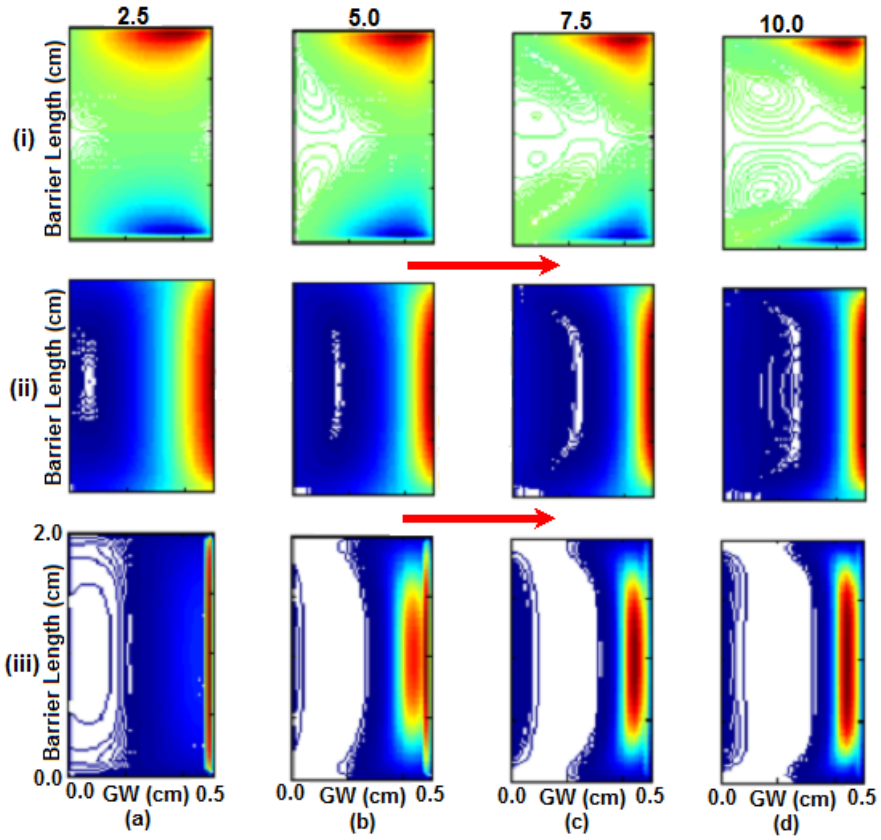

Figure 5.16. Effect of relative permittivity (2.5, 5.0, 7.5 and 10) on the radial and axial electric field (E_x, E_y) and ionization rate for $f = 30$ kHz, Barrier width = 0.1 cm and $V_{appl} = 1.5$ kV with 20 ppm N_2 impurities.

The relative permittivity of dielectric barrier is an important parameter influencing on the characteristics of atmospheric pressure discharge modes, which are described with the spatial distribution of discharge parameters. It is defined as the way to characterize the reduction in the effective electric field due to the polarization of the dielectric material. The electrical characteristics of atmospheric pressure discharge are described by the effect of relative permittivity, which exhibits the decrease of gas gap voltage with the increase in barrier permittivity [87]. This section investigates the spatial distribution of discharge parameters due to the influence of relative permittivity of barrier. The internal structure of the radial and axial electric field, and ionization rate provide a sufficient variation at different relative permittivities as shown in figure 5.16 (i - ii - iii) (a - d), when the discharge current density is maximum during the half cycle. The charged particles are drifted towards the dielectric barriers due to the imposed electric field, which accumulate charge on the dielectric surface and induce a surface charge density on the barriers. Therefore, the dielectrics are polarized due to this charge accumulation and the strength of polarization is directly proportional to the relative permittivity of the material. The accumulation of surface charge on the dielectric barriers serves to diminish the voltage across the discharge gap and results a rapid decrease of gap voltage until the discharge current density attains a smaller value for the increase of external voltage. The extinction of dielectric barrier discharge is developed due to reduction of gap voltage that stops the formation of cathode spot [15, 98]. The profile of electric field is enhanced by the change of relative permittivity of barriers at the maximum discharge current density, whereas the axial electric field strength is increased from $\sim 4.0 \times 10^3$ to 1.2×10^4 V cm^{-1} and the radial electric field is varied from $\sim \pm 5.0 \times 10^2$ to $\pm 2.0 \times 10^3$ V cm^{-1} on both sides as the relative permittivity of the dielectric barriers changes from 2.5 to 10. The radial electric field causes the extension of ionization flit on the surface of dielectric barrier in the radial direction. The ionization rate is gradually increased near the cathode barrier as shown in figure 5.16 (iii) (a - d) and the magnitude varies from $\sim 1.0 \times 10^{15}$ cm^{-3} s^{-1} to $\sim 1.0 \times 10^{17}$ cm^{-3} s^{-1} with the change in permittivity from 2.5 to 10. The highest distortion of axial electric field and ionization rate are observed in the cathode fall region at $\varepsilon_r = 10$ as shown in figure 5.16 (ii - iii) (d) and they have the maximum values in this case.

5.7.1 Influence of nitrogen impurities

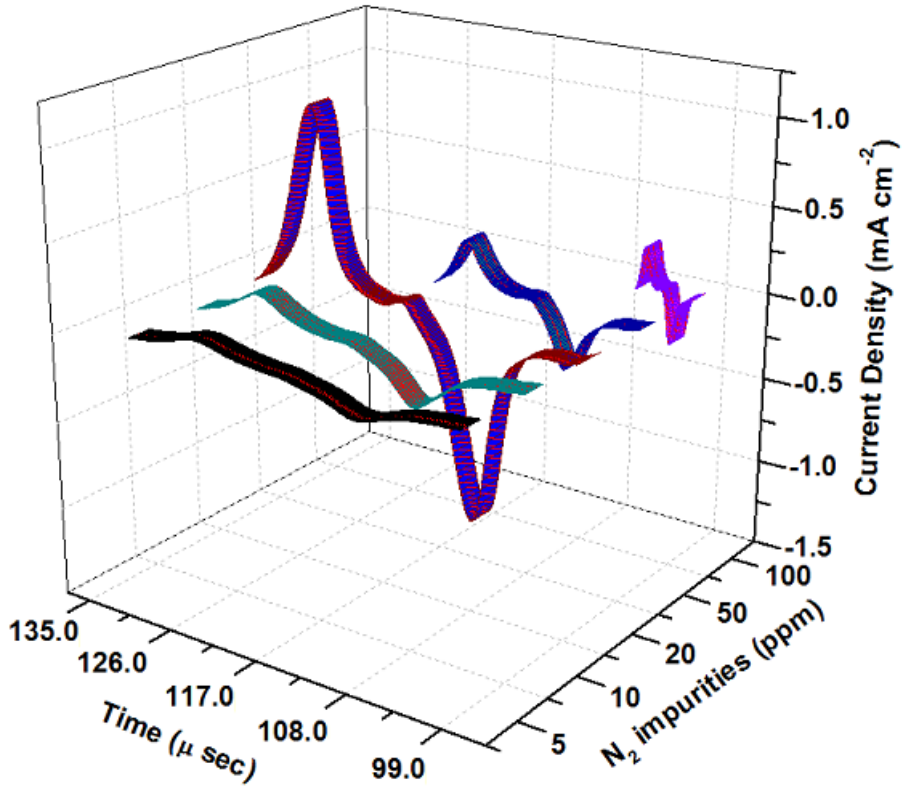

Figure 5.17. Temporal evolution of discharge current density for $f = 30$ kHz, $\varepsilon_r = 7.5$, Barrier width = 0.1 cm and $V_{appl} = 1.5$ kV with 5, 10, 20, 50 and 100 ppm N_2 impurities.

We now examine the influence of variable amount of nitrogen impurities in the He-N2 gas for the atmospheric pressure discharge, which is illustrated by the temporal evolution of discharge current densities as displayed in figure 5.17. The approximate amount of nitrogen impurities performs an indicative role for the formation of atmospheric pressure glow discharge. When the amount of nitrogen impurities is high, the destruction of metastables becomes dominant and eventually the discharge plasma evolves in the lower ionization mode. On the contrary, if the amount of nitrogen impurities is very small, the Penning effect becomes extremely insufficient and the discharge avoids to emerge in the uniform glow discharge form. As the quantity of nitrogen impurities varies from 5 to 100 ppm under the similar imposed conditions, the discharge plasma is operated in the lower and higher ionization modes. It is observed that the discharge current densities are smaller at 5 and 10 ppm nitrogen impurities and the discharge operates in the Townsend mode in the presence of very small impurities. This confirms that the Penning ionization is not enough to produce sufficient electrons and ions for the glow discharge mode and the discharge falls in the lower ionization mode with small discharge current densities. The

Penning ionization becomes sufficient for the production of the glow discharge mode at 20 ppm nitrogen impurities and the sharp discharge current density evolves with four prominent regions of APGD, which discussed in section 5. At further higher nitrogen impurities, the Penning ionization becomes stronger and intensifies the quenching of metastables and excimers consecutively. This is elaborated with the decrease of discharge current density from 50 to 100 ppm nitrogen impurities under the similar operating conditions. The structure of lower discharge current density in case of 100 ppm falls in the category of Townsend discharge mode, i.e., lower ionization mode because the electric field is not disturbed efficiently by the space charges and the smaller densities of species are evolved than the 20 ppm nitrogen impurities. The structure of discharge species is perfectly modified for the higher amount of nitrogen impurities, especially from 500 to few thousands ppm. It is also pointed out that the overvoltage alter the behavior of discharge plasma even in case of small or large amount of nitrogen impurities. Thus, the magnitude of overvoltage has a substantial effect to modify the internal structure of atmospheric pressure discharge plasma.

5.7.2 Spatial distribution of discharge participating species

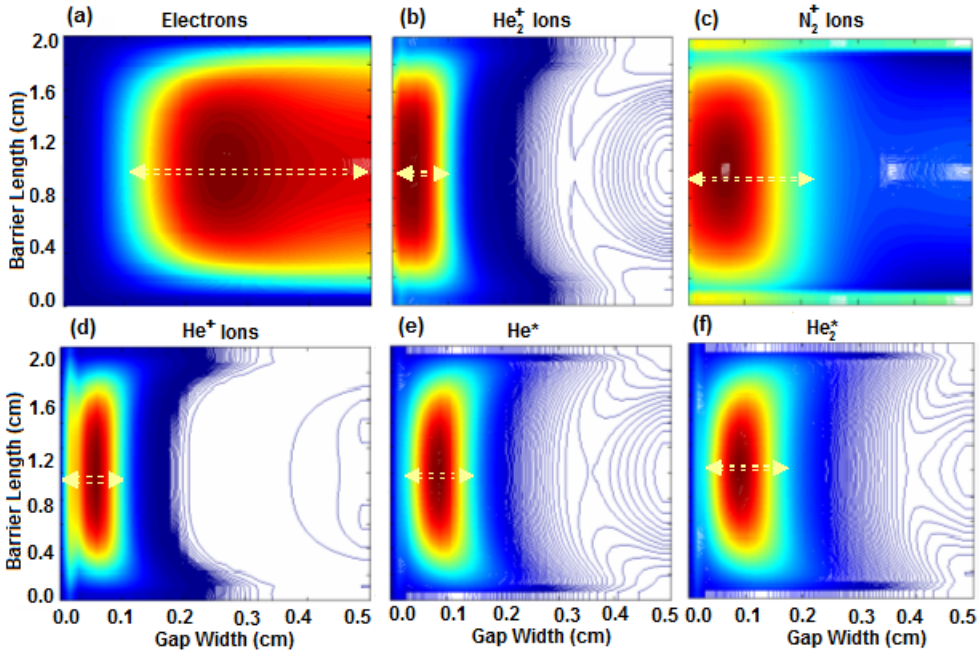

Figure 5.18. Spatial distribution of discharge species for $f = 30$ kHz, $\varepsilon_r = 7.5$, Barrier width = 0.1 cm and $V_{appl} = 1.5$ kV with 20 ppm N_2 impurities.

To get an overall spatial view of distribution of discharge species, the figure 5.18 enhances an insight and behavior of all species in the uniform glow discharge at 30 kHz driving frequency. The characteristics of discharge species are discussed for the atmospheric pressure glow and Townsend discharge modes

in the previous sections of this chapter. These structures are extracted from the discharge half cycle when the current density has the maximum value. The comparison of their role in the uniform glow phase is prominently displayed and the species width near the cathode barrier elaborates their active participation in the discharge plasma. Due to the difference between the electrons and ions mobility, a positive space charge layer is formed which enhances an accumulation of ions on the cathodic barrier as exhibited in the figure 5.18 (b, c, d). It is clear that the neutral and ionic species are spread near the cathode barrier and the electrons occupy a space in the remaining part of the gap. The Penning mixture of He-N_2 gas shows that the spread of molecular nitrogen ions is greater than other ionic species near the cathode barrier as shown in figure 5.18 (c). The magnitude of electrons, He^+, He_2^+, N_2^+, He^* and He_2^* species are $\sim 7.3 \times 10^9$, 2.0×10^{10}, 1.0×10^{10}, 8.0×10^8, 2.0×10^{11}, and 8.3×10^{10} cm^{-3} respectively as displayed in figure 5.18 (a - f). It is observed that the major difference between the density of He_2^+ ions and electrons is greater in pure helium gas as displayed in figure 5.1 (b, c) than the He-N_2 gas because of the absence of strong Penning ionization of impurities as displayed in figure 5.18 (a, b). From the above review analysis, a sharp picture about the behavior of discharge species is developed during the evolution of atmospheric pressure glow discharge.

5.8 Effect of driving frequencies

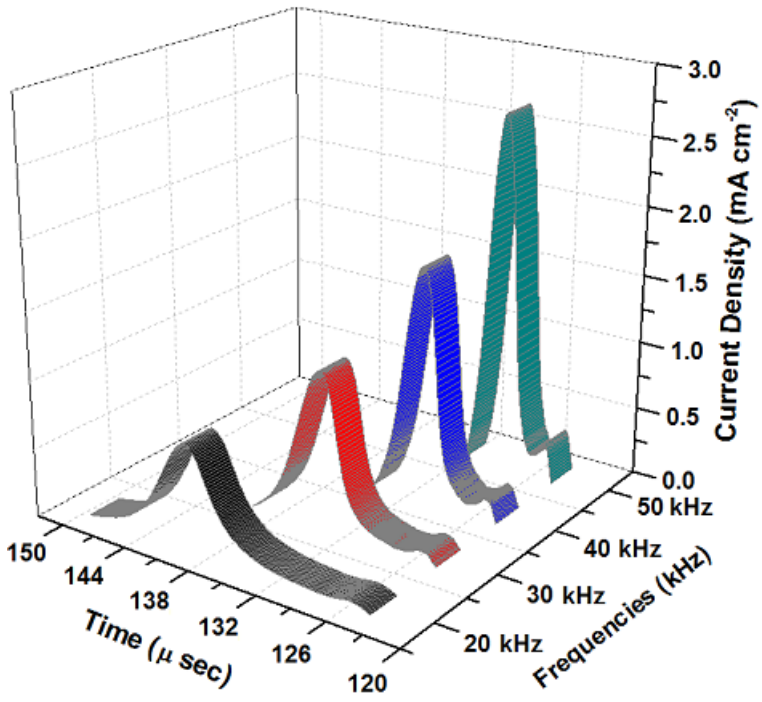

Figure 5.19. Temporal evolution of discharge current density for $f = 20$, 30, 40 and 50 kHz, $\varepsilon_r = 7.5$, Barrier width = 0.1 cm and $V_{appl} = 1.5$ kV with 20 ppm N_2 impurities.

As the electrical energy is supplied to the dielectric barrier discharges by sinusoidal voltage with a driving frequency, this energy is used to excite and ionize the gas atoms and molecules. The basic structures of discharge characteristics do not change but only an increase in the current density is observed and the discharge oscillates fastly with the increase in frequency. The physical significance of this increase can be linked with the electron energy losses and ionic species heating mechanism. It has been observed that the electrical energies are transformed into kinetic energies sharply under high frequency as compared to the low frequency dielectric barrier discharges [106, 107]. The different kinds of energy losses, such as joule heating, elastic and inelastic collision energy losses are dominant at lower frequencies than higher because the discharge plasma operates in a longer time span at lower frequencies. Although, the dynamic response of ionic species density is higher at smaller frequencies than higher frequencies in the atmospheric pressure glow discharges. The ionization rate becomes larger at higher frequencies due to the collisions of ions with gas atoms as well as secondary electrons emission. The temporal evolution of current density reveals that the discharge current density is directly proportional to the driving frequency in the mentioned range from 20 to 50 kHz under similar input conditions as shown in figure 5.19.

5.9 Conclusions and summary

We have developed a two-dimensional self-consistent homogeneous fluid model to describe the spatio-temporal characteristics of atmospheric pressure discharge in pure helium and He-N_2 gases. This chapter provides an understanding of dielectric barrier discharge in three different phases. In first phase, the uniform glow discharge structure is discussed in pure helium gas, which illustrates the four distinct regions of atmospheric pressure discharge and describes the effective role of chemical processes. In the second phase, the profile of constricted filamentary glow discharge is explored by the help of streamer breakdown mechanism and the decay phase elaborates the filamentary behavior of discharge. The transition between the uniform and non-uniform discharges are investigated with and without combined imposed conditions in the dielectric barrier discharges. In third phase, the electrical characterization and spatial distribution of discharge species parameters are examined for the uniform atmospheric pressure discharges. The uniform discharge modes are expressed by an adjustment of barrier thickness, which develops the atmospheric pressure glow and Townsend discharge modes. The temporal evolution of the discharge species density exhibits that the metastables and excimers are actively interacted with other discharge species because they have a dominant concentration during the complete cycle. The influence of nitrogen impurities, Penning ionization of metastables, relative permittivity of the dielectric barriers and variable frequencies are analyzed with the spatio-temporal distribution of the dielectric barrier discharges. It is noted that the major difference between the electrons and He_2^+ ions density is

greater in pure helium as compared to the He-N_2 discharge because of the absence of Penning ionization of nitrogen impurities. This confirms that the nitrogen impurities have a huge impact and decrease the difference between the electrons and He_2^+ ions density with Penning ionization process. Overall, the two-dimensional fluid model is useful to deliver a meaningful information for the uniform and non-uniform atmospheric pressure discharges, and describes the origin of non-uniformities.

Chapter 6

Effects of constant bulk gas flow in APD

6.1 Introduction

This chapter is an enhancement of the two-dimensional fluid model under specific conditions and assumptions in the presence of bulk gas flow. Recently, there has been significant advances in the numerical modelling of flowing gas discharges as well as experimental progress in this area. The bulk flow of gas performs an efficient role to change the dynamic features of the discharge in the parallel plate dielectric barrier discharge configuration. The influence of high speed gas flow has a considerable impact on the uniform and filamentary profiles of surface dielectric barrier discharge and these effects are discussed with the electrical characterization of discharge at subsonic and supersonic gas flow speeds in [108]. The significant impact of asymmetric and symmetric configuration of electrodes are analyzed experimentally by the influence of gas flow [109, 110] and the mechanism of supersonic gas flow control is examined and evaluated in [111]. The different modes of direct current glow discharge plasma actuators provide the concise understanding of properties in the low pressure supersonic flow regime [112]. The spectroscopic emission, stagnation pressure and drag enhancement effects are conferred on the supersonic rarefield air flow over a flat plate [113]. Corresponding, the development and formation of non-uniform discharge plasma is elaborated by providing the experimental results in high-speed air flows [114].

In this chapter, a self-consistent nonequilibrium multispecies multitemperature two-dimensional plasma-gas dynamic fluid model is developed to implement the parallel plate dielectric barrier discharge geometry with symmetric boundary conditions along the vertical discharge axis. The chemistry of discharge plasma is composed of major chemical reactions to describe the discharge characteristics in He-N_2 atmospheric

pressure discharge. The spatial distribution of electrons and ionic species, such as He^+, He_2^+ and N_2^+ are described in the stagnant, subsonic and supersonic bulk gas flow regimes. The spatial structures of metastables, excimers, electric field strength and electron mean energy show that the structures of uniform and filamentary discharge are observed in the lower and moderate subsonic bulk gas flow regimes. The distribution of neutral gas species density illustrates that the reduction of neutral species density (He) near the cathode barrier is in accordance with the constant pressure supposition. The rates of production and destruction of different species play a significant role in the glow discharge activity and the ionization rate is illustrated at the maximum discharge current density in the filamentary discharge mode. The atmospheric pressure bulk gas temperature is reduced with the increase in imposed gas flow speed and converts into near room temperature at higher subsonic bulk gas flow. The distribution of electronic and ionic fluxes exhibit that the portion of input energy is carried by the electrons and ions at different places in the gap during the formation of filamentary glow discharge.

In the stagnant and lower subsonic bulk gas flow regimes, the uniform distribution of electrostatic body force illustrates that the force strength is maximum near the cathode barrier and decreases sharply in the gap away from the cathode barrier. On the contrary, the non-uniform distribution shows that the force strength is dilatational and constricted filamentary near the cathode in the higher subsonic and supersonic bulk gas flow. The force strength is varied randomly in the gap and possesses the highest value in the constricted part of the discharge plasma because of high local ionic species density. The temporal evolution of discharge current density manifests that there is very small decrease in the lower subsonic bulk gas flow regime. The current density is suddenly reduced in the moderate subsonic flow regime and follows the trend to the supersonic bulk gas flow regime. The major aim of this chapter is to understand the influence of different bulk gas flow regimes for the uniform, filamentary and constricted filamentary atmospheric pressure discharge modes. This establishes a clear view point that the high-speed imposed gas flow ($\geq 1.0 \times 10^4$ cm s^{-1}) is not useful for the uniform glow discharge plasma applications and lower speed flow ($\leq 1.0 \times 10^4$ cm s^{-1}) provides the homogeneous uniform glow discharge plasma at atmospheric pressure. The influential properties of atmospheric pressure discharge are examined systematically under different operating conditions in the presence of imposed bulk gas flow speed.

In this chapter, Sections 6.2 and 6.3 describe the assumptions of formulation of fluid model and effect of bulk gas flow for the atmospheric pressure discharge variables. Section 6.4 is dedicated to provide the numerical simulation results in the stagnant and flowing He-N_2 gas, and their physical interpretation in the atmospheric pressure discharges. Section 6.5 distinguishes the filamentary and constricted filamentary atmospheric pressure discharges by exploring the electron and gas temperature. Section 6.6 examines the ionic and electronic flux distributions and influence of lower subsonic bulk gas flow speed. Sections 6.7 and 6.8 elaborate the effect of electrostatic body forcing and temporal evolution

of discharge current density at variable bulk gas flow speeds. The last section 6.8 is devoted to express the conclusions of atmospheric pressure discharge in the presence of bulk gas flow.

6.2 Assumptions of fluid model formulation

We now proceed to formulate a multispecies multitemperature two-dimensional fluid model in such a way that the parallel plate dielectric barrier discharge configuration is employed in the presence of He-N_2 bulk gas flow under the specific boundary conditions. Suppose a sinusoidal voltage is applied on the top driven electrode (ABCD) and zero potential is applied at the bottom grounded electrode (EFGH) as shown in figure 6.1.

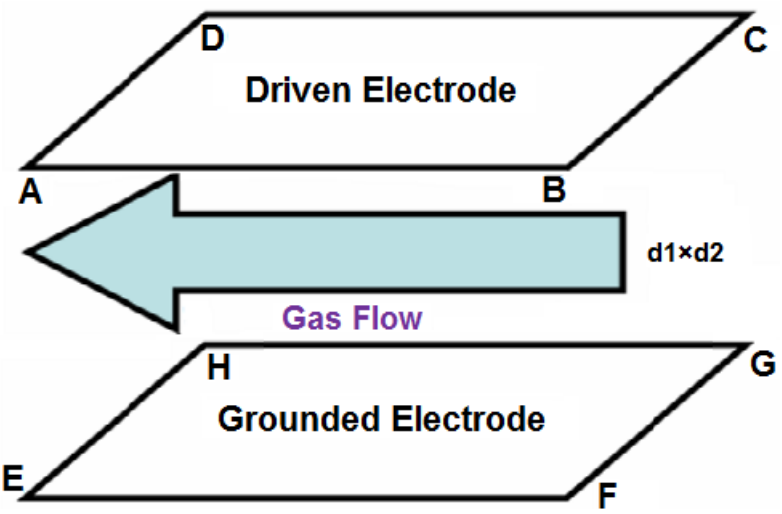

Figure 6.1. Parallel plate dielectric barrier reactor with driven and grounded electrodes in the presence of bulk gas flow.

The following numerical assumptions are considered for the implementation of numerical model as,

1. The two-dimensional uniform grid geometry of size 34×34 cells, a dielectric barrier length 2.5 cm in the radial direction, a barrier width 0.1 cm and parallel plate gap 0.5 cm are applied for the present numerical investigations.

2. The chemistry of atmospheric pressure discharge is composed of all major chemical processes, such as excitation, ionization, Penning ionization of nitrogen impurity (20 ppm) molecules, charge transfer and recombination, which discussed in the chapter 2.

3. The virtual discharge boundaries AD to EH and BC to FG represent that the discharge is symmetric along the vertical direction (y-axis).

4. The Reynold number is defined as $Re = \frac{\rho V L}{\nu}$, where ρ is density of bulk gas, V is free stream velocity, L is the gap distance between the parallel plates and μ is dynamic viscosity of the gas. The Reynold number in the reactor channel is varied from 200 to 14000, which covers the laminar, transient and turbulent gas flow regimes.

5. The Mach number in the channel reactor is found by the following equation $M = \frac{v_o}{v_s}$, where v_s is the speed of sound and v_o is the velocity of bulk gas relative to the medium. The Mach number in the numerical simulations is changed from subsonic to supersonic range, such as 0.1 to ~ 1.0.

6. The plasma gas fluid is supposed to obey the ideal gas law and freestream gas temperature, i.e., 300 K is considered in the reactor chamber.

7. A fixed bulk gas flow is assumed between the parallel rectangular plates by using the parabolic profile and no-slip condition is applied on the bulk gas flow velocity. The bulk flow velocity profile is calculated by the following expression $V_x = \frac{V_0}{4}\left(\frac{y}{\delta}\right)^2 \mathbf{i}$ for $y \leq \delta$ from the lower and upper parallel plates and $V_x = V_0\mathbf{i}$ for $y > \delta$ corresponding to a turbulent boundary layer profile. δ is the turbulent boundary layer thickness that is supposed to be 0.1 cm on both sides of plates.

8. The velocity component (V_x) is taken along the direction of bulk gas flow and the components in the perpendicular direction are ignored because of the small changes in the perpendicular directions for simplicity. A freestream velocity (V_o) of bulk gas is considered along x-axis and enter in the reactor channel through the cross section d1×d2 as shown in figure 2.1.

The number of experimental and modelling studies discussed the effects of the variable convective bulk gas flow rate in the atmospheric pressure discharge plasmas [115, 116, 117]. The He-N_2 gas is highly collisional at atmospheric pressure and the individual behavior of atoms and molecules is disappeared because the mean free path is very small. The energy exchange between the gas particles take place through the elastic and inelastic collisions. The distribution of discharge species are effected sharply at higher bulk gas flow stream, which pull each other along by their internal frictional interaction in the direction of bulk flow stream. This type of mentioned flow is designated as viscous flow and it can be divided into two major parts, laminar and turbulent [21].

6.3 Influence of bulk gas glow

We consider a parallel plate dielectric barrier discharge reactor in the presence of fixed bulk gas flow along the horizontal direction and the marked regimes, such as stagnant, subsonic and supersonic are developed with the parabolic profile of bulk gas flow. The drift-diffusion fluid model of He-N_2 gas mixture

provides the spatio-temporal characteristics of the atmospheric pressure glow and filamentary discharges in the presence of imposed bulk gas flow speed. A AC sinusoidal voltage is applied on the electrodes with a driving frequency of 30 kHz at reference gas pressure (760 torr) and initially, a quasi-neutral plasma is assumed in the gap with equal electrons and ions density of $\sim 10^8$ cm^{-3}. When the bulk gas flow velocity has significant changes in the x - direction, the components in the y - direction can be ignored because of small changes in this direction [42]. The freestream velocity (V_o) of bulk gas and freestream gas temperature (300 K) are considered, whereas the details and conditions of velocity profile discussed in the previous section. The spatial distribution of discharge species at atmospheric pressure are elaborated in the stagnant, subsonic and supersonic bulk gas flow regimes, which provide the insight and perception of discharge properties. The stationary-state achievement requires several number of cycles after the first breakdown in the dielectric barrier discharges.

6.3.1 Spatial distribution of discharge species parameters

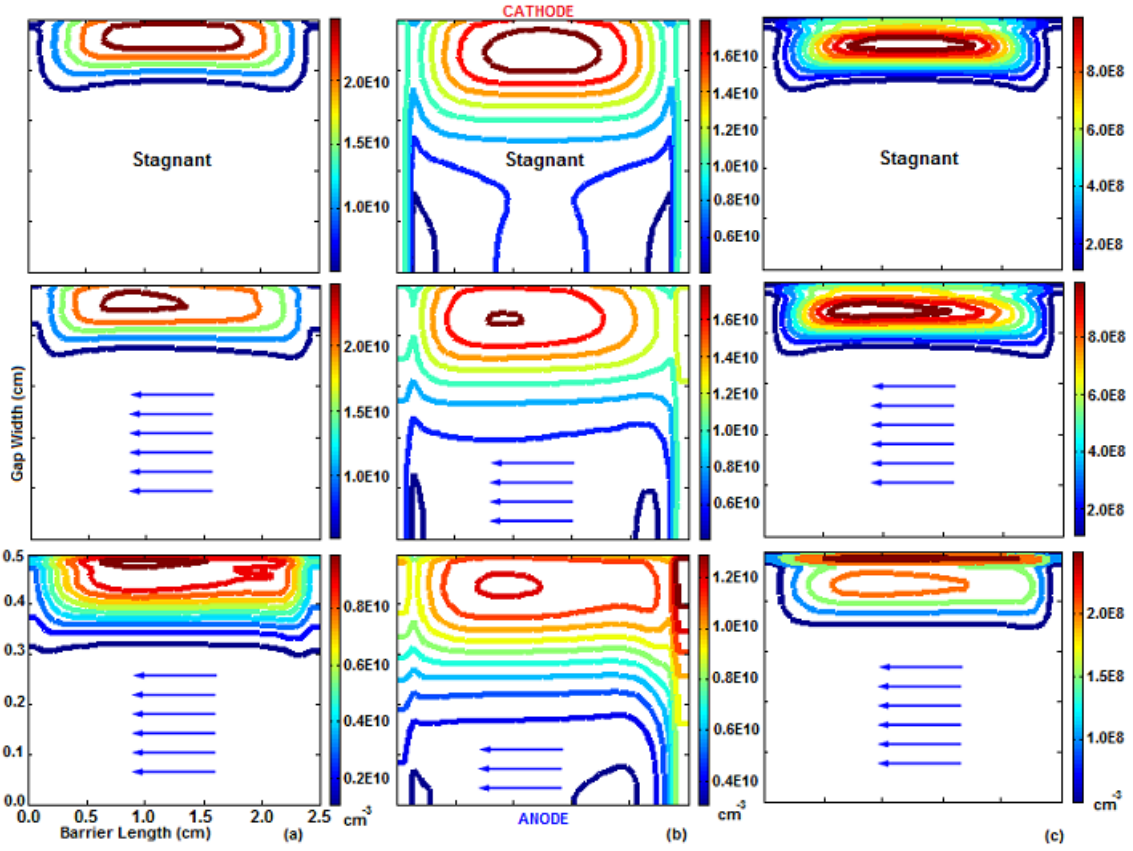

Figure 6.2. Spatial distribution of He_2^+, N_2^+ and He^+ ions density for $f = 30$ kHz, $\varepsilon_r = 7.5$, $V_o = 0$, 1.0×10^4 and 2.0×10^4 cm s^{-1} and $V_{appl} = 1.5$ kV with 20 ppm N_2 impurities.

To understand the effect of bulk gas flow in the atmospheric pressure glow and filamentary discharge modes, the spatial distributions of ionic species density are analyzed as shown in the three rows of figure 6.2 (a, b, c). The ionic species density of He_2^+, N_2^+ and He^+ in the first row of figure 6.2 exhibit that they are symmetric along the axial direction and have maximum density magnitudes in case of stagnant bulk gas. The second row in figure 6.2 represents the structure of ionic species in the lower subsonic bulk gas flow regime at bulk gas flow speed 1.0×10^4 cm s^{-1} and the magnitudes of species density are slightly decreased from the stagnant bulk plasma as shown in the first row of figure 6.2 (a, b, c). In this case, the profile of bulk gas flow is turbulent in the reactor gap. The magnitudes of ionic species density (He_2^+, N_2^+ and He^+) are reduced from 2.7×10^{10}, 1.9×10^{10} and 1.1×10^9 cm^{-3} to 2.6×10^{10}, 1.8×10^{10} and 0.9×10^9 cm^{-3} at the maximum discharge current density near the cathode barrier in case of stagnant and 1.0×10^4 cm s^{-1} bulk gas flow speed. As the gas flow speed increases further to 2.0×10^4 cm s^{-1}, therefore the structure of ionic species is completely changed into filamentary form and dragged along the barrier surface on the downstream direction of bulk gas flow in the presence of non uniformities. The numerical magnitudes of ionic species density (He_2^+, N_2^+ and He^+) in filamentary discharge are sharply reduced to 9.9×10^9, 1.2×10^{10} and 2.7×10^8 cm^{-3} at the peak discharge current density, which show the influence of fast bulk gas flow in the reactor chamber. It is clear from the three rows of figure 6.2 (a, b, c) that the density of helium ionic species (He^+ and He_2^+) are decreased significantly, whereas the density of molecular nitrogen ions (N_2^+) is not effected as moderately in case of even fast bulk gas flow. This indicates that the behavior of N_2^+ ions is entirely different than helium ionic species in the atmospheric pressure discharges. The authors in [33] discussed the experimental observations of species density in He - N_2 discharge plasma and showed that the fall of molecular nitrogen ions density is smaller and gradual than helium ions in the presence of variable bulk gas flow rate. The filamentary structure of ionic species in the third row of figure 6.2 (a, b, c) exhibits that the maximum density of species is appeared on the downstream edge of the dielectric barrier. The major shift of ionic species structure is observed along the bulk gas flow but a small spread also appears in the perpendicular direction. The spread in the perpendicular direction is more prominent in case of N_2^+ ions density as compared to other ionic species, which shows the glaring impact of small nitrogen impurities in the atmospheric pressure discharges. The smaller density of He^+ ions exhibits that it is transformed into He_2^+ ions fastly by using the channel of three body chemical reaction (R3 in table 2.1) in the presence of variable bulk gas flow speeds. The leading and dominant source of production of molecular nitrogen ions is the Penning ionization process of metastables and excimers. The reduction in density of helium ionic species is marked in case of fast bulk gas flow as compared to small change in the density of molecular nitrogen ions. This means that the electrostatic force of discharge plasma is stronger than the force exerted by the gas flow and the glow discharge structure is not effected distinctly at smaller gas flow speed as compared to higher bulk

gas flow speed. The above discussion verifies that the atmospheric pressure glow discharges are uniform at lower subsonic bulk gas flow and filamentary at moderate subsonic bulk gas flow regime.

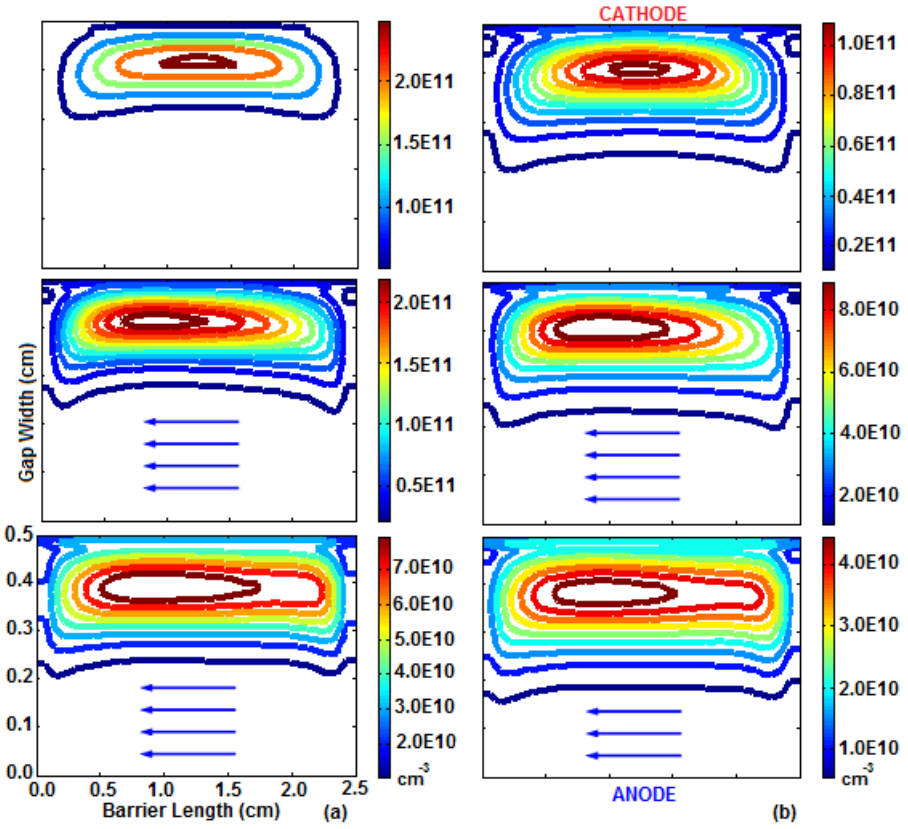

Figure 6.3. Spatial distribution of He^* and He_2^* density for $f = 30$ kHz, $\varepsilon_r = 7.5$, $V_o = 0$, 1.0×10^4 and 2.0×10^4 cm s^{-1} and $V_{appl} = 1.5$ kV with 20 ppm N_2 impurities.

As the excitation rate is larger than all other production processes during the whole discharge cycle, the metastables (He^*) and excimers (He_2^*) perform a leading a role in the atmospheric pressure discharges and interact with the helium gas atoms and nitrogen impurity molecules through chemical processes as shown in the tables 2.1 and 2.2. The metastables have negligible density near the cathode peripheral edges as compared to the excimers for the stagnant bulk gas as displayed in the first row of figure 6.3 (a, b). In case of atmospheric pressure glow discharge, the trapped electrons in the positive column produce the metastables, which can further generate the electrons and ions with different chemical processes. The ionic species are further responsible for the emission of secondary electrons from the dielectric barrier surface. The above mentioned activities are effected in the presence of variable bulk gas flow and the resultant distribution of metastables and excimers are illustrated in the second and third rows of figure 6.3 (a, b). The metastables and excimers are dragged along the surface of cathode barrier towards the downstream edge, which represents the influence of bulk gas flow as shown in the second and third rows of

figure 6.3 (a, b). The density of metastables and excimers are decreased extensively by the introduction of the moderate subsonic bulk gas flow and they drag along the direction of bulk gas flow, and smaller spread in the perpendicular direction. The numerical values of metastables (He^*) and excimers (He_2^*) are $\sim 2.6 \times 10^{11}$ and 1.1×10^{11} cm^{-3} in the stagnant glow discharge plasma, whereas the magnitudes reduce to $\sim 8.9 \times 10^{10}$ and 4.8×10^{10} cm^{-3} in the moderate subsonic bulk gas flow at $V_o = 2.0 \times 10^4$ cm s^{-1} and appears in the filamentary discharge mode. The spread of metastables and excimers density is significant in the radial and axial directions, and they supply the electrons and ions through stepwise ionization, charge transfer and Penning ionization for the maintenance of the atmospheric pressure glow discharges in the stagnant and flowing bulk gases.

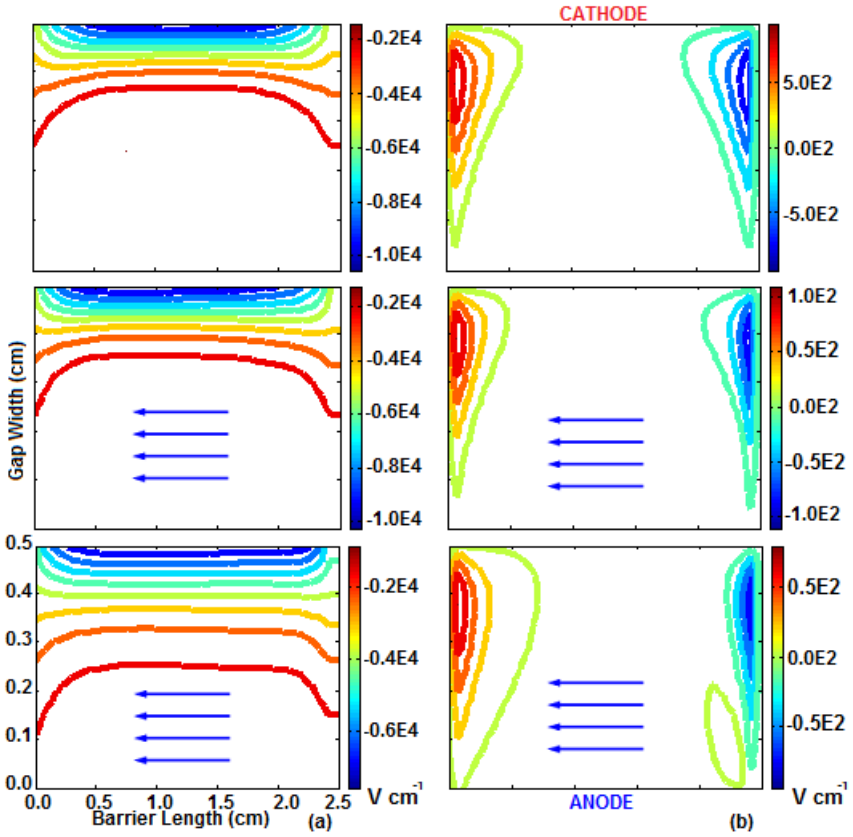

Figure 6.4. Spatial distribution of axial E_y and radial E_x electric field strengths for $f = 30$ kHz, $\varepsilon_r = 7.5$, $V_o = 0$, 1.0×10^4 and 2.0×10^4 cm s^{-1} and $V_{appl} = 1.5$ kV with 20 ppm N_2 impurities.

The distribution of the axial (E_y) and radial (E_x) electric field strengths are calculated by using the gradient of electric potential along the horizontal and vertical directions as described by equation (2.19). The first row of figure 6.4 (a, b) represents the distribution of axial and radial electric field strength in the stagnant bulk gas. The structure of axial electric field shows that there is a sudden fall of electric field from higher to lower values near the cathode surface. The higher electric field shows that the glow

discharge activity is dominated near the cathode dielectric barrier as shown in the first row of figure 6.4 (a). The electric field is decreased by the influence of bulk gas flow and the numerical value reduces from $\sim -1.1 \times 10^4$ V cm^{-1} to -0.7×10^4 V cm^{-1} in case of bulk gas flow speed $V_o = 2.0 \times 10^4$ cm s^{-1}. The magnitude of electric field is stronger in the axial (E_y) direction as compared to the radial (E_x) electric field as shown in the three rows of figure 6.4 (a, b) and the contour structure shows that the maximum rate of change in the radial electric field is found near the edges of cathode surface in the reactor gap. The newly developed structures after bulk gas flow are shown in the second and third rows of figure 6.4 (a, b).

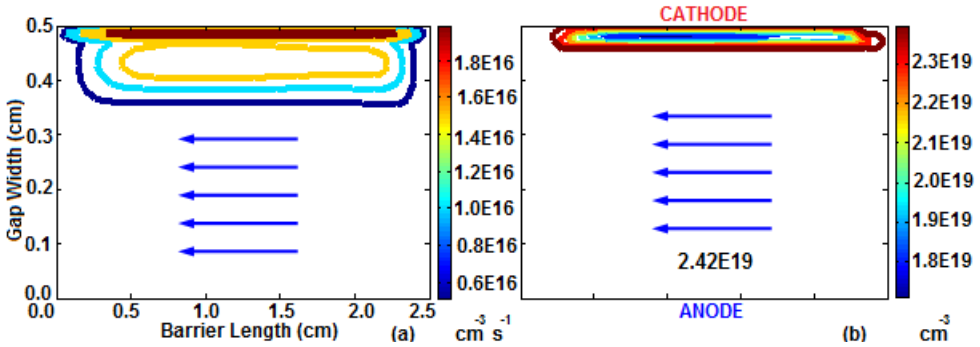

Figure 6.5. Spatial distribution of (a) ionization rate and (b) neutral gas density for $f = 30$ kHz, $\varepsilon_r = 7.5$, $V_o = 2.0 \times 10^4$ cm s^{-1} and $V_{appl} = 1.5$ kV with 20 ppm N_2 impurities.

In addition to the above discussion, the characteristics of atmospheric pressure discharge depend on the production and destruction rates of discharge participating species during the complete cycle. The spatial distribution of ionization rate and neutral helium gas species density are explored during the peak glow discharge activity in the presence of bulk gas flow speed $V_o = 2.0 \times 10^4$ cm s^{-1}. The He-N_2 gas is ionized by the electron impact chemical reactions for the creation of electrons and positive ions in the uniform glow and filamentary discharge modes. The ionization process has substantial influence on the properties of atmospheric pressure discharge and responds effectively in the presence of bulk gas flow. The numerical value of ionization rate decreases from $\sim 1.0 \times 10^{17}$ to 2.4×10^{16} cm^{-3} s^{-1} and drags along the cathode barrier surface, when the speed of bulk gas flow varies from 0 to 2.0×10^4 cm s^{-1}. The same trend of radial expansion and axial spread of ionization rate is observed in the parallel and perpendicular directions of bulk gas flow, which exhibits in figure 6.5 (a). The neutral background helium gas density has smaller values near the cathode during the atmospheric pressure glow and filamentary discharge modes, which is in accordance with the constant atmospheric pressure supposition. The change in neutral gas species density is noticeable in the filamentary discharge region near the cathode surface, and the density stands constant in the remaining part of the reactor as shown in figure 6.5 (b). The above observations illustrate that the decrease of discharge species parameters is inversely proportional

to the bulk gas flow speed. This result agrees generally and follows the similar trend as discussed in the previous modelling results in [117].

6.4 Spatial structure of electrons and gas temperature

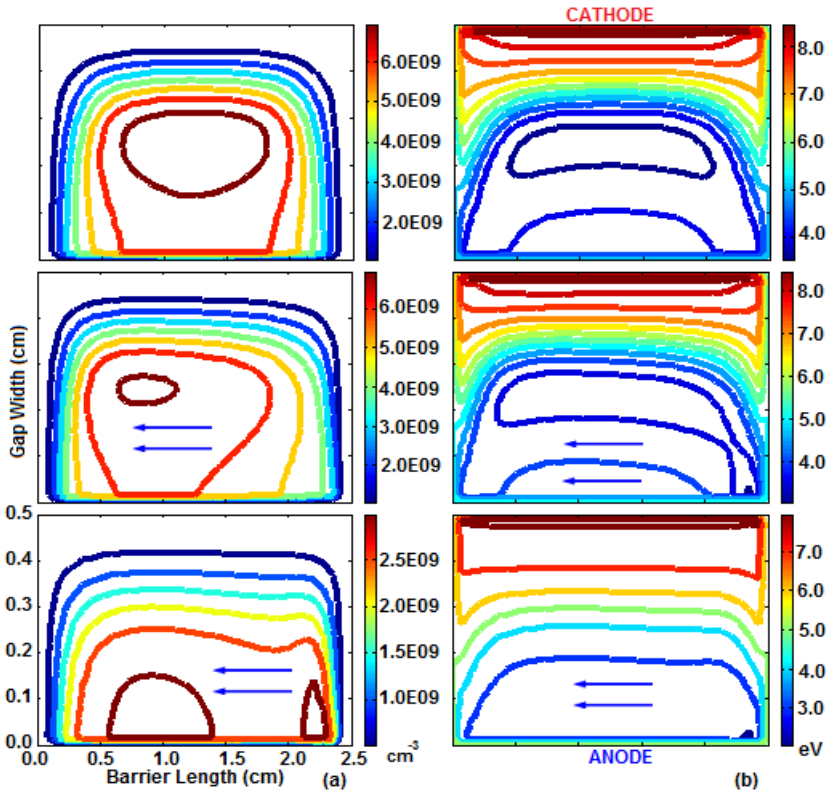

Figure 6.6. Spatial structures of electron density and electron mean energy for $f = 30$ kHz, $\varepsilon_r = 7.5$, $V_o = 0$, 1.0×10^4 and 2.0×10^4 cm s^{-1} and $V_{appl} = 1.5$ kV with 20 ppm N_2 impurities.

In order to physically understand the response of electrons in the stagnant and flowing He-N_2 discharge plasma, the electrons are mainly responsible to describe the distinguishing features and properties of atmospheric pressure glow and filamentary discharge modes. We consider the spatial distributions of electrons density and electron mean energy in the stagnant, lower and moderate subsonic bulk gas flow regimes as shown in the three rows of figure 6.6 (a, b). The structure of electron density is uniform and symmetric along the axial direction in the stagnant bulk gas, which displaces slightly towards the downstream edge in the direction of lower subsonic bulk gas flow. The electron density is dragged along the bulk gas flow to smaller extent at $V_o = 1.0 \times 10^4$ cm s^{-1} but the uniformity exists in atmospheric pressure glow discharge as shown in the second row of figure 6.6 (a). The filamentary structure of electron density is emerged at moderate subsonic bulk gas flow speed $V_o = 2.0 \times 10^4$ cm s^{-1}, which

possesses approximately the half magnitude of electron density than the stagnant bulk gas as shown in the third row of figure 6.6 (a). The distribution of electron density becomes non-uniform in the moderate subsonic bulk gas flow regime and the maximum electron density is shifted near the anode barrier on the downstream direction of the reactor gap, and smaller constriction is located at $x = 2.2$ cm and $y = 0.1$ cm as shown in the third row of figure 6.6 (a). The electron density in the filamentary structure is reduced from $\sim 6.0 \times 10^9$ to 2.5×10^9 cm^{-3}, when the discharge transits from the uniform to filamentary mode. The electron mean energy illustrates the strength of electrons in the gap, which is calculated from the solution of electron energy density balance equation with a number of elastic and inelastic collision energy losses. The electron mean energy in glow discharge plasma has a sudden fall in the stagnant bulk gas than the gradual fall in the moderate subsonic bulk gas flow, which explores the filamentary form of spatial structure as shown in the third row of figure 6.6 (b). As the structural pattern of electron mean energy moves from the uniform to filamentary phase as displayed in the second column of figure 6.6 (b), therefore the peak numerical magnitude of electron mean energy is decreased from 8.0 eV to 7.0 eV approximately. The authors in [33] illustrated that the uniform and filamentary discharge plasma modes are occurred in the presence of variable bulk gas flow in the parallel plate dielectric barrier discharge arrangement. The uniform glow discharge mode with large current density is obtained at the lower bulk gas flow regime, which transforms into filamentary form with smaller current density at higher bulk gas flow speeds. The structures of uniform and filamentary discharge species in this chapter partially follow the similar fashion of experimental observations, which discussed in [33] at variable bulk gas flow speeds. The above information elaborates the brief role of electrons and other discharge species in the atmospheric pressure glow and filamentary discharge modes under different bulk gas flow constraints. It also verifies that the behavior of uniform discharge plasma is central in lower subsonic bulk gas flow and transforms into filamentary mode in the moderate subsonic flow regime as shown in detail in figure 6.6 (a, b).

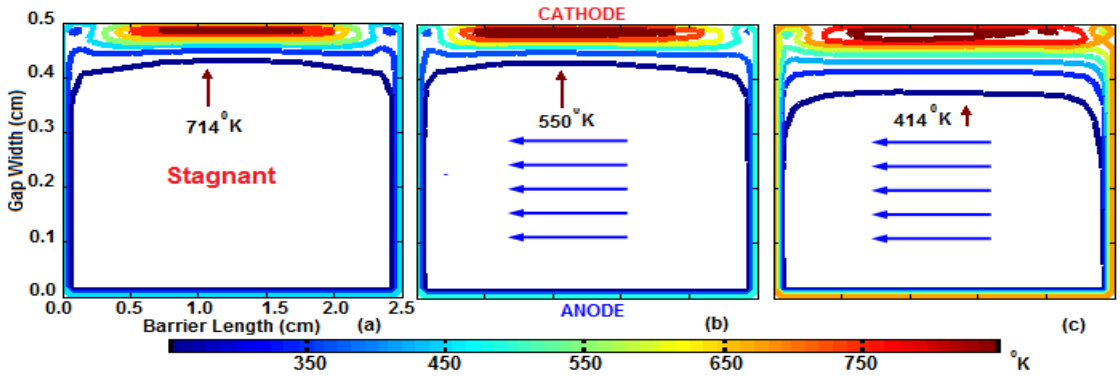

Figure 6.7. Spatial distribution of gas temperature (K) for $f = 30$ kHz, $\varepsilon_r = 7.5$, $V_o = 0$, 1.0×10^4 and 2.0×10^4 cm s^{-1} and $V_{appl} = 1.5$ kV with 20 ppm N_2 impurities.

As the hydrogen and helium are light gases, they normally possess higher thermal conductivity values. The bulk gas temperature in the atmospheric pressure glow and filamentary discharge modes depends on the thermal conductivity and bulk gas flow rate through the reactor. The numerical magnitude of thermal conductivity of helium gas is of $\sim 1.6 \times 10^4$ dynes s^{-1} K^{-1} at room temperature (300 K), which is considered as the higher value as compared to other gases. The spatial distribution of bulk gas temperature is shown for three different cases, such as 0, 1.0×10^4 and 2.0×10^4 cm s^{-1} gas flow speeds. It is apparent from the figure 6.7 (a, b, c) that the gas temperature in the atmospheric pressure glow discharge mode is maximum in the stagnant bulk gas as compared to the filamentary mode at moderate subsonic bulk gas flow regime. The bulk gas temperature approaches to the maximum value of $\sim$ 700 K near the surface of cathode barrier and decreases to the freestream temperature of $\sim$ 300 K away from the glow discharge plasma region in case of smaller subsonic bulk gas flow regime from 1.0×10^2 to 2.5×10^3 cm s^{-1}. The temperature of bulk gas in the glow and filamentary discharge modes is decreased from $\sim$ 700 K to 400 K as shown in figure 6.7 (a, b, c), when the bulk gas flow speed increases from 0 to 2.0×10^4 cm s^{-1}. The physical interpretation of this temperature fall can be expressed by the help of conduction and convection processes in the bulk gas flow. The ionic joule heat, elastic and inelastic energy losses play an important role for the bulk gas heating in the atmospheric pressure glow and filamentary discharge modes. The conduction is dominant process in the helium bulk flow for gas cooling because of higher thermal conductivity and the convection performs a sufficient role with the bulk gas flow. These transport processes are responsible for the cooling of discharge plasma in the reactor. The maximum value of gas temperature in the glow and filamentary discharge plasma modes for three different cases are of $\sim$ 714, 550 and 414 K near the cathode barrier at 0, 1.0×10^4 and 2.0×10^4 cm s^{-1}. This shows that the reduction of bulk gas temperature in the atmospheric pressure glow discharge mode is inversely proportional to the bulk gas flow speed in the subsonic flow regime. This indicates that the numerical solution of gas heat equation is necessary to analyze the exact behavior of bulk gas temperature distributions in the atmospheric pressure discharge modes.

6.5 Distribution of constricted filamentary discharge

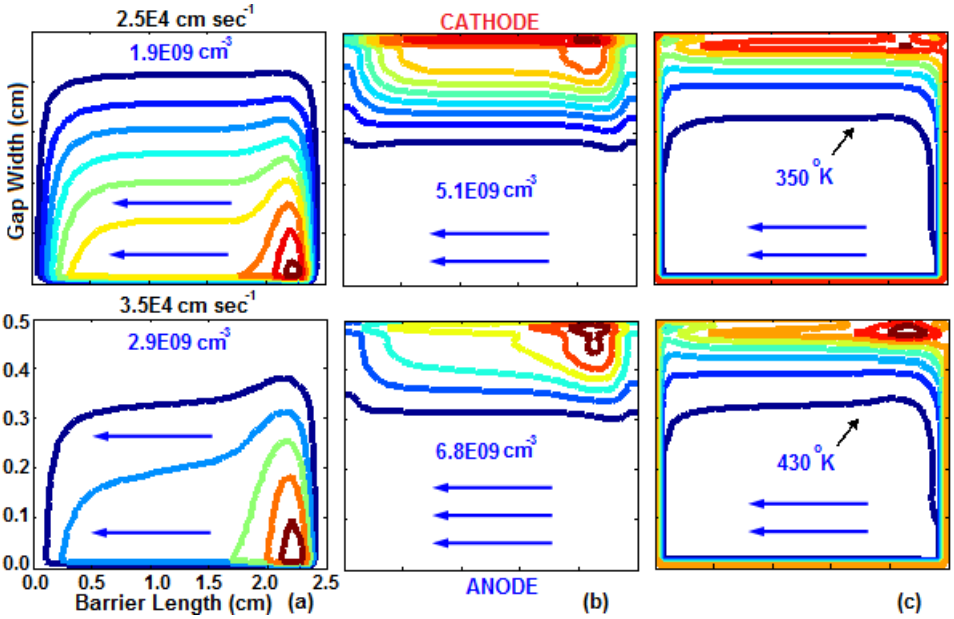

Figure 6.8. Spatial distribution of electrons, He_2^+ ions density and gas temperature for $f = 30$ kHz, $\varepsilon_r = 7.5$, $V_o = 2.5 \times 10^4$ and 3.5×10^4 cm s^{-1} and $V_{appl} = 1.5$ kV with 20 ppm N_2 impurities.

The analysis of dielectric barrier discharge is not completed without considering the consequences of supersonic bulk gas flow in the He-N_2 atmospheric pressure discharges. The transition of spatial structures of discharge parameters are discussed in the variable bulk gas flow regimes as explained in the previous sections. Now, the structures of electrons and He_2^+ ions density are explored at higher subsonic and supersonic bulk gas flow speeds, such as 2.5×10^4 and 3.5×10^4 cm s^{-1}. The four distinct regions of atmospheric pressure glow discharge are observed at the maximum discharge current density from 0 to 1.0×10^4 cm s^{-1}, which correspond to the criteria of uniform glow discharge and described in the number of studies [41, 118] . The spatial distributions of discharge species slightly disturb from 1.0 to 1.0×10^4 cm s^{-1} in the uniform glow discharge mode and a remarkable change is observed after 1.0×10^4 cm s^{-1} bulk gas flow speed in the filamentary discharge mode as shown in the figures 6.2, 6.3 and 6.6. Consequently, the structures of uniform and homogeneous glow discharge plasma are noticed in the lower subsonic bulk gas flow regimes, and transformed into constricted filamentary form in the higher subsonic and supersonic bulk gas flow regimes. The first and second rows of figure 6.8 (a, b) exhibit that the sharp constriction is developed in the start of filamentary discharge distribution, when the glow discharge plasma interacts with the strong flowing of bulk gas. The species density is maximum in the constricted region and reduces to smaller values along the barrier surface in the direction of bulk gas flow. A contraction in the structure of electron density is formed for the constricted filamentary discharge mode at

the location $x = 2.25$ cm and $y = 0.07$ cm in the second row of figure 6.8 (a) because the residence time of flowing gas is very small in the reactor. The chemical reactions are not properly advanced during the passage of higher subsonic and supersonic bulk gas flow in the reactor. The atmospheric pressure filamentary discharge plasma is momentary in the constricted filamentary form near the start of parallel plate reactor and the magnitudes of species density are further decreased than the filamentary discharge phase as shown in first two columns of figure 6.8 (a, b). Therefore, the higher speed of bulk gas flow provides the constricted filamentary and abnormal form of discharge as compared to the lower speed of bulk gas flow at atmospheric pressure. The gas temperature in constricted filamentary discharge mode is reduced to near room temperature ($\sim$ 350 K) at higher subsonic bulk gas flow speed of $\sim 2.5 \times 10^4$ cm s^{-1}, whereas the bulk gas temperature again begin to increase at supersonic bulk gas flow speed, as shown in third column of figure 6.8 (c). The higher value of gas temperature occurs in the constricted part of discharge near the surface of cathode barrier and decreases to the freestream temperature in the remaining part of gap.

This enables us to understand the above mentioned discussion that the high speed bulk gas flow is not suitable for the uniform discharge plasma applications because the filamentary and constricted filamentary behavior of discharge is dominant during these phases. The lower speed of bulk gas flow does not disturb the basic structure of uniformity and it is used for the uniform atmospheric pressure glow discharge plasma applications. So, we can distinguish the three modes of operation for the atmospheric pressure discharges in the presence of bulk gas flow

a) Uniform glow discharge (Stagnant and lower subsonic bulk flow speed, $V_o \leq 1.0 \times 10^4$ cm s^{-1})

b) Filamentary discharge (Moderate subsonic, $1.0 \times 10^4 < V_o \leq 2.0 \times 10^4$ cm s^{-1})

c) Constricted filamentary discharge (Higher subsonic and supersonic, $V_o > 2.0 \times 10^4$ cm s^{-1})

The above uniform, filamentary and constricted filamentary discharge structures provide the precise understanding of these atmospheric pressure discharge modes under the mentioned bulk gas flow regimes.

6.6 Distribution of electronic and ionic flux

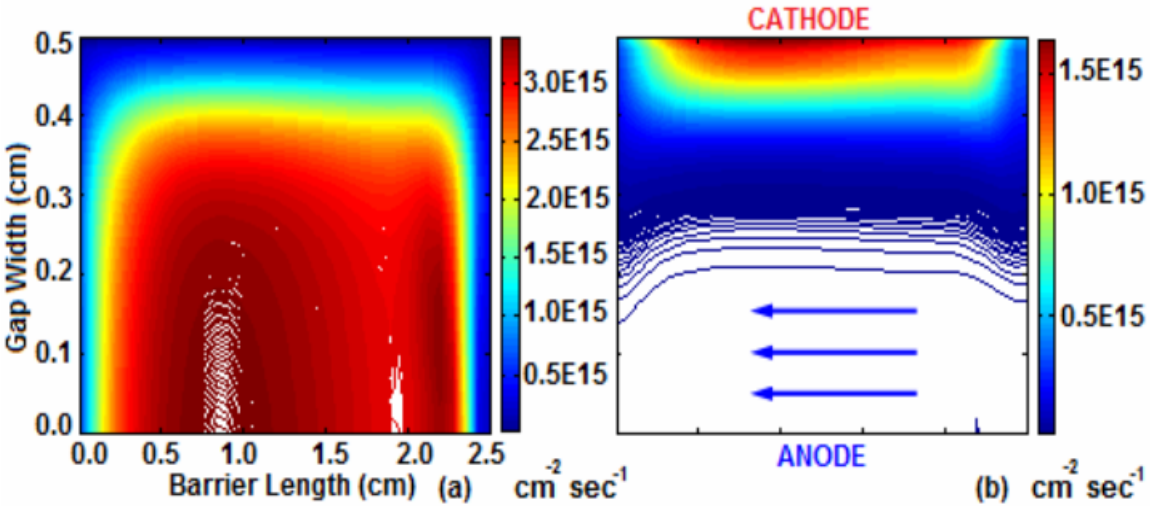

Figure 6.9. Distribution of electronic and He_2^+ ions flux for $f = 30$ kHz, $\varepsilon_r = 7.5$, $V_o = 2.0 \times 10^4$ cm s^{-1} and $V_{appl} = 1.5$ kV with 20 ppm N_2 impurities.

To physically understand the role of conduction and convection processes in the atmospheric pressure discharges, the spatial structures of electronic and ionic fluxes are analyzed in the moderate subsonic bulk gas flow regime. The electronic flux ionizes the gas atoms and molecules in the gap, as a result, the electrons and ions move towards the anode and cathode barriers respectively. The flux of He_2^+ ions is maximum near the cathode barrier as compared to other ionic species and very small in the whole reactor gap, whereas the flux of electrons is higher near the anode barrier as well as near the cathode fall region due to the shielding of cathode barrier with the ionic species. The evolution of electronic and ionic fluxes are displayed at the particular instant, when the discharge current density possesses a maximum value during the half cycle. The spatial distribution of axial electric field in figure 6.4 (a) shows that the higher strength of electric field is reduced drastically to smaller values away the surface of cathode barrier. The electronic and ionic fluxes in figure 6.9 (a, b) exhibit that the input energy is consumed for the development of atmospheric pressure discharge by the electrons, ions as well as other discharge species in the He-N_2 gas. The ion pumping effect becomes very important in the glow discharge plasma, which is created by the electric field across the bulk gas flow containing electrons and ions. The authors [119, 120, 121] discussed and explored in their work that the properties of glow discharge plasma are effected in the presence of bulk gas flow. However, the flux of electrons is present in the whole gap approximately as compared to He_2^+ ionic species flux near the cathode barrier only, so the electronic species carry the portion of input energy and also interact with other discharge species through the multiple production and destruction processes as mentioned in the tables 2.1 and

2.2. However, the electronic flux is also responsible for the source of production of metastables in the positive column. Thus, the distributions of electronic and ionic flux provide the simple concept of species energy consumption during the glow and filamentary discharge modes in the gap.

6.6.1 Structure of uniform electron density in lower subsonic flow

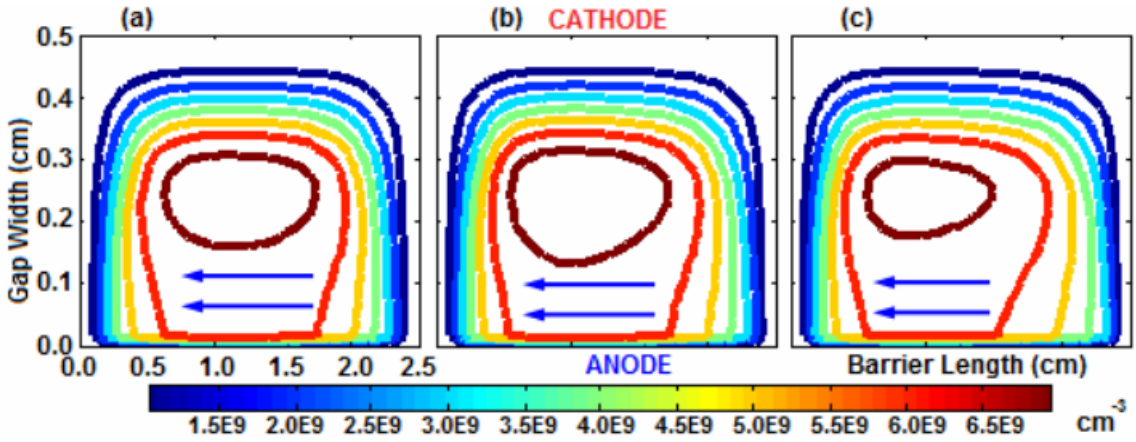

Figure 6.10. Distribution of electrons density for $f = 30$ kHz, $\varepsilon_r = 7.5$, $V_o = 2.5 \times 10^3$, 5.0×10^3 and 7.5×10^3 cm s^{-1} and $V_{appl} = 1.5$ kV with 20 ppm N_2 impurities.

As we have described the characteristics of spatial distribution of discharge species at different speeds of bulk gas flow, such as 1.0×10^4, 2.0×10^4, 2.5×10^4 and 3.5×10^4 cm s^{-1} in the previous part of this chapter. Here, the spatial distributions of electron density are displayed in the lower subsonic bulk gas flow regime to verify the uniformity of atmospheric pressure glow discharge at very small bulk gas flow speeds. The figure 6.10 (a, b, c) provides the clear picture of uniform structure of electron density in the mentioned bulk gas flow regime at 2.5×10^3, 5.0×10^3 and 7.5×10^3 cm s^{-1}. There is slight movement of electron density in the direction of bulk gas flow and the magnitudes of electron density do not influence strongly. This helps us to explain that the smaller bulk gas flow speed is useful and beneficent for the uniform atmospheric pressure glow discharge applications.

6.7 Properties of electrostatic body forcing in gas flow

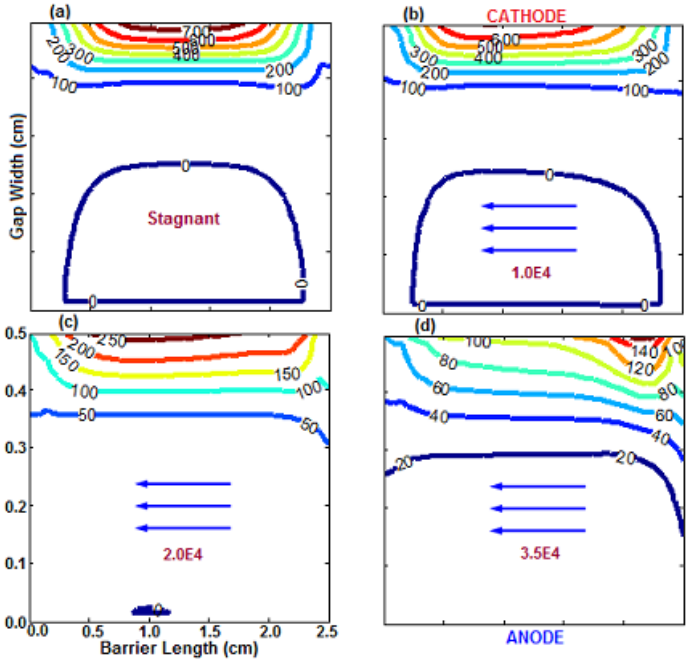

Figure 6.11. Distribution of electrostatic body force magnitude for $f = 30$ kHz, $\varepsilon_r = 7.5$, $V_o = 0$, 1.0×10^4, 2.0×10^4 and 3.5×10^4 cm s^{-1} and $V_{appl} = 1.5$ kV with 20 ppm N_2 impurities.

The electrostatic body force field is evaluated due to the combined effect of electrons density, positive ionic species density and electric field. The mathematical form of electrostatic body force can be written as

$$\mathbf{F}_{ESB} = \sum_{p} q_p Z_p n_p \mathbf{E} \tag{6.1}$$

where p corresponds to the index of ionic species and electrons, here $q_p Z_p n_p$ is the space charge density for the particular discharge species, $\mathbf{E}$ corresponds to the electric field. The smooth, scattered and random effects of electrostatic body force field are observed in the uniform, filamentary and constricted filamentary discharge modes as shown in figure 6.11 (a, b, c, d), which displays the magnitude of $\mathbf{F}_{ESB}$ at different positions in the gap.

As we change the flow speed from the subsonic to supersonic range, the combined effects due to electrostatic body force vary with the discharge characteristics accordingly. The electric field and ionic space charge density are substantial near the cathode barrier region of atmospheric pressure glow and filamentary discharge modes as shown in the figures 6.2 and 6.4. This means that the electrostatic body forcing of the bulk gas flow is confined in the uniform and filamentary discharge regions near the surface of cathode barrier. The numerical magnitude of electrostatic body force is displayed at different points in the reactor gap by the numbers and the maximum values are found near the cathode barriers. The

magnitude of electrostatic body force increases towards the cathode barrier in the stagnant and lower subsonic bulk gas flow regimes than the higher subsonic and supersonic bulk flow as shown in figure 6.11 (a, b, c, d). The small dilatational effects are produced in case of $V_o = 2.0 \times 10^4$ cm s^{-1} and become more intense in case of supersonic bulk gas flow speed $V_o = 3.5 \times 10^4$ cm s^{-1}. The above spatial distributions verify that the speed of lower bulk gas flow produces the uniform and smooth influence of electrostatic body forcing, and the higher bulk gas flow speed destroys the uniform structures as shown in figure 6.11 (c, d).

The uniform and small random effects are distinguished with the strength of electrostatic body forcing near the cathode barrier as exhibited in figure 6.11 (a, b, c). On the contrary, the electrostatic body force is diluted to smaller values and spreads in the larger area of the reactor gap as shown in figure 6.11 (c, d). The numerical magnitude of electrostatic body force decreases from 700 to 140 dynes cm^{-3}, whereas the atmospheric pressure glow discharge shifts from the uniform to constricted filamentary mode as displayed in figure 6.11 (a, b, c, d). The resultant force of atmospheric pressure glow and filamentary discharge is obtained by the average of all force field points of cartesian grid between the parallel plate dielectric barriers. These observations lead to a result that the role of electrostatic body forcing is different in variable bulk gas flow regimes.

6.8 Temporal evolution of discharge current density

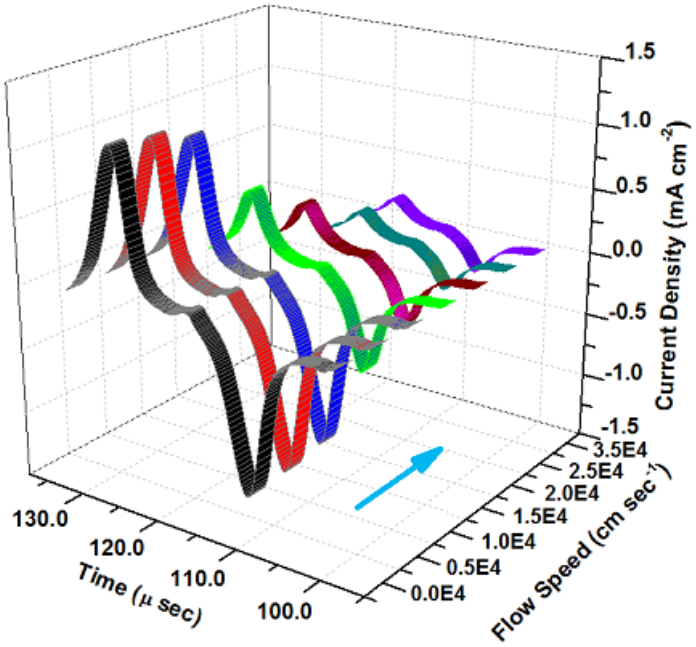

Figure 6.12. Temporal evolution of discharge current density for $f = 30$ kHz, $\varepsilon_r = 7.5$, $V_o = 0$ to 3.5×10^4 cm s^{-1} and $V_{appl} = 1.5$ kV with 20 ppm N_2 impurities.

The temporal evolution of atmospheric pressure discharge current density exhibits that the different modes of discharge are conceived at variable imposed bulk gas flow speeds as shown in figure 6.12. It is clear from the figure 6.12 that the discharge current density slightly decreases from 0 to 1.0×10^4 cm s^{-1} imposed bulk gas flow speed. In this range, the discharge is present in the uniform glow mode at lower subsonic bulk flow regime and exists in favorable form for the uniform discharge plasma applications. The discharge current density falls instantly to smaller values when the gas flow speed increases after 1.0×10^4 cm s^{-1}. The sharp falling trend of discharge current density appears at 1.5×10^4 cm s^{-1} and forwards to supersonic bulk gas flow regime continuously. The conversion of discharge current density from the higher to lower values support the argument that the uniform glow discharge plasma is shifted into filamentary form and the uniformity is completely destroyed at the higher imposed speed of bulk gas flow. So, the homogeneous uniform glow discharge plasma is obtained at lower imposed speed of bulk gas flow from 0 to 1.0×10^4 cm s^{-1} and the filamentary discharge structure develops from 1.0×10^4 to 2.0×10^4 cm s^{-1} in the moderate subsonic bulk gas flow regime. Finally, the constricted filamentary discharge mode is evolved after 2.0×10^4 cm s^{-1} bulk flow speed in the higher subsonic and supersonic bulk flow regimes as shown in figure 6.12. Consequently, the temporal evolution of discharge current density in different bulk gas flow regimes correspond to the uniform, filamentary and constricted filamentary discharge modes.

6.9 Conclusions and summary

We have discussed the spatio-temporal characteristics of uniform and filamentary dielectric barrier discharges in the stagnant and variable bulk gas flow regimes. The distribution of different discharge species parameters are distinguished due to the influence of bulk gas flow, which provides the uniform and filamentary behavior under various circumstances. The spatial structures of discharge species show that the uniform, homogeneous and symmetric pattern along the axial direction are formed in the stagnant bulk gas. The profile of gas temperature is described by the numerical solution of gas temperature equation at atmospheric pressure and the bulk gas temperature is measured during the glow discharge mode, which shows the higher value in the discharge plasma near the surface of cathode barrier than the room temperature, i.e., 300 K. It means that the discharge species parameters are overestimated in the stagnant bulk gas than flowing He-N_2 gas. In second phase, the lower speed of bulk gas flow is introduced in the reactor, which modifies the spatial distribution of discharge species in the lower and moderate subsonic bulk gas flow regimes. The distributions of discharge species change into uniform, slightly disturbed and non-symmetric form along the axial direction from 1.0 to 1.0×10^4 cm s^{-1} bulk gas flow speed, and convert further into filamentary structures of discharge species in the moderate subsonic

bulk gas flow regime, i.e., $1.0 \times 10^4 < V_o \leq 2.0 \times 10^4$ cm s^{-1}. The temperature of gas is a function of bulk gas flow speed and decreases with the increase in bulk gas flow speed in the subsonic bulk flow regime. The numerical magnitudes of discharge species density are reduced sharply and the bulk gas temperature is approached to near room temperature in the higher subsonic bulk gas flow regime. The uniform and filamentary structures of electrons and He_2^+ ions density are discussed in the stagnant, lower and moderate subsonic bulk gas flow regimes, which provides the precise intuition of discharge species in different modes of atmospheric pressure discharge. Finally, the discharge species respond entirely different in the higher subsonic and supersonic bulk gas flow regimes, and the constricted filamentary discharge mode dominates in this phase. The filamentary distribution of atmospheric pressure discharge parameters are completely transformed into constricted filamentary form in the mentioned bulk gas flow regimes. The temperature of bulk gas again lifts up from the room temperature in supersonic gas flow regime and the modified structures are described in this domain. The comparison of spatial distributions of electrostatic body force elucidate the satisfactory information and perception in the stagnant and various bulk gas flow regimes, which are helpful for the understanding of discharge characteristics in the uniform and filamentary discharge modes. The temporal evolution of discharge current density demonstrates that the distinct pattern is noticed in the stagnant, subsonic and supersonic bulk gas flow regimes. Therefore, the current numerical simulation results articulate the atmospheric pressure discharge features in different bulk gas flow regimes, which boosts our insight for the uniform and filamentary atmospheric pressure discharge modes.

Chapter 7

Characteristics of APD using three-dimensional fluid model

7.1 Introduction

This chapter elaborates the real time distribution of atmospheric pressure discharge parameters in three-dimensional volume space at variable driving frequencies and external applied voltages. The spatio-temporal characteristics of atmospheric pressure discharge species are illustrated for the uniform and filamentary discharge modes in different frequency regimes. The attributes of atmospheric pressure discharge are described in the uniform glow and filamentary discharge modes with the spatial volumetric distribution under different operating conditions. We have examined and discussed the origin of non-uniformities in the stagnant and flowing discharge plasma with the help of two-dimensional numerical fluid model in chapters 5 and 6. Although, the distribution of discharge species can be explained in the uniform atmospheric pressure discharge by two-dimensional fluid model effectively but the non-uniform or filamentary discharge has very dynamic behavior especially during the complete breakdown pulse, i.e., start of avalanche and formation of cathode fall layer. Therefore, the three-dimensional distribution of discharge species is essential to represent the spatial volumetric structures of filamentary discharge plasma. As we observed in chapter 4, the chaotic behavior is prominently dominant in the lower frequency regime ($\lesssim$ 7 kHz). It is noticed that the emergence of filaments during the breakdown pulse is remarkable in this frequency limit ($\leq$ 20 kHz) as compared to the higher frequencies. The mechanism of mode transformation from the uniform to filamentary discharge and vice versa is very complex and dynamic, while different justifications are available in the literature for their physical understanding of transition mechanism in the atmospheric pressure discharges [81, 122, 123]. The creation, measurement

and stable structure of filaments are described in number of studies [124, 125, 126, 127] by employing the various techniques under different categories of discharges. The volume distribution of electrons in the filamentary discharge are compared from 5 to 20 kHz, which demonstrate the association between the configuration and size of filaments in the presence of imposed conditions. The spatial evolution of filamentary discharge species is explicated at 10 kHz for a quarter of cycle in which the different prominent phases, such as prebreakdown, breakdown, filamentary cathode fall layer and decay phases are specified with the volumetric concentration of electrons and He_2^+ ions density. The occurrence of localized higher density gradients are precisely observed at different places in the reactor gap. The spatial volumetric structures illuminate the pattern and shape of filaments by depicting their sequence of emergence, growth and decay steps in the reactor gap. However, it is possible to explore the structure of distinct filaments sharply at lower frequencies because the filaments coalesce to form a uniform or partially uniform distribution of discharge in the higher frequency regime ($>$ 20 kHz). The temporal evolution of discharge current density exhibits that it increases with the increase in frequency from 20 to 50 kHz under similar input conditions, start decreasing from 50 to 70 kHz and becomes approximately smooth and stable at further higher frequencies (70 - 100 kHz).

7.2 Spatial evolution of discharge species parameters

To validate the three-dimensional fluid model simulations, the distributions of discharge species are analyzed for the uniform atmospheric pressure glow discharge in helium gas with 20 ppm nitrogen impurities. Although, the evolution of breakdown process has been explained in chapter 5, which discussed the formation of uniform glow and filamentary atmospheric pressure discharges with two-dimensional fluid model. In order to provide more details of discharge species distributions for the uniform atmospheric pressure discharge, the combination of slice distributions of discharge species give the spatial change of densities at different locations in x, y and z directions respectively. As the advancement of discharge plasma involves the number of phases, which will be discussed briefly to perceive the knowledge of numerical simulations of atmospheric pressure discharge in the uniform and filamentary discharge modes. Initially, the discharge is created from the presence of seed electrons and ions in the reactor gap, which move towards their respective anode and cathode dielectric barriers. During this process, the Townsend first ionization coefficient provides the electron multiplication in the Townsend ionization phase. After a certain level of electron density achievement, a breakdown starts up and a sharp change is observed in the electric field, which enhances an ionization rate in the gap. When the avalanche approaches near the cathodic barrier, a complete cathode fall layer is formed with three more distinct regions in the reactor gap. Finally, the cathode fall region collapes and the decay phase is started in atmospheric pressure

glow discharge. This process performs normally in the uniform atmospheric pressure glow discharge.

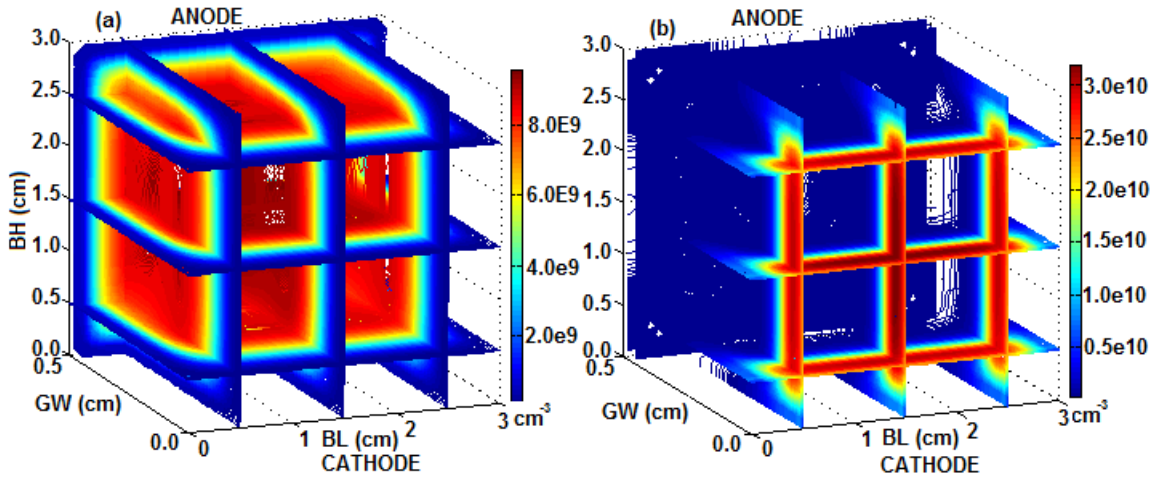

Figure 7.1. Spatial slice distributions of electrons and He_2^+ ions density for $f = 30$ kHz, $\varepsilon_r = 7.5$ and $V_{appl} = 1.5$ kV with 20 ppm N_2 impurities.

The discharge species parameters are represented with the combination of different slice distributions in the uniform glow discharge mode, which exhibit the uniform changes of species density in the specific spatial directions at different places in the parallel plate reactor as exhibited in figure 7.1 (a, b). The characteristics of electrons and He_2^+ ions density are similar which discussed in the previous chapters for the cathode fall region in the uniform atmospheric pressure glow discharge. When the cathode fall region is completely developed with the four distingusihed regions, the figure 7.1 (a, b) provides the three-dimensional spatial slice distributions of electrons and He_2^+ ions density. Correspondingly, the major difference is the change of electron density in z direction as well as in x and y directions. The magnitude of electrons and He_2^+ ions density are nearly same in the fourth region which forms a quasineutral plasma in the positive column with a strong electric field bulge in the cathode fall layer. The different slice structures of electron density are perfectly matched in x, y and z directions at variable places in the reactor gap which illustrate the uniformity in three-dimensions as shown in figure 7.1 (a). The magnitude of He_2^+ ions density is higher in the cathode fall region as compared to other ionic species, which shows the clear uniformity in x, y and z directions. The numerical magnitude of He_2^+ ions density is $\sim 3.0 \times 10^{10}$ cm^{-3} in the cathode fall layer, whereas the electrons density has the value of $\sim 8.0 \times 10^{9}$ cm^{-3} in the negative glow region. The criterion for the uniform distribution of atmospheric pressure glow discharge is satisfied for the electrons and He_2^+ ionic species as shown in figure 7.1 (a, b) in helium gas with 20 ppm nitrogen impurities at 30 kHz. The magnitude of electrons and He_2^+ ions density are approximately matched with two-dimensional fluid model simulations, which reveal the consistency between the two and three-dimensional fluid model results.

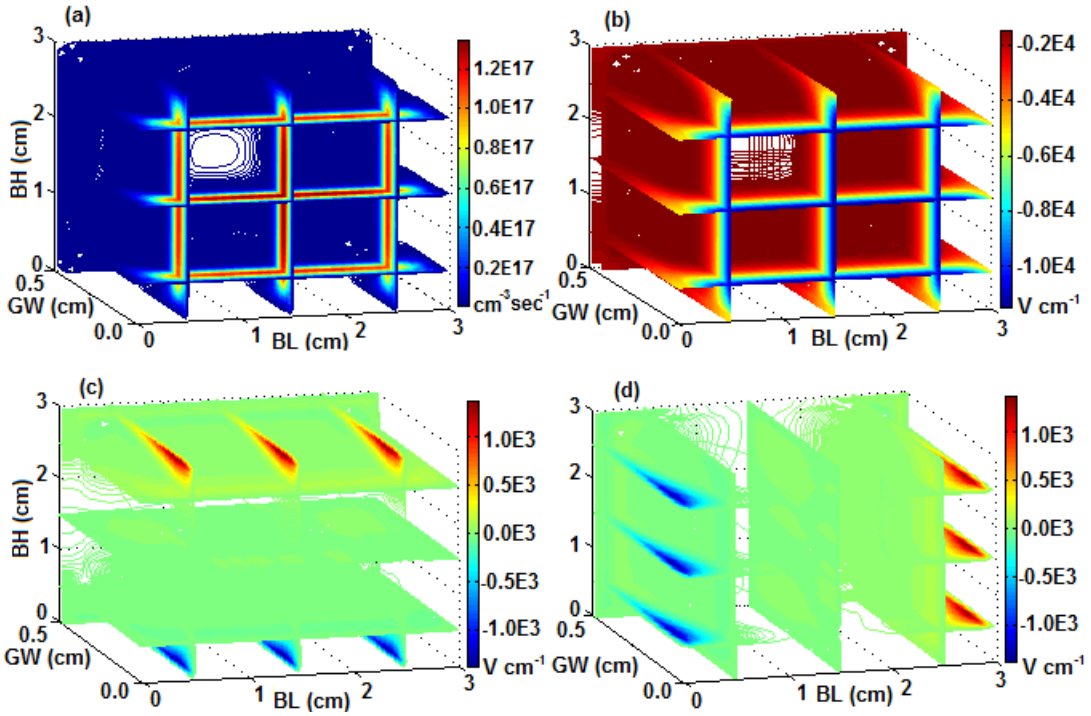

Figure 7.2. Spatial slice distribution of ionization rate and electric field (E_y, E_x, E_z) for $f = 30$ kHz, $\varepsilon_r = 7.5$ and $V_{appl} = 1.5$ kV with 20 ppm N_2 impurities.

In order to illuminate the further details of uniform atmospheric pressure discharge parameters, the different slice distributions of ionization rate and the electric field (E_y, E_x, E_z) in three spatial directions are examined in figure 7.2 (a - d). The ionization rate gives the production of electrons and ions from different chemical processes in the reactor gap. The magnitude of ionization rate provides the net ionization in the discharge plasma, which is sum of the multiple chemical processes (in tables 2.1 and 2.2) during the evolution of uniform atmospheric pressure glow discharge. The major sources of production of electrons are the direct ionization and Penning ionization of metastables and excimers. The three-dimensional structure of ionization rate exhibits that the different slice distributions are perfectly uniform in x, y and z directions in the positive column as shown in figure 7.2 (a) and the strong bulge appears near the cathode barrier with the numerical magnitude $\sim 1.0 \times 10^{17}$ cm^{-3} s^{-1} at the maximum discharge current density. Correspondingly, the stronger axial electric field (E_y) forces the electrons and ions to move along the direction of applied potential, which can be verified with the uniform distribution of axial electric field as shown in figure 7.2 (b) and the numerical magnitude in this case is $\sim -1.0 \times 10^4$ V cm^{-1}. The electric fields in the x and z directions are weaker than the axial direction (y), which bound the discharge plasma in the reactor gap as shown in figure 7.2 (c, d) and their magnitudes are approximately $\sim \pm 1.0 \times 10^3$ V cm^{-1}. The different slice distributions of ionization rate and electric field (E_y, E_x, E_z) in x, y and z directions enhance their spatial evolution in the uniform atmospheric

pressure glow discharge plasma.

7.3 Evolution of volume distribution of electrons and He_2^+ ions density

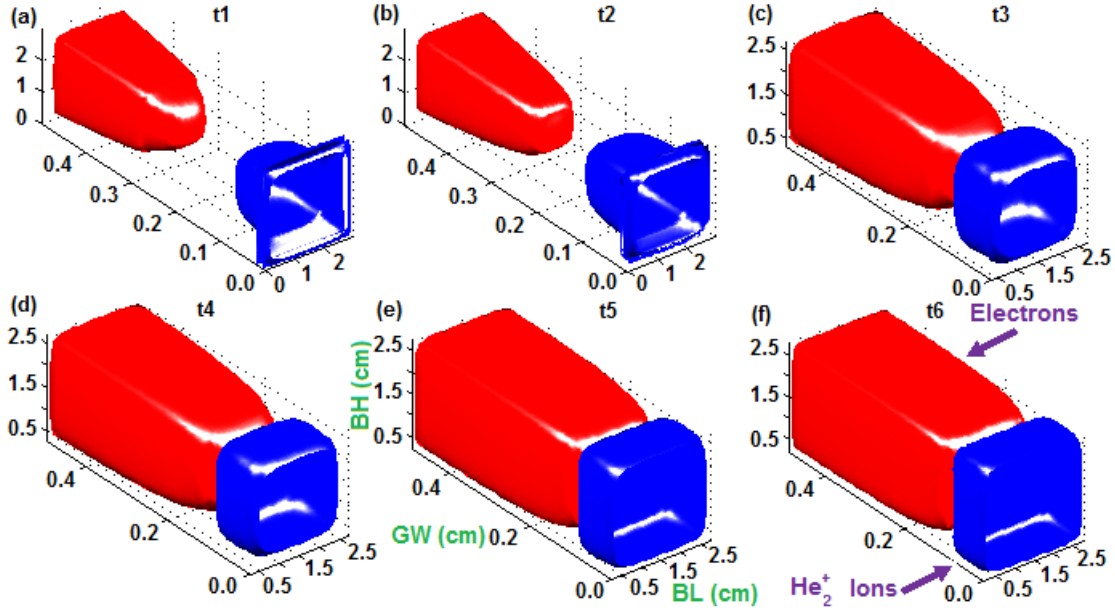

Figure 7.3. Phases of spatial volume distributions of electrons (red) and He_2^+ ions (blue) density for $f = 30$ kHz, $\varepsilon_r = 7.5$ and $V_{appl} = 1.5$ kV with 20 ppm N_2 impurities.

As the space and time variation of electrons and He_2^+ ions density are necessary to understand their evolvement during the different phases of uniform atmospheric pressure glow discharge. We describe the evolution of uniform volume distribution of electrons and He_2^+ ions density from the time duration t1 to t6 in the three-dimensional space for 30 kHz driving frequency as shown in figure 7.3 (a - f). The cathode and anode dielectric barriers change their polarities with the external applied voltage, which are not shown in figure 7.3. The BL, GW and BH labels correspond to the barrier length, gap width and barrier height of the parallel plate reactor configuration. The figure 7.3 (a - f) represents the stationary spatial structures of discharge species which covers the prebreakdown, breakdown and progression of cathode fall region with the maximum discharge current density. There is an interval of approximately 1 μs between the consecutive time instants in the range from t1 to t3. The volumetric distribution of electrons and He_2^+ ions density are examined in the prebreakdown phase as displayed in figure 7.3 (a - c). In the last structure of prebreakdown, the electrons and He_2^+ ions density acquire the numerical magnitudes of $\sim 5.0 \times 10^9$ and 1.0×10^{10} cm^{-3}. The figure 7.3 (d) exhibits the species density in the start of breakdown phase, whereas the electrons and ions proceed towards their respective anode and

cathode barriers. The electrons and He_2^+ ions density are increased to further higher values in the start of breakdown pulse and reached to the values $\sim 6.0 \times 10^9$ and 1.6×10^{10} cm^{-3}. The movement of electrons show that the ionization flit travels fastly towards the cathode barrier and the volumetric density of electrons and He_2^+ ions increase to $\sim 8.0 \times 10^9$ and 2.6×10^{10} cm^{-3} as shown in figure 7.3 (e). It is clear from the figure 7.3 (f) that the electrons exist near the cathode fall region as well as in the whole gap. The volumetric structures of electrons and He_2^+ ions density provide a precise picture of electronic and ionic species at the maximum discharge current density as shown in figure 7.3 (f). However, the volume distribution of electrons and He_2^+ ions density show that the electrons occupy a large space in the reactor gap and He_2^+ ions squeeze near the cathode barrier surface. The time span between t3 and t6 is approximately ~ 2.1 μs. The volumetric structure in figure 7.3 (f) corresponds to the uniform distribution of atmospheric pressure discharge with four remarkable regions in the gap. The change in He_2^+ ions density is larger than electrons and it varies from $\sim 4.0 \times 10^9$ to 3.0×10^{10} cm^{-3}, whereas the electrons density changes from $\sim 3.0 \times 10^9$ to 8.0×10^9 cm^{-3} during the time interval from t1 to t6. The volumetric structure of electrons and He_2^+ ions density prominently illustrate the evolvement of prebreakdown, breakdown and cathode fall region formation from t1 to t6. Thus an overall movement of electrons and He_2^+ ions density can be observed sharply from the above six distributions, which develop a smooth picture of the evolution of electrons and He_2^+ ions density.

7.4 Comparison of discharge species

This section highlights the difference between the spatial distributions of species in the uniform atmospheric pressure discharges at variable driving frequencies. Although the fundamental operation of gas breakdown is similar in different frequency regimes but the spatial volume distribution of discharge species are effected with the operating input parameters. The distribution of discharge species are compared by using the spatial distribution of different slices at the maximum discharge current density. In addition to the above uniform distribution of discharge species, the spatial profile of electrons, neutrals, i.e., He^* and He_2^* and ionic species, i.e., He^+ and N_2^+ are compared from 30 to 90 kHz frequencies.

7.4.1 Slice distribution of electrons density

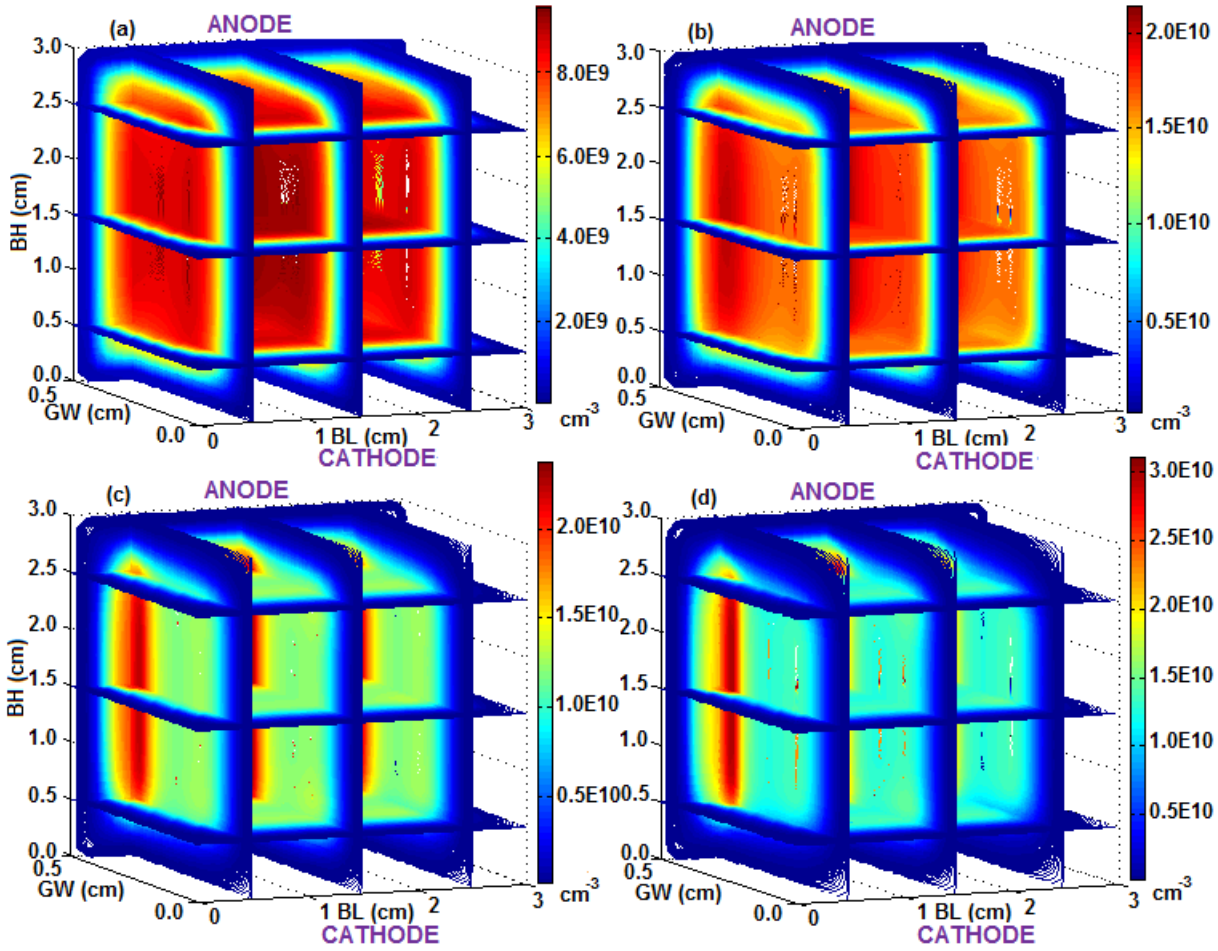

Figure 7.4. Spatial slice distributions of electrons density for f = 30, 50, 70 and 90 kHz, $\varepsilon_r = 7.5$ and $V_{appl} = 1.5$ kV with 20 ppm N_2 impurities.

As the behavior of electrons is effected sharply in different frequency regimes, we compare the various slice distributions of electrons at 30 to 90 kHz under the similar operating conditions. The spatial slice distribution of electrons shows that it is uniform in three spatial directions from the anode barrier towards the cathode barrier for 30 kHz as shown in figure 7.4 (a), whereas the electron density is higher near the anode barrier as compared to the near cathode fall layer at 50 - 90 kHz as exhibited in figure 7.4 (b). The density of electrons is uniform along x, y and z directions at 30 kHz as compared to 50 - 90 kHz, which shows the strong gradient in the electron density near the anode barrier as displayed in figure 7.4 (b) in case of 50 kHz. This highlights a distinct observation that the electrons trapped in the positive column do not dissociate entirely during the half cycle, which also enhance the higher residual current density during the polarity reversal of electric field at 50 - 90 kHz. The magnitude of electrons

density is higher for 90 kHz than 30 - 70 kHz, and the numerical values are modified from $\sim 8.0 \times 10^9$ and 3.5×10^{10} cm^{-3} as shown in figure 7.4 (a - d). The basic operation of discharge plasma is same at these frequencies, although they have sharp contrast in their electronic distributions near the anode barrier at the maximum discharge current density as shown in figure 7.4 (b - d). The strong gradients in the slice distributions of electronic species exhibit that the electrons are prominently trapped near the anode barrier at higher frequencies. This confirms that the electrons are influenced quite remarkably and the volumetric confinement of electron density decreases near the anode barrier with the increase of frequencies in the mentioned range as displayed distinctly.

7.4.2 Slice distribution of neutral and ionic species

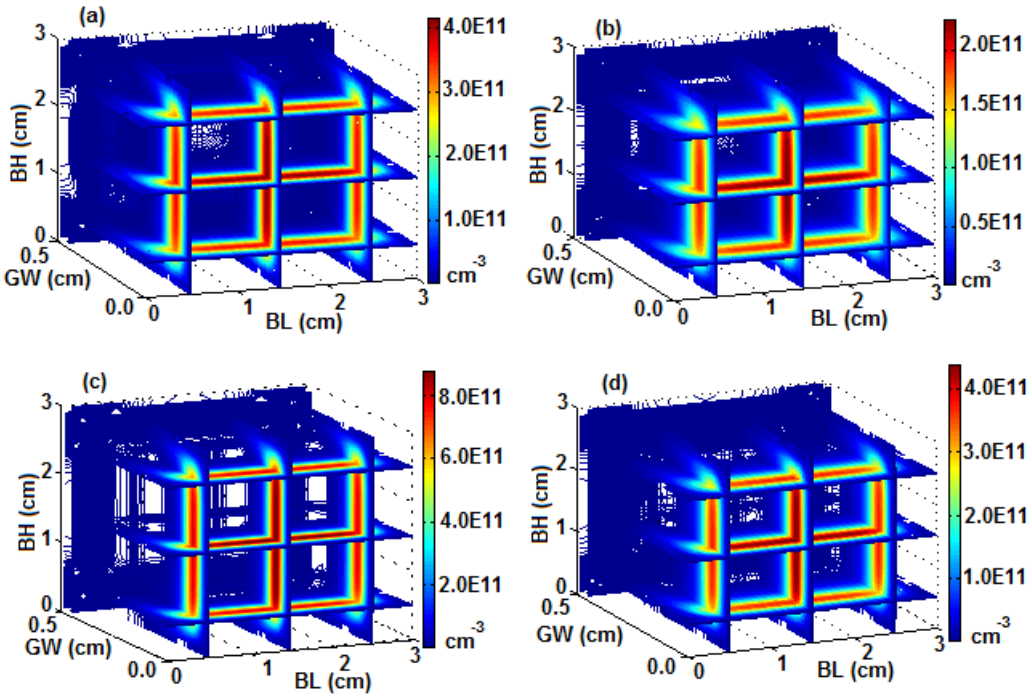

Figure 7.5. Spatial slice distributions of He^* (metastables) and He_2^* (excimers) density for $f = 30$ and 50 kHz, $\varepsilon_r = 7.5$ and $V_{appl} = 1.5$ kV with 20 ppm N_2 impurities.

The metastables are very important for the production of electrons and ions in the atmospheric pressure discharges especially in the presence of nitrogen impurities, which accelerate with the axial electric field in the reactor gap. The metastables can provide a substantial source of ionization with the interaction of different chemical processes (in tables 2.1 and 2.2) and produce further secondary electrons in the gap. The three-dimensional spatial slice structures of metastables (He^*) and excimers (He_2^*) manifest

that their population are dense near the cathode barrier in x, y and z directions as shown in figure 7.5 (a - d) for two different driving frequencies, such as 30 and 50 kHz at the maximum discharge current density. The density of metastables is maximum as compared to other discharge species and actively interacts through multiple chemical reactions in the uniform glow discharge mode, which matches with the one and two-dimensional fluid model results. It is clear from the figure 7.5 (a, b) that the sharp change is occurred in the neutral species density near the cathode barrier but not exactly with the dielectric barrier surface. The metastables and excimers have higher densities at 50 kHz than 30 kHz and, they provide the ions and electrons for the uniform glow discharge plasma. However, the numerical magnitudes of metastables and excimers are $\sim 4.0 \times 10^{11}$ and 2.0×10^{11} cm^{-3} as shown in figure 7.5 (a, b) in case of 30 kHz, whereas they have similar spatial slice distributions at 50 kHz except different numerical magnitudes $\sim 8.0 \times 10^{11}$ and 4.0×10^{11} cm^{-3} as shown in figure 7.5 (c, d).

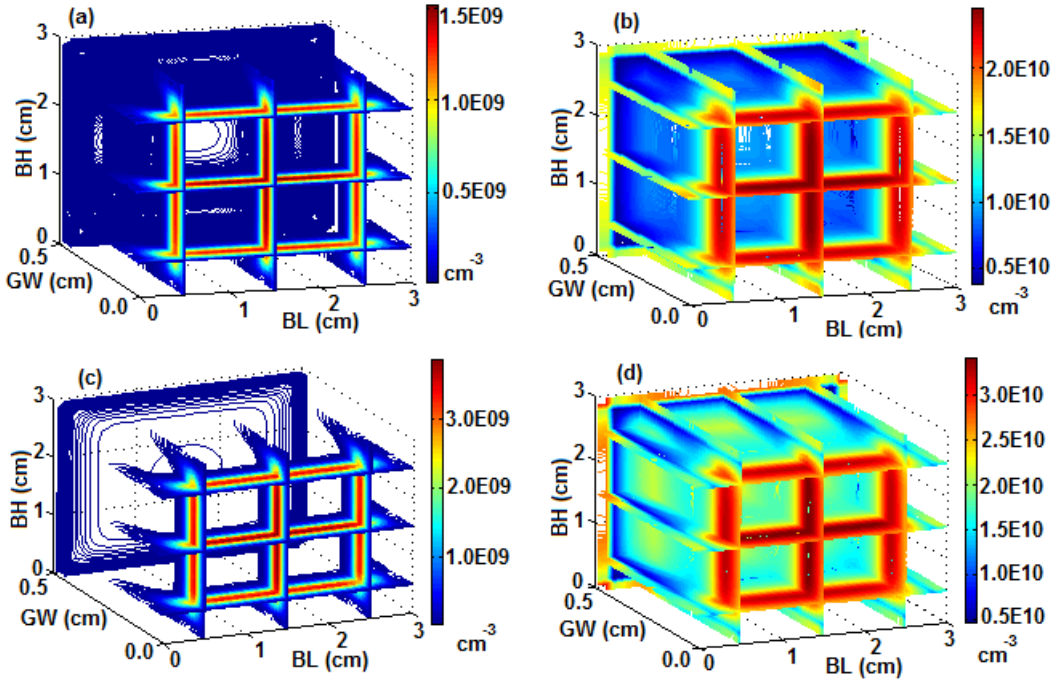

Figure 7.6. Spatial slice distributions of He^+ and N_2^+ ions density for $f = 30$ and 50 kHz, $\varepsilon_r = 7.5$ and $V_{appl} = 1.5$ kV with 20 ppm N_2 impurities.

The behavior of ionic species (He^+ and N_2^+) has been discussed by using one and two-dimensional fluid models in the previous chapters. The spatial evolution of He^+ and N_2^+ ions density are explored for different frequencies, such as 30 and 50 kHz in the uniform atmospheric pressure discharge. The numerical magnitudes of ionic species are maximum near the cathode barrier, whereas the He^+ ions

have the smallest magnitude during the glow discharge phase in the cathode fall layer because of fast conversion into He_2^+ ions. The molecular nitrogen ions density is also higher near the edges as well as near the cathode barrier than other ionic species in the reactor gap. The magnitudes of He^+ and N_2^+ ions density are $\sim 1.5 \times 10^9$ and 2.0×10^{10} cm^{-3} for 30 kHz as shown in figure 7.6 (a, b) as compared to other ionic species. The spatial slice distributions of ionic species (He^+ and N_2^+) show that they are modified and increased in the numerical magnitudes of $\sim 3.0 \times 10^9$ and 3.0×10^{10} cm^{-3} as shown in figure 7.6 (c, d). The stronger electric field in the axial direction forces the ions to move along the direction of applied potential, which can be verified with the uniform distribution of axial electric field as exhibited in figure 7.2 (b). The three-dimensional fluid model provides the more and accurate information for the discharge parameters than one and two-dimensional fluid models because all the spatial dimensions are covered in this case. Therefore, the three-dimensional fluid model simulations are reliable and consistent with the previous modelling results.

7.5 Emergence of filamentary discharge plasma

Suppose an electrical energy is supplied to the gas particles with an external applied voltage in the parallel plate reactor. This energy is used to excite and ionize the atoms and molecules in helium gas with trace amount of nitrogen impurities. The streamers are defined as the ionization waves that can propagate through the small channels with $E_{\text{streamer}} > E_{\text{gas}}$, while E_{streamer} is the electric field in the streamer and E_{gas} is the electric field in the gas. These streamers can be produced by the influence of an overvoltage effect. In case of streamer ionization of gas, the electrons and ions are created at enormous rate due to the overvoltage and number of chemical reactions described in the tables 2.1 and 2.2, which develop a further chain of processes in the gas. When the primary electrons strike with the gas particles and electrode surface, the secondary electrons are formed and ultimately build a strong avalanche after some time. The ionic species in this avalanche form a positive layer at the cathode end of the evolved plasma channel, which attracts the next generation of electrons quite significantly. In this way, the primary avalanche is dragged due to the ionization along the ionic species, which starts from the location where the positive charge and electric field are greatest. Correspondingly, the streamers are protruding from the anode surface because of high conductivity. Due to the high strength of electric field at the head of the streamers, the lines of force are circularly dispersed from their head. The lines of force are capable of attracting the secondary avalanches from all sides, which cause the development and growth of streamers. The mechanism which controls the potential in the streamer is the polarization of the dielectric barriers by the external imposed electric field. Consequently, the electrons are displaced towards the anode barrier, which cause the positive ions near the cathode barrier. The enhanced electric

field of the resulting dipole is opposite to the external imposed electric field, partly cancels the latter and reduces the potential difference along the developed conductor. It is possible to deduce the basic physics of spatial evolution of the atmospheric pressure discharge species by using the one-dimensional fluid model but the internal details and dynamics of discharge plasma species can only be possible with the multi-dimensional fluid model simulations.

Suppose an avalanche growth is very fast, the rate of streamer growth is limited by the neutralization of positive space charge at the cathode side of the streamer not by the rate of avalanche production. During this process, the electrons move into this region at the drift velocity corresponding to the electric field within it. This field strength is higher inside the needle than the external field in the gap. A streamer is created from the avalanche when the space charge electric field equals to the external imposed electric field. For example, $E^{'} \approx E_0$ can be regarded as the criterion of the streamer formation, where $E^{'}$ is the space charge electric field and E_0 is the imposed electric field [4]. To grasp the filamentary behavior of atmospheric pressure discharge, the analysis is performed by the help of imposed conditions, which provides the physical insight about the non-uniformities. In order to achieve this goal, the different sets of input discharge parameters are considered for the uniform and filamentary discharges under these conditions. The configuration and pattern of species distribution establish an overview about their spatial linkage with the filamentary and uniform discharge structures. In this analysis, the filamentary discharge structures are observed due to the imposed conditions, such as i) overvoltage effect ii) increased recombination coefficient of molecular nitrogen ions, in the He-N_2 gas. The above mentioned artificial imposed conditions develop a filamentary discharge, which give an opportunity to explore the effects of these conditions and identify the types of non-uniformities.

7.5.1 Comparison between the filamentary and uniform discharge

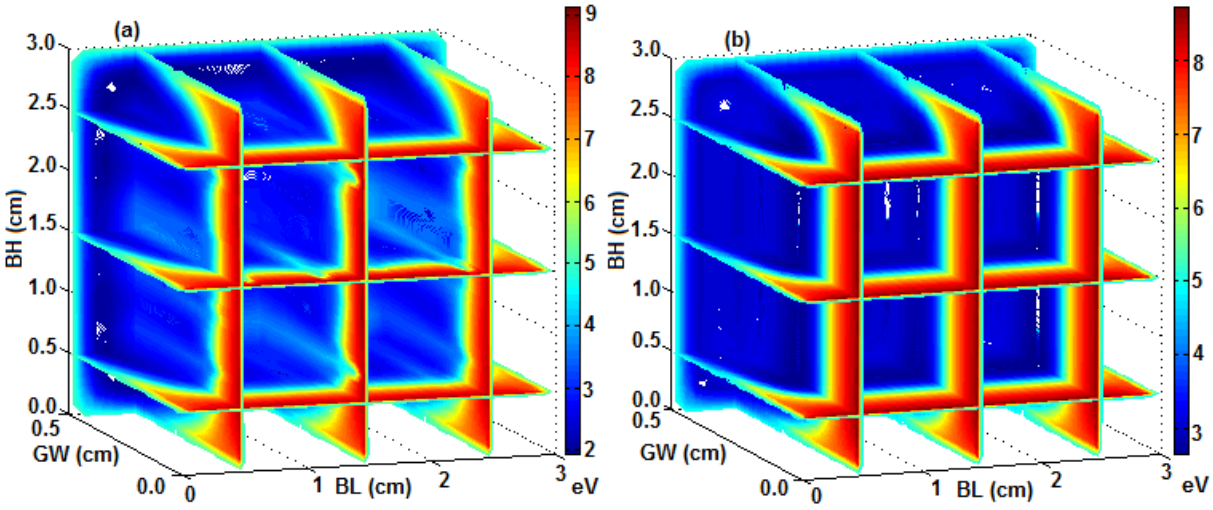

Figure 7.7. Spatial slice distributions of electron mean energy for $f = 15$ kHz, $\varepsilon_r = 7.5$ and $V_{appl} = 1.6$ and 1.5 kV with 50 ppm N_2 impurities.

To understand the change in the electron mean energy for the filamentary and uniform discharges, the spatial distribution of electron mean energy is analyzed for 15 kHz driving frequency with and without imposed conditions. The different slice distributions of electron mean energy exhibit that they are atypical and regular for the filamentary and uniform atmospheric pressure discharges especially in the cathode fall region as shown in figure 7.7 (a, b). The filamentary discharge has a thin bulge at 15 kHz but the large electron mean energy gradients prominently exist due to the presence of non-uniformities in the cathode fall region as well as their effect in the positive column. The filamentary discharge is observed due to the effect of overvoltage as mentioned in the previous subsection. It is evident from the figure 7.7 (a) that the electron mean energy is started to change from the head of filament near the surface of cathode barrier towards the tail near the anode barrier. The numerical value of electron mean energy is varied from ~ 9 to 5 eV in the filaments as shown in figure 7.7 (a). It is apparent from the different slice distributions that the numerical magnitude of electron mean energy is smaller for the uniform discharge as compared to the filamentary discharge plasma. In case of uniform atmospheric pressure discharge, the electron mean energy has a small wide bulge in the cathode fall region relative to the filamentary discharge and the numerical value varies from ~ 8 to 4 eV as exhibited in figure 7.7 (b). The profile of electron mean energy is substantially disturbed and smooth in the positive column of filamentary and uniform atmospheric pressure discharge consecutively as displayed in figure 7.7 (a, b). The spatial distributions of electron mean energy enhance a precise insight about the filamentary and uniform discharge modes. The electron temperature is very important parameter for breaking the

chemical bonds of different samples as discussed in [6]. So the exact evaluation and understanding of this parameter is very helpful for the atmospheric pressure discharge applications.

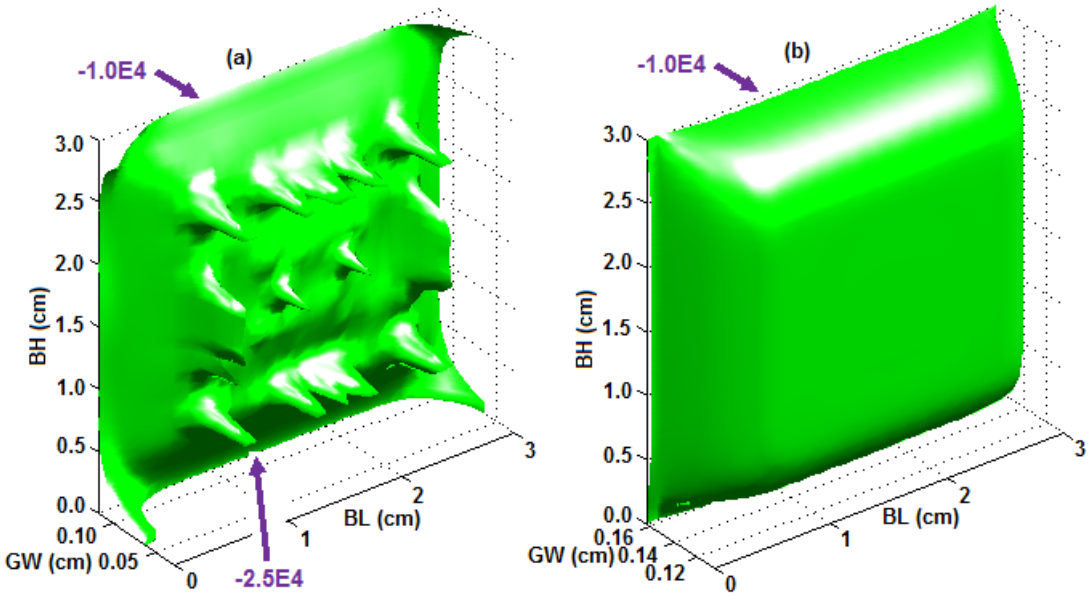

Figure 7.8. Spatial volume distribution of axial electric field (E_y) for $f = 15$ kHz, $\varepsilon_r = 7.5$ and $V_{appl} = 1.6$ and 1.5 kV and 50 ppm N_2 impurities.

Now the major objective is to investigate the properties of filaments and their combined and individual effects on the filamentary atmospheric pressure discharge. The figure 7.8 (a, b) explores the spatial distribution of axial electric field by using the method of isosurfaces in three-dimensional space. The filamentary and uniform volume structures of axial electric field are considered at the maximum discharge current density as shown in figure 7.8 (a, b). The artificial imposed conditions are capable of modifying the discharge characteristics and transformed the uniform discharge into filamentary discharge plasma as shown in figure 7.8 (a). The evolution of uniform axial electric field is displayed in figure 7.8 (b), which shows the flat and smooth profile of spatial volume distribution of axial field strength in the absence of imposed conditions. The large field gradients are present on the surface of dielectric barrier because of non-uniformities due to the effect of overvoltage. The non-uniform distribution of axial electric field illustrates that the field strength is higher in the constricted part as compared to the smooth part in the cathode fall region. However, the maximum magnitude of the axial electric field in the filamentary and uniform discharge plasma are of $\sim -2.5 \times 10^4$ and -1.0×10^4 V cm^{-1} respectively. Due to the non-uniform distribution on the surface of dielectric barrier, the filamentary discharge plasma is not useful for the sophisticated industrial applications as compared to the uniform atmospheric pressure glow discharge as shown distinctly in figure 7.8 (a, b).

7.6 Phases of species distribution in filamentary discharge

Let us consider a filamentary discharge to express the origin and shape of non-uniformities under different imposed conditions. The non-uniformities are emerged due to different mechanisms, which enhance a major hurdle in the development of uniform atmospheric pressure discharge sources. Here, we discuss the three-dimensional volume distribution of electrons and He_2^+ ions density for a quarter of cycle during the evolution of filamentary atmospheric pressure discharge at 10 kHz driving frequency. An overvoltage is defined as the magnitude of voltage, which is 10 to 20 percent higher than the breakdown voltage. The streamers are observed in nitrogen plasma when the overvoltage exceeds a value 17 % of the breakdown voltage [4]. The 10 to 15 % overvoltage value is sufficient for the production of streamers in the reactor gap, in which the breakdown at static voltage occurs with the Townsend ionization mechanism. After completion of initial steps of breakdown as discussed previously, the analysis proceeds to cover the effects of streamer breakdown at atmospheric pressure. As the streamer breakdown mechanism acts as a source of creation of non-uniformities at high pressure, the streamers are created in the atmospheric pressure discharges by the imposition of different conditions as discussed in chapter 5. The electric current is a collection of transient microdischarges in the gap. Normally, the uniform discharge structures are observed due to the Townsend ionization mechanism rather than streamer mechanism under different operating conditions. The streamer and Townsend ionization mechanisms are responsible for the development of non-uniform and uniform discharges at atmospheric pressure. Generally, the streamers can march from the anode barrier towards the cathode barrier and vice versa under different circumstances. This type of effect is prominently observed from 5 to 20 kHz driving frequency most because of the coalesce of filaments at further higher frequencies ($>$ 20 kHz). Presumably, the electrons perform an outstanding role in the uniform and filamentary discharges and the treatment to handle them is significantly different than other discharge species. The exact properties of electrons help us to determine the effects of discharge in different regimes during the progression. The two-dimensional fluid model can provide the shape and configuration of filaments in two-dimensional space (x-y), whereas the complete shape and geometry of filaments are possible only in three-dimensional space. This type of three-dimensional distribution of filaments enhances an insight about the non-uniformities in high pressure discharges. However, the volume structures of filaments provide the visualizations in three-dimensional space during the evolution, which illuminate completely their spatial and time variations in different discharge regimes. We can explore and discuss the internal dynamic characteristics in detail with the help of three-dimensional fluid model, such as localized density inside the filaments, diameter and length, and geometrical configuration of filaments. The filamentary behavior is dominant remarkably in the lower frequency regime, which will be described by the volume distribution of electrons at variable driving frequencies.

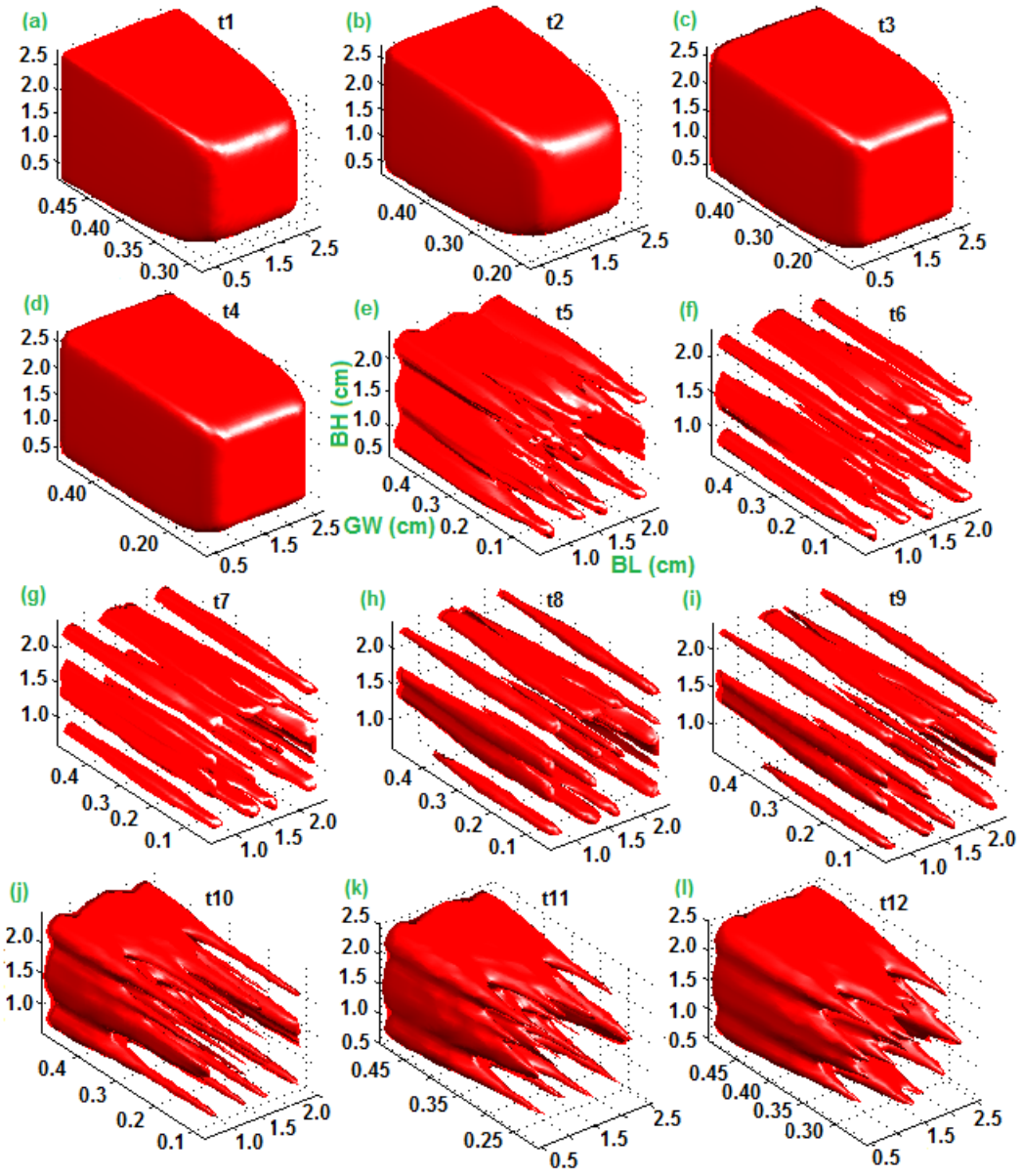

Figure 7.9. Spatial volume distribution of electrons density for $f = 10$ kHz, $\varepsilon_r = 7.5$, RC $= 5.0 \times 10^{-6}$ cm^3 s^{-1} and $V_{appl} = 1.6$ kV with 50 ppm N_2 impurities.

The figure 7.9 (a - l) illustrates about the space and time variations of electron density in the filamentary atmospheric pressure discharge at a driving frequency of 10 kHz from time t1 to t12. The spatial volume distribution of electrons density cover the range from 1 to 25 μs with an interval of 2 μs approximately. It is evident from the evolvement of different phases of electron density that how the filaments start to come out from the avalanche bulk due to the streamer ionization mechanism. These filaments adopt a shape of thin non-uniform long rods with higher localized electron density and exist approximately in

the whole gap except near the cathode barrier. The quarter of cycle is divided into thirteen parts as shown in the figures 7.9, 7.10 and 7.11, which explore the different patterns of electron density during the development in different stages of atmospheric pressure filamentary discharge. The considered quarter of cycle covers the different phases, usually called as prebreakdown, breakdown, filamentary distorted cathode fall region and decay of current pulse, whereas the volume space varies according to the presence of electrons density in the reactor gap. The figure 7.9 (a - l) exhibits that the avalanche expands in x, y and z directions but a major distorted change is observed in the y direction. In the prebreakdown phase, the electron density avalanche is in the middle of gap approximately and the front edge exists between 0.30 and 0.35 cm from the cathode barrier as shown in figure 7.9 (a) and the magnitude of electron density is $\sim 1.1 \times 10^9$ cm^{-3} at time t1. As the mobility of electrons is significantly larger than the ionic species, the avalanche development becomes greater during the discharge progression and the figure 7.9 (b) represents the situation just before the breakdown with a density magnitude $\sim 4.5 \times 10^9$ cm^{-3} at t2. The front edge of the electron density is shifted fastly towards the cathode barrier due to the population of ionic species with smaller mobility near the cathode barrier as shown in figure 7.9 (a - d), which exhibits the uniform structure of electron density in the three-dimensional volume space with the numerical magnitude of $\sim 1.4 \times 10^{10}$ cm^{-3} as displayed in figure 7.9 (d). After further progress in the breakdown phase due to the overvoltage effect, the filaments are emerged which appear in the front face of the avalanche bulk near the cathode barrier as shown in figure 7.9 (e) and the density magnitude shoots to the value $\sim 1.5 \times 10^{11}$ cm^{-3}. Subsequently, the peg like filaments become larger and adopt the shape of thin long atypical rods during the filamentary cathode fall layer formation and the discharge attains a maximum discharge current density of ~ 3.16 mA cm^{-2} with the electron density magnitude in the filaments of $\sim 2.0 \times 10^{11}$ cm^{-3} as exhibited in figure 7.9 (f) at time t6. The secondary electrons emission is enhanced in filamentary discharge when the streamers collide with the surface of dielectric barrier material. These independent long filaments persist their shape at higher values of discharge current density as shown in figure 7.9 (f - i). However, the sharp pattern of thin rods show that they are protruded from the anode and directed towards the cathode barrier. This type of filamentary structure is developed due to the effect of overvoltage. The details of streamer breakdown mechanism and types under different conditions partially follow the similar trend, which explained in [4] at relatively high pressure. We have checked that these filaments are disappeared and the uniform discharge structure emerges with the removal of imposed conditions, i.e., overvoltage value and increased recombination coefficient. In the decay phase, these thin atypical rods join each other near the anode due to higher conductivity and small thin needles appear in the front edge of electron volume density. These needles are thin from the head and look like the spikes as shown in the figure 7.9 (j, k). The diameter of the spikes from the bottom becomes larger and expands in the three-dimensional volume space. This represents the

process of reuniting filaments from the bottom near the anode barriers. The spatial volume distribution of electrons density displays that it becomes dense near the anode, and decreases in the gap along the x, y and z directions. The process of formation and reunion of filaments are entirely different because the filaments are emerged by the influence of overvoltage from the bulk of electrons density in the breakdown pulse, whereas the thin shape needles are formed during the decay of discharge current pulse. The reunion process of filaments is slower than the abrupt formation during the breakdown phase as shown in figure 7.9 (e, f) and 7.9 (j - l). The different types of physical processes perform an important role during the creation and reunion of the filaments in the filamentary atmospheric pressure discharge. The recombination of charged particles is fast in the afterglow phase, which plays a significant role at this stage. The magnitude of electrons density falls to a value $\sim 2.0 \times 10^{10}$ cm^{-3} in this phase from t10 and t12. The complete figure 7.9 (a - l) provides a perception of prebreakdown, breakdown, constricted filamentary distorted cathode fall layer and decay phases of filamentary discharge due to the artificial imposed restrictions. The last structure of the quarter of cycle will be discussed to compare the electronic and ionic species distributions in the gap simultaneously. It is noticed that the filamentary behavior is totally different due to the effect of overvoltage effect under different imposed conditions. In the case of 20 kHz in section 5.3, the electron density approaches to the peak values at the end of current pulse due to the continuing ionization at the position of the new cathode fall layer. In case of 10 kHz, the overvoltage has a significant impact on the discharge characteristics and the maximum electron density occurs at the higher values of discharge current density. In this phase, the electron density decreases to smaller values as shown in figure 7.9 (j, k). This observation develops a strong reason to distinguish the behavior of discharge characteristics in the filamentary discharge mode. The effect of imposed conditions has different types of impact in the filamentary discharge at variable driving frequencies.

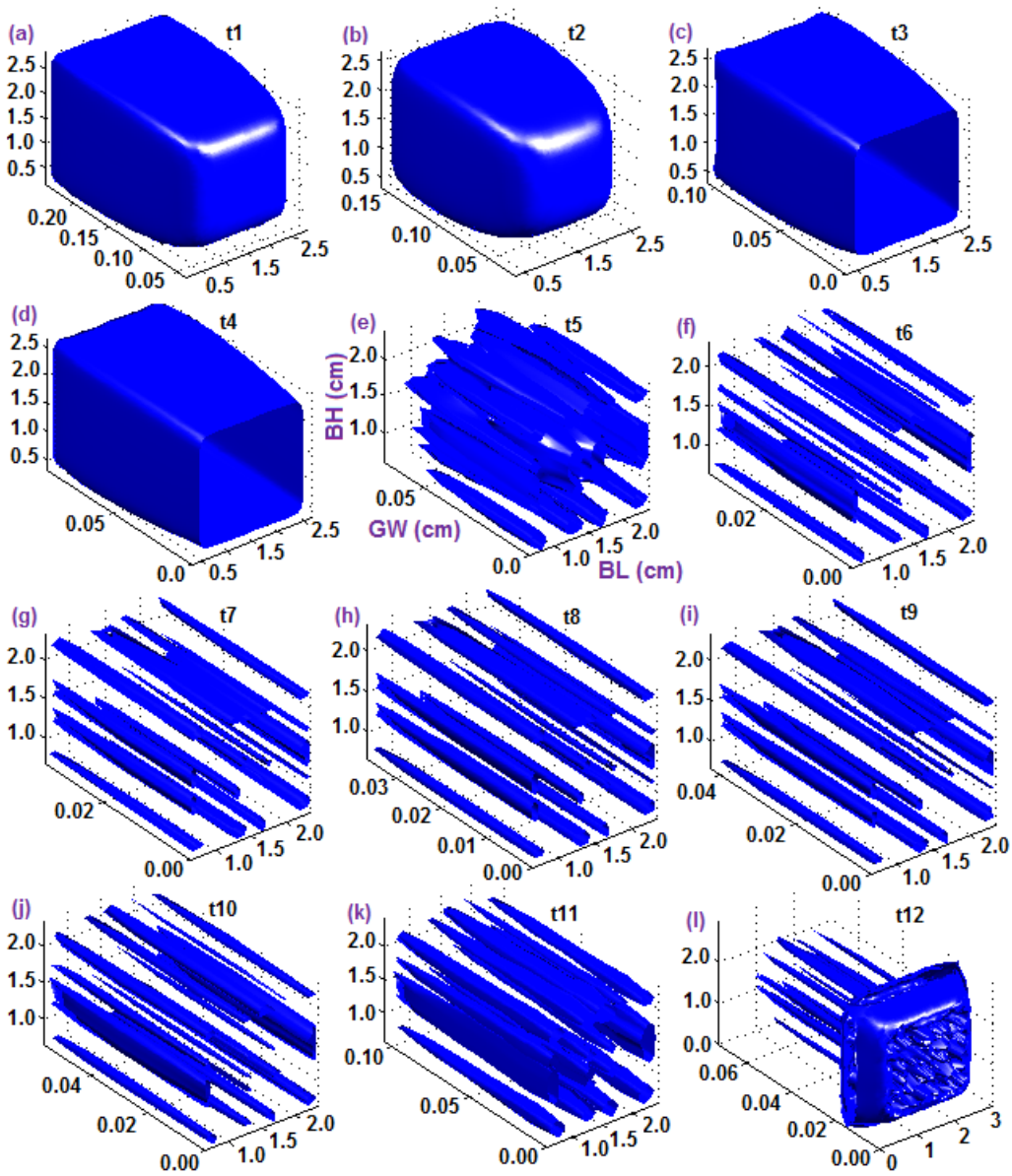

Figure 7.10. Spatial volume distribution of He_2^+ ions density for $f = 10$ kHz, $\varepsilon_r = 7.5$, RC $= 5.0 \times 10^{-6}$ cm^3 s^{-1} and $V_{appl} = 1.6$ kV with 50 ppm N_2 impurities.

The physical understanding is not completed without considering the major ionic species He_2^+ of atmospheric pressure filamentary discharge. The analysis of different phases of He_2^+ ions density distribution is essential to discuss the properties of ionic species near the cathode barrier when the filamentary discharge plasma evolves from t1 to t12 as shown in figure 7.10 (a - l) at 10 kHz. The ionic species He_2^+ move towards the cathode barrier gradually because of smaller mobility but they occupy the maximum density in small spatial volume of the gap as compared to the electrons during the formation of cathode fall layer. In the prebreakdown phase, the He_2^+ ions march towards the cathode barrier and have the den-

sity magnitude of $\sim 1.0 \times 10^9$ cm^{-3} as shown in figure 7.10 (a) at t1. The density of He_2^+ ions approaches to the value of $\sim 9.0 \times 10^9$ cm^{-3} as illustrated in figure 7.10 (b) just before the breakdown at time t2, whereas the width of ionic volume distribution is ~ 0.10 cm approximately. The density of He_2^+ ions are increased with a decrease of volumetric width in the gap from time t3 to t4 as shown in figure 7.10 (c, d). Subsequently, the uniform volume distribution of He_2^+ ions density is distorted into filamentary form as displayed in figure 7.10 (e) with a density magnitude of $\sim 3.5 \times 10^{11}$ cm^{-3} during the breakdown phase at t5. These ionic non-uniformities are developed in the form of thin small filamentary pegs in the cathode fall region and become further thin at the higher discharge current density values. They proceed to the maximum value of localized He_2^+ ions density $\sim 4.0 \times 10^{11}$ cm^{-3} as shown in figure 7.10 (f) at t6 when the discharge current density achieves a maximum value. The width of volume distribution of He_2^+ ions density is compressed to ~ 0.03 cm during the formation of distorted filamentary cathode fall region as shown in figure 7.10 (f). The localized ionic density gradients are formed on the surface of cathode barrier, which exhibit the thin ionic small non-uniformities in the filamentary atmospheric pressure discharge. These ionic non-uniformities persist their shape at higher values of discharge current density. When the electronic filaments start reuniting as shown in figure 7.9 (j), there is not any sudden impact on the distribution of He_2^+ ions density as displayed in figure 7.10 (j, k), which verify the distinct behavior of the electrons and He_2^+ ions in the decay phase. The magnitude of He_2^+ ions density is further reduced to $\sim 4.0 \times 10^{10}$ cm^{-3}, although the process of reuniting does not begin in case of He_2^+ ionic non-uniformities. However, the ionic non-uniformities join near the surface of cathode barrier and then the small thin pegs appear in the central part of the barrier surface as shown in figure 7.10 (l). The pattern of volumetric distributions exhibit that the He_2^+ ionic non-uniformities are synchronized with the electronic filaments during the breakdown phase but the synchronization halts in the decay phase as illustrated clearly in figure 7.9 (j, k) and 7.10 (j, k). This delay in reuniting of ionic species near the cathode barrier shows that the behavior of electrons and He_2^+ ions density are different in the filamentary atmospheric pressure discharge under the artificial imposed conditions, especially in the decay phase. The fluid model simulations are started with a quasineutral plasma with equal electrons and ionic species in the reactor chamber. Initially, the uniform discharge plasma is enhanced and converted into filamentary form by the influence of imposed conditions. The temporal evolution of discharge current density is observed in asymmetric form but the breakdown occurs at the same position during the evolution of different half cycles, which corresponds to the memory effect of dielectric barrier discharge. To deduce the reliability of three-dimensional fluid model simulations, the steady state of filamentary discharge is necessary to provide physical significance of numerical simulations.

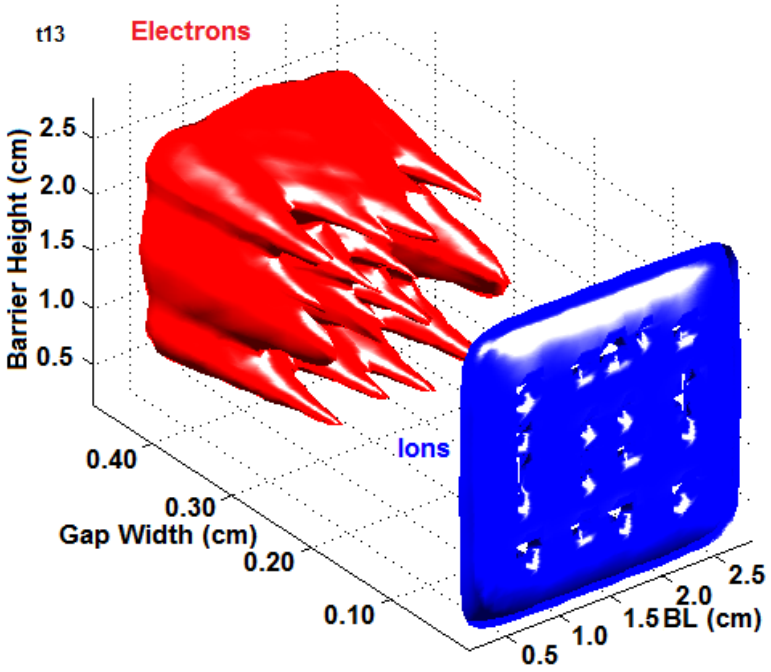

Figure 7.11. Spatial volume distribution of electrons (red) and He_2^+ ions (blue) density for $f = 10$ kHz, $\varepsilon_r = 7.5$, RC $= 5.0 \times 10^{-6}$ cm^3 s^{-1} and $V_{appl} = 1.6$ kV with 50 ppm N_2 impurities.

As the last structure of electrons and He_2^+ ions density is shown in figure 7.11 near the anode and cathode barriers during the quarter of cycle, this provides a clear three-dimensional view of both electrons and He_2^+ ions existence during the decay phase of discharge current pulse in the filamentary discharge simultaneously. The size of electronic filaments (spikes) becomes smaller gradually, which is recognized in red color as highlighted in figure 7.11 near the anode barrier. The ionic non-uniformities are suppressed near the cathode barrier and the electronic filaments are nicely observed near the anode barrier in the decay phase. The spikes of electronic structure help us to understand the decay and coalesce processes of filaments simultaneously. The ionic non-uniformities on the cathode barrier become vanish approximately and their magnitudes decrease to very smaller values in the decay phase. The magnitude of electrons and He_2^+ ions density are $\sim 1.2 \times 10^{10}$ and 0.9×10^8 cm^{-3} as shown in figure 7.11 at t13. However, the emergence of filaments are enhanced in the breakdown phase by the streamer ionization mechanism, whereas the source of filaments creation correspond to the Townsend ionization mechanism in the decay phase as discussed in chapter 5. During this process, the electrons in the gap try to quickly join their companions due to their higher mobility near the anode and the density gradients are occurred in the gap, which appear in the form of thick spikes. This process is performed at very smaller scale near the cathode barrier due to the smaller mobility of He_2^+ ions.

7.6.1 Configuration and path of filaments

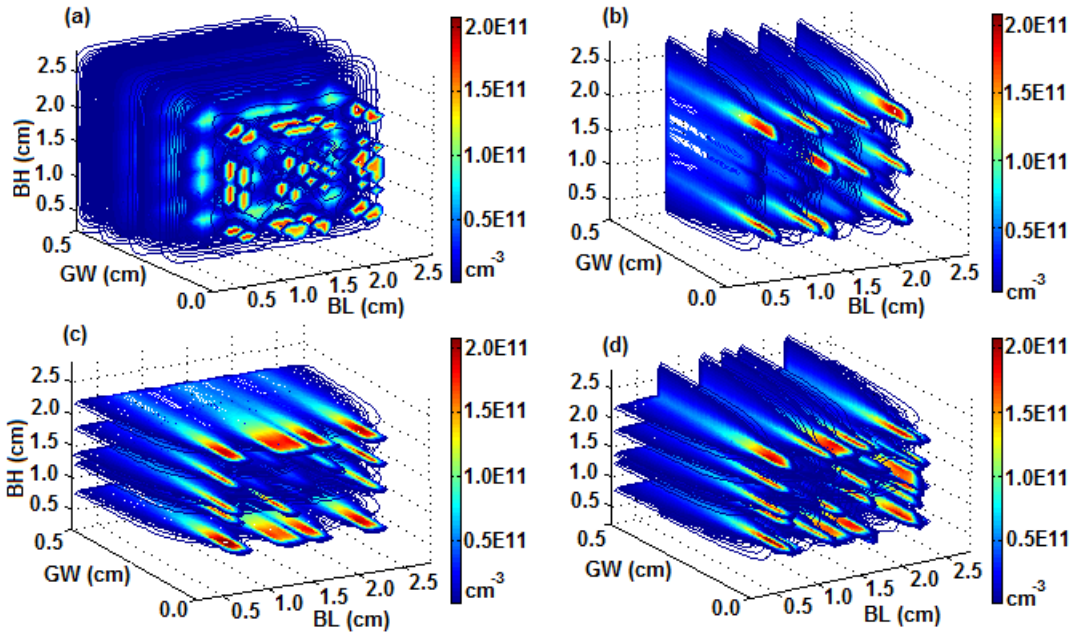

Figure 7.12. Combination of different slice structures of electron density for $f = 10$ kHz, $\varepsilon_r = 7.5$, RC $= 5.0 \times 10^{-6}$ cm^3 s^{-1} and $V_{appl} = 1.6$ kV with 50 ppm N_2 impurities.

The configuration and spatial volumetric occurrence of filamentary discharge in three-dimensional space are exhibited and examined in the figures 7.9, 7.10 and 7.11 for 10 kHz driving frequency. They provide the volume distribution of discharge species in the reactor gap during the evolution of different phases of atmospheric pressure filamentary discharge. It is apparent from the figure 7.12 that the lines of force come out from the different heads of filament, which stimulate the attraction of secondary avalanches on all sides of the filaments and enhance their growth. The mechanism which controls the strong electric field in the filament is the polarization of the dielectric barriers by the external electric field. In order to know the exact density of electrons in these thin atypical filaments internally, the different slice distributions of electrons are analyzed in x, y and z directions as shown in figure 7.12 (a - d). We consider the different slice distributions of electrons in x, y and z directions independently at different locations in the reactor gap. The different slice distributions in x and z directions are combined to analyze the locus of filaments in the discharge plasma at different locations as shown in figure 7.12 (d). The configuration of these filaments show that they expand and modify their structures along the x and z directions as well as in the y direction. The density of electrons in different filaments fall gradually from the head to tail and looks like a moving rifle bullet as shown in figure 7.12 (b - d). The density of electrons from the head is not suddenly reduced to very smaller values but follows a steady path in the axial direction. The effect of filaments in the helium gas are clearly observed during the travel at a particular instant as shown in

figure 7.12 (b - d). The electron density from the filament head is not extended uniformly in the x, y and z directions, whereas the constriction is prominently noticed near the head. The electrons occupy a maximum density of $\sim 2.0 \times 10^{11}$ cm^{-3} in the centre of filaments head and start reducing from the negative glow region towards the positive column as clearly observed from the different slice structures of electron density. It is observed from the figure 7.12 (a) that the spread of electron density is smaller in x and z direction than the y direction. The filaments are directed towards the cathode barrier and away from the anode barrier, which have the maximum density in their front heads as compared to the tails. These different slice distributions enhance the perception of filamentation in the non-uniform atmospheric pressure discharges. However, the authors in [128, 129] observed the filamentary behavior in the atmospheric pressure discharges. Therefore, the three-dimensional spatial structures of discharge species provide the opportunity for the real time comparison of atmospheric pressure discharges.

7.7 Effect of frequency in filamentary discharge

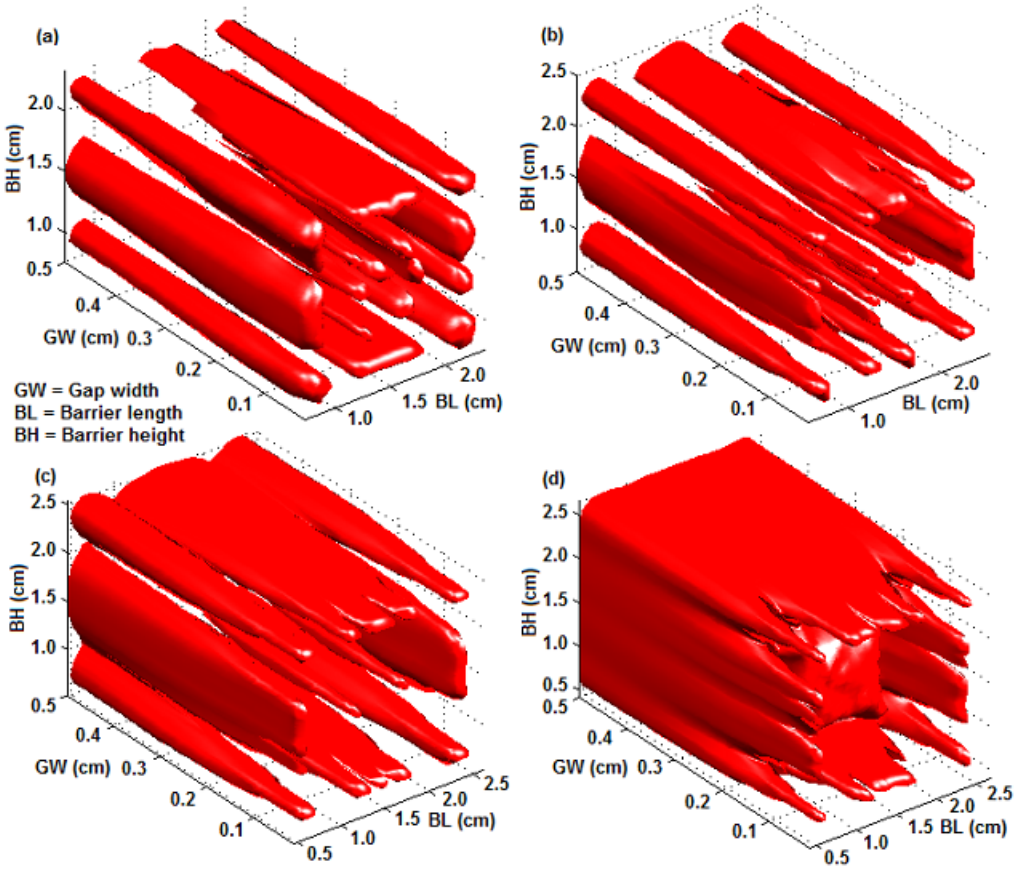

Figure 7.13. Spatial volume distribution of electrons density for $f = 5, 10, 15$ and 20 kHz, $\varepsilon_r = 7.5$, RC $= 5.0 \times 10^{-6}$ cm^3 s^{-1} and $V_{appl} = 1.6$ kV with 50 ppm N_2 impurities.

The comparison of three-dimensional spatial volume structures of filamentary discharge are demonstrated at 5, 10, 15 and 20 kHz driving frequencies under the similar imposed conditions as shown in figure 7.13 (a - d). The filamentary structures provide the electronic volume distribution of filaments when the discharge current density is maximum during the progression of atmospheric pressure filamentary discharge. The filaments are detached from each other at lower frequencies, whereas they coalesce at higher frequencies due to the reduction of electron energy losses. It is clear from the figure 7.13 (a) that the filamentary structure at 5 kHz has not precise resemblance with other filamentary discharge structures at 10 - 20 kHz. This supports the argument that the discharge plasma has complex behavior at lower frequencies especially $\lesssim 7$ kHz, which is consistent with the previous modelling results. We have checked the filamentary structure at 7 kHz under the similar imposed conditions, which also differs from the filamentary distributions at 10 - 20 kHz. As the intricate and filamentary behavior are dominant at the lower frequencies, the figure 7.13 (a) provides the distinct structure at 5 kHz than other mentioned frequencies. It is apparent from the figure 7.13 (b - d) that the diameter and width of filaments are extended widely and reunited at higher frequencies. The volume distribution of filaments show that the electron density is localized at different locations in the reactor gap during the presence of filamentary distorted cathode fall layer. The comparison of these electronic distributions give a brief intuition about the filamentary behavior of non-uniform discharge. However, the above filamentary structures illustrate that the formation of localized density gradients due to the filaments at lower frequencies are more feasible because the discharge cycle takes longer time in this case as compared to the higher frequencies. The asymmetric breakdown is very strong at lower frequencies and the creation of electrons and ions rise to the very large values. However, the charge carriers are not strongly trapped between the dielectric barriers at lower frequencies. Therefore, the electron impact energy losses are also enhanced in the lower frequency regime than higher. It is evident from the figure 7.13 (b, c) that the central front edge of the filament is distributed significantly near the cathode barrier at 10 kHz, which becomes less at 15 kHz and minimizes further to zero at 20 kHz because of the reduction of energy losses. The small localizations of electron density become negligibly small in the central of volume density at 20 kHz as displayed in figure 7.13 (d). The maximum density of filaments in this frequency range is $\sim 2.0 \times 10^{11}$ cm^{-3} approximately as shown in figure 7.13 (a - d). The above filamentary volume distributions at variable frequencies are described in the presence of overvoltage and increased recombination coefficient of molecular nitrogen ions. The confining potential is developed between the dielectric barriers to localize the density of electrons. This develops a precise and comprehensive understanding of the coalesce of filaments at higher frequencies and agrees with [100].

7.7.1 Slice distribution of filamentary discharge

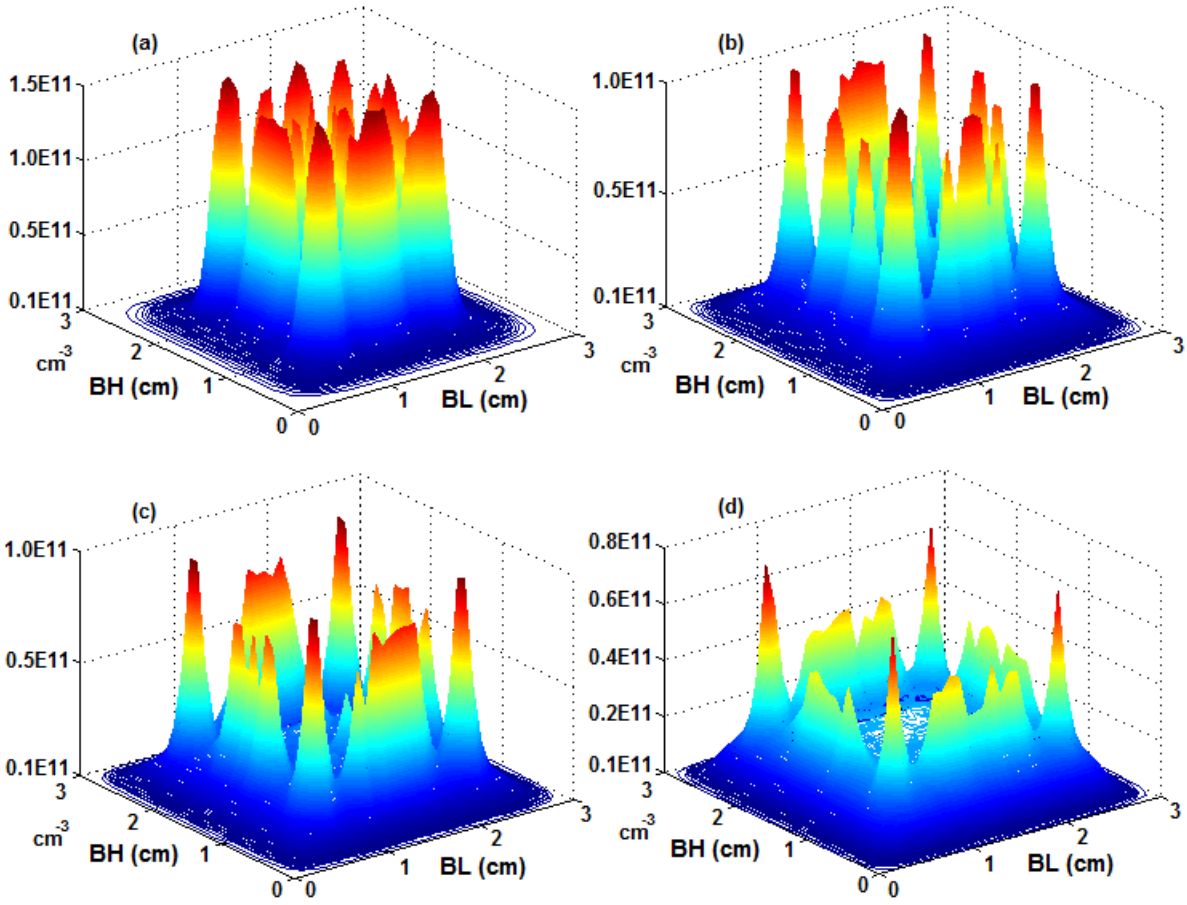

Figure 7.14. Single slice distribution of electron density for $f = 5$, 10, 15 and 20 kHz, $\varepsilon_r = 7.5$, RC $= 5.0 \times 10^{-6}$ cm^3 s^{-1} and $V_{appl} = 1.6$ kV with 50 ppm N_2 impurities.

As the spatial volume distribution and emergence of filaments are described by the profile of electrons density at different frequencies in the filamentary discharge plasma. We consider a single slice distribution of electrons density in the two-dimensional (x-z) space and deduce the variations in the electrons density from the centre of filaments to circularly outward in the reactor gap. To consider an analysis of electrons density in the filaments at variable frequencies, the slice distribution of electrons density in three-dimensional contour format is shown in figure 7.14 (a - d). When the distorted cathode fall region is fully developed in the filamentary discharge, the slice distributions of electrons are considered from their maximum values near the cathode barrier. The slice distributions in two-dimensional space verify that the electron density is higher in the centre of filaments and extends to smaller values away from this point during the movement in the axial direction. However, the four distinct patterns of electron density show that the number of filaments are coalesced at higher frequencies, starting from 10 kHz. As the

properties and mechanism of creation of filaments in the discharge plasma are substantially different at lower frequencies ($\lesssim$ 7 kHz) than higher, so the analysis is performed necessarily in both regimes. At 5 kHz, the structure of filaments is different than higher frequencies under the similar imposed conditions as shown in figure 7.14 (a - d). The peak values in the slice distribution represent the constrictions in the filamentary discharge plasma, which are clearly distinguished by the spatial distributions at lower frequencies than higher frequencies. The values of electrons density and size of the filaments are varied from 10 to 20 kHz as shown in figure 7.14 (b - d). The numbers of filaments are coalesced from 10 to 20 kHz, which exhibit clearly in the central part as well as at the edges of single slice distribution. The size and configuration of single filament is smaller and independent from the neighboring filaments at 10 kHz as compared to 15 and 20 kHz as shown in figure 7.14 (b - d). Although, the electrons are present dominantly in the whole gap instead of near the cathode fall region, so the shape and configuration of filaments vary accordingly and the numerical magnitudes are shown in the figure 7.14 (a - d).

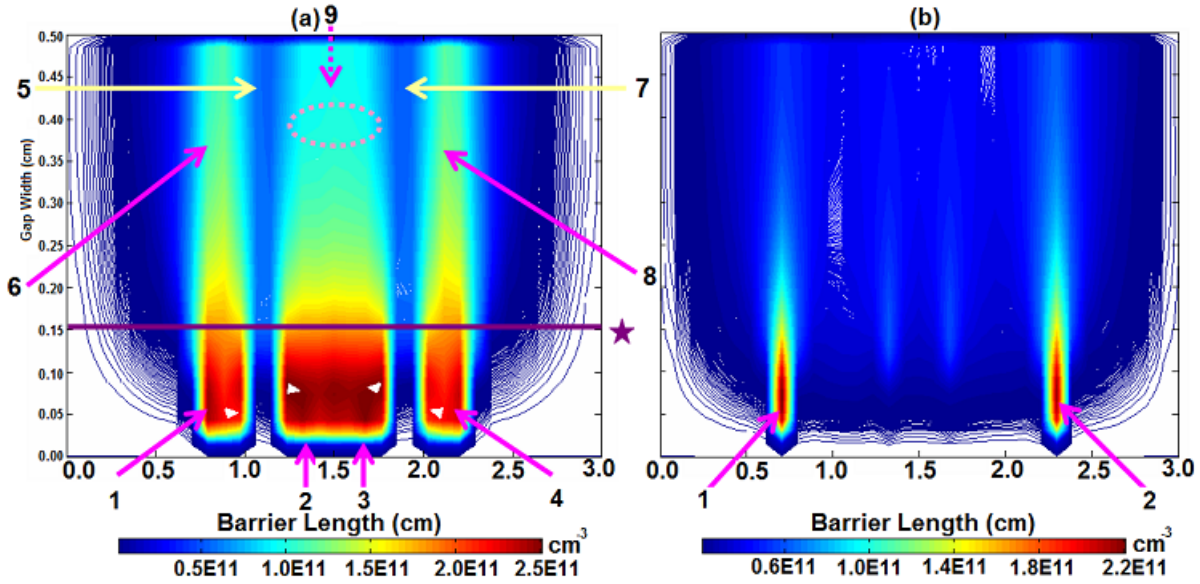

Figure 7.15. Spatial slice distribution of electron density for $f = 5$ and 10 kHz, $\varepsilon_r = 7.5$, RC $= 5.0 \times 10^{-6}$ cm^3 s^{-1} and $V_{appl} = 1.6$ kV with 50 ppm N_2 impurities.

Now the further analysis is performed for a single sheet in the axial direction from the three-dimensional mesh at 5 and 10 kHz frequencies, which provide the comparison between the effect of different possible types of filaments during the evolution of filamentary discharge. There is a possibility of existence of different types and shapes of filaments at different frequencies. We consider the slices of electron density from the different locations in case of 5 and 10 kHz, which illustrate the difference between the properties of thick and thin filaments in the reactor gap during the evolution of filamentary discharge. Here, the different types of configuration of filaments are considered to understand their effect in the

filamentary atmospheric pressure discharge at 5 and 10 kHz. The volumetric spatial distribution of filaments exhibit their emergence with the clear electron density gradients in figure 7.13 (a - d). It is evident from the figure 7.15 (a) that the filaments 1, 2, 3 and 4 have higher density magnitudes in the reactor gap than the surrounding filamentary discharge plasma. The variations of electron density in the filaments change according to their shapes and configurations. The central two filaments are joined to form a larger filament and the electron density remains similar approximately from the head of filament to the line denoted by star. The electron density decreases to the smaller values sharply in the reactor gap as shown by the arrows 6, 8 and 9. There are rifts between the filaments in the reactor gap where the electron density has very small values and represented by the arrows 5 and 7. However, the above pattern of filaments enhances the perception for the variations of electron density and the path followed by the filaments in the reactor gap. There are distinct types of filaments present in the gap, which have variable magnitudes of electron density during the evolution of the different phases of a cycle. The maximum number of filaments are observed at 10 kHz frequency, which coalesce to smaller number at higher frequencies as displayed in figure 7.13 (b - d). It is evident from the figure 7.14 (b - d) that the filaments are smaller and thin at 10 kHz than 15 and 20 kHz frequencies. The filaments have maximum electron density near the cathode barrier and quickly reduce to smaller values in the gap as shown by the arrows 1 and 2 in figure 7.15 (b). The fall of electrons density does not follow a long path in the reactor gap at 10 kHz as compared to 5 kHz frequency. The distribution of filaments demonstrate that the different possible types of non-uniformities exist in the filamentary atmospheric pressure discharge. Thus, the filaments are distinguished precisely from the slice distributions in the two-dimensional space as shown in figure 7.15 (a, b), which have the values of localized electron density $\sim 2.5 \times 10^{11}$ and 2.2×10^{11} cm^{-3} at 5 and 10 kHz. This confirms that the strong and weak filaments are prominently existed quite at different locations of the reactor gap in the filamentary atmospheric pressure discharge at variable driving frequencies.

7.8 Influence of driving frequency in uniform APD

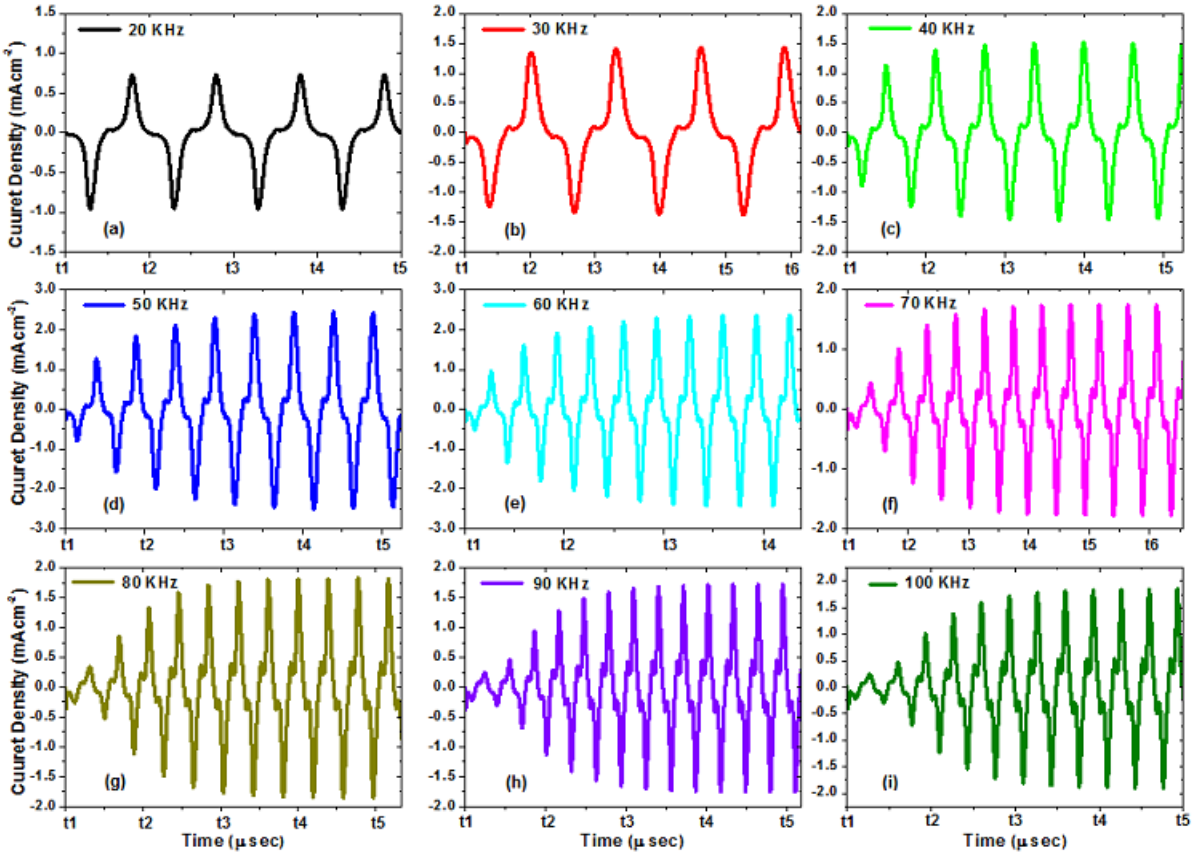

Figure 7.16. Temporal evolution of discharge current density at variable frequencies f = 20 - 100 kHz, $\varepsilon_r = 7.5$ and $V_{appl} = 1.5$ kV with 20 ppm N_2 impurities.

It has been mentioned in the previous section that the filamentary discharge is formed by the application of different imposed conditions. In this section, we cover the frequency range from 20 to 100 kHz for the temporal evolution of discharge current density in the uniform atmospheric pressure glow discharge without any imposed conditions as shown in figure 7.16 (a - i). The time t1 to t6 represents the time span for the particular driving frequencies and it is different for various driving frequencies. The stationary-state is acquired to describe the physical significance of numerical simulation results of atmospheric pressure discharge because the non-stationary state corresponds to the non-physical situations. On the basis of the temporal profiles of discharge current density, the characteristics of uniform atmospheric pressure discharge are distributed into different groups under the similar operating conditions at variable driving frequencies. It is explicit from the pattern of different discharge current density structures in this domain ($20 \leq f \leq 100$ kHz) that the current density increases initially from the lower to higher values. The steady-state is achieved after a few number of cycles as displayed in figure 7.16 (a - i) at different

frequencies. To describe the physical significance of discharge current density at variable frequencies, the breakdown phase can be considered as the production of large number of charged particles as compared to their losses. As we know that the electrical energy is supplied to the dielectric barrier discharges by the external applied voltage, this energy is used to enhance the excitation and ionization processes of gas atoms and molecules. These processes depend on the chemical interactions of electrons with the helium gas atoms in the presence of impurities. Although, the internal distributions of discharge species effect to smaller extent when the discharge current density increases from 20 to 50 kHz. This means that the four distinct regions, such as cathode fall layer, negative glow, Faraday's dark space and positive column are developed approximately in this frequency range. The discharge oscillates fastly as well as with the rise in the residual current density at further higher frequencies. The Townsend ionization mechanism is dominant in the breakdown pulse of uniform atmospheric pressure glow discharge as displayed in the figures 7.3 - 7.6 and 7.16. The physical justification of this increase can be linked with the electron energy losses and ionic species heating mechanisms. It has been discussed and observed that the electrical energies are prominently transformed into kinetic energies quite at higher frequencies as compared to the lower frequency discharge regimes [106]. The different types of energy losses, such as joule heating, elastic and inelastic collision energy losses are dominant in the lower frequency regime because the dynamic response of ionic species density is higher due to the collisions with gas particles and barrier surface at lower than the higher frequencies in the uniform atmospheric pressure glow discharge. The electrons and ions are not strongly trapped in the positive column at lower frequencies and they are produced due to the kinetic interactions of chemical processes as well as with the secondary electrons emission from the dielectric barrier due to the ionic bombardment. The temporal evolution of discharge current density reveals that it is directly proportional to the driving frequency in the mentioned range from 20 to 50 kHz as shown in figure 7.16 (a - d). The mechanism of discharge operation is changed at further higher frequencies, which stops the increase in discharge current density. The discharge current density is remarkably reduced from 50 to 70 kHz as illustrated in figure 7.16 (d - f) and then a steady situation is reached approximately. In this range, the direction of drift motion of the large number of charged carriers is inverted before reaching the parallel plate dielectric barriers of opposite polarity. This increases the collisions with gas particles and molecules, moreover the creation of electrons become greater in this phase. At the same time, the source of secondary electrons is also reduced because the ionic species change their path before collisions with the barrier surface. It has been described in the chapter 4 that the discharge characteristics are effected due to the impact of secondary electron emission coefficient of cathodic dielectric barrier material. The density of metastables and excimers are reduced in the mentioned higher frequency regime because of the fast polarity reversal of AC field. Therefore, the stable and smooth structure of discharge current density is reached partially in this frequency regime

(70 $\leq f \leq$ 100 kHz) as represented in figure 7.16 (f - i). The temporal evolution of discharge current density follows a similar trend at variable frequencies, which has been predicted in [107, 130, 131] in the lower frequency range. The further intuition of discharge current density is explored by considering their peak values in the positive current pulse during the half cycle. The large current density peak represents the glow discharge plasma during the evolution, while the residual current density is induced during the polarity reversal of the electric field. To deduce the variation of these current densities, the quantitative analysis is performed in this frequency range from the magnitudes of peak values of positive glow discharge current density and residual current of the previous glow discharge, which exhibits in figure 7.17.

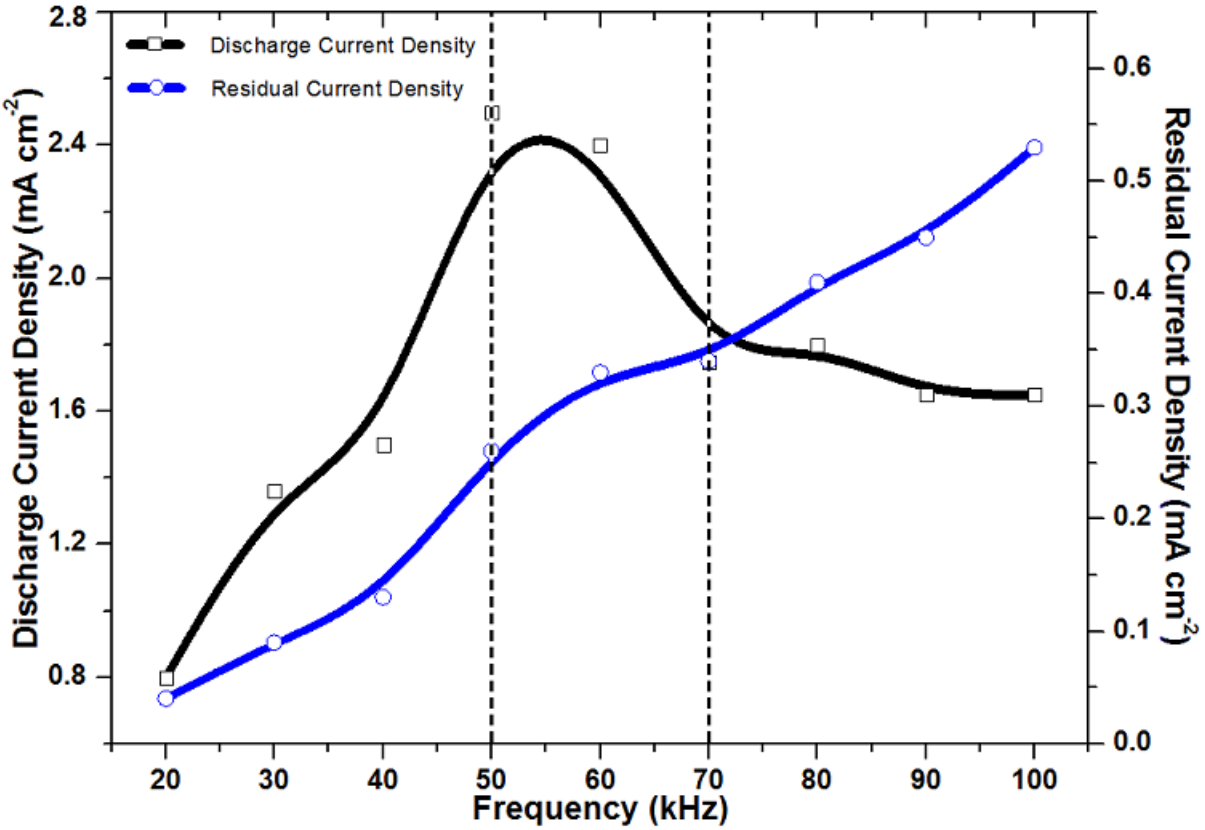

Figure 7.17. Evolution of discharge and residual current density for f = 20 - 100 kHz, ε_r = 7.5 and V_{appl} = 1.5 kV with 20 ppm N_2 impurities.

As the discharge current density is varied in different driving frequency regimes for the uniform atmospheric pressure discharges, the characteristics of discharge plasma are categorized into the following three groups. In the first group (< 20 kHz), the chaotic, filamentary and uniform behavior of atmospheric pressure discharge are dominant under different operating conditions. The properties of first group has been described in chapters 4 and 5, which provide the spatio-temporal evolution of discharge parameters

in the uniform and non-uniform atmospheric pressure discharges. The second part of first group contains the filamentary and uniform discharges with and without imposed conditions, which is not illustrated in figure 7.17. The homogeneous uniform atmospheric pressure glow discharge is remarkably occurred in the second group ($20 \leq f \leq 50$ kHz), which can be verified with the several spatial and temporal distributions of discharge variables during the breakdown pulse. The two and three-dimensional fluid model simulations deliver a concise understanding in this regime. The discharge current density increases in this phase by the reduction of electron energy losses. However, the residual current density depends on the trapped electrons in the positive column and they swiftly move during the polarity reversal of electric field. At higher frequencies, the density of electrons is higher near the anode barrier during the glow discharge phase as shown in figure 7.4 (b) and they tried to rush during the polarity reversal and enhance a strong residual current pulse. Therefore, the residual current density is also increased in this phase with the increase in driving frequencies as shown in figure 7.17. In the third group, the properties of uniform discharge are decomposed into two parts, such as falling and steady current density regimes. It is evident from the figure 7.17 that the discharge current density sharply falls from 50 to 70 kHz and attains the steady current density values approximately at further higher frequencies in this domain ($70 \leq f \leq 100$ kHz). The uniform atmospheric pressure glow discharge depends substantially on the chemistry of gas. It has been noticed in chapter 5 that the different types of ionization and excitation processes play an important role for the development of glow discharge plasma. These production processes are enhanced to their peak values at 50 kHz when the discharge plasma has the maximum current density. At further higher frequencies, the chemical production and destruction processes are not completely progressed and generate smaller number of electrons and ions because the time duration for a complete cycle reduces in this frequency regime as well as the smaller effect of secondary electrons emission coefficient. Thus, the discharge current density is reduced in this regime as shown in the figure 7.17 and the discharge plasma achieves the steady situation at further higher frequencies. This means that the creation and destruction of discharge species due to the chemical reactions reach a steady state in this frequency range. This elaborates that the discharge current density becomes approximately smooth and stable in this particular region of frequency. The residual current density has not very complex behavior and it increases approximately in a linear fashion with the rise in frequency in the mentioned groups as displayed in figure 7.17. The above three groups provide a comprehensive perception of atmospheric pressure uniform discharge plasma in different frequency regimes. Thus, the probability of uniform atmospheric pressure glow discharge is greater in the second group than first and third groups from the different frequency regimes. We can explain the uniform and filamentary behavior of discharge with the trapping mechanism of charge carriers. It is observed from the previous simulation results of multi-dimensional fluid model in this research work that the moderate range of frequencies is acceptable for the uniform atmospheric

pressure discharges, i.e., 10 to 50 kHz approximately because the ions and electrons are trapped and released freely at higher as well as at lower frequencies during the positive and negative half cycles in the reactor gap. Therefore, the chaotic behavior is emerged at lower frequencies due to the absence of trapping mechanism of charge carriers and the residual current is higher with the trapping of electrons and ions at higher frequencies in the gap. It is evident from the physical understanding of atmospheric pressure discharge that the filamentary discharge is obtained in the above mentioned lower and higher frequency regimes sharply. The whole discussion clearly elaborates the intricate and smooth regions of the atmospheric pressure discharges as a function of driving frequency without any imposed conditions.

7.9 Conclusions and summary

In this chapter, the three-dimensional fluid model is formulated and developed in the presence of discharge species, which illustrate the spatial volume distributions of atmospheric pressure discharge parameters such as, particle species density, electric field in x, y and z spatial directions, ionization rate and electron mean energy under different operating conditions. The real time distributions of uniform discharge plasma are elaborated and discussed in He-N_2 gas at variable driving frequencies and external applied voltages. The analysis of spatio-temporal species distribution demonstrates that the different discharge regimes are distinguished with their distinctive properties in the uniform glow and filamentary atmospheric pressure discharges. The evolvement of species density in different phases are investigated and compared during the progress of uniform glow discharge plasma at 30 and 50 kHz. The behavior of discharge current density is varied in different frequency regimes with external applied voltage, which exhibits the relation between these quantities from 20 to 100 kHz. The appearance and configuration of filaments are elucidated by using the spatial pattern of electronic species in the constricted filamentary discharge. However, the mechanism of emergence of filaments is explored in the lower frequency regime, which describes the specific internal dynamic details of their temporary shapes and pattern during the breakdown and decay phases of filamentary atmospheric pressure discharge. The distinct structure of filaments is shown at lower frequencies ($<$ 20 kHz) as compared to the higher frequencies because of the coalescence of filaments at higher frequencies and prominently form a uniform or partially uniform distribution of discharge. The strength of axial electric field inside the filament is greater than the axial electric field of filamentary discharge plasma and varies from the head to the tail of filament. The magnitude and direction of movement of filaments are examined with the slice distributions of electrons at different locations in the reactor gap, which illuminate the path and constricted part of density during the progression in the filamentary discharge. The temporal evolution of discharge current density exhibits that it prominently increases from 20 to 50 kHz, after this it starts decreasing and then ultimately

follows an approximately smooth path at further higher frequencies.

Chapter 8

Conclusions

We have formulated and developed a multispecies multi-dimensional self-consistent fluid model of atmospheric pressure discharge for the parallel plate dielectric barrier geometry. The fluid model solves the continuity equation of discharge species, the electron and gas energy equations using drift-diffusion approximation. The Poisson equation is employed to find the profile of electric field strength in the presence of charged species. The set of coupled fluid model equations together provide the spatio-temporal evolution of particle species densities and fluxes, electron mean energy, gas energy, reaction rates and the electric field under different operating conditions for the uniform and filamentary atmospheric pressure discharges. The characteristics of atmospheric pressure discharge are investigated in the lower and higher frequency regimes to elaborate the filamentary and uniform behavior of discharge in the pure helium and He-N_2 gas mixtures. The influence of chemical reaction kinetics is analyzed during progression in the variable regimes of atmospheric pressure discharge plasma. The fluid model is capable of simulating the complete space and time distributions of the atmospheric pressure discharge variables in different phases of a cycle. However, the multi-dimensional fluid models are developed in this research work to understand the spatio-temporal profiles and internal dynamics of atmospheric pressure discharge species.

The accuracy, authenticity and reliability of fluid model simulations can be provided by the comparison of experimental and numerical modelling results wherever it is possible. The following landmark features are inspected and examined in this research work as

- The atmospheric pressure uniform glow and Townsend discharge modes are studied numerically due to the effect of variable quenching frequencies of excimers and small amount of nitrogen impurities, which establish an understanding of four distinct regions of glow discharge mode and extinction of these regions in the Townsend discharge mode. The influence of variable secondary electron emission coefficient is deduced by the temporal evolution of discharge current density.

- The intricate behavior prominently appears in the lower frequency regime ($1.0 \lesssim f \lesssim 7.0$ kHz), which exhibits the presence of chaotic and bifurcation processes in pure helium gas. These instabilities are suppressed under different operating conditions, which develop and enhance the physical intuition of the atmospheric pressure discharges. We have calculated the transport coefficients, ionization and excitation rates of different gas species using the interpolation techniques from the solution of Boltzmann equation in the uniform electric field. The one-dimensional fluid model simulations are compared with the experimental results in He-N_2 gas.

  In order to examine the internal distributions of uniform and filamentary atmospheric pressure discharges, the two and three-dimensional fluid models are developed in the stagnant and flowing He-N_2 gas. To estimate the influential effects in the radial and axial directions, the major and important chemical processes, such as direct ionization, excitation, Penning ionization, stepwise ionization, charge transfer and dissociative recombination are included in the two-dimensional fluid model simulations, which explore the remarkable properties for the understanding of atmospheric pressure discharge. The following points address the brief perception of two-dimensional fluid model in the stagnant helium gas with the variable amount of small nitrogen impurities.

- The two-dimensional fluid model presents the numerical simulations with symmetric boundary conditions and investigates the evolution of atmospheric pressure discharge parameters in pure helium and He-N_2 gases. We have imposed successfully the Dirichlet boundary conditions on the solid dielectric barriers, moreover the Von Neumann symmetry boundary conditions are considered for the open boundaries of parallel plate reactor. The eminent semi-implicit technique is considered and applied for the self-consistent calculation of the electric field in the discharge plasma.

- The space and time variations of discharge species are illustrated for the filamentary and uniform atmospheric pressure discharges, which explain the comprehensive awareness about the internal dynamic structures of species in different phases of a cycle. The current-voltage characteristics are described to demonstrate the stationary-state of dielectric barrier discharge and to explore the evolution of electrons density during the breakdown pulse. Correspondingly, the residual current density is confirmed during the polarity reversal of electric field, which emerges due to the trapped electrons in the positive column of the atmospheric pressure glow discharge.

- The growth of electric field in the radial and axial directions as well as species density are explicated due to the effect of external input operating conditions. The average values of species density, production and destruction rates of chemical processes and influence of driving frequencies are expressed by their temporal evolution for a complete cycle. The effect of relative permittivity of barrier, radial diameter and width of barrier are analyzed for the atmospheric pressure glow and

Townsend discharge modes. The temporal evolution of discharge current density shows that it increases with the increase in driving frequency and decreases with the increase in small nitrogen impurities in the particular domain of influential quantities.

In the context of atmospheric pressure discharge temperature, we have solved the gas energy equation for the stagnant as well as for the flowing gas between the parallel plate dielectric barriers. The supposition of room temperature is not a strictly valid assumption for the numerical simulation modelling at atmospheric pressure. To resolve this issue, the constant subsonic and supersonic bulk flow of gas is introduced in the horizontal direction of the reactor by using the parabolic profile. We have evaluated the gas temperature for the stagnant and flowing helium gas during the atmospheric pressure glow discharge phase. It is found that the gas temperature decreases with an introduction of constant bulk gas flow in the subsonic flow regime. However, the overall trend of discharge current density in the presence of variable bulk gas flow is compared with the experimental work to check the reliability of fluid model simulations under the gas flow restrictions. Correspondingly, the electron temperature in discharge plasma is slightly modified in the flowing helium gas, whereas the gas temperature changes appreciably due to the turbulent bulk gas flow. The properties of uniform and filamentary atmospheric pressure discharge are described in the presence of constant subsonic and supersonic flow of bulk gas, which enhance the better perception in different gas flow regimes. The temporal growth of discharge current density provides the information of the different bulk gas flow regimes, whereas the glow discharge plasma operates in the uniform, filamentary and constricted filamentary modes of atmospheric pressure discharge.

Regarding the real time distribution of discharge species for their perfect shape and configuration, this problem can be solved by the help of three-dimensional numerical fluid model. In order to achieve this goal, we have developed a three-dimensional fluid model to describe the real time distribution of atmospheric pressure glow and filamentary discharges. The configuration and pattern of filaments are identified and discussed under different imposed conditions, which show the mechanism for their generation and annihilation processes. The following numerical simulation results are deduced with the help of three-dimensional fluid model that constitute the emergence of different domains in helium gas with nitrogen impurities.

- The analysis of spatial and temporal distribution of species demonstrates that the different discharge regimes are distinguished with their distinctive properties in the uniform glow and filamentary atmospheric pressure discharges by using three-dimensional fluid model. We have described the evolvement of volume distribution for the uniform atmospheric pressure glow discharge at 30 kHz and compared with the discharge parameters at 50 kHz at the maximum discharge current

density. The numerical simulation results are similar instead of few contrasts, which build up the precise approach in the considered frequency domain. We have explored the volume distribution of space and time variations of discharge parameters at different frequencies, which elucidate the prebreakdown, breakdown, cathode fall layer and decay phases of atmospheric pressure discharge.

- The values of discharge current density are modified in different driving frequency regimes under similar external operating conditions, which exhibit the association between these mentioned quantities. The appearance and configuration of filaments are diagnosed by using the spatial pattern of electronic and ionic species of constricted filamentary discharge at 10 kHz frequency in the presence of imposed conditions, such as overvoltage and increased recombination coefficient of molecular nitrogen ions.

- We have compared the distinct structure of filaments at lower frequencies because the filaments coalesce at higher frequencies and form a uniform or partially uniform distribution of discharge. It is observed that the strength of axial electric field inside the filament is greater than the filamentary discharge plasma, which varies from the head to the tail of filament. However, the magnitude and direction of the movement of filaments are examined with the slice distribution of electrons at different locations in the reactor gap, which illuminate the path and constricted part of density during the progression in the filamentary discharge.

Finally, the three-dimensional fluid model provides the well-defined internal details of atmospheric pressure discharge parameters in the uniform and filamentary discharge modes. The spatial and temporal profiles of discharge species are simulated at variable driving frequencies, which explore the physical significance of uniform and filamentary discharge with the trapping mechanism of charge carriers. Thus, on the basis of multi-dimensional fluid model observations, findings and analysis, we can say that the fluid model simulations are reliable and make a satisfactory bridge between the experiment and theory in order to uncover the complex characteristics and hidden features of atmospheric pressure discharge. The above mentioned distinctions allow a promising and remarkable future for the atmospheric pressure discharge applications and sources in different scientific disciplines for the progress and betterment of humanity.

Bibliography

[1] L. Kennedy and A. Fridman, Plasma Physics and Engineering, April 15, 2004.

[2] L. Loeb, Electrical Coronas and their Basic Physical Mechanisms, University of California Press, 1965.

[3] Vernadsky, G., Rise of Science in Russia 1700 - 1917, Russian Review A, Vol. 28, No. 1, 37 - 52, 1969.

[4] Y. P. Raizer, Gas Discharge Physics, Springer-Verlag Berlin, 1991.

[5] R. A. Haas, Phys. Rev. A8, 1017, 1973.

[6] M. Laroussi, G. E. Sayler, B. B. Glascock, B. Mccurdy, M. E. Pearce, N. G. Bright and C. M. Malott, IEEE Transactions on Plasma Science, Vol. 27, No. 1, 34 - 35, February 1999.

[7] T. Yokoyama, M. Kogoma S. Kanazawa, T. Moriwaki and S. Okazaki, J. Phys. D: Appl. Phys., Vol. 23, 374 - 377, 1990.

[8] S. Kanazawa, M. Kogoma, T. Moriwaki, and S. Okazaki, J. Phys. D: Appl. Phys., Vol. 21, 838 - 840, 1988.

[9] S. T. Surzhikov and J. S. Shang, Journal of Computational Physics, 199, 437 - 464, 2004.

[10] S. T. Surzhikov, High Temperature, Vol. 43, No. 6, 825 - 842, 2005.

[11] B. Eliasson and U. Kogelschatz, IEEE Transactions on Plasma Science, Vol. 19, 1063 - 1077, 1991.

[12] U. Kogelschartz, B. Eliasson, and W. Egli, Pure Appl. Chem., Vol. 71, 1819 - 1828, 1999.

[13] Kogelschatz U., IEEE Transactions on Plasma Science, Vol. 30, 1400 - 1408, 2002.

[14] Sobel A., IEEE Transactions on Plasma Science, Vol. 19, 1032 - 1047, 1991.

[15] F. Massines, A. Rabehi, P. Decomps, R. B. Gardi, P. Segur and C. Mayoux, J. Appl. Phys., Vol. 83, No. 6, 15 March 1998.

[16] A. P. Napartovich, Plasmas and Polymers, Vol. 6, No. 1/2, June 2001.

[17] A. M. Howaton, Introduction to gas discharge, second edition, Pergamon press, Oxford.

[18] M. A. Liebermann and A. J. Lichtenberg, Principles of Plasma Discharges and Materials Processing, John Wiley & Sons, Inc., New York, New York, 1994.

[19] F. M. Penning, Electrical Discharges in Gases, The Macmillan Company, New York, New York, 1957.

[20] J. A. Hornbeck, Phys. Rev. 84, 615, 1951.

[21] B. Chapman, Glow discharge processes, A Wiley-Interscience publication, John Wiley & Sons, New York.

[22] E. E. Ferguson, F. C. Fehsenfeld, and A. L. Schmeltekopf, Phys. Rev. A, Vol. 138, 381 - 385, 1965.

[23] Annemie Bogaerts, Ph.D Thesis, 1996, Universitet Antwerpen, Universitaire Instelling Antwerpen.

[24] J. M. Meek and J. D. Graggs, Electrical breakdown of gases, Clareendon, Oxford 1953.

[25] S. C. Brown, Basic data of plasma physics, MIT Press, Cambridge, MA 1959.

[26] M. Meyyappan Editor, Computational Modeling in Semiconductor Processing, 1995 Artech House, Inc., 685 Canton Street, Norwood, MA 02062.

[27] E. Gogolides and H. H. Sawin, J. Appl. Phys. 72, Vol. 9, 3971 - 3987, 1992.

[28] R. Veerasingam, R. B. Campbell and R. T. McGrath, Plasma Sources Sci. Technol. 6, 157 - 169, 1997.

[29] X. M. Zhu and M. G. Kong, J. Appl. Phys. 97, 083301, 2005.

[30] T. J. Sommerer and M. J. Kushner J. Appl. Phys. Vol. 71, No. 4, 15 February 1992.

[31] Yu. B. Golubovskii, V. A. Mairov, J F Behnke, J. Tepper and M. Lindmayer, J. Phys. D: Appl. Phys., Vol. 37, 1346-1356, 2004.

[32] Anderson C., Hur M. and Zhang P, J. Appl. Phys., Vol. 96, 1835-1839, 2004.

[33] G. Nersisyan and W. G. Graham, Plasma Sources Sci. Technol., Vol. 13, 582-587, 2004.

[34] P. Boeuf, Phys. Rev. A 36, Vol. 6, 2782, 1987.

[35] J. Meunier, Ph. Belenguer and J. P. Boeuf, J. Appl. Phys. Vol. 78, 731-745, 1995.

[36] F. Chen, Introduction to Plasma Physics and Controlled Fusion, Plenum Press, New York, 1984.

[37] G. J. M. Hagelaar, Ph.D Thesis, Technische Universiteit Eindhoven, 2000.

[38] H. W. Ellis, R. Y. Pai, E. W. McDaniel, E. A. Mason, and L. A. Viehland, Atomic Data and Nuclear Data Tables 17 (3), 177 - 210, 1976.

[39] H. W. Ellis, M. G. Thackston, E. W. McDaniel, and E. A. Mason, Atomic Data and Nuclear Data Tables 31, 113 - 156, 1984.

[40] J. P. Boeuf and L. C. Pitchford, Phys. Ref. E 51, Vol. 2, 1376 - 1390, 1995.

[41] J. D. P. Passchier and W. J. Goedheer, J. Appl. Phys. 74, No. 6, 15 September 1993.

[42] F. M. White, Viscous Fluid flow, 2nd edition, New York, McGraw-Hill, 1991.

[43] Number of Meetings with Prof. Miles Turner, NCPST, DCU, 2005 - 2009.

[44] P. S. Kothnur and L. L. Raja, Contrib. Plasma Phys. 47, No. 1, 9 - 18, February 2007.

[45] P. S. Kothnur and L. L. Raja, J. Appl. Phys., No. 97, 043305, 2005.

[46] Scharfetter D. L. and Gummel H. K., IEEE Transactions on Electron Devices, Vol. 16, 64 - 77, 1969.

[47] J. K. Lee, Lecture notes, ECE4900, EM-Plasma, 2006.

[48] L. L. Alves, G. Gousset and C. Ferreira, Phys. Rev. E 55, Vol. 1, 890, 1997.

[49] A. Salabas, Ph.D Thesis, Instituto Superior Techico, October 2003.

[50] R. Morrow and N. Sato, J. Phys. D: Appl. Phys., Vol. 32, pp. L20 - L22, 1999.

[51] BOLSIG+, freeware, www.siglo-kinema.com/bolsig.htm.

[52] Brunger M., Buckman S. J. and Allen L. J., J. Phys. B: At. Mol. Opt. Phys. 25 1823 - 38, 1992.

[53] X. Yuan and L. L. Raja, IEEE Transactions on Plasma Science, Vol. 31, No: 4, August 2003.

[54] A. S. Petrusev, S. T. Surzhikov, and J. S. Shang, High Temperature, Vol. 44, No. 6, 804 - 813, 2005.

[55] R. Deloche, P. Monchicourt, M. Cheret, and F. Lambert, Phys. Rev., Vol. 13, No. 3, 1140 - 76, March 1976.

[56] J. Stevefelt, J. M. Pouvesle and A. Bouchoule, J. Chem. Phys., Vol. 76, 4006, 1982.

[57] C. B. Collins, H. S. Hicks, W. E. Wells and R. Burton, Phys. Rev. A 6, 1545, 1972.

[58] S. Rauf and M. J. Kushner, J. Appl. Phys., Vol. 85, 3460 - 3469, 1999.

[59] Pouvesle J. M., Bouchoule A. and Stevefelt J., J. Chem. Phys., Vol. 77, 817 - 825, 1982.

[60] Yu. B. Golubovsskii, V. A. Mairov, J. Behnke and J. F. Behnke, J. Phys. D: Appl. Phys., Vol. 36, 39 - 49, 2003.

[61] E. W. McDaniel, Collision phenomena in ionized gases, John Wiley & Sons, Inc., New York London Sydney, 1964.

[62] M. McFarland, D. L. Albritton, F. C. Fehsenfeld, E. E. Ferguson, and A. L. Schmeltekopf, J. Chem. Phys. 59, Vol. 12, 6610 - 6619, 1973.

[63] K. W. Morton and D. F. Mayers, Numerical Solution of Partial Differential Equations, Cambridge University Press, 1994.

[64] J. D. Anderson, JR, Computational Fluid Dynamics, McGraw-Hill, Inc, 1995.

[65] K. W. Morton and D.F. Mayers, Numerical Solution of Partial Differential Equations, Cambridge University Press, 1994.

[66] P. J. Roache, Computational Fluid Dynamics, Hermosa, Albuquerque NM, 1976.

[67] M. S. Barnes, T. J. Colter and M. E. Elta, J. Appl. Phys. 61, Vol. 1, 81 - 89, 1987.

[68] J. P. Boeuf and L. C. Pitchford, Phys. Ref. E 51 (2), 1376 - 1390, 1995.

[69] G. Lapenta, F. Iinoya, and J. U. Brackbill, IEEE Trans. Plasma Sci. 23, Vol. 4, 769, 1995.

[70] J. Thibault, Numerical Heat Transfer, Vol. 8, 281 - 298, 1985.

[71] M. Peric, Numerical Heat Transfer, Vol. 11, 251 - 279, 1987.

[72] Peaceman, D. W., Rachford, H. H., Jr., J. Soc. Indust. Appl. Math. 3, 1955, 28 - 41.

[73] Douglas Jr., Jim, 1962, Numerische Mathematik 4, 41 - 63.

[74] B. A. Carré, The Computer Journal, 1961, Vol. 4, 1, 73 - 78.

[75] M. Zedan and G. E. Schneider, AIAA Journal, Vol. 21, No. 2, Feb 1983.

[76] F. Massines, N. Gherardi, N. Naude and P. Segur, Plasma Phys. Control. Fusion 47, B577 - B588, 2005.

[77] R. Brandenburg, V. A. Mairov, Yu. B. Golubovsskii, H-E Wagner, J. Behnke and J. F. Behnke, J. Phys. D: Appl. Phys., Vol. 38, 2187 - 2197, 2005.

[78] Yu. B. Golubovsskii, V. A. Mairov, J. Behnke and J. F. Behnke, J. Phys. D: Appl. Phys., Vol. 35, 751 - 761, 2002.

[79] Z. Navratil, R. Brandenburg, D. Trunec, A. Brablec, P. Stahel, H-E Wagner and Z. Kopecky, Plasma Sources Sci. Technol. 15, 8 - 17, 2006.

[80] Y. H. Wang, Y. T. Zhang, D. Z. Wang and M. G. Kong, J. Appl. Phys., Vol, 94 No. 9, 1 November 2003.

[81] L. Mangolini, C. Anderson, J. Heberlein and U. Kortshagan, J. Phys. D: Appl. Phys., Vol. 37, 1021 - 1030, 2004.

[82] Yu. B. Golubovsskii, V. A. Mairov, J. Behnke and J. F. Behnke, J. Phys. D: Appl. Phys., Vol. 36, 39 - 49, 2003.

[83] X. Yuan, J. Shin and L. L. Raja, Vauuum 80, 1199 - 1205, 2006.

[84] D. S. Nikandrov and L. D. Tsendin, Technical Physics, Vol. 50, No. 10, 2005, pp. 1284 - 1294.

[85] D. Lee, J. M. Park, A. H. Hong and Y. Kim, IEEE Transactions on Plasma Science, Vol. 33, No. 2, 949 - 957, 2005.

[86] Y. Wang, D. Wang Physics of Plasmas 12, 023503, 2005.

[87] F. Tochikubo, T. Chiba and T. Watanabe, Jpn. J. Appl. Phys. Vol. 38, 5244 - 5250, 1999.

[88] Y. T. Zhang, D. Z. Wang and M. G. Kong, J. Appl. Phys., Vol, 100, 063304, 2006.

[89] T. Braun, J. A. Lisboa and R. E. Francke, Vo. 59, No. 6, Physical Review Letters, August 1987.

[90] F. Massines, P. Segur, N. Gherardi, C. Khamphan and A Ricard, Surface and Coating Technology, 174 - 175, 8, 2003.

[91] K. R. Stalder, G. Nersisyan and W. G. Graham, J. Phys. D: Appl. Phys. 39, 3457 - 3460, 2006.

[92] Yu. V. Yurgelenas and H-E Wagner, J. Phys. D: Appl. Phys., Vol. 39, 153 - 163, 2006.

[93] F. Massines and G. Gouda, J. Phys. D: Appl. Phys. Vol. 39, 4031 - 4043, 2006.

[94] I. Brauer, C. Punset, H. G. Purwins and J. P. Boeuf, J. Appl. Phys., Vol. 85, No. 11, 1 June 1999.

[95] D. Braun, V. Gibalov and G. Pietsch, Plasma Sources Science and Technology, Vol. 1, 166 - 174, 1992.

[96] F. F. Young and Chwan-Hwa Hohn John Wu, IEEE Trans. Plasma Sci., Vol. 21, No. 3, June 1993.

[97] A. A. Kulikovsky, J. Phys. D. Appl. Phys., Vol. 28, 2483 - 2493, 1995.

[98] S. Okazaki, M. Kogoma, M. Uehara, and Y. Kimura, J. Phys. D: 26, 889, 1993.

[99] Y. Wang and D. Wang, Plasma Science and Technology, Vol. 8, No. 5, September 2006.

[100] P. Zhang and U. Kortshagan, J. Phys. D: Appl. Phys., Vol. 39, 153 - 163, 2006.

[101] Anderson C., Hur M. and Zhang P, J. Appl. Phys., Vol. 96, 1835 - 1839, 2004.

[102] L. Mangolini, K. Orlov and U. Kortshagan, Appl. Phys. Lett., Vol. 80, 1722 - 4, 2002.

[103] Y. P. Raizer and S. T. Surzhikov, Teplifizika Vysokikh Temperatur, Vol. 26, No. 3, 428 - 435, 1988.

[104] Zhang Y. T., Wang D. Z., Wang Y. H. and LIU Cheng-Sen, Chin. Phys. Lett., Vol. 22, No. 1, 171 - 174, 2005.

[105] Yu. B. Golubovsskii, V. A. Mairov, J F Behnke, J. Tepper and M. Lindmayer, J. Phys. D: Appl. Phys., Vol. 37, 1346 - 1356, 2004.

[106] QU Qiong-Rong and Meng Zhao-Xing, Chin. Phys. Lett., Vol. 21, No.7, 1317, 2004.

[107] LIU Peng, ZHAN Ru-juan, WEN Xiao-hui, ZHU Xiao-dong and LI Ding, Plasma Science and Technology, Vol. 4, No.3, May 2002.

[108] S. Pavon, J-L Dorier, Ch Hollenstein, P. Ott and P. Leyland, J. Phys. D: Appl. Phys. 40, 2007, 1733 - 1741, 2007.

[109] N. Takeuchi, K. Yasuoka and S. Ishii, IEEE Trans. Plasma Sci., Vol. 35, No. 6, December 2007.

[110] R. Sh. Islamov, IEEE Trans. Plasma Sci., Vol. 27, No. 1, pp. 88 - 89, February 1999.

[111] S. B. Leonov, K. V. Savelkin, D. A. Yarantsev and A. S. Yuriev, International Conference “High Speed Flow: Fundamental Problems”, Moscow region, Russia, September 21 - 24, 2004.

[112] J. Shin, V. Narayanaswamy, L. L. Raja and N. T. Clemens, AIAA Journal, Vol. 45, No.7, July 2007.

[113] E. Menier, L. Leger, E. Depussay, V. LAgo and G. Artana, J. Phys. D: Appl. Phys. 40, 695 - 701, 2007.

[114] S. Leonov, V. Bityurin, K. Savelkin and D. Yarantsev, PDL-33, AIAA-2002 - 2180.

[115] S. T. Surzhikov and J. S. Shang, AIAA 2005 - 0406, Reno, NV, January 2005.

[116] E. Meeks and M. A. Cappelli, IEEE Trans. on Plasma Science, Vol. 21, No. 6, December 1993.

[117] T. Deconinck, S. Mahadevan and L. L. Raja, IEEE Trans. Plasma Sci., Vol. 35, No. 5, October 2007.

[118] J. S. Shang, AIAA J., 2002; 40 (6): 1178 - 1186.

[119] P. S. Kother and L. L. Raja, J. Appl. Phys., 97, 043305, 2005.

[120] Q. Wang, F. Doll, V. M. Donnelly, D. J. Economou, N. Sadeghi and G. F. Franz, J. Phys. D: Appl. Phys. 40, 4202 - 4211, 2007.

[121] G. I. Font and W. L. Morgan, Contrib. Plasma Phys. 47, No. 1 - 2, 103 - 110.

[122] K. H. Becker, U. Kogelschatz, K. H. Schoenbach, R. J. Barker, Series in Plasma Physics, Bristol and Philadelphia, ISBN0-7503 - 0962 - 8.

[123] I. Muller, C. Punset, E. Ammelt, H. G. Purwins and J. P. Boeuf, IEEE Transactions on Plasma Science, Vol. 27, No. 1, February 1999.

[124] A. Nouri and C. Schmeiser, Z angew Math Phys, Vol. 47, 553 - 566, 1996.

[125] T. Shirafuji, T. Kitagawa, T. Wakai and K. Tachibana, Appl. Phys. Lett., vol. 83, No. 12, 22 September 2003.

[126] L. Stollenwerk, Sh. Amiranashvili, J. -P. Boeuf and H. -G. Purwins, Phys. Rev. Lett., PRL 96, 255001, 2006.

[127] A. A.Kulikovsky, J. Phys. D, Appl. Phys., Vol. 30, pp. 441 - 450, 1997.

[128] H. Akashi, A. Oda and Y. Sakai, IEEE Transactions on Plasma Science, Vol. 33, No. 2, pp. 308 - 309, February 2005.

[129] F. Iza and J. A. Hopwood, IEEE transactions on plasma science, Vol. 33, No. 2, pp. 306 - 307, April 2005.

[130] I. Radu, R. Bartnikas, M. R. Wertheimer, IEEE Transactions on Plasma Science, Vol. 31, No. 6, pp. 1363 - 1378, December 2003.

[131] Xu Tao Deng and M. G. Kong, IEEE Transactions on Plasma Science, Vol. 32, No. 4, pp. 1709 - 1715, December 2004.